Charged Pion and Kaon Production in Central Au+Au Collisions at $\sqrt{s_{NN}} = 200$ GeV

Djamel Ouerdane
Niels Bohr Institute
Denmark

Ph.D. Dissertation in Physics
Faculty of Science — University of Copenhagen

Supervisor : Jens Jørgen Gaardhøje

Preface

In the course of a central ultra–relativistic heavy ion collision, a short–lived state of high energy density ($\gtrsim 1\,\mathrm{GeV/fm^3}$ for $\sim 10^{-23}\,\mathrm{s}$) is formed. As a result of this high excitation, thousands of charged particles are produced. It is this environment which is thought to recreate conditions prevailing early in the universe. During the summer and fall 2001, the Relativistic Heavy Ion Collider (RHIC) collided gold ions at $\sqrt{s_{NN}} = 200\,\mathrm{GeV}$, i.e. the highest center of mass energy achieved so far by a heavy ion accelerator.

The BRAHMS detector, located in the RHIC experimental area, has made unique measurements, among the four RHIC experiments, of charged hadrons over a broad range of rapidity and transverse momentum ($-0.1 < y_\pi < 3.6$ and $0.1 < p_T \lesssim 5\,\mathrm{GeV/c}$). The hadrons produced consist to a large extent of pions and kaons. These unstable particles survive long enough to be directly observed. Therefore, they serve as a probe of the collision dynamics. Of special interest are the kaons, which carry the quark flavor called strangeness, not present in the initial state.

The thesis is divided into eight chapters. After an introduction reviewing the field of relativistic heavy ion collision physics, Chap. 2 focuses on pions and kaons produced in heavy ion collisions. The existing data, from SIS to RHIC energy ranges, are introduced in order to start a discussion on the evolution of the collision dynamics with $\sqrt{s_{NN}}$. This is followed by theoretical descriptions of meson production (statistical models and parton cascade models). Chap. 3 is devoted to the BRAHMS experimental setup while details on particle identification are given in Chap. 4. In Chap. 5 is explained how invariant transverse momentum spectra are constructed. From there, results are presented in Chap. 6, where pion and kaon distributions are investigated as a function of rapidity, together with estimations of systematic errors. In Chap. 7, the energy systematics introduced in Chap. 2 is fully discussed in the light of the results given in Chap. 6. Theoretical predictions are then compared to the data. A conclusion in Chap. 8 puts an end to the thesis.

The results presented in this thesis are preliminary, and as such, not official published BRAHMS results. Before quoting the results, please contact the author [1] and the spokespersons of the BRAHMS collaboration [2].

Research carried out in part at the Relativistic Heavy Ion Collider, Brookhaven National Laboratory, which is supported by the U.S. Department of Energy, Division of Nuclear Physics of the Office of Science, under contract with BNL (No. DE–AC02–98CH10886).

[1] Djamel Ouerdane, ouerdane@nbi.dk
[2] Flemming Videbæk, videbaek@bnl.gov and Jens Jørgen Gaardhøje, gardhoje@nbi.dk

Acknowledgments

This thesis is the result of three years of hard work that would not have been possible without a constant and close collaboration with many people. Since it is the only place in this dissertation where personal feelings and gratitude can be expressed, let me do it properly. First of all, let me warmly thank my supervisor Jens Jørgen Gaardhøje. My danish adventure would not have become real without his trust and support since the very beginning, three years and a half ago. Jens Jørgen has always been supportive and inspiring in periods of doubt or when I was rushing to finish preparing presentations, critical and sharp when some aspects of my work needed (severe) improvements, and most of all, I found in Jens Jørgen that professionalism and easy attitude in such a competitive domain can naturally and simply coexist. Thanks a lot JJ! Another special thank goes to the other seniors of the HEHI group, Ole Hansen, Ian Bearden, Hans Bøggild and Pawel Staszel. The four of them, in very different ways, have been sources of experience and knowledge that I could benefit from at times. Their constant availability was really helpful. I also appreciated working with these four francophiles, although I must say they have rather different ways of showing their (deep) love for France! I also have to express my gratitude to the HEHI students, Peter, Claus, Marco, Christian, David and Erik. We had quite some fun working or partying together and I must say we made a great team. A special thank goes to Peter, my office mate with whom I shared the sweet and sour of being a Ph.D. student in nuclear physics. My stay in Copenhagen was not a continuous three years in Denmark, sitting behind the same computer, in the same office, day after day. I came to travel a lot around the world and had the great opportunity to stay a few weeks in New York, where the BRAHMS experiment and RHIC collider reside. I met there the rest of the BRAHMS collaboration, in particular its spokesman Flemming Videbæk, from whom I really learned a lot. Many thanks to all the people who make BRAHMS. As I said, my stay in Copenhagen was not that stable, especially during the first year where I had to move around quite a lot. I have to thank here the many people, living in Copenhagen or abroad, that helped me in all sorts of ways. Sorry for not listing names, there are far too many! The last and warmest thank go to my family, especially my mother who encourages me wherever my fate leads me. T'as vu m'man, j'y suis arrivé!

Djamel Ouerdane
Copenhagen, July 2003

Contents

List of Figures

List of Tables

Chapter 1

Introduction

Ultra–relativistic heavy ion collisions are a powerful tool for probing properties of matter under extreme conditions. The main goal is to characterize the properties of highly dense and hot states that matter under ordinary conditions does not exhibit, and measure a transition to a phase called the Quark Gluon Plasma, not yet clearly put in evidence. This chapter introduces the field of relativistic heavy ion collisions by reviewing relevant theoretical tools and some key experimental data.

1.1 Heavy Ion Collisions and Phase Transitions

The goal of heavy–ion collisions is to study hot and dense states of hadronic matter. The order of magnitude of temperatures and pressures reached in such collisions bears no comparison with everyday life conditions due to the strong binding energy existing in the heart of atomic nuclei in contrast with the weak bonds between e.g. water molecules. Nevertheless, like water becoming steam when heated up above a critical temperature, nuclear matter undergoes phase transitions. The nature of the phase transition depends on the initial energy converted into matter excitation. For example, the liquid–gas phase transition happens when the energy is above the Coulomb barrier of the colliding nuclei (a few tens of MeV per nucleon). It has been experimentally put in evidence, as can be seen in Fig. 1.1 showing the correlation between the temperature and the excitation energy per nucleon, called caloric curve. The universality of the data as well as the plateau–like shape are characteristic of a first order[1] liquid–gas phase transition [1, 2]. Another phase–transition from hadron gas to a more exotic

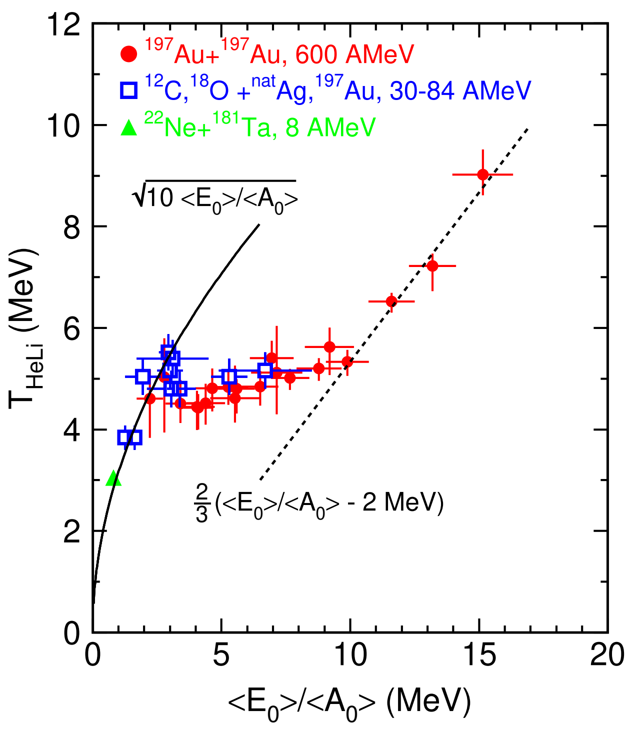

Fig. 1.1: Caloric curve constituted by the nuclear temperature as a function of the excitation energy per nucleon [1].

[1] i.e. showing a discontinuity.

state is predicted to happen when much higher temperature and pressure are reached. The next sections give an overview of the theoretical framework and predictions of this "new" form of matter and its implication in the current knowledge of the fundamental properties of matter.

1.2 The Quark Gluon Plasma

Hadronic matter is made of quarks. Hadrons are divided into two groups, the baryons consisting of three quarks like the nucleons (qqq), and mesons consisting of a quark and anti–quark like pions and kaons ($q\bar{q}$). Quarks are characterized by the flavor quantum number. There are six flavors: u (up), d (down), s (strange), c (charm), b (bottom) and t (top). Quarks also carry a charge called color, together with the well known electrical charge[2]. Color charges are red, green and blue + anti–colors. It happens that only color neutral objects have been observed in nature so far. A baryonic color state is always ($q_r q_b q_g$), a mesonic color state is ($q_c \bar{q}_{\bar{c}}$) while flavor combinations are not so much restricted (the total electrical charge has to be a multiple of the unit charge e). The interaction between color charges is called the strong interaction, formally described by the Quantum–Chromo–Dynamics (QCD), a gauge theory like Quantum–Electro–Dynamics (QED) describing the electromagnetic interaction, but based on the symmetry of the special unitary group $SU(3)$. The generators of this symmetry group[3] are related to the physical gluons, the vectors of the strong interaction binding quarks with each other. There is a fundamental difference between gluons (QCD) and photons (QED): although massless like photons, gluons carry color charges. This remarkable fact leads to color confinement.

1.2.1 QCD Confinement

Since gluons carry color charges, they are subject to a color self–interaction. This gives rise to a coupling constant α_s, indicator of the strength of the interaction, which can be written as follows:

$$\alpha_s\left(|Q|^2\right) = \frac{\alpha_0}{1 + \frac{\alpha_0}{12\pi}\left(11n_c - 2n_f\right)\log\frac{|Q|^2}{\mu^2}} \tag{1.1}$$

where Q is the four–momentum transfer involved in the interaction process, μ a scale constant such that $\mu \ll |Q|$, n_c the number of color charges (3) and n_f the number of flavors (see Fig. 1.2). From this formula, it can be seen that if Q is small, α_s is large and vice-versa. This affects the form of the potential between two heavy quarks (V_{qq}) as a function of their relative distance:

$$V_{qq}(r) = -\frac{A(r)}{r} + a\,r \tag{1.2}$$

where $A(r)$ is proportional to $1\,/\,\log(1/r)$ and a is a constant called the string tension which is the slope of the linear part of the potential, whose value is $\sim 1\,\mathrm{GeV/fm}$ (see Fig. 1.3). The form of the potential V_{qq} implies that as the distance r between quarks increases, the potential increases as well and acts against the separation, this is the color confinement. Due to the

[2]Constituent quarks carry fractions of the unit electrical charge e.
[3]from the Lie algebra formalism

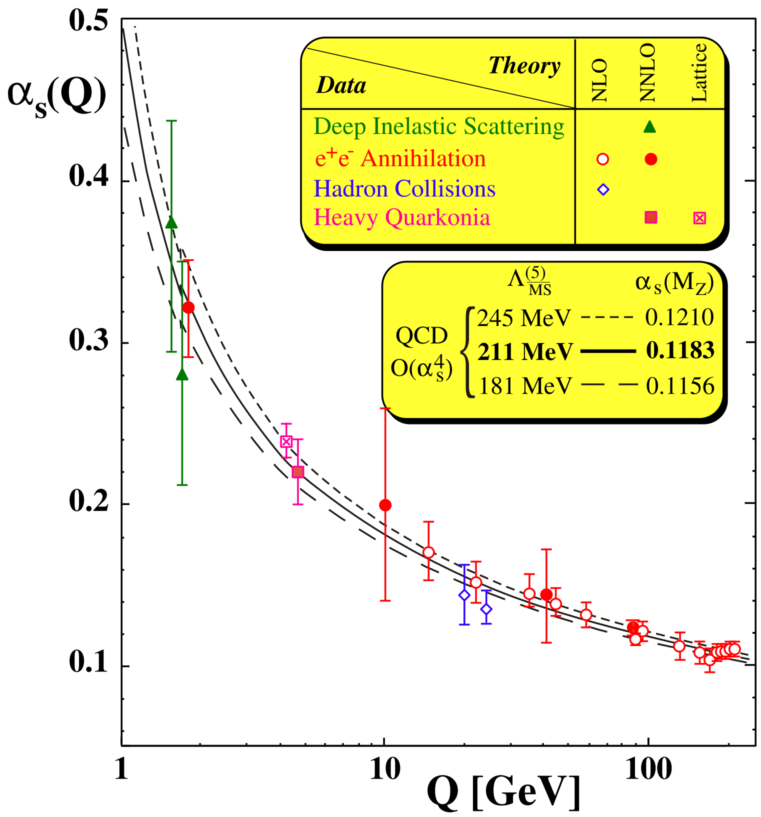

Fig. 1.2: Running coupling constant α_s of the strong interaction as a function of the momentum transfer Q (figure from [3]).

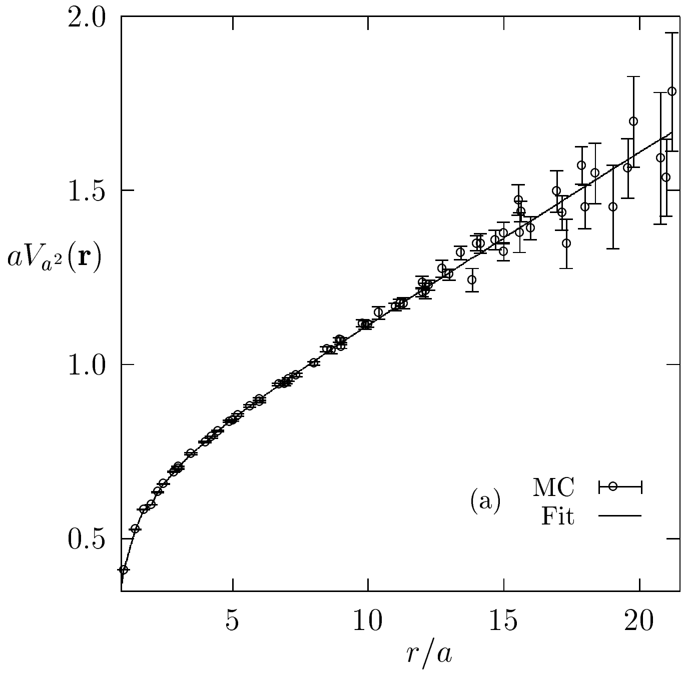

Fig. 1.3: Quark–quark potential $V_{qq}(r)$. The parameter a is the string tension (figure from [4]).

gluon self–interaction, the color field between the quarks is confined in a narrow flux tube, so the system reminds of a string. When r becomes large, i.e. quarks are separated, it is energetically possible to form a pair or more of quark and anti–quark from the large potential energy between them. The color string eventually breaks up and new hadrons are formed. This is why no "free" quarks have been yet observed at normal temperatures ($T \sim 0$) and densities ($\rho \sim 0.17\,\mathrm{GeV/fm^3}$). But if the distance r gets small, the bond between quarks becomes loose, this is the so–called asymptotic freedom.

1.2.2 Deconfinement and QGP

In heavy–ion collisions, the nuclear material gets compressed for a short while ($\sim 10^{-23}\,\mathrm{s}$). The nucleons overlap in such a way that their constitutive quarks could interact directly and roam freely inside the nuclear volume: the hadrons "melt" (see Fig. 1.4).

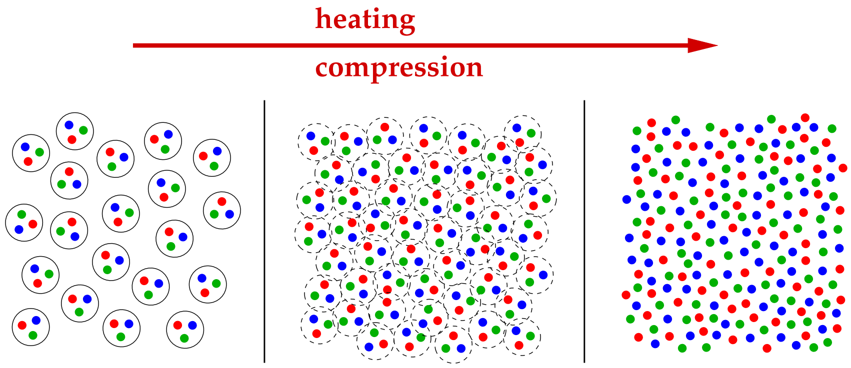

Fig. 1.4: Simple picture of nuclear matter matter melting into QGP.

If this deconfined phase is thermally equilibrated, meaning that it can be characterized by a thermodynamical temperature (cf. Chap. 2), it is called the Quark Gluon Plasma (QGP). If the transition from confined to deconfined matter is a first order transition, it is characterized by a critical temperature T_c.

Lattice QCD

The number of degrees of freedom is expected to increase dramatically at the phase transition from the hadronic (hadron gas) to partonic phase (QGP). Since QCD becomes perturbative only at very large values of Q (or small α_s), it is not possible to get an analytical derivation of the phase transition. However, numerical methods are used such as Lattice QCD [5, 6] to investigate the evolution of the nuclear matter states. Figure 1.5 illustrates results from such calculations. As can be seen, the energy density shows a sharp rise when the temperature increases above the critical temperature T_c and vary very little at T well above T_c. Lattice QCD therefore does predict the phase transition hadron gas–QGP. The calculated critical temperature is $T_c \sim 172 \pm 3\,\mathrm{MeV}$ at vanishing baryo–chemical potential μ_B[4]. The same lattice calculations estimate the evolution of the heavy quark–quark potential V_{qq} with temperature. As can be seen from the right panel of Fig. 1.5, the potential decreases at distances beyond $r \sim 0.25\,\mathrm{fm}$ and eventually flattens for $T > T_c$. This means that the color charge gets screened at distances of this order, dissolving the bound state of quarks. From an experimental

[4] see definition of μ_B in Chap. 2.

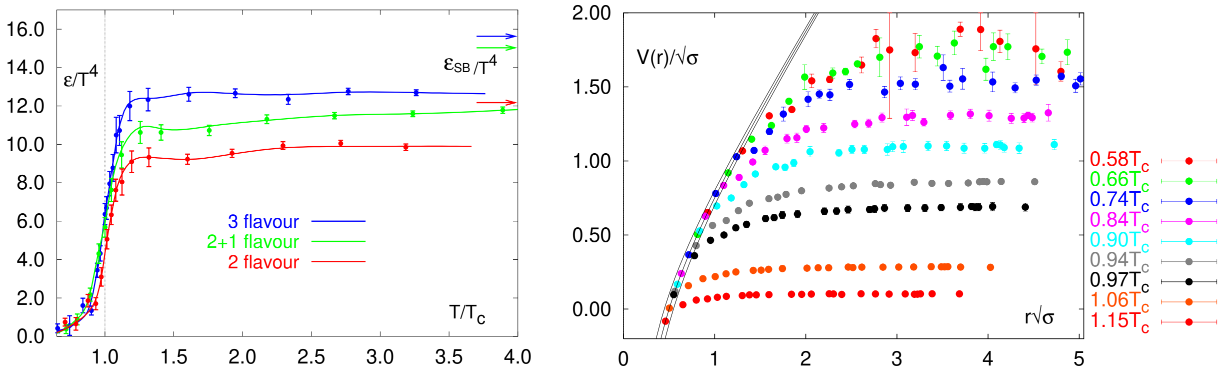

Fig. 1.5: Left: Evolution of the energy density with temperature predicted by Lattice QCD calculations. For all calculations, the sharp energy increase around a temperature $T = T_c$ reveals a phase transition to QGP. Right: Evolution of the QCD potential with temperature. As T increases, the potential flattens off. At $T > T_c$, the potential is negligible, the color charge is screened and quarks evolve freely (figure from [5]).

point of view, ultra–relativistic heavy–ion collisions are the sole existing laboratory tool to apprehend such high temperatures and measure this phase–transition. It also gives the unique opportunity to characterize the properties of "*extended space–time regions containing a locally modified vacuum state*" [7].

1.3 Relativistic Heavy Ion Collisions

In this section are given some central "pictures" of relativistic heavy–ion collisions. The variables used are defined in Appendix B. Figure 1.6 illustrates a schematic view of two nuclei of the same kind approaching each other in the center of mass (CM) frame of these nuclei. The nuclei are Lorentz contracted in their direction of motion due to their relativistic

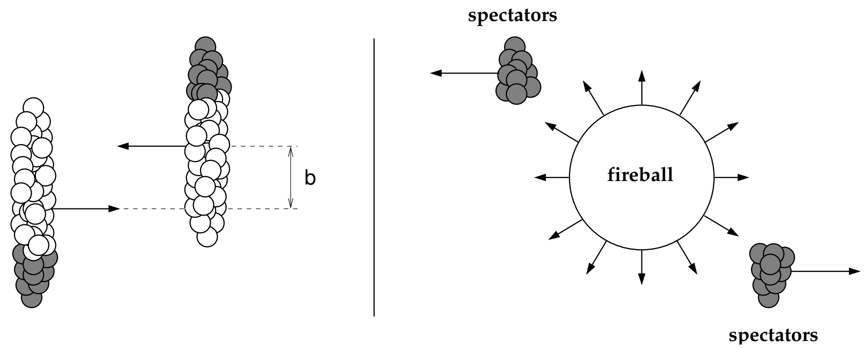

Fig. 1.6: Schematic view of a relativistic heavy ion collision : two nuclei approaching each other at an impact parameter b (left), spectators flying away and expanding fireball (right).

speed. The transverse distance between their trajectories (defined by the motion of their respective centers) is called the impact parameter b. In the region of overlap, nucleons are called participants, they interact strongly and give rise to an expanding volume of high energy density called the fireball. Outside this overlap, non interacting nucleons are spectators, they keep their original momentum and fly away from the hot zone without "participating".

1.3.1 Collision Centrality

The spectator–participant picture is used to characterize the centrality C. The latter is related to the overlap surface in the transverse plane of the colliding nuclei and is defined as

$$C = \left[\int_0^{b_c} \frac{d\sigma_{in}(b')}{db'} \, db' \right] / \sigma_{in} \tag{1.3}$$

where σ_{in} is the total inelastic cross–section and b_c the impact parameter cut–off. From this definition, C is the probability that a collision occurs at $b \le b_c$. For two identical colliding solid spheres, $\frac{d\sigma_{in}(b)}{db} = 2\pi b db$. Therefore, since $b_{max} = 2R$, where R is the sphere radius, one obtains $C = \frac{b_c^2}{4R^2}$. For gold nuclei with 197 nucleons each, $R = 1.2 \times 197^{1/3}$. Therefore, the centrality range 0–5% corresponds to impact parameters ranging from 0 to 3.1 fm.

Since the impact parameter b is not directly measurable, one uses experimental observables like the number of produced charged particles. Indeed, this number is correlated to the number of participants. Quantitatively, the number of participants is estimated by the Glauber model [8, 9]. Figure 1.7 shows the correlation between the number of participating nucleons and the impact parameter for Au+Au collisions, based on the Glauber parametrization (used e.g. by the event generator HIJING [10]). In this model, three assumptions are made:

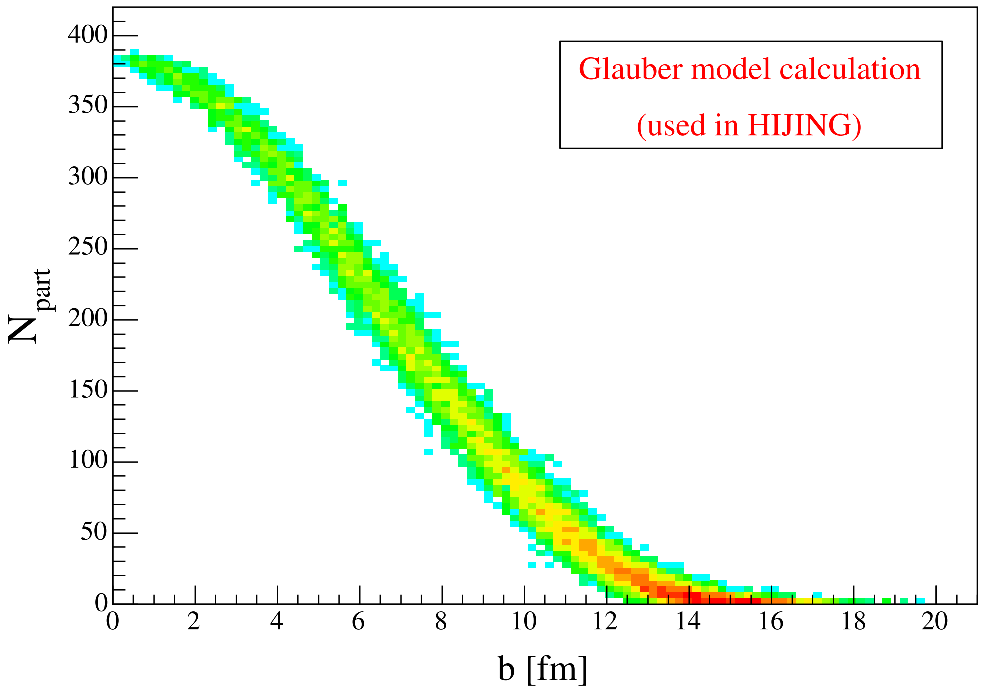

Fig. 1.7: Number of participants versus impact parameter based on the Glauber model.

→nucleons are distributed according to a density function (e.g. Wood–Saxon),
→nucleons travel in straight lines and are not deflected by interactions,
→nucleons interact with the inelastic cross–section σ_{NN} measured in p+p collisions at the same initial energy even after multiple interactions

There are two practical ways to use the Glauber model. One is a Monte Carlo (MC) calculation where nucleons are distributed in the nuclei according to the density function while the other uses the optical–limit approach where the problem is solved by numerical integrals. Both methods agree in the number of participants calculated at a given impact parameter but differ in the total cross–section because the optical–limit approach imposes a cut–off in the maximum impact parameter. Therefore, large differences exist between the two calculations in peripheral collisions.

1.3.2 Collision Transparency

The concept of transparency is linked to the baryon stopping. It is illustrated in Fig. 1.8. A collision is called transparent when the original nucleons left little of their initial kinetic

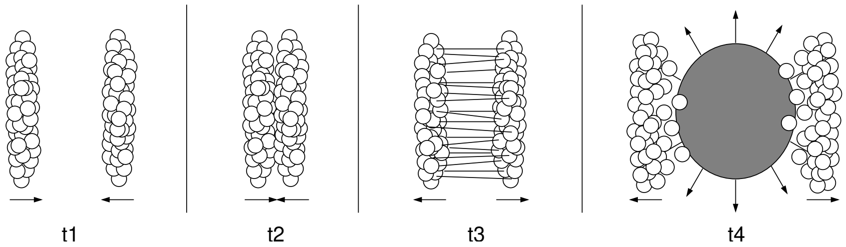

Fig. 1.8: Simplistic view of a transparent collision. The participant nucleons keep most of their initial momentum but leave a highly excited zone between the nuclei (excited color fields) that give rise to a net–baryon poor fireball.

energy during the interpenetration of the colliding nuclei. In that case, as the original nucleons move away from the interaction zone at a barely altered rapidity[5], the mid-rapidity zone is characterized by a net–baryon density ($N_{net} = N_B - N_{\bar{B}}$) close to zero due to baryon number conservation, meaning that the baryons and anti-baryons detected at mid-rapidity are all produced.

Conversely, the full–stopping scenario implies that the original nucleons are mostly distributed around mid-rapidity, with a maximum at $y = y_{CM}$ (see Fig. 1.9). In that case, N_{net} is greater

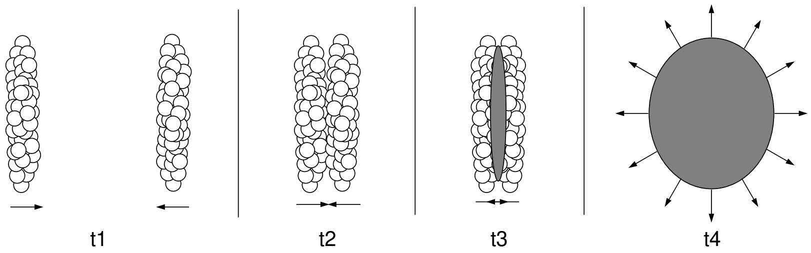

Fig. 1.9: Simplistic view of the nucleon stopping. The participant nucleons lose most of their initial momentum, they are stopped. In that case, the fireball is net–baryon rich.

than zero at y_{CM} and the fireball is net–baryon rich. The concept of transparency and stopping were investigated by Bjorken in 1983 [11]. He described the evolution of the central rapidity region in heavy–ion collisions based on observations from p+p collisions and hydrodynamics. The assumptions in the Bjorken picture are:

[5]The concept of rapidity density is explained in appendices B and E.

Boost invariance Since rapidity densities dN/dy are independent of rapidity for at least a few units of rapidity around mid–rapidity in p+p and p+A collisions, it is assumed to be true in A+A collisions as well.

Transparency Fragments of the original nuclei do not end up in the central rapidity region, solely populated by particles produced from the breaking of color strings.

2D–problem The transverse expansion of the source is ignored because of the large initial transverse scale of the source compared to its longitudinal scale. This is at least true from central collisions and reduces the problem to the coordinate z (ion direction of motion) and t (time).

Expansion At some early time, assumed to be of the order of the characteristic hadronic formation time scale $t \sim 1\,\mathrm{fm/c}$, the system thermalizes and hydrodynamics governs the evolution and expansion of the source.

The boost invariance assumption implies that the initial energy density is the same in different Lorentz frames at the same local time. Due to the homogeneity of the source in all frames, there is no pressure gradient to change the longitudinal flow and the velocity of each fluid element remains the same. If at $t = 0$, right after the nuclei have collided, the longitudinal extent of the source is negligible, the relation $z = \beta t$ holds true at all times $t > 0$. The proper time τ is then

$$\tau = \frac{t}{\gamma} = \sqrt{t^2 \left(1 - \frac{z^2}{t^2}\right)} = \sqrt{t^2 - z^2} \tag{1.4}$$

As the evolution looks the same in all mid–rapidity like frames, energy density and pressure only depend on τ. Isoenergy and density curves are therefore hyperbolas in the (z, t) space and can be used to distinguish between the different phases of the collision evolution. A possible evolution of A+A collisions is illustrated in Fig. 1.10.
During hydrodynamical expansion, entropy[6] is preserved. Therefore, the entropy at thermalization is the same at freeze–out, when no more interactions between particles occur. If the initial entropy can be calculated, the final multiplicities can be predicted. Hence, the initial energy density ϵ can be deduced from the measured multiplicities dN/dy:

$$\epsilon = \frac{\langle E \rangle}{V} = \frac{\langle m_T \rangle \cosh{(y)} \frac{dN}{dy} \Delta y}{\mathcal{A} \Delta z} = \frac{\langle m_T \rangle}{\mathcal{A} \tau} \frac{3}{2} \frac{dN^{ch}}{dy} \tag{1.5}$$

where τ is the initial formation time, usually taken to be the thermalization time–scale 1 fm/c and $\mathcal{A}$ is the transverse area of the zone (the relation $z = \tau \sinh{(y)}$ is used to get the final term).

1.4 Experimental Highlights

(Ultra)relativistic heavy–ion collision experiments carried out at the Heavy–ion Synchrotron (SIS), Alternating Gradient Synchrotron (AGS), Super Proton Synchrotron (SPS) and the Relativistic Heavy–Ion Collider (RHIC) have provided an outstanding amount of interesting data. This section reviews a few of them illustrating the potential of this field for "new physics" like the existence of the QGP.

[6] cf. Chap. 2 for details on entropy production.

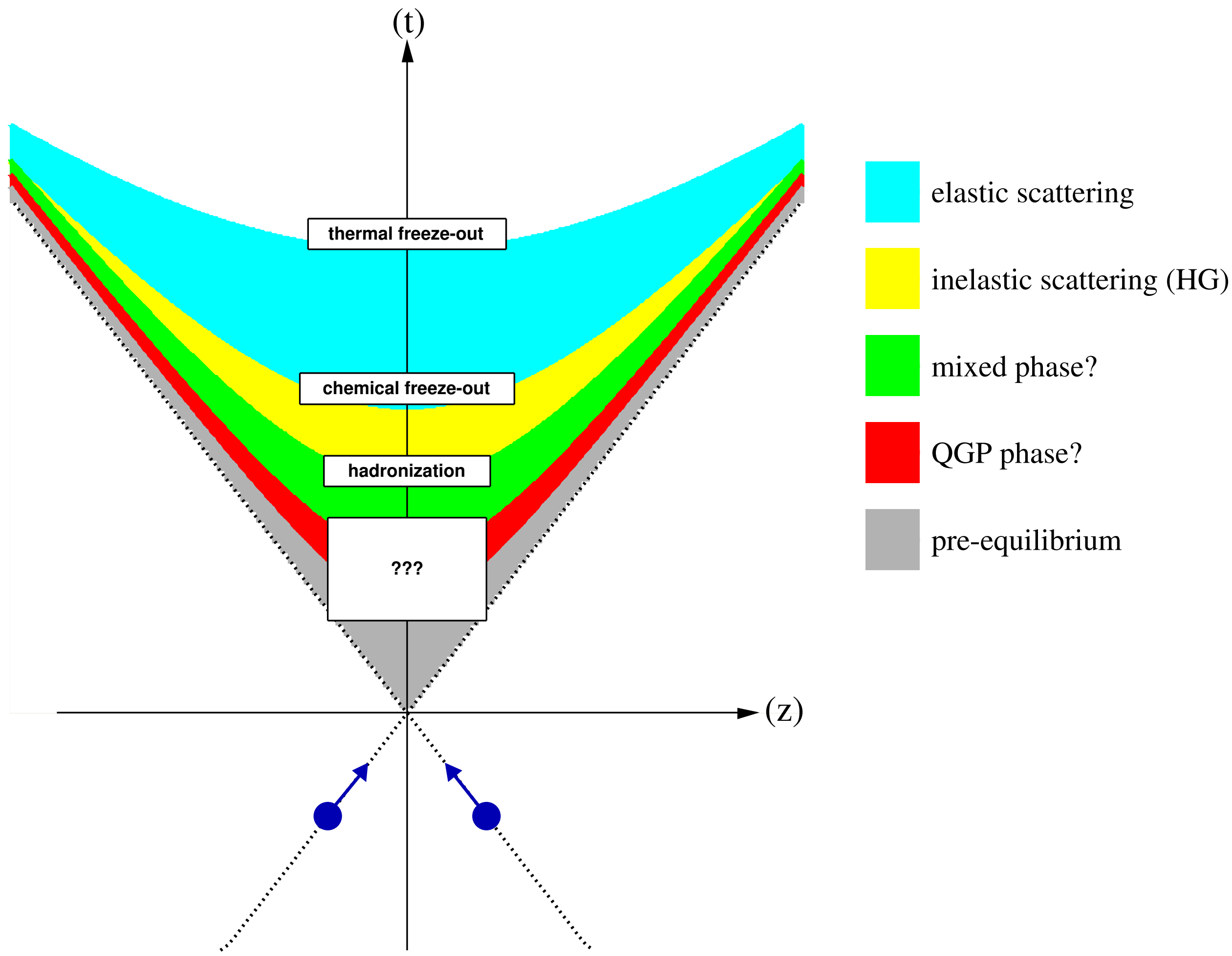

Fig. 1.10: Possible space–time evolution of a relativistic heavy ion collision according to the Bjorken picture.

1.4.1 Results prior to RHIC

In this section are presented a few published results from relativistic heavy ion collision experiments prior to RHIC. Note that this is not an exhaustive review.

In–medium Effects Near Kaon Production Threshold

Mean–field calculations [12] predict a change of the K^+ and K^- masses when the nuclear density ρ increases above its value at saturation ρ_0. This effect is caused by a repulsive K^+N potential and an attractive K^-N potential. A direct consequence is a change of the kaon production energy threshold $\sqrt{s_{th}}$ which increases for K^+ and decreases for K^-. The KaoS collaboration [13] (SIS) has measured the K^+ and K^- multiplicities per number of participating nucleons in C+C / Ni+Ni as a function of $Q = \sqrt{s_{NN}} - \sqrt{s_{th}}$ (left panel of Fig. 1.11), and Au+Au / C+C collisions as a function of the beam energy (right panel of Fig. 1.11). The solid lines on the left panel represent parameterizations of the available *pp* data (see [14] and references therein). In NN collisions, the K^+ multiplicity exceeds the K^- multiplicity by one or two orders of magnitude at the same Q value. This large difference is not seen in AA collisions where kaon data nearly fall on the same curve, showing a strong

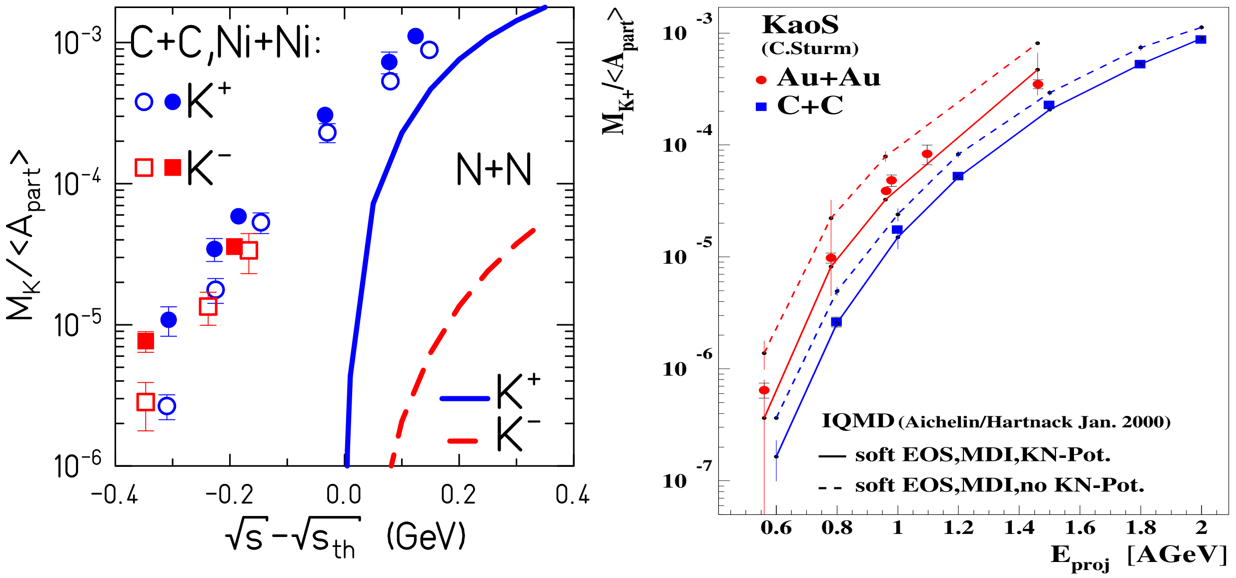

Fig. 1.11: Left: K^+ and K^- multiplicities per participant as a function of Q (see text) [13, 14]. Right: K^+ multiplicity per participant in C+C and Au+Au collisions as a function of beam energy where lines represent IQMD simulations with in–medium effects (solid) and without (dashed).

enhancement of K^- interpreted as a lowering of $\sqrt{s_{th}}_{K^-}$ due to in–medium effects. On the right panel is shown a comparison between K^+ data and IQMD prediction with and without in–medium effects. The data is reproduced if in–medium effects are included. Note also that the difference data–simulation with bare K^+ mass is larger in Au+Au than in C+C because of a much richer baryonic environment. The nuclear density is therefore higher in Au+Au where the K^+ mass is more affected by in–medium effects. $\sqrt{s_{th}}_{K^+}$ is therefore increased more strongly than in C+C, leading to a larger K^+ suppression.

Transverse Flow

The transverse flow reveals its print on the transverse mass spectra. The latter can be described by the Boltzmann–like distribution, as long as the particle source is thermalized and has a temperature $T \gtrsim 50\,\text{MeV}$, where bosonic and fermionic effects can be ignored:

$$\frac{dN}{m_\perp dm_\perp} \propto exp\left(-\frac{m_\perp - m}{T}\right) \tag{1.6}$$

where T is the inverse slope parameter or apparent temperature of the emitting source. For an ideal source at rest where particle motions are purely thermal, the slope parameter is expected to be the same for all particle types. When the inverse slope parameters obtained from fits are plotted against the corresponding mass, one sees a quasi–linear dependence up to $m \approx 1\,\text{GeV}/\text{c}^2$, as can be seen on Fig. 1.12. Moreover, the magnitude of this linearity depends on the system size: the bigger the system, the bigger the slopes [15]. On the other hand, for hyperons which carry a certain amount of strangeness, the linearity slope–mass does not hold anymore. This feature is interpreted as an early (chemical) decoupling of the heavy hyperons from the system before thermal freeze–out, when particles have built up the full flow through subsequent elastic collisions [18, 19]. Nevertheless, since the inverse slope parameters reveal

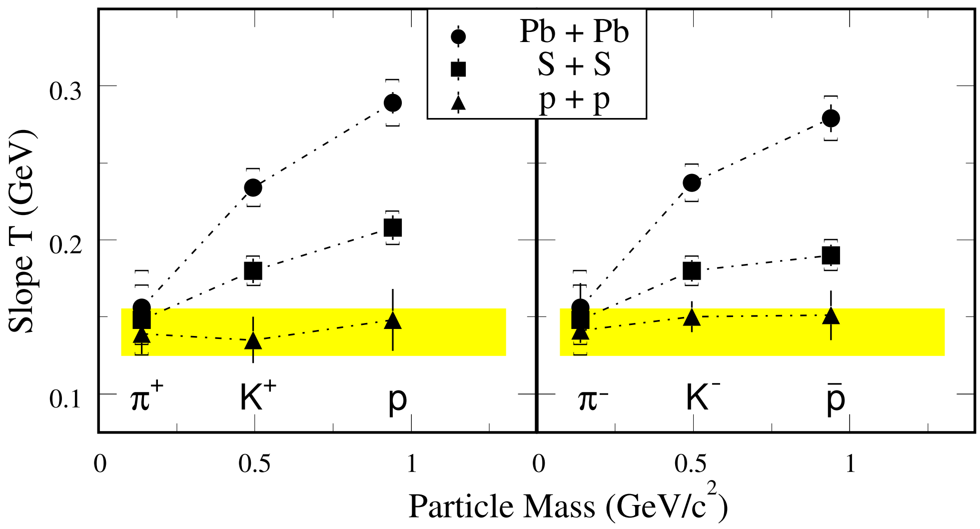

Fig. 1.12: Inverse slope parameter as a function of mass from the reaction Pb+Pb at 158 AGeV [15].

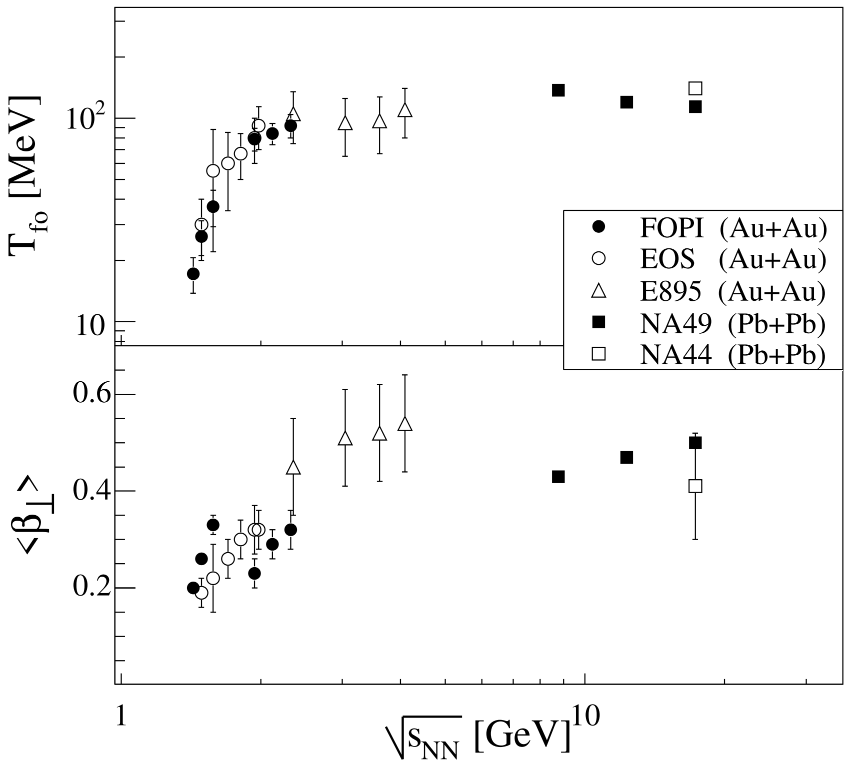

Fig. 1.13: Energy dependence of the thermal freeze–out temperature T and average transverse flow velocity $\langle\beta_\perp\rangle$ from SIS to SPS (see [16, 17] and references therein).

the state at thermal freeze–out, populated mostly by light hadrons, it has been suggested to split the parameter T into two components, a thermal part T_{fo} and a part resembling the collective expansion:

$$T = T_{fo} + m \langle \beta_\perp \rangle^2 \tag{1.7}$$

with $\langle \beta_\perp \rangle$ defined as the average transverse flow velocity, owing to the fireball pressure. An alternative to this simple parametrization was proposed in [20], which aims at describing the transverse flow by a hydrodynamical ansatz. Transverse mass spectra are modeled as follows:

$$\frac{dN}{m_\perp dm_\perp} \propto \int_0^R r\, dr\, m_\perp\, I_0 \left[\frac{p_\perp \sinh\rho}{T_{fo}}\right] K_1 \left[\frac{m_\perp \cosh\rho}{T_{fo}}\right] \tag{1.8}$$

where $\rho = \tanh^{-1}\beta_\perp(r)$ and $\beta_\perp(r) = \beta\,(r/R)^\alpha$. I_0 and K_1 are modified Bessel functions. The exponent α describes the evolution of the flow velocity (or flow profile) from any radius r to the freeze–out radius R. Figure 1.13 compiles the incident energy dependence of T_{fo} and $\langle \beta_\perp \rangle$ from SIS to SPS energy regimes, whether the exponential or blast–wave description was used. As the incident energy increases, the freeze–out temperature increases rapidly (low $\sqrt{s_{NN}}$) but tends to level as $\sqrt{s_{NN}}$ enters the SPS regimes. This behavior is seen in the general trend of the energy dependence of $\langle \beta_\perp \rangle$ within the systematic errors of all experiments.

J/ψ suppression

In early spring 2000, a CERN press release announced that a "new state of matter" was observed in Pb+Pb collisions at $\sqrt{s_{NN}} = 17.2\,\mathrm{GeV}$. Such enthusiasm is mainly motivated by a study of the J/ψ multiplicity carried out by the NA50 experiment. J/ψ is a tightly bound state of charm and anti–charm quarks ($c\bar{c}$). It is predicted [21] that its yield is suppressed in a deconfined medium due to the screening of the attractive color interaction which normally binds the c and $\bar{c}$ quarks together. Moreover, J/ψ is particularly interesting because it probes the state of matter in the earliest stages of the collisions since $c\bar{c}$ pairs can only be produced at that time (J/ψ interacts little with the hadronic medium due to its large binding energy of the order of 600 MeV, and therefore can survive the different collisions stages until it weakly decays). The J/ψ production is studied via its decay into two muons $\mu^+\mu^-$. The suppressed J/ψ production is visible in Fig. 1.14 which shows the ratio between the measured J/ψ multiplicity normalized to the yields expected if nuclear absorption is the only source of suppression, as a function of the energy density. As can be seen, a clear suppression is visible above $\epsilon \sim 2.3\,\mathrm{GeV/fm^3}$, which is consistent with the formation of a QGP (see [21, 22]).

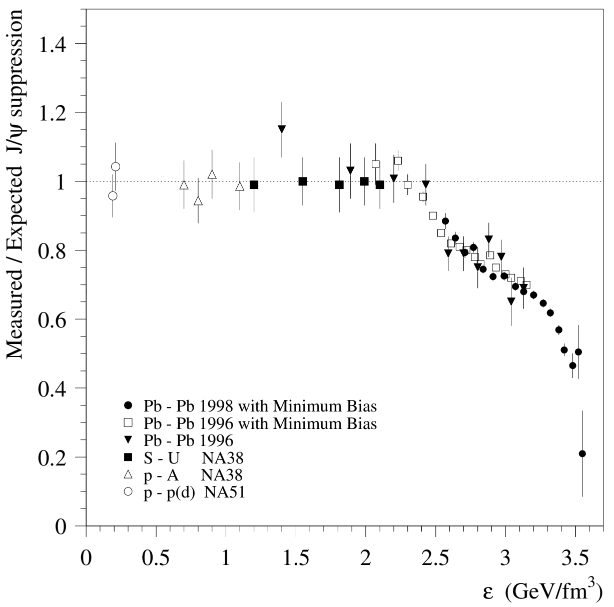

Fig. 1.14: J/ψ suppression measured by NA50 [21, 22].

Strangeness Enhancement

Another possible signature of the QGP existence is the enhanced production of strangeness. It is predicted that the strange quark and anti-quark $s\bar{s}$ production is enhanced in a deconfined medium ([7] and references therein) by thermal glue based processes. Indeed, the gluon density in a QGP is high while chiral symmetry might be (partly) restored [23, 24]. The latter point leads to a decrease between the mass differences between the various (anti)quarks. Consequently, a relative enhancement of the production of heavy quarks comparatively with confined medium production is expected. This enhanced heavy quark content has to be reflected in the final chemical state of the collision. On the other hand, secondary processes like $\pi + n \to K + \Lambda$ can also lead to strangeness enhancement when the production process approaches equilibrium conditions but this hadronic process would require a much longer equilibration time due to the energy required ($\gtrsim 100\,\mathrm{fm/c}$) than in a QGP scenario (in the order of a few fm/c) for (multi)strange baryons. For these resonances, the enhancement is relative to the production yields measured in pA collisions. Figure 1.15 shows the ratio between measured yields of (multi)strange baryons from p+Pb, Pb+Pb and p+Be collisions at $\sqrt{s_{NN}} = 17.3\,\mathrm{GeV}$ as a function of the number of participants (centrality) [25].

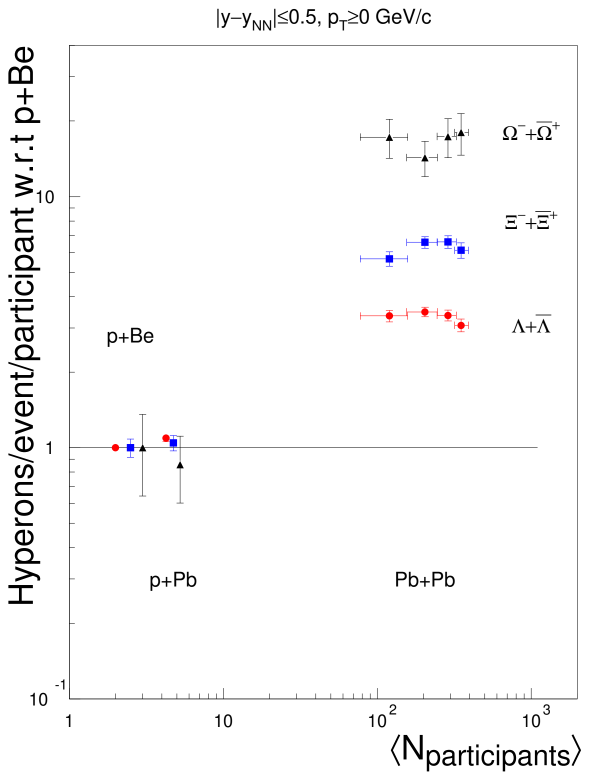

Fig. 1.15: (Multi)strange baryon enhancement relative to pA collisions [25].

As can be seen, while the ratio is consistent with unity for p+Pb yields, a clear enhancement is seen in Pb+Pb, directly related to the strangeness content on the baryon specie ($s_\Lambda = 1 < s_\Xi = 2 < s_\Omega = 3$). Another way to address the strangeness enhancement is to study the production of (anti)kaons (composed of $u, \bar{u}$ and $s, \bar{s}$ quarks) relative to pionic production ($u, \bar{u}$ and $d, \bar{d}$). These observables are discussed in details in this thesis (cf. Chap. 2, 6 and 7).

1.4.2 News from RHIC

After only three years of operation, the four RHIC experiments, BRAHMS, PHOBOS, PHENIX and STAR, have provided a wealth of new results contributing to the understanding of hot and dense matter properties, and more results are to come (the following items only represent a small fraction of the most recent results).

Apparent Chemical Equilibrium

Particle abundances and ratios are successfully described by the statistical model from SIS to RHIC energies [26, 27, 28]. The picture emerging from this model is that the fireball reaches chemical equilibrium and then freezes out chemically (no more inelastic scatterings occur). This model is characterized by a remarkable simplicity, two or three parameters are enough to describe most of all existing data on ratios and multiplicities from SIS to RHIC: chemical freeze–out temperature T_{fo} and baryo–chemical potential μ_B, a quantity that can be understood as the affinity of the medium to create a baryon at a certain energy and temperature (see details in Sec. 2.4.1). A third parameter is sometimes used to account for the failure of the model to describe the amount of strangeness but the most recent models do not use such a parameter. The right panel of Fig. 1.16 shows statistical model calculations confronted to experimental particle ratios measured from Au+Au at $\sqrt{s_{NN}} = 130$ GeV [26].

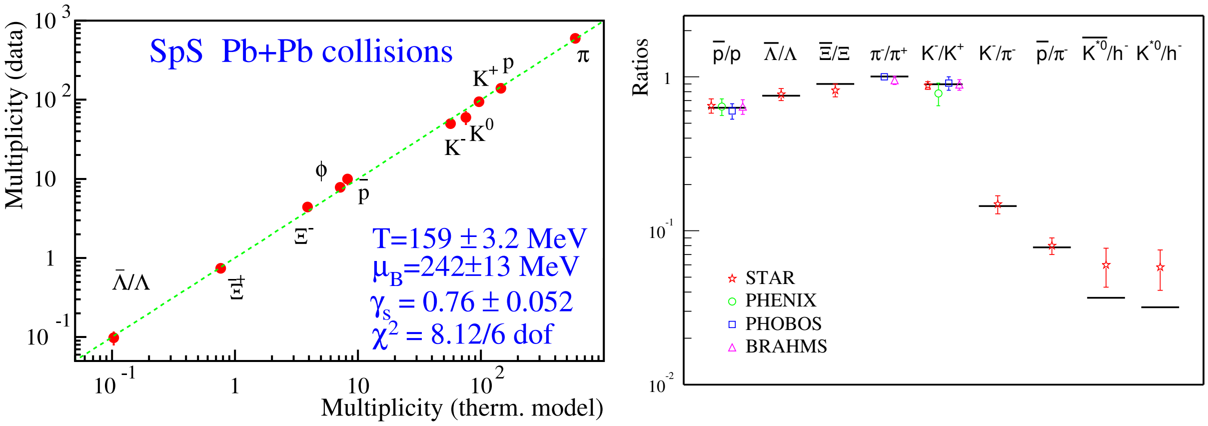

Fig. 1.16: Left: Hadron multiplicities from central Pb+Pb collisions at $\sqrt{s_{NN}} = 17.3$ GeV measured by NA49 confronted with the grand–canonical statistical model [28, 29]. Right: Experimental particle ratios measured in Au+Au collisions at $\sqrt{s_{NN}} = 130$ GeV and statistical model calculations with $T = 174$ MeV and $\mu_B = 46$ MeV [26].

Note that the ratios reported in Fig. 1.16 are measured at mid–rapidity. Total multiplicities of identified particles measured at SPS are also presented here to stress the good agreement between the model and the data. Total multiplicity calculation at RHIC energies cannot yet be compared with experimental measurements. However, this thesis presents the first estimation of total multiplicities of pions and kaons produced in Au+Au collisions at $\sqrt{s_{NN}} = 200$ GeV (cf. Chap. 6 and 7).

Net–Baryon, Transparency and Degree of Stopping

As mentioned in Sec. 1.3.2, the transparency, related to the degree of stopping, is investigated by measuring the net–baryon multiplicities: transparent collisions are devoid of net–baryon in the central rapidity region. The initial conditions of the hot and dense fireball are therefore driven by the net–baryon density which leads to different QGP scenarios: on one hand a high temperature and low μ_B (transparency) reminding of the early universe conditions, on the other a large μ_B and lower temperature (stopping) reminding of conditions existing inside dense stellar objects like neutron stars. Figure 1.17 shows the net–proton rapidity density as a function of rapidity measured at three energy domains (AGS, SPS and RHIC). As $\sqrt{s_{NN}}$

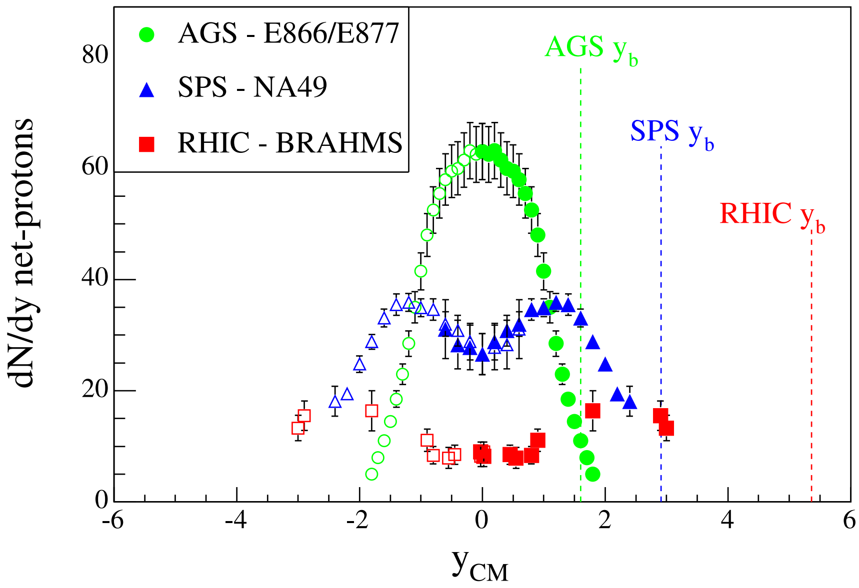

Fig. 1.17: Net–proton rapidity density as a function of rapidity at three energy domains. A higher collision transparency is achieved at higher $\sqrt{s_{NN}}$, revealed by an increasing depopulation of net–protons at mid-rapidity. Figure is from [30].

increases, the mid-rapidity densities decrease quite dramatically, showing that more transparency is achieved. This explains why heavy–ion collisions at RHIC are sometimes referred to as "micro–bangs". More details can be found in [30].

High-p_T Jet Suppression

Particles with transverse momenta above 2 GeV/c are primarily produced by hard scatterings, i.e. with large momentum transfer Q, domain of perturbative QCD. Such high p_T particles are produced when the nuclei start interacting and hence serve as a probe of the early dense phase of the system. In order to study the effect of the dense medium, p+p data at $\sqrt{s_{NN}} = 200$ GeV have been collected in 2001 by the RHIC experiments. Since hard scatterings are likely to happen no more than once per hard nucleon early in the reaction, their number is expected to scale with the number of binary collisions N_{coll}. The nuclear modification factor is thus defined as

$$R_{AA}(p_T) = \frac{\text{(Yield per A+A collision)}}{\langle N_{coll}\rangle \, \text{(Yield per p+p collision)}} \tag{1.9}$$

Figure 1.18 shows R_{AA} obtained from mid–rapidity π^0 as a function of p_T, measured by PHENIX [31]. R_{AA} is consistent with unity within the covered p_T range in peripheral collisions,

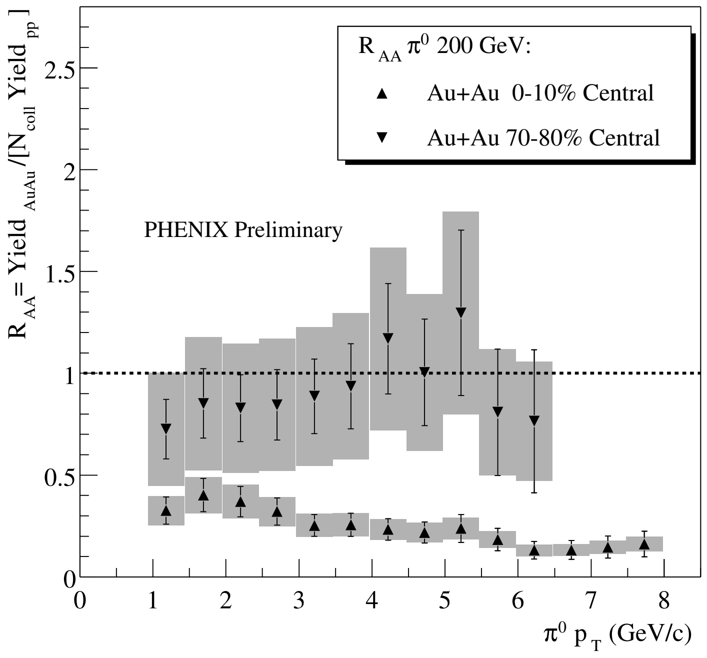

Fig. 1.18: Nuclear modification factor R_{AA} showing hight p_T π_0 suppression in Au+Au central collisions compared with peripheral collisions at $\sqrt{s_{NN}} = 200\,\text{GeV}$. The shaded boxes are errors on the normalization of the ratio ($\langle N_{coll} \rangle$). The figure is from [31].

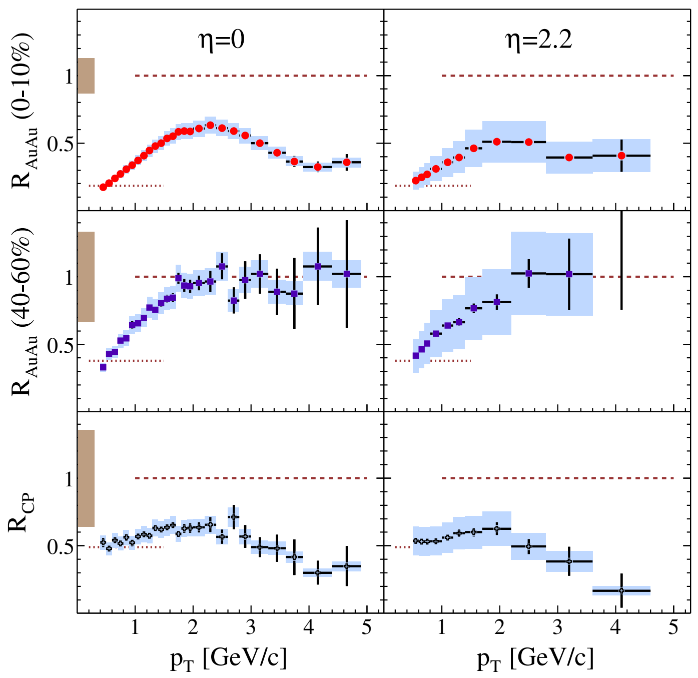

Fig. 1.19: High p_T suppression measured by BRAHMS at two different locations in the rapidity space ($y = 0$ and $y \sim 2$) for Au+Au collisions at $\sqrt{s_{NN}} = 200\,\text{GeV}$. The bottom panel is the ratio between the nuclear modification factors obtained from the most central collisions and collisions from a more peripheral centrality class (figure from [32]).

meaning that peripheral collisions consist of a bare superposition of binary NN collisions. But central collisions exhibit a strongly suppressed nuclear modification factor, decreasing from 0.4 to 0.15 with increasing p_T. This strong suppression indicates that produced high p_T particles loose energy while traversing a very dense medium, possibly a QGP.

BRAHMS has also measured such a suppression at $y = 0$ and $y \sim 2$ from Au+Au collisions at $\sqrt{s_{NN}} = 200\,\text{GeV}$. Results are shown in Fig. 1.19 (from [32]). It shows that the suppression of high p_T particles extends at least to $\eta \sim 2$. Conversely, in collisions between deuterons and gold ions (d+Au) at the same center of mass energy ($\sqrt{s_{NN}} = 200\,\text{GeV}$), no high p_T suppression is observed, as can be seen in Fig. 1.20.

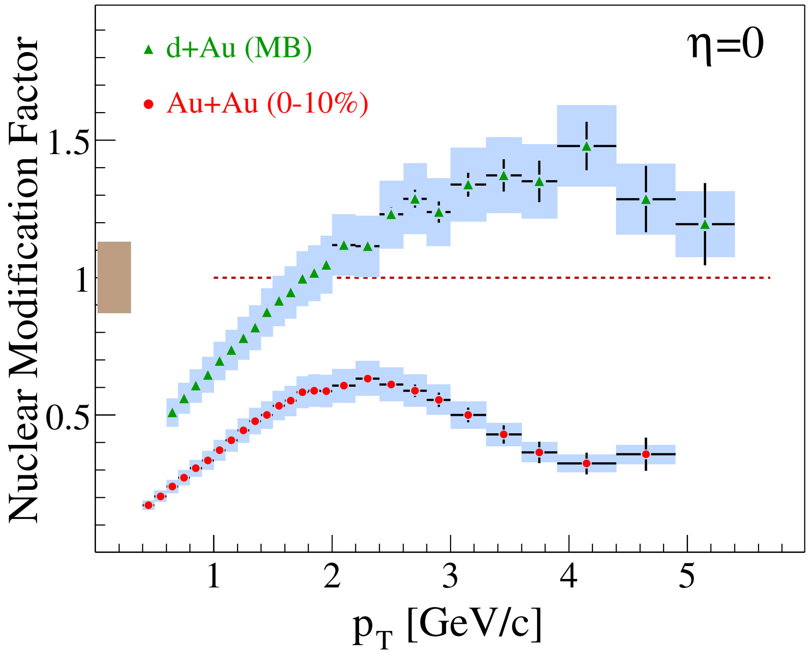

Fig. 1.20: Nuclear modification factor measured by BRAHMS at mid-rapidity from d+Au collisions at $\sqrt{s_{NN}} = 200\,\text{GeV}$, compared with Au+Au collisions (figure from [32]).

Thus, high p_T suppression appears to be directly correlated with the size of the participant volume. It is "*reasonable to surmise that [the suppression] is related to medium effects tied to a large volume with high energy density*" [32]. In other words, this signal can be seen as a signature of the occurrence of a QGP phase in central Au+Au collisions at the topmost RHIC energy.

♣♣♣♣♣♣

Chapter 2

Charged Pion and Kaon Production

Mesons are the lightest hadrons. Therefore, the large energy density achieved in the course of relativistic heavy ion collisions is mostly converted into pion and kaon production by strong interactions. Unlike pions, kaons carry strangeness, a quark flavor that is not present in the initial system. Kaons are therefore the most abundant outcome of the produced strangeness and constitute an interesting probe of the hot and dense conditions.

Chapter Content

After an introduction on pions and kaons, a review of existing data from relativistic heavy ion collisions is presented. Then follows the introduction of two families of theoretical models aiming at predicting particle multiplicities: the thermodynamical models (hadron resonance gas and statistical model of the early stage), and two microscopic models (HIJING and AMPT), describing ultra–relativistic collisions from the dynamics of partons (quarks and gluons).

2.1 Properties of Charged Mesons

2.1.1 Some History

Pions (π) were discovered experimentally in 1947 [33, 34] by investigating pictures capturing tracks of decaying particles. This discovery was welcomed with a great enthusiasm: pions had been predicted to be the carriers of the strong force by H. Yukawa in 1935 [35]. The kaon (K) discovery [36] came shortly after the pion discovery during the same year (Fig. 2.1). Kaons seemed to decay more slowly than would have been expected from the large amount of energy released in the process. M. Gell-Mann assigned them a quantum number s with no physical meaning to account for this "strange" behavior. As particle accelerators provided higher and higher collision energies, many new exotic and "strange" particles were discovered whose systematics was not understood until Gell-Mann again and Zweig proposed the quark model to unify and describe the whole hadron family. Pions and kaons belong to the meson group, particles made of a quark and anti–quark ($q\bar{q}$) according to the principle that hadrons have to be color neutral. As the understanding of the strong force improved with the development of the formalism of non abelian gauge theories from which QCD derives, the pion was finally replaced by the gluons as vectors of the strong force, and the strangeness s acquired a real physical meaning as being one of the six quark flavors.

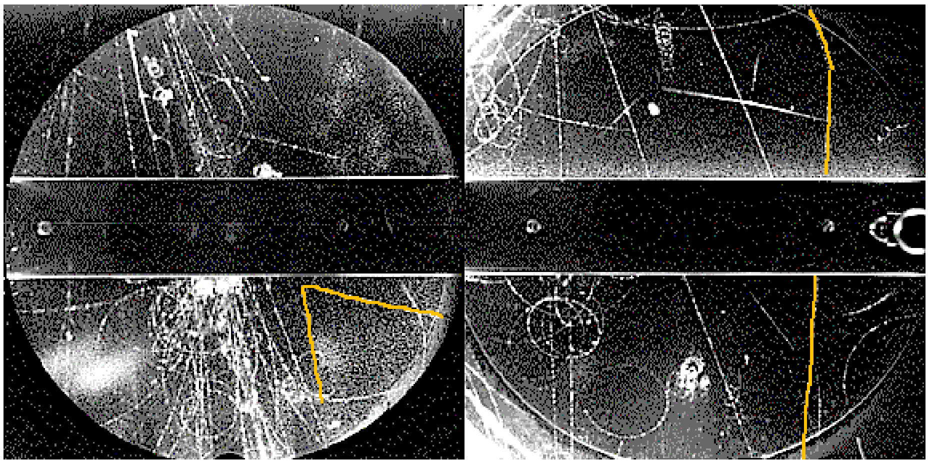

Fig. 2.1: First picture showing the decay of a neutral kaon, called at that time "V" particle due to its decay topology (left), and of a charged kaon, characterized by a kink along the track path (right).

2.1.2 Basic Properties

The pion is an isospin triplet ($I = 1$ with degeneracy $g_I = 2I + 1 = 3$), components are π^+, π^- and the charge neutral π^0. The kaon is also isospin degenerated ($I = 1/2$), components are K^+, K^0 ($u \leftrightarrow d$) and K^-, $\bar{K}^0$ ($\bar{u} \leftrightarrow \bar{d}$). Note that two neutral linear combinations are observed, $K^0_S = \frac{1}{2}\left|K^0 + \bar{K}^0\right\rangle$ (*s*hort lifetime) and $K^0_L = \frac{1}{2}\left|K^0 - \bar{K}^0\right\rangle$ (*l*ong lifetime), but it is not discussed in this thesis. These particles are unstable, they decay into lighter particles due to the weak interaction that does not conserve the quark flavor (unlike the strong interaction). The decay is characterized by the mean lifetime τ (defined in the reference frame of the decaying particle), commonly expressed as $c\tau$ with c the speed of light. Table 2.1 summarizes the main characteristics of charged pions and kaons in the vacuum.

	Quarks	mass (GeV/c^2)	Q	B	S	I	J	$c\tau$ (cm)	Decay modes	Br. ratio
$\pi^\pm$	$u\bar{d}$ ($\bar{u}d$)	0.1396	±1	0	0	1	0	780.4	$\mu^+ + \nu_\mu$ (c.c.)	99.99%
$K^\pm$	$u\bar{s}$ ($\bar{u}s$)	0.4937	±1	0	±1	1/2	0	371.3	$\mu^+ + \nu_\mu$ (c.c.)	63.51%
									$\pi^+ + \pi^0$ (c.c.)	21.16%
									$\pi^+ + \pi^+ + \pi^-$ (c.c.)	5.59%
									$\pi^0 + e^+ + \nu_e$ (c.c.)	4.82%
									$\pi^0 + \mu^+ + \nu_\mu$ (c.c.)	3.18%

Tab. 2.1: Charged pion and kaon characteristics in the vacuum, where Q, B S, I and J are the electrical charge, baryon, strangeness, isospin and spin quantum numbers respectively. Negatively charged mesons are charge conjugates – c.c. – of positive mesons. Only the main decay modes and their respective branching ratio are tabulated.

2.2 Charged Meson Production

2.2.1 Basic NN Reactions

In elementary nucleon–nucleon collisions, charged pions and kaons are produced either directly $NN \rightarrow \pi/K$, or indirectly $NN \rightarrow ... \rightarrow \pi/K$. The basic production reactions governed by the strong force conserve electrical, baryonic and strange quantum numbers. From these rules, the following reactions are derived:

$n+n$	$\rightarrow$	$\pi^- + n + p$	($u\bar{u}$ creation with rearrangement)
$p+n$	$\rightarrow$	$\pi^- + p + p$	($u\bar{u}$ creation with rearrangement)
$p+p$	$\rightarrow$	$\pi^+ + n + p$	($d\bar{d}$ creation with rearrangement)
$n+p$	$\rightarrow$	$\pi^+ + n + n$	($d\bar{d}$ creation with rearrangement)
$p+p$	$\rightarrow$	$K^+ + \Lambda + p$	($s\bar{s}$ creation with rearrangement)
$N+N$	$\rightarrow$	$K^+ + K^- + N + N$	($s\bar{s}$ and $u\bar{u}$ creation without rearrangement)

Tab. 2.2: Meson production from NN reactions.

The production energy threshold $\sqrt{s_{th}}$ in the NN center of mass is deduced by summing the mass of the products:

$$\sqrt{s_{th}} = 2m_p - Q = 2m_p - \left(2m_p - \sum m_{\text{products}}\right) = \sum m_{\text{products}} \tag{2.1}$$

For example, $\sqrt{s_{th}}_{K^+} = m_{K^+} + m_\Lambda + m_p = 2.55\,\text{GeV}$. The other meson threshold energies in NN interactions are $\sqrt{s_{th}}_{\pi^\pm} = 2.01\,\text{GeV}$ and $\sqrt{s_{th}}_{K^-} = 2.87\,\text{GeV}$. As an illustration, the experimental *pp* reaction cross–section is shown in Fig. 2.2. Above $\sqrt{s_{NN}} \approx 2\,m_p + m_\pi$, the

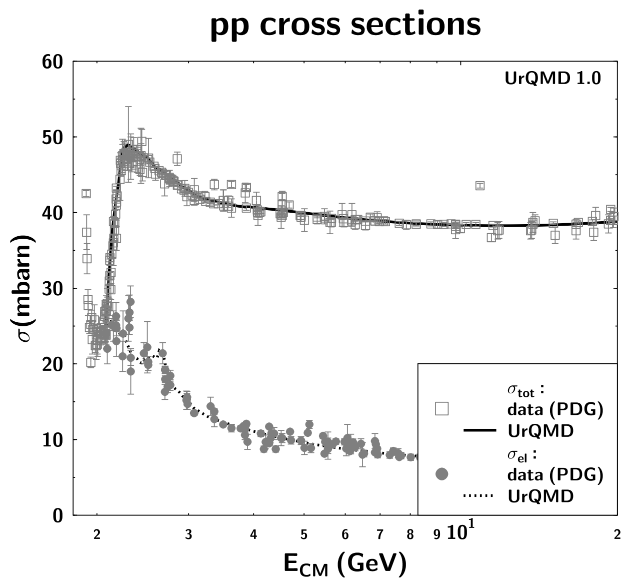

Fig. 2.2: *pp* cross–section as a function of $\sqrt{s_{NN}}$ (figure from [37]).

cross–section is dominated by inelastic processes, i.e. particle production. At RHIC, incident energies are much higher than the threshold energies $\sqrt{s_{th}}$ (about 100 times higher).

Associated Production, Pair Production and String Fragmentation

Prior to the quark model, it had been noticed in NN collisions that the production of a positive kaon occurred together with the creation of a Λ or Σ particle. This phenomenon is called associated production and is characteristic of the conservation of a charge–like quantity that was then named strangeness. With the quark model in mind, associated production is straightforward to understand. By examining the reactions listed in Tab. 2.2, the creation of a single $s\bar{s}$ pair is enough to produce a K^+ if the quarks recombine into Λ (Σ) and N. This is not the case for K^- since its production requires the creation of an extra $u\bar{u}$ pair. Therefore, an asymmetry exists between the production of K^+ and K^- in a baryon rich environment:

$$\begin{aligned} N(K^+) &\sim N(K^+)_{p.p.} + N(K^+)_{a.p.} \\ N(K^-) &\sim N(K^-)_{p.p.} \end{aligned}$$

where $a.p.$ refers to associated production and $p.p.$ to pair production. Moreover, K^- can be reabsorbed by the medium via a (reversible) process called strangeness exchange reaction:

$$\begin{aligned} K^- + n &\leftrightarrow \pi^- + \Lambda \\ \bar{u}s + udd &\leftrightarrow \bar{u}d + uds \end{aligned}$$

where the s quark of the K^- replaces a d quark of the neutron and vice–versa. Again, in a baryon rich environment (no anti–nucleons), this channel is forbidden to K^+, which leads to an excess of K^+ w.r.t. K^-. For pions, one does not talk about associated production but charge exchange reaction between the isospin states of the nucleon (neutron and proton). Unlike kaons, both π^- and π^+ can be produced by charge exchange reaction (cf. Tab. 2.2).

Pair production means that a particle is created together with its antiparticle. For example, the reaction $p + p \to K^+ + K^- + p + p$ is a pair production reaction, in contrast with associated production. Note that in both cases, quarks are produced by pair $q\bar{q}$ in order to respect flavor conservation. For pions, pair production is not the dominant mechanism. Indeed, they are mainly produced by strangeness exchange reaction in a baryon rich environment (lower energy threshold than pair production), higher mass string break–up or, as is detailed below, by resonance decays. The last two processes can produce many pions at once. For kaons, pair production should play a more important role than for pions due to the absence of associated production of K^-. Production by string fragmentation is expected to be dominant at RHIC around mid–rapidity, where the net–baryon densities are low [30, 38]. The model describing string break–up is based on the formalism of strings [39]. The dynamics of the color flux between two quarks $q\bar{q}$ is modeled by a relativistic string [40]. When the tension reaches enough potential energy by stretching, it fragments into pairs of quark–antiquark. These quarks cannot evolve freely, unless a QGP is formed for a short while during the phase of high density and temperature, and hadronize by flavor and color recombination.

2.2.2 Meson Production by Hadronic Decays

Charged mesons are also products of resonance decays. Resonances are excited hadronic states. Each resonance is characterized by its Breit–Wigner width Γ that can be related to the resonance lifetime τ and mass width Δm by the following equations :

$$\Delta m = \Gamma / c^2 \tag{2.2}$$

$$\tau = \hbar / \Gamma \tag{2.3}$$

For this reason, resonances are considered as quasi–particles since their mass is not completely well–defined. One distinguishes between mesonic and baryonic resonances. A common baryonic resonance is the $\Delta(1232)$ of width $\Gamma = 120\,\mathrm{MeV}$. It occurs in NN interactions and decays into a pion and a nucleon:

$$NN \rightarrow N\Delta \rightarrow NN\pi$$

Hyperons, which are not resonances but baryons containing one strange quark (Λ's) up to three strange quarks (Ω's) are also unstable. Their lifetime is much shorter than that of kaons and therefore decay very close to the primary interaction point (vertex). Kaons are therefore the only strange charged particles surviving long enough to leave tracks in detectors. This point, together with their relatively high multiplicity, makes kaons the most handy strangeness probe in the experimental point of view.

The products from hyperon decays often contain a charged meson, e.g:

$$\Lambda \rightarrow p + \pi^-$$

In Appendix C are listed the most common resonances and hyperons with their main decay modes containing a charged meson.

2.3 Data Review

The energy systematic of charged meson production, via the study of their rapidity densities, total multiplicities and transverse momentum spectra, is a powerful probe of the collision dynamics. In this section are reviewed the existing data of charged pion and kaon production from $\sqrt{s_{NN}} = 1\,\mathrm{GeV}$ (SIS) to $\sqrt{s_{NN}} = 130\,\mathrm{GeV}$ (RHIC), two orders of magnitude in energy. The SPS data are from central Pb+Pb collisions, i.e. 2×208 nucleons (5% more nucleons than in the Au+Au system). AGS and SIS data are from Au+Au collisions. A special focus is put on the relative abundance of kaons with respect to pions. Indeed, an anomalous increase of the kaon to pion ratio with increasing $\sqrt{s_{NN}}$ has been proposed as a signature of hadron deconfinement in the early phase of the fireball [7], as was already mentioned in Sec. 1.4.1. The discussion opened in this section will be carried along in Chap. 7 where these data are compared to the results of this thesis.

2.3.1 Pion Production

Figure 2.3 shows the rapidity distribution of π^- for the top 5% central collisions measured by different experiments. The overall multiplicity systematically increases with increasing incident energy. At RHIC, only mid–rapidity data have been available so far. Figure 2.4 shows the mid–rapidity and 4π multiplicities of positive and negative pions as a function of $\sqrt{s_{NN}}$ (top panel). Ratios are shown in the bottom panel of this figure. It reveals that the isospin asymmetry visible at SIS energy, where produced pions are dominated by the $\Delta(1232)$ resonance decay and charge exchange reactions [46], is reduced with increasing $\sqrt{s_{NN}}$. The evolution of the ratio $N^{\pm}/(dN^{\pm}/dy)_{y=0}$ shows that the total multiplicity of positive and negative pions is less and less dominated by the mid–rapidity multiplicity as $\sqrt{s_{NN}}$ increases. It can be explained by an increasing longitudinal flow with $\sqrt{s_{NN}}$.

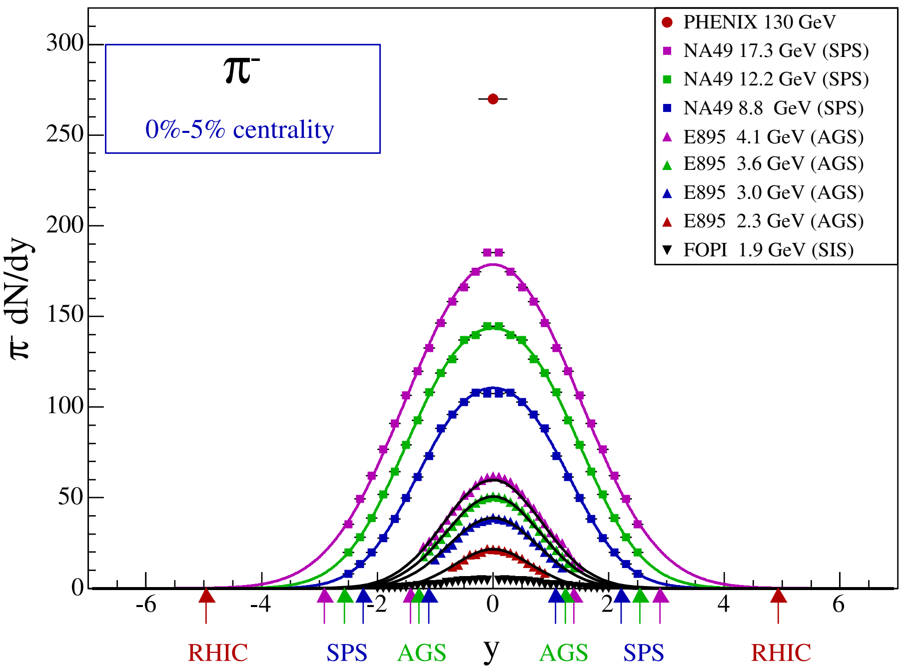

Fig. 2.3: Pion rapidity density as a function of rapidity and $\sqrt{s_{NN}}$ from $\sqrt{s_{NN}} = 1\,\text{GeV}$ to $\sqrt{s_{NN}} = 130\,\text{GeV}$. The RHIC data are from [41], the SPS data from [42], the AGS data from [43, 44] and the SIS data from [45, 46].

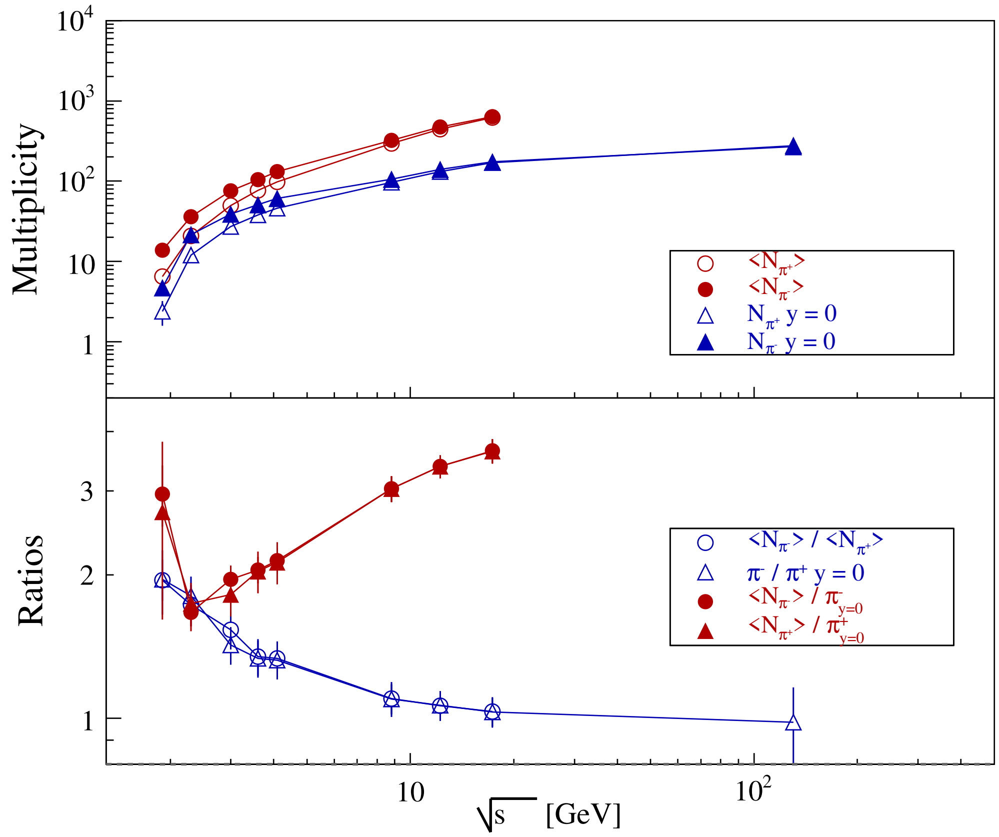

Fig. 2.4: Energy systematic of positive and negative pion multiplicities and ratios. Solid lines are drawn to guide the eye. The errors are systematic.

2.3.2 Kaon Production

In Fig. 2.5 are plotted rapidity density distributions of K^+ and K^- at different $\sqrt{s_{NN}}$. The overall feature that pion distributions exhibit is also visible for kaons, i.e. a substantial increase of the multiplicities with $\sqrt{s_{NN}}$, but there is a significant difference de visu between pions and kaons: the K^- multiplicities are significantly lower than that of K^+, even at $\sqrt{s_{NN}} = 130\,\mathrm{GeV}$. These differences are quantified and plotted in Fig. 2.6. Like for pions, the big discrepancies seen at low energy between K^+ and K^- decrease as $\sqrt{s_{NN}}$ approaches the RHIC top energy. The ratios $\langle K \rangle \,/\, (dN/dy)_{y=0}$ also show (together with pion ratios) that the source is more and more elongated as $\sqrt{s_{NN}}$ increases.

Another remarkable feature that goes along with this statement is the energy systematics of the inverse slope parameter extracted from kaon transverse momentum spectra at mid–rapidity[1]. At all energies, the kaon spectra could be fitted with a exponential function in m_T. Inverse slope parameters are plotted as a function of $\sqrt{s_{NN}}$ in Fig. 2.7. As can be seen, the transverse activity characterized by a fast increase at low energies becomes smoother from SPS to RHIC energies, meaning that the longitudinal expansion is taking over the transverse expansion. In a recent preprint [52] is reported an anomaly in this transverse activity: "*The inverse slopes of the spectra increase with energy in the AGS and RHIC domains, whereas they are constant in the intermediate (SPS) energy range*". The authors "*argue that this anomaly is probably caused by a modification of the equation of state in the transition region between confined and deconfined matter*". Indeed, a plateau structure is visible in the SPS energy range. But in order to follow the argument of these authors, a systematic energy scan is needed between the top SPS energy and the intermediate RHIC energy. In this thesis, an evaluation of the kaon slope is given at $\sqrt{s_{NN}} = 200\,\mathrm{GeV}$ and gives new information on this intriguing systematic.

2.3.3 Kaons versus Pions

The previous sections describe the pion and kaon energy systematics independently. This section reviews the energy dependence of the correlation between kaon and pion multiplicities. Since pions are non–strange and made of the lightest quarks ($u\bar{u}d\bar{d}$) with u's and d's present in the initial state, correlating kaon multiplicities with pion multiplicities as a function of $\sqrt{s_{NN}}$ is relevant for investigating fluctuations of strangeness production w.r.t. lighter flavors, and probe anomalies that can be interpreted as a signature of an early deconfined state of the system [7, 53]. Figure 2.8 shows the kaon multiplicities $N_{K^+} + N_{K^-}$ as a function of $N_{\pi^+} + N_{\pi^-}$ at mid–rapidity. The behavior is similar to the evolution of the kaon slope. At low energy, the kaon multiplicity rises quickly within a small energy domain (1 to $\sim 8\,\mathrm{GeV}$), not much higher than the kaon production threshold. Then, a plateau structure at the SPS energy range, like the one seen in Fig. 2.7 is visible in the ratio $N_{K^+ + K^-}/N_{\pi^+ + \pi^-}$. At RHIC, the relative amount of kaon is increased from SPS. However, one needs to investigate the total strangeness by including the multiplicity of strange baryons. Moreover, the expected deconfinement signature is a strangeness enhancement relative to non strange quarks. The observation of the SPS plateau does not go in this direction. It can be in fact explained by studying the signed ratios. Since K^+ (K^-) contains a $\bar{s}$ (s) quark, K^+ production in a dense baryonic medium should be favored, as can be expected from reactions listed in Sec. 2.2.1. Figure 2.9 shows the kaon to pion ratios obtained from mid–rapidity multiplicities. The expectation is verified: as the baryon

[1] cf. Appendix E for definitions.

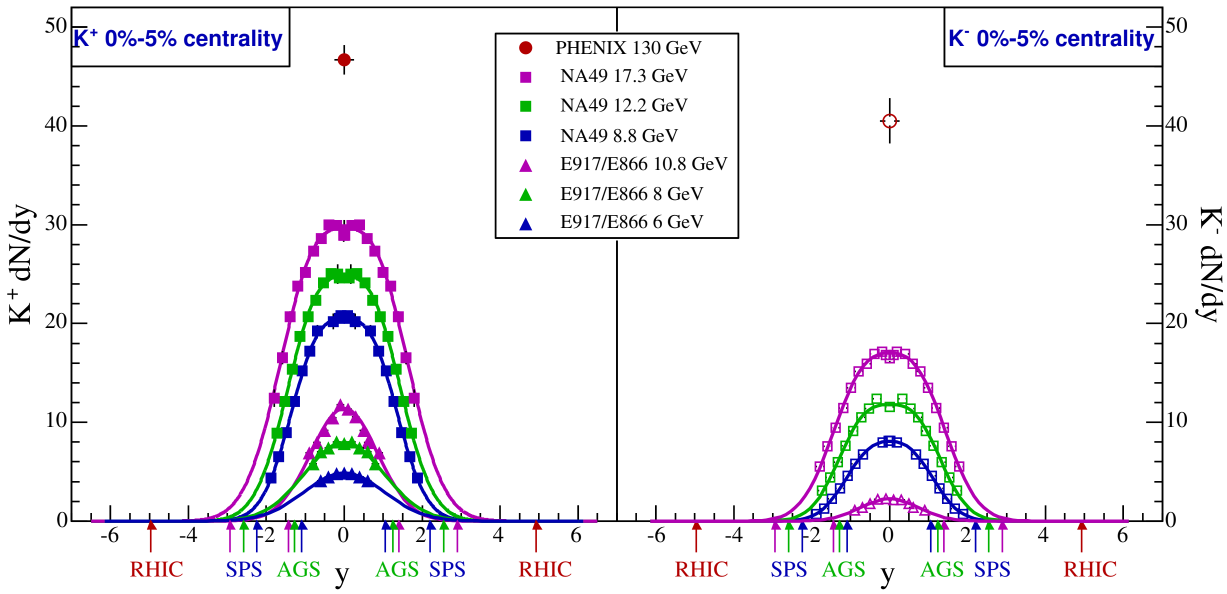

Fig. 2.5: Kaon rapidity density as a function of rapidity and $\sqrt{s_{NN}}$. RHIC and SPS data are from the same references as in Fig. 2.3. The AGS data are taken from [47, 48, 49].

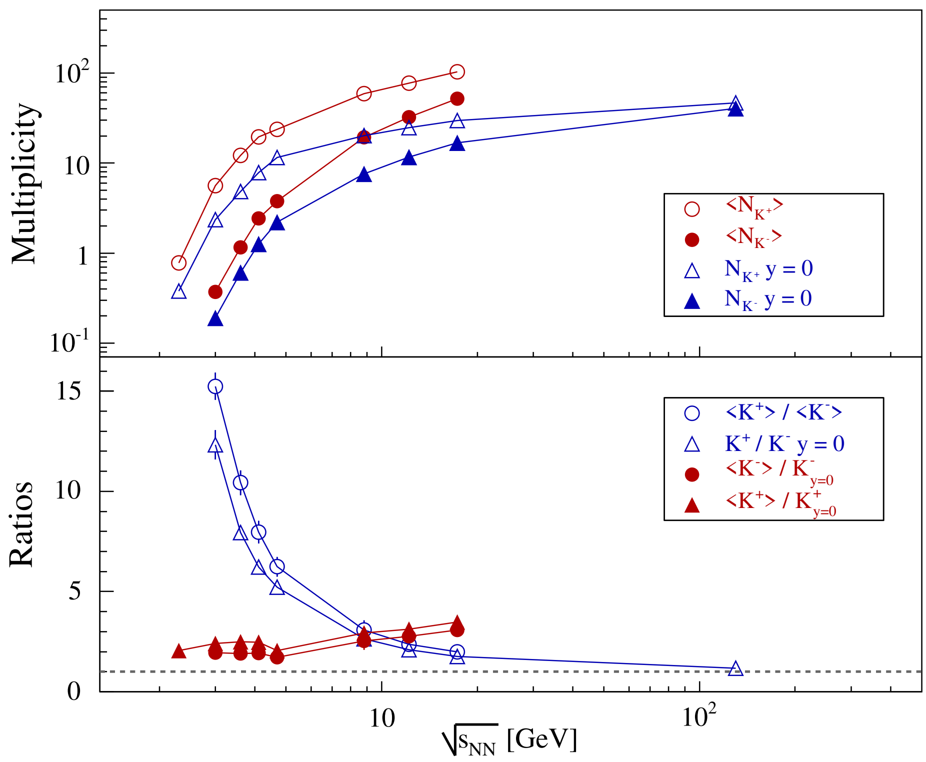

Fig. 2.6: Energy systematic of positive and negative kaon multiplicities and ratios. Solid lines are drawn to guide the eye. Errors are systematic.

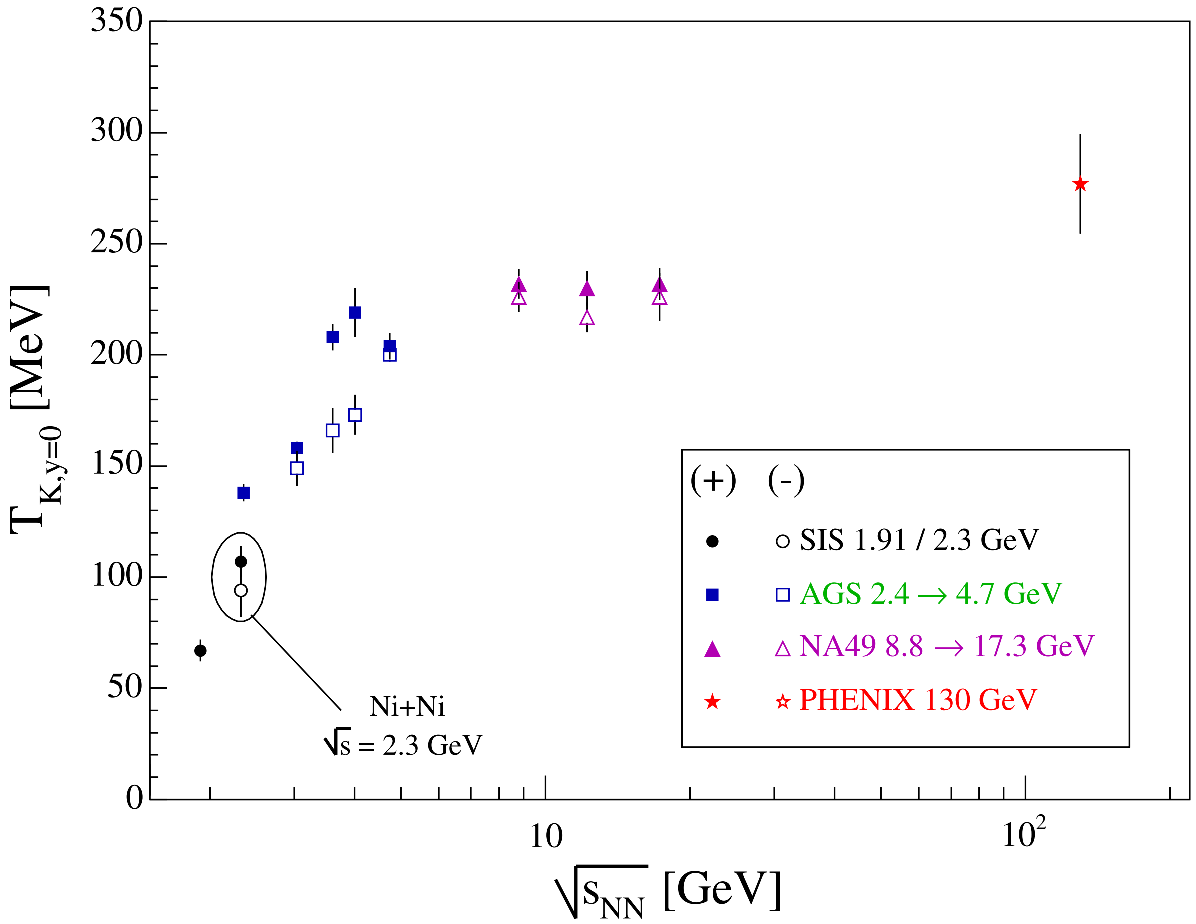

Fig. 2.7: Inverse slope parameter extracted from a fit to an exponential in m_T of kaon spectra as a function of $\sqrt{s_{NN}}$. SIS data are taken from [50, 51]. Error bars are full errors (syst. + stat).

density increases to its maximum at the top AGS energy, the K^+/π^+ ratio increases sharply from threshold to $\sim 21\%$ at $\sqrt{s_{NN}} \sim 8\,\text{GeV}$. Beside increasing pair production, the sharp increase is explained by an important contribution from associated production. Indeed, the net–baryon multiplicity reaches a maximum at the top AGS energy. In Fig. 1.17), one can note ~ 60 net–protons at mid–rapidity. The K^-/π^- ratio also increases but not so dramatically: negative kaons are mainly created by pair production that the strangeness exchange reaction tends to attenuate. As $\sqrt{s_{NN}}$ enters the SPS energy regime, the positive ratio starts dropping steadily with $\sqrt{s_{NN}}$ but much more smoothly than the initial fast increase. Indeed, the ratio ranges between $\sim 20\%$ to $\sim 16\%$ between $\sqrt{s_{NN}} = 8\,\text{GeV}$ and $\sqrt{s_{NN}} = 130\,\text{GeV}$. In contrast, the negative ratio keeps on increasing, consequence of a decreasing net–baryon multiplicity (less strangeness exchange and more string fragmentations).

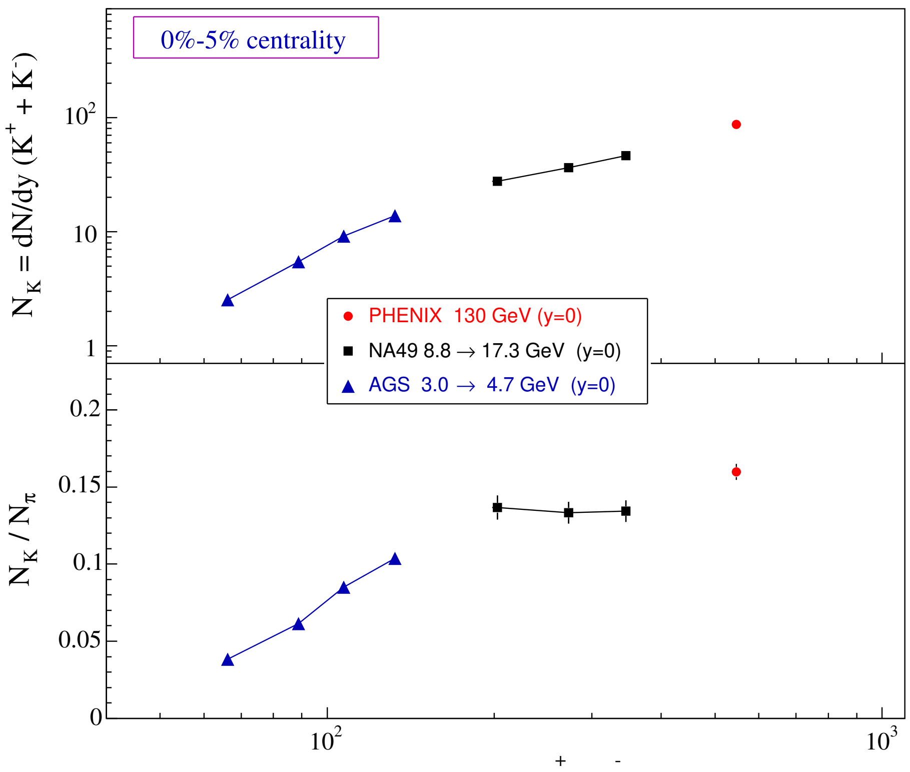

Fig. 2.8: Top: Sum of K^+ and K^- dN/dy versus sum of π^+ and π^- dN/dy. Bottom: ratio between kaon and pion multiplicities versus pion multiplicities. Errors are statistical.

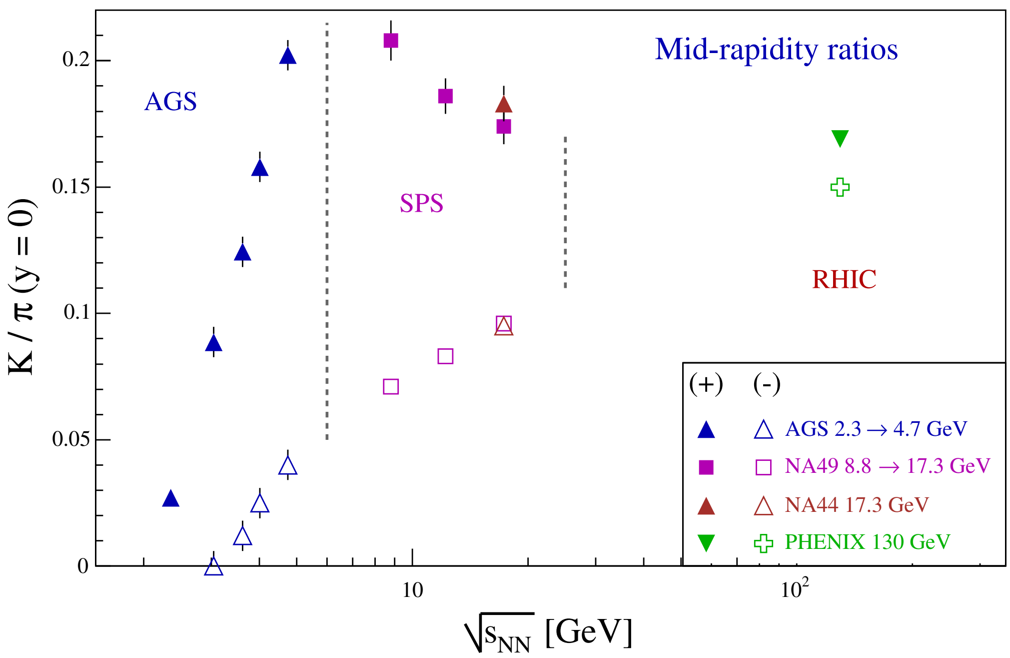

Fig. 2.9: Mid–rapidity kaon to pion ratio as a function of $\sqrt{s_{NN}}$ from AGS to RHIC energies. Errors are statistical.

2.4 Theoretical Views

Many theoretical approaches exist that try to explain and describe the dynamics and multiplicities of particle produced in relativistic heavy ion collisions. The nuclear matter under extreme conditions can be described e.g. as an expanding relativistic fluid, main assumption of hydrodynamical models, or as a classical hadron gas governed by thermodynamical laws, which is the statistical model assumption. More ambitious approaches try to explain collisions from the elementary reactions between the constituents. The models derived are called microscopic. Some models such as the event generator RQMD [54], UrQMD [55], VENUS [56] or HSD [57] follow the space–time evolution of particles through the dense medium according to known elementary interaction cross–sections, they take into account scattering between the produced particles. Other models do not do this, like FRITIOF [58] or LEXUS [59]. However, they have the ambition to treat collisions at the partonic level, they use the Lund string fragmentation model [60] as the basis of parton interaction and hadronization.

In this section, the statistical models are first presented. Then follows an introduction on parton cascade models HIJING [10] and AMPT [61, 62]. This choice is motivated by the relatively good agreement they show with the measured proton and anti–proton data of reference [30].

2.4.1 Statistical Models

In relativistic NN or AA collisions, experience shows that the strongly interacting matter eventually reaches a hadron gas state whose composition is governed by statistical laws. The population of this gas is not uniformly distributed among particle species. Indeed, the system hadronizes[2] more easily by producing pions and kaons than a heavy baryon, e.g. Ω (sss). Therefore, the final hadronic spectrum is populated in the order of mass of the hadrons. The hadron gas is hence an ensemble of maximum entropy, i.e. a de-coherent, classical system which exhibits a characteristic ordering pattern concerning the relative abundance of the hadronic species [63].

The Hadron Resonance Gas Model

The hadron resonance gas model aims at describing the multiplicities and energy density of hadrons produced in particle collisions prevailing "*at birth of the multi-hadronic final state, i.e. the point in the fireball dynamics where it decouples, by de-coherence, from the state of high energy density/temperature created in the early phase of the collisions*" [64], be they leptonic such as e^+e^- or hadronic like pp or AA. The term "resonance" means here that hadronic resonances are taken into account by the model [3]. In the context of statistical physics, the hadron gas is seen as a statistical ensemble (or Gibbs ensemble). It is either the canonical ensemble where conservation laws are exactly satisfied, i.e. particles produced in pairs close in phase–space, or the grand–canonical ensemble where conservation laws are respected only on average in the total volume of the system, i.e. particles produced independently in phase–space. The canonical ensemble is typical of low multiplicity reactions, e.g. pp, $p\bar{p}$ or e^+e^- collisions whose multiplicities are successfully described by the modern version of the Hagedorn model [66]. Conversely, central Au+Au collisions are characterized by large multiplicities, typical example of a grand–canonical ensemble. In summary, the model captures the

[2] regardless of the phase from which it does it (partonic or highly compressed hadronic state)

[3] If resonances were not included, the model would not reproduce the data [65].

image of the instant where the unknown state of high density and temperature of the fireball decays into a de-coherent, classical hadron gas. The conditions of temperature, energy density and net–baryon number density are thus *common to all hadrons emerging from the fireball.* The last statement is the fundamental postulate of the model[4].

Formally, the grand–canonical statistical analysis starts from the formulation of the partition function which specifies the weight $\mathcal{Z}_i$ (sum of possible states) for each particle or resonance specie i in the multi-hadronic mixed gas at temperature T:

$$\ln \mathcal{Z}_i = \frac{g_i V}{6\pi^2 T} \int_0^\infty \frac{k^4 dk}{E_i(k)\, \exp\left[(E_i(k) - \mu_i)/T\right] \pm 1} \tag{2.4}$$

where g_i is the statistical Lande or "degeneracy" factor of specie i, V the total common volume shared by all species, $E_i^2(k) = k^2 + m_i^2$ the total energy of specie i at momentum k, and $\mu_i = \mu_B B_i + \mu_S S_i + \mu_I Ii$, the "chemical potential" of specie i. The latter quantity arises from the need to enforce global conservation of net quantum numbers that are specific to the total system contained in volume V. In this case, these are the net quantum numbers initially carried into the fireball by the incident nuclei. The total baryon number B, strangeness S and isospin I (its third component) are $B = 2 \times (N + Z)$, $S = 0$ and $I = (Z - N)/2$ (since $I = 1/2$ for nucleons) in AA collisions. The exponential term is a "penalty" factor, depending on the total energy of specie i (if this term is big, the weight $\mathcal{Z}_i$ is low and vice–versa). It thus expresses the cost of realizing a hadron of energy $E_i(k)$ within a bath of temperature T. The chemical potential μ_i modifies the penalty factor by taking into account the "affinity" that the medium offers to specie i, it acts like an average potential, modifying the vacuum energy $E_i(k)$ of specie i. The medium is called "affine" when μ_i is positive since it increases the statistical weight $\mathcal{Z}_i$.

From Eq. 2.4, the distribution of number density of specie i (i.e. the multiplicity divided by volume V) and energy density ϵ_i are derived:

$$n_i = \frac{g_i}{2\pi^2} \int_0^\infty \frac{k^2 dk}{\exp\left[(E_i(k) - \mu_i)/T\right] \pm 1} \tag{2.5}$$

$$\epsilon_i = \frac{g_i}{2\pi^2} \int_0^\infty \frac{E_i(k)\, k^2 dk}{\exp\left[(E_i(k) - \mu_i)/T\right] \pm 1} \tag{2.6}$$

where $\pm$ distinguishes between bosons (-1) and fermions (+1). The total multiplicity of specie i in a collision is thus $N_i = n_i \times V$ (same for the energy). The experimental quantities are the multiplicities and ratios of particle species. From this information, the parameters of the model, T, V and $\mu_{B,S,I}$ can be determined. It turns out that the three chemical potentials $\mu_{B,S,I}$ are not independent. From baryon, strangeness and isospin conservation, μ_S and μ_I can be expressed in terms of μ_B. Indeed, considering the quark chemical potentials μ_u, μ_d and μ_s of quarks u, d and s respectively, it follows that

$$\mu_u = \frac{\mu_B}{3} + \frac{2}{3}\mu_I \tag{2.7}$$

$$\mu_d = \frac{\mu_B}{3} - \frac{1}{3}\mu_I \tag{2.8}$$

$$\mu_s = \frac{\mu_B}{3} - \frac{1}{3}\mu_I - \mu_S \tag{2.9}$$

[4] which does not explain *why* the de-coherent hadronic state exhibits an apparent chemical and thermal equilibrium (statistics of Gibbs ensembles).

The potential μ_s is set to zero due to total strangeness $S = 0$ (not to be confused with μ_S). In isospin symmetric system, μ_I is zero. In general, it is a small quantity (a few MeV) and decreases with collision energy [67], therefore μ_u and μ_d are set to the same value. Estimating T and μ_B are done first (V requires a second iteration) by investigating particle to antiparticle ratios. For high temperatures, the Bose or Fermi statistics can be replaced by the Boltzmann statistics by dropping the ± 1 in the integral denominator of Eq. 2.5. The multiplicity ratio for particle and antiparticle species i is

$$\frac{N_i}{\bar{N}_i} = \frac{n_i V}{\bar{n}_i V} = \frac{n_i}{\bar{n}_i} \tag{2.10}$$

By using Eq. 2.5 in the Boltzmann approximation and noticing that statistics and phase–space are identical for particles and antiparticles, it follows that

$$\frac{N_i}{\bar{N}_i} = \exp\frac{\mu_i - \bar{\mu}_i}{T} = \exp\frac{2\mu_i}{T} \tag{2.11}$$

Doing this for several measured ratios like π^+/π^-, K^+/K^-, $p/\bar{p}$, etc, a set equations is obtained from which, by maximum likelihood, μ_B and T are calculated. In a second step, the volume parameter V is fixed by fitting Eq. 2.5 to the total pion multiplicity N_π with known T and μ_B. A complication arises from particles produced by resonance decays. At chemical freeze–out, the hadron gas contains hadronic resonances like Δ, N^*, K^*, ρ, ω, etc. Eq. 2.5 describes their population and not specifically the final state hadrons π, K, p, Λ, etc. The latter serve as an observational input to a grand–canonical ensemble fit via a procedure invented by Wroblewski [68] which relates the final observed set of hadron multiplicities to a set of excited hadron and resonance multiplicities, via the known decay branching ratios.

The hadron resonance gas model has been successful at describing particle ratios and multiplicities from SIS to RHIC collisions ($\sqrt{s_{NN}} = 2\,\text{GeV}$ to $\sqrt{s_{NN}} = 200\,\text{GeV}$). Figure 2.10 shows particle ratios described by the model (from [26]) at different RHIC collision energies correlated to the experimentally measured observables. The temperatures derived are $T = 176\,\text{MeV}$ at $\sqrt{s_{NN}} = 130\,\text{GeV}$ and $177\,\text{MeV}$ at $\sqrt{s_{NN}} = 200\,\text{GeV}$ with a baryo–chemical potential $\mu_B = 41\,\text{MeV}$ and $29\,\text{MeV}$ respectively. Figure 2.11 and 2.12 shows multiplicities and ratios from Pb+Pb collisions at $\sqrt{s_{NN}} = 8.8$ and $17.3\,\text{GeV}$ (SPS). From fits performed on data at all available energies, the phase diagram of nuclear matter can be drawn by correlating T and μ_B (chemical freeze–out points). It is shown in Fig. 2.13. At low beam energies, the freeze–out points are far from the phase boundary, indicating that the system has probably not been dense enough for QGP formation. As the beam energy increases up to SPS and RHIC energies, the temperatures are close to the transition temperature as obtained from Lattice QCD [70, 71] and Bag Model [72]. Is it a coincidence that the correlation $T - \mu_B$ derived from relativistic heavy–ion data approaches the independent predictions of the transition curve calculated from Lattice QCD and the Bag Model? It can be speculated that at RHIC the fireball experiences higher temperatures during its early evolution. The statistical description of the early stage of the fireball is presented in the next section.

Statistical Model of the Early Stage

The hadron resonance gas model only describes the collision in terms of the hadronic degrees of freedom. It does not explain *why* the system exhibits this thermodynamical ordering in the abundances of particles. Moreover, it does not make predictions but fits the data. The

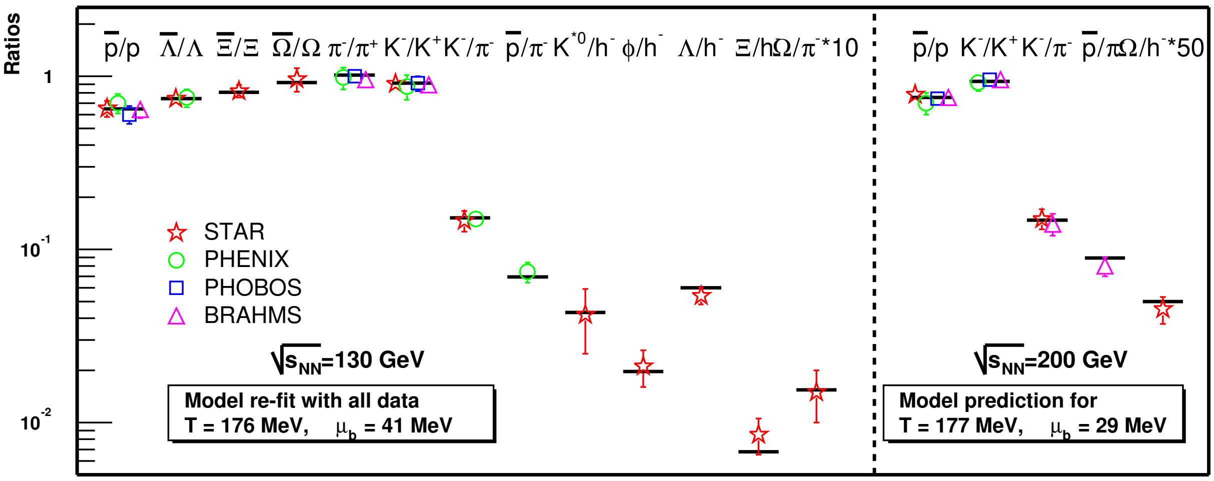

Fig. 2.10: Statistical model description of particle ratios from Au+Au collisions at $\sqrt{s_{NN}} = 130\,\text{GeV}$ and $\sqrt{s_{NN}} = 200\,\text{GeV}$. See data references therein.

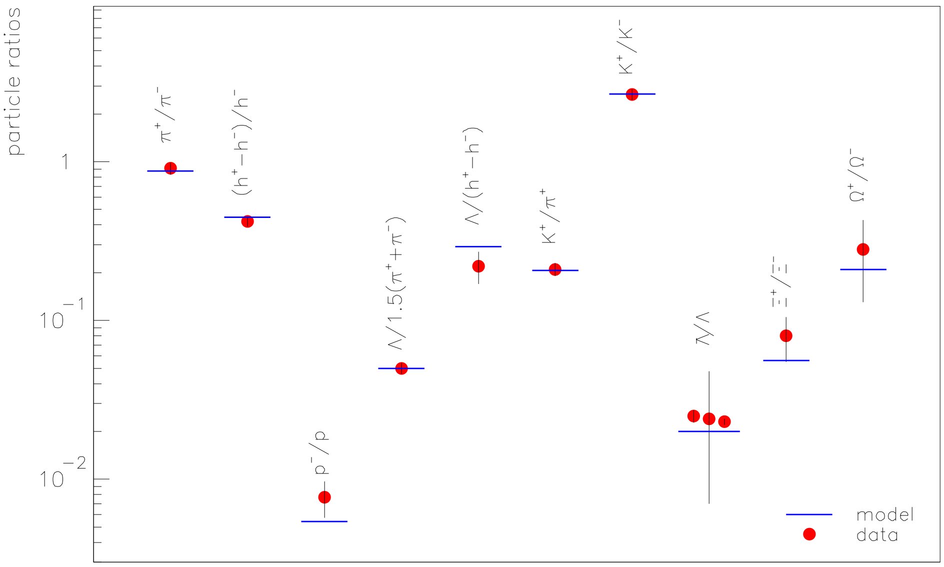

Fig. 2.11: Statistical model description of particle ratios from Pb+Pb collisions at $\sqrt{s_{NN}} = 8.8\,\text{GeV}$ (from [26]).

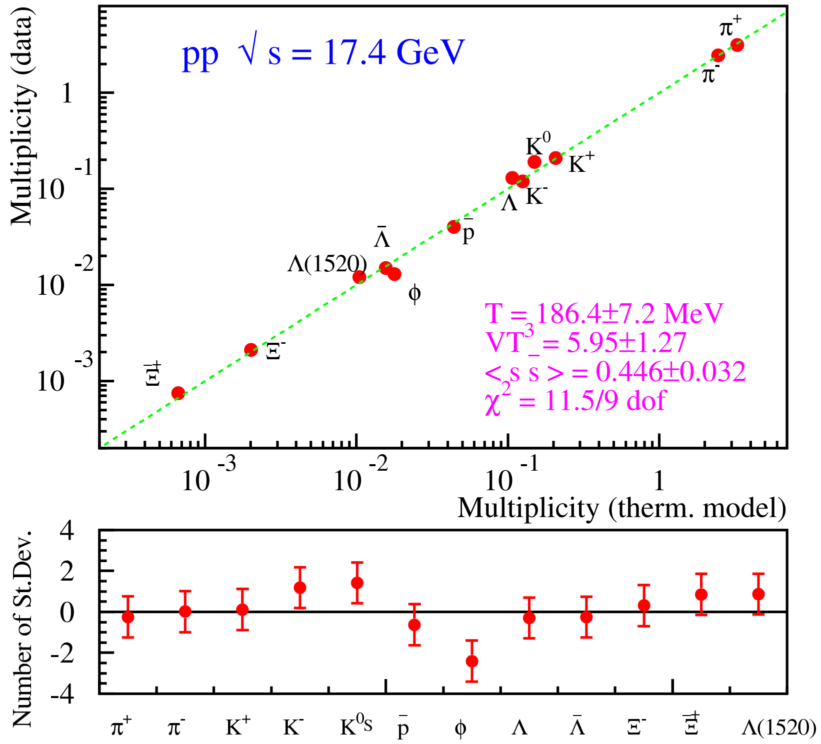

Fig. 2.12: Statistical model description of particle multiplicities at $\sqrt{s_{NN}} = 17.3\,\text{GeV}$ (from [69]).

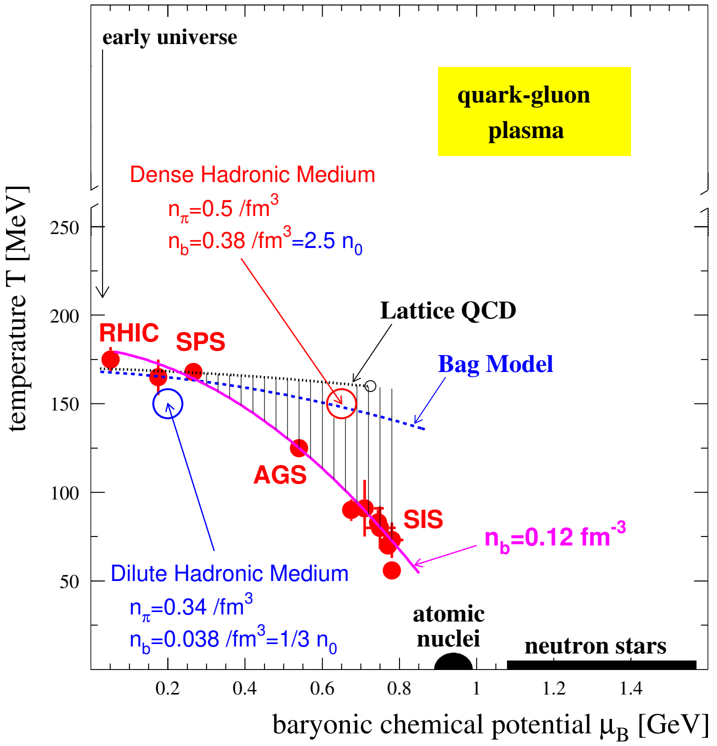

Fig. 2.13: Nuclear matter phase diagram. The temperature and baryo–chemical potential calculated from RHIC and SPS data are very close to transition curves predicted by Lattice QCD [70, 71] and the Bag Model [72].

Statistical Model of the Early Stage (SMES) [73] is an alternative statistical description. It assumes a QGP phase in statistical equilibrium where quarks and gluons are the degrees of freedom. A special role is played by the the entropy, mainly carried by produced pions and heavy quark flavor production (strangeness and charm). The hadronic (confined) state of the fireball that follows the early deconfined phase is parameterized according to the available AA collision data. Comparing the evolution of entropy as a function of $\sqrt{s_{NN}}$ to data with and without the QGP phase assumption is the SMES strategy for probing such phase in the data.

The SMES is based on the pioneer work of Fermi [74] and Landau [75], extended by Van Hove [76] to heavy ion collisions. In a QGP, the color degrees of freedom of the liberated partons introduce a significant number of new energy states unavailable in a hadron gas. Discontinuities in the observed pion or strange particle multiplicities as a function of $\sqrt{s_{NN}}$ might indicate the onset of QGP formation. Fermi introduced an analogy between the thermodynamical model of a relativistic photon gas, where the energy density ϵ is proportional to the fourth power of the temperature $\epsilon \sim T^4$, and the (massless) pion gas produced in NN collisions, whose equation of state is $p = 1/3\,\epsilon$ where p is the pressure. Landau developed these ideas, applying hydrodynamics of an ideal fluid to the (expanding) system of high density and temperature. In this approach, if S_E is the total entropy at an early stage (before expansion), it can be related to the so–called Fermi variable F (see Appendix F):

$$S_E \sim \frac{\left(\sqrt{s_{NN}} - 2m_N\right)^{\frac{3}{4}}}{\left(\sqrt{s_{NN}}\right)^{\frac{1}{4}}} \equiv F \tag{2.12}$$

where m_N is the nucleon mass. Landau further assumed that the fireball expansion is isentropic, so that the final entropy S is equal to S_E. This entropy model was confronted to NN collision data [77]. It is shown that the measured pion multiplicities $\langle \pi \rangle$ are proportional to F up to $\sqrt{s_{NN}} \sim 20\,\mathrm{GeV}$. At higher energies, the proportionality tends to break down. It is due to the fact that more and more initial energy goes into leading particles, i.e. there is not full stopping anymore.

In AA collisions, Landau calculated that $S \sim \langle h \rangle \sim A^{3/4}$ where $\langle h \rangle$ is the hadron multiplicity. He assumed that all nucleons participate and are stopped. The analysis done from NN collisions has been carried out for heavy–ion collisions [78, 79, 80] with a modern version of the SMES [73], where $A^{3/4}$ has been replaced by the number of participants stopped according to the measured AGS and SPS net–baryon. The approximation used is

$$S_E \sim S \sim \langle N_{part} \rangle \times F \tag{2.13}$$

where $\langle N_{part} \rangle$ is the average number of participating nucleons. The entropy also includes contributions from particles other than pions, notably kaons, and the energy required to heat the incident nucleons up to the thermalized system temperature [78]:

$$S_E \sim S = 4\,S_\pi = \langle \pi \rangle + \kappa \langle K \rangle + \delta \langle N_{part} \rangle \sim \langle N_{part} \rangle \times F \tag{2.14}$$

where S_π is the entropy in units of pion entropy. The factor 4 is the conversion from the total entropy to entropy in units of pion entropy [73]. The factor κ is approximately 1.45, deduced from measurements of the AGS experiment E917 [81]. From differences between $\langle \pi/N_{part} \rangle_{AA}$ and $\langle \pi/N_{part} \rangle_{NN}$ data ($N_{part} = 2$) at lower energies (SPS and below), δ is determined to be 0.35 [78]. It is found that the entropy per participating nucleon in AA reactions is different

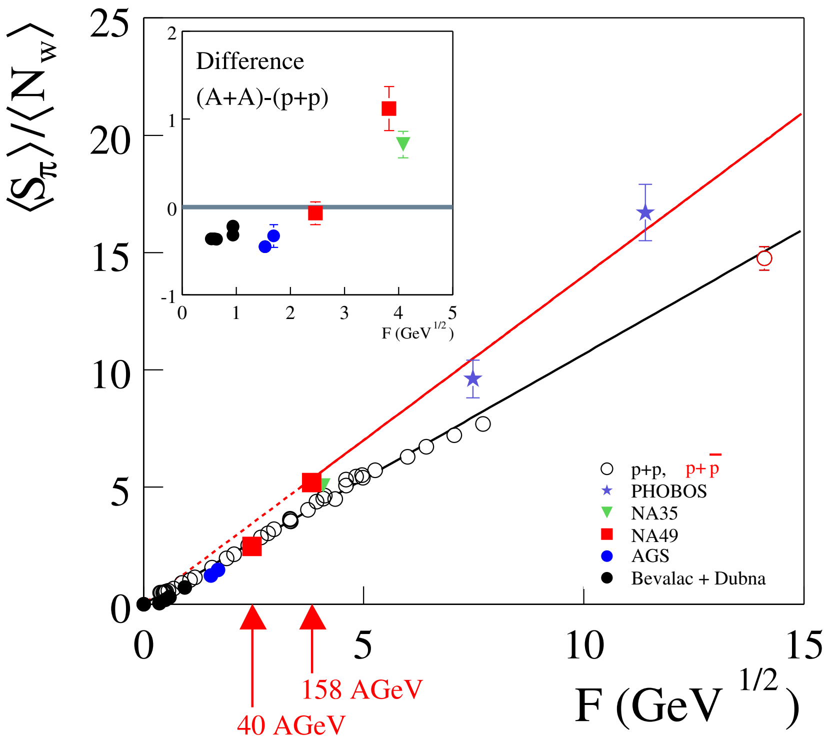

Fig. 2.14: Pion multiplicity, defined as $\langle \pi \rangle = \frac{3}{2}\left(\langle \pi^+ \rangle + \langle \pi^- \rangle\right)$, per wounded nucleons (participants) as a function of the Fermi energy variable F for central A+A collisions (solid symbols) and p+p ($\bar{\text{p}}$) reactions (open symbols).

than that in NN collisions and lies on a steeper slope (about a factor of 1.33 increase), as shown in Fig 2.14. The assumption $S \sim g^{1/4} \times \langle N_{part} \rangle \times F$ where g is the effective number of degrees of freedom implies an increase of about a factor of 3 of g. This result is interpreted as an "unusual increase of the entropy density at the early stage" of the collision, which can be related to the existence of a deconfined phase in AA collisions that doesn't occur in NN collisions. However, this result relies on the RHIC data, where the model parameters valid for AGS and SPS are assumed to be valid. It is known that collisions are more transparent [38] (the nucleon rapidity loss has been estimated in [30]) at RHIC. Furthermore, the entropy estimated from the PHOBOS data plotted in Fig. 2.14 is a rough estimation based on the total number of charged particles, corrected after the particle ratios measured at RHIC. The PHOBOS experiment cannot provide an estimation of the total multiplicity of identified pions and kaons. However, this thesis presents a first and unique measurement of the total multiplicity of charged pions and kaons by studying the rapidity dependence of meson yields. The results are discussed in Chap. 7 in the context of the SMES.

2.4.2 Strangeness: Enhancement and QGP

Strangeness as a probe for early deconfinement in the dense fireball in AA collisions has been suggested by Rafelski and Letessier (see full reviews [7, 53]). The term "enhancement" can be understood in two ways: enhancement with respect to NN collisions or enhancement relative to non strange particles with increasing $\sqrt{s_{NN}}$ (or energy density). The SPS experiment NA57 measured yields of strange and multi–strange baryons in pp, pA and AA collisions [25], as mentioned in the thesis introduction (cf. Fig. 1.15). Rather than reviewing all theoretical arguments, strangeness enhancement is discussed here in the context of the statistical models introduced above.

Strangeness...Suppression

The relative enhancement of the K/π ratio from pp to AA collisions is explained in the hadron resonance gas model by a canonical suppression from AA to pp. Remember that the chemical potential μ_i of specie i is introduced to enforce conservation of the quantum numbers. However, the equation $\mu_i = \mu_B B_i + \mu_S S_i + \mu_I Ii$ is an approximation that is only valid when the number of particles carrying the conserved quantum numbers is large (grand–canonical statistics). Indeed, the calculation of the Boltzmann distribution includes states of the system which violate the conservation laws. It can be shown that if a system contains a large number of particles carrying the conserved quantum numbers, the contribution of such states is small, which makes the approximate treatment valid. In contrast, when the number of particles is small, the conservation laws must be explicitly taken into account, using the canonical formalism. Following references [82, 83], the canonical kaon yield N_K^C is derived from the grand–canonical yield N_K^{GC} according to the following equation:

$$N_K^C = N_K^{GC} \frac{N_{S=1}}{\sqrt{N_{S=1}\, N_{S=-1}}} \times \frac{I_1(x_1)}{I_0(x_1)} \tag{2.15}$$

where $N_{S=1}$ ($N_{S=-1}$) is the total number of particles with strangeness 1 (-1), mainly K^+ (K^-) and $\bar{\Lambda}$ (Λ), calculated using the grand–canonical formalism (from Eq. 2.5). I_0 and I_1 are modified Bessel functions and $x_1 \equiv 2\sqrt{N_{S=1}\, N_{S=-1}}$. The ratio I_1/I_0 determines the difference between canonical and grand–canonical yields and is called the 'canonical suppression factor'. This ratio depends on the system size through x_1. The general expression for the strangeness canonical suppression factor is $I_s(x_1)/I_0(x_1)$. It is shown in Fig. 2.15 as a function of the number of wounded nucleons (number of participants) for two collision energies and $s = 1, 2, 3$ (one, two and three strange quarks). At large number of participants, the canonical suppression factor is close to unity (grand–canonical limit). For kaons ($s = 1$), the factor is 0.5 at $N_w = 2$, i.e. pp collisions. According to this model, the production of kaons is suppressed in NN w.r.t AA due to exact strangeness conservation (canonical statistics). The statistical arguments explaining pp and AA differences have been used in [84] and predictions turn out to reproduce the data on the relative enhancement of strange baryons w.r.t to yields measured from p+Be collisions (see Fig. 2.16). However, the hadron resonance gas model fails at describing the evolution of the $\langle K^+\rangle / \langle \pi^+\rangle$ ratio as a function $\sqrt{s_{NN}}$, as can be seen on Fig. 2.17. The statistical model of the early phase (SMES) has the ambition to describe and predict the evolution of the strangeness to entropy ratio as a function $\sqrt{s_{NN}}$.

Statistical Model of the Early Stage

The approach of the SMES for predicting the strangeness evolution with $\sqrt{s_{NN}}$ does not focus on the strangeness enhancement, seen in this context as a change of the statistical order (canonical to grand–canonical) as mentioned before. The SMES aims at showing that the strangeness to entropy ratio exhibits a discontinuity as $\sqrt{s_{NN}}$ increases. The model explicitly introduces a statistically equilibrated QGP where all the entropy S and strangeness are produced. At hadronization, entropy and strangeness content do not evolve anymore (adiabatic expansion of the fireball). For the QGP state, the model considers 6 number of degrees of freedom per quark u, d, s and anti–quarks (3 color states $\times$ 2 spin states). Light non strange quarks are taken massless while $m_s = 175\,\mathrm{MeV/c^2}$. The gluonic degrees of freedom

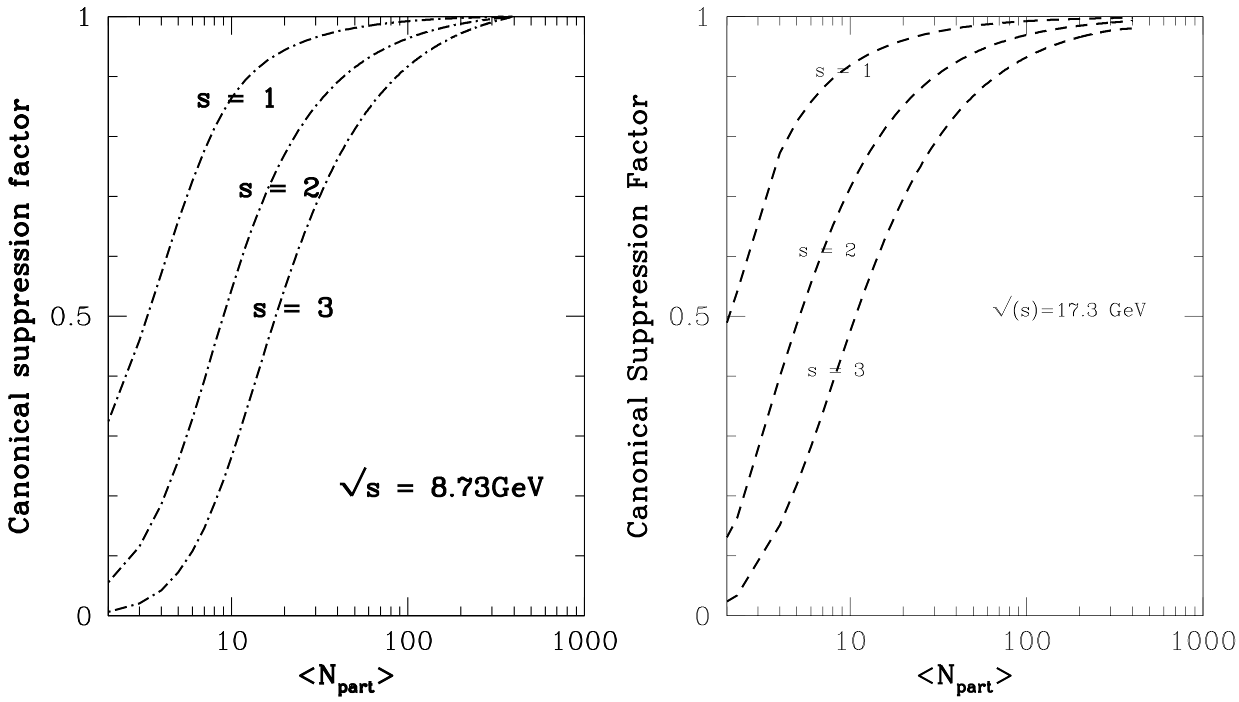

Fig. 2.15: Strangeness canonical factor expressing the difference in strangeness production between large collision systems (grand–canonical ensembles) and small reactions like pp or pA (canonical treatment), as a function of the number of wounded nucleons.

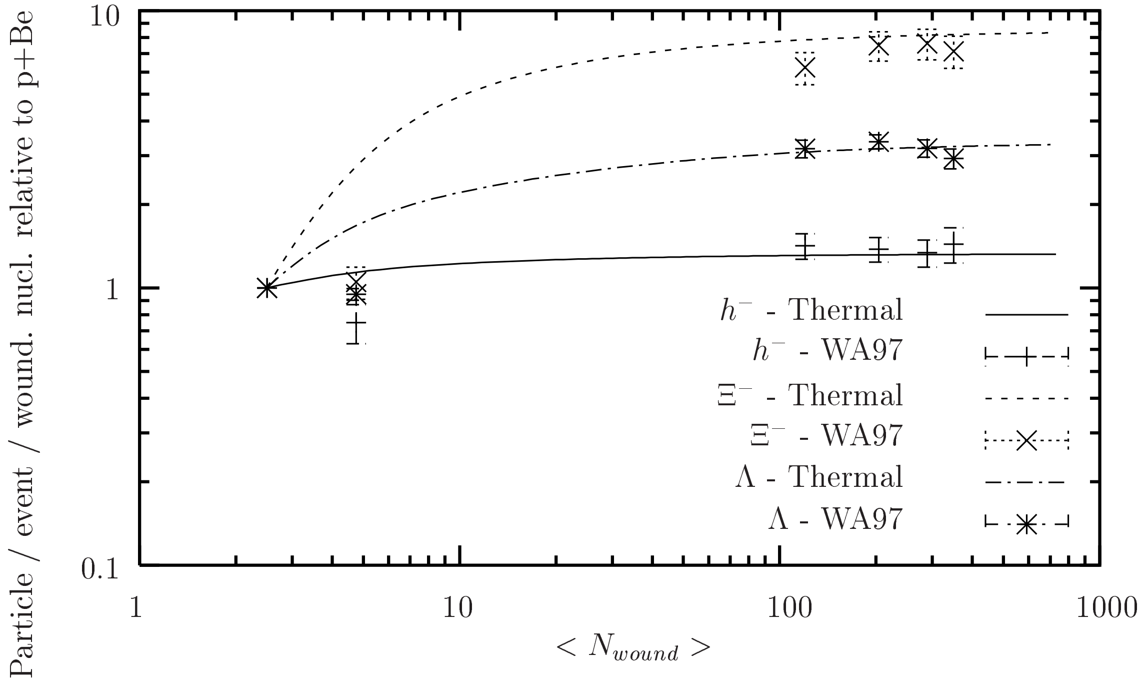

Fig. 2.16: Comparison of the hadron gas model with exact strangeness conservation and CERN WA97 data for negatives and strange particles (from [84]).

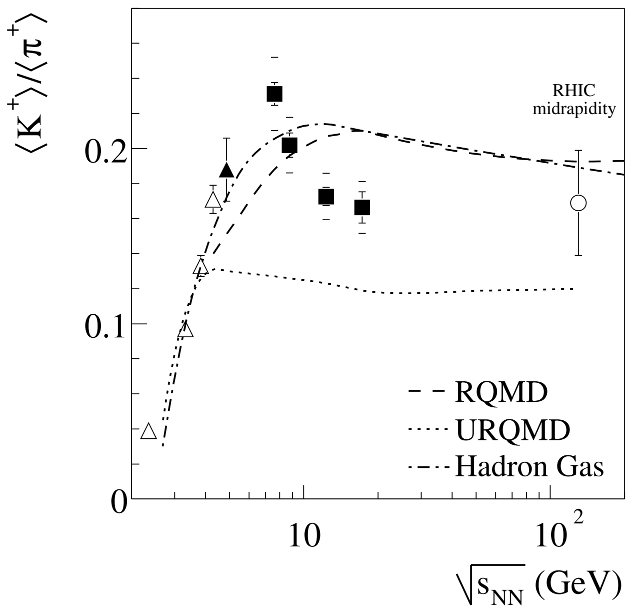

Fig. 2.17: The hadron gas model does not describe the details of the measured $\langle K^+\rangle \,/\, \langle\pi^+\rangle$ ratio as a function of $\sqrt{s_{NN}}$ (figure from [85]).

amount to 16 (8 color states $\times$ 2 spin states). For the hadronic state (after hadronization), the number of degrees of freedom is chosen three times lower than that of the QGP state (based on experimental measurements [78]). The mass of strange hadronic degrees of freedom is taken to be 500 MeV (kaon mass). For all other assumptions and initial conditions, see [73]. Figure 2.18 shows two relevant results that can be compared to the data already shown in Sec. 2.3. The strangeness to entropy ratio is defined as follows:

$$E_s = \frac{\left\langle \Lambda + \bar{\Lambda} \right\rangle + \left\langle K + \bar{K} \right\rangle}{\langle \pi \rangle} \tag{2.16}$$

In the model, the initial temperature keeps increasing with beam energy. At high temperature and energy density, when the strange degrees of freedom become effectively massless, the strangeness to entropy ratio saturates at a value of

$$\frac{N_{\bar{s}s}}{S} = \frac{1}{4}\,\frac{g_s}{g} \tag{2.17}$$

where g and g_s are the total and strange number of degrees of freedom. The factor of $1/4$ comes from the fact that each massless quark carries 4 units of entropy [73]. The ratio g_s/g is expected to be equal to ~ 0.22 in a QGP state and 0.5 in a hadronic state. Therefore, a transition from a hadronic to partonic state should lead to a decrease of the strangeness to entropy ratio by a factor of 2. The discontinuity in the strangeness to entropy ratio of Fig. 2.18 is due to the phase transition. Note also the temperature evolution, the plateau structure of Fig. 2.7 looks like it, although the inverse slope parameters reported in Fig. 2.7 are characteristic of the final kinetic freeze–out and consequently modified by transverse flow.

2.4.3 Microscopic Models

The heavy ion collision dynamics at a microscopic level is so complex that a complete analytical description is not possible. An alternative way is to use Monte Carlo event generators, based

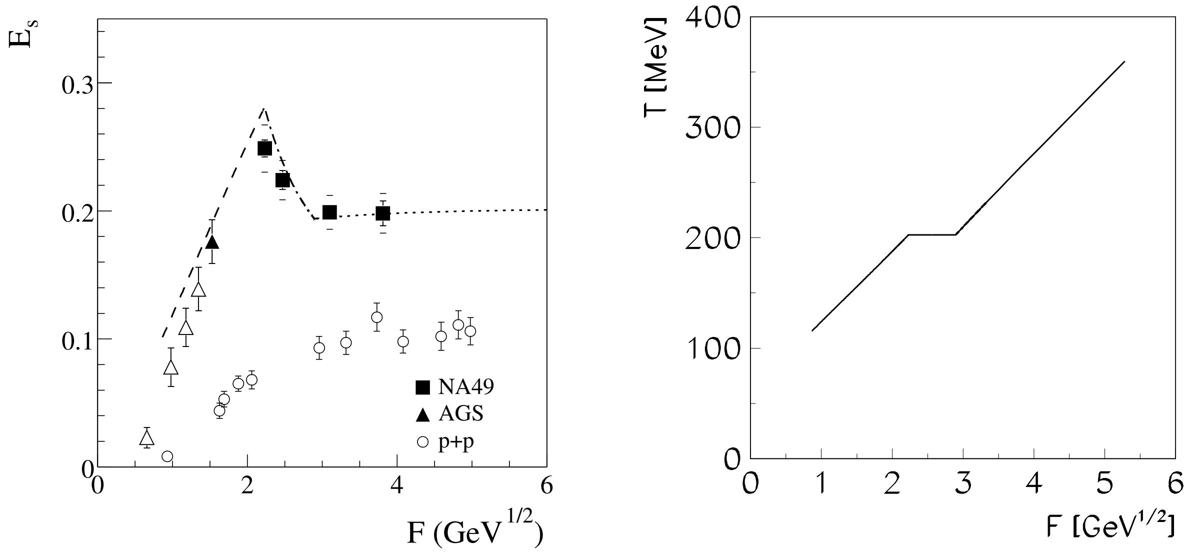

Fig. 2.18: Left: Energy systematics of strangeness to entropy ratio predicted by the statistical model of the early stage (figure from [85]). Right: Evolution of the temperature with F.

on the generation of random numbers. They consist of computer programs with three distinct parts: the input conditions, particle interactions and propagation, and the final state (output). Two models are presented here, with similar inputs but different final state treatment.

HIJING

The Heavy Ion Jet Interaction Generator (HIJING) [10] is a model that incorporates perturbative QCD (pQCD) mini–jet production and quenching that occur in collisions at RHIC energies and above.

• Motivation: Mini–Jet production:
Hard parton scattering is well established in hadronic interactions and play a major role in $p\bar{p}$ collisions at SPS and Tevatron at Fermilab [86]. Experimentally, when the transverse energy E_T of a jet becomes smaller than $E_T < 5\,\mathrm{GeV/c}$, it is difficult to resolve it from the background of soft particles. These jets are referred to as mini–jets. At RHIC, mini–jets have been estimated to produce 50% of the transverse energy in central heavy–ion collisions [87, 88, 89]. While not resolvable as distinct jets, they would "*lead to a wide variety of correlations, as in NN collisions, among observables such as multiplicity, transverse momentum, strangeness and fluctuations that compete with the expected signatures of a QGP*" [90]. The other motivation for calculating mini–jet production is to address the issues of thermalization and equilibration of a QGP. Thus the actual interest of high p_T jet–quenching (cf. 1.4.2).

• How It Works:
In this model, multiple mini–jet production is combined together with a Lund–type model for soft interactions ($p_T < 2\,\mathrm{GeV/c}$). The typical interaction in string models is diquark–quark or quark–anti–quark strings, but some models also include sea–quarks to simulate multiple collisions. The number of binary collisions at a given impact parameter is determined from

a Glauber calculation. The possibility of hard pQCD scattering is considered first. After subtracting the energy loss due to hard scatterings, the soft interactions are calculated from the number of collisions which, in turn, is calculated according to geometric probabilities. The first collision between two nucleons creates diquark–quark strings that are assumed to decay within a time–scale larger than the collision time. The wounded nucleon strings can interact in the same way with other nucleon strings, but the probability of exciting them further or deexciting them is modified. Once the strings decay, the produced particles do not rescatter anymore (no space–time evolution).

• Results:
The success of HIJING is the prediction of the charged particle multiplicity $dN/d\eta$ at mid–rapidity in collisions at $\sqrt{s_{NN}} = 56$ and 130 GeV [91] but it should be noted that the physics conditions of the model can be tuned in order to reproduce the results [92]. The recent measurement of nuclear stopping [30] is also compared to several microscopic models. Figure 2.19 shows the net–proton rapidity density in central Au+Au collisions at $\sqrt{s_{NN}} = 200$ GeV. The

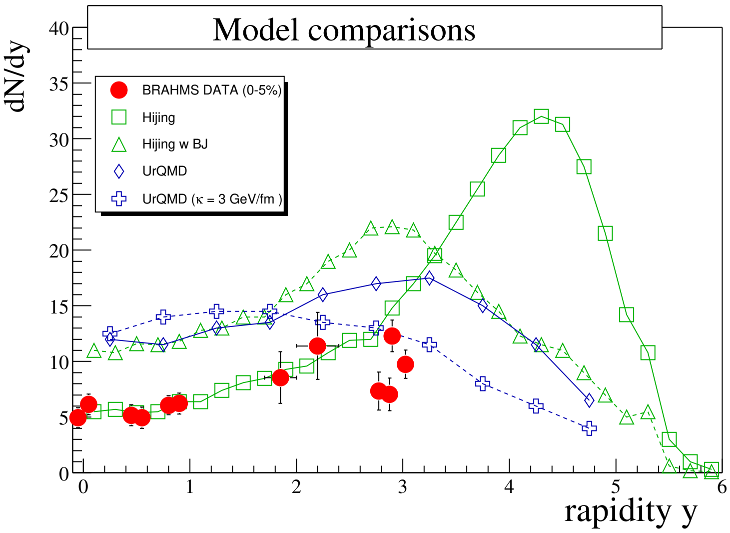

Fig. 2.19: Model comparison of net–proton rapidity densities. HIJING is the best description (from [30]).

best agreement is achieved by HIJING. Therefore, the model predictions on charged meson production are investigated. A comparison with the results of this thesis is detailed in Chap. 7.

AMPT

AMPT is A Multiple Phase Transport model [61]. AMPT uses the HIJING model for generating the initial parton phase–space generation, and the ZPC model [93] to follow their rescatterings. The hadronization is taken care of by HIJING again. The main difference with HIJING is the treatment of the evolution of the produced hadrons within the framework of the ART transport model [94].

• Partonic phase:
After the parton phase–space is populated using the HIJING engine, the parton cascade is carried out using the ZPC model which includes only gluon–gluon elastic scattering. Once

parton stop interacting, they are converted into hadrons using the HIJING fragmentation scheme. While HIJING treats diquarks as a single entity, which leads to an average rapidity shift of about one unit in the net–baryon distribution [30], AMPT modifies the fragmentation scheme to allow the formation of diquark–antidiquark pairs. In addition, the baryon–meson–antibaryon formation probability is taken to be 80% for the produced diquark–antidiquark pairs, while the rest consists baryon–antibaryon production. The resulting effect is a reasonable description of the measured net–baryon rapidity distribution in Pb+Pb collisions at $\sqrt{s_{NN}} = 17.3\,\mathrm{GeV}$.

• Hadronic phase:
The evolution of hadrons is processed by the ART model, which is successful at describing heavy ion collisions at AGS energies. The extension of the model to RHIC consists of the introduction of nucleon–antinucleon annihilation channels, inelastic interactions of kaons and antikaons, and neutral kaon production. In the ART model, multiparticle production is modeled through the formation of resonances.

• Predictions:
The $\bar{p}/p$ ratio predicted by AMPT for central Au+Au collisions at $\sqrt{s_{NN}} = 130\,\mathrm{GeV}$ is

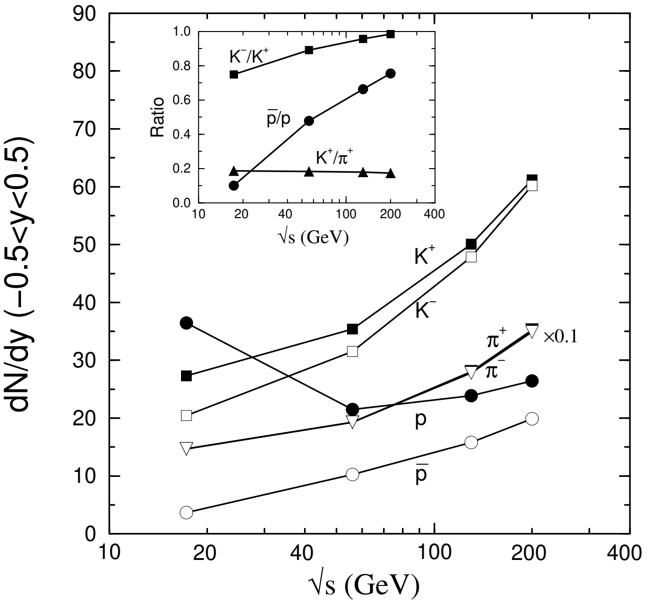

Fig. 2.20: Charged meson yields and ratios as a function of $\sqrt{s_{NN}}$ calculated by AMPT [62] for the top 5% central Au+Au and Pb+Pb collisions.

0.6 [61]. The experimental measurement amounts to 0.62 ± 0.04 [95]. The meson rapidity distributions have also been calculated as a function of $\sqrt{s_{NN}}$ for central Au+Au and Pb+Pb collisions. Figure 2.20 shows the pion and kaon yields as well as their relative ratio as a function of $\sqrt{s_{NN}}$. The data presented in this thesis will confirm or infirm the prediction at $\sqrt{s_{NN}} = 200\,\mathrm{GeV}$.

♣♣♣♣♣♣

Chapter 3

The BRAHMS Experiment

The data presented in this thesis were collected by the Broad Range Hadron Magnetic Spectrometers (BRAHMS), during the first full energy Au+Au run at the Relativistic Heavy Ion Collider (RHIC). BRAHMS is one of the four experiments at RHIC. This chapter gives a description of the BRAHMS experimental setup, as well as the RHIC accelerator complex.

3.1 The Relativistic Heavy Ion Collider

The Relativistic Heavy Ion Collider at the Brookhaven National Laboratory (BNL) began running in 2000, after a twenty year period of design and construction.

3.1.1 RHIC: A Significant Energy Boost

Prior to RHIC, only light particles were accelerated in the existing colliders like the Large Electron Positron Collider (LEP) at CERN or the Tevatron proton anti–proton collider at Fermi Lab. Pre–RHIC heavy ion collision experiments were carried out with an accelerated beam and a fixed target at accelerators like the Heavy Ion Synchrotron (SIS) at the GSI, the Alternating Gradient Synchrotron (AGS) at BNL or the Super Proton Synchrotron (SPS) at CERN. A simple kinematic study of a mass symmetric collision system ($A_{proj} = A_{target}$) shows that the available energy for particle production $\sqrt{s_{NN}}$ (nucleon–nucleon center of mass energy) is not the total energy in the laboratory frame (see end of appendix B). Table 3.1 summarizes the various values of $\sqrt{s_{NN}}$ and corresponding beam energy per nucleon in the laboratory E_{lab}/A achieved at the different facilities.

Facility	SIS	AGS	SPS	RHIC	LHC
$\sqrt{s_{NN}}$ (GeV)	1.9	2.3 – 3.0 – 3.6 – 4.8	8.8 – 12.2 – 17.3	22 – 130 – 200	7000
E_{lab}/A (GeV)	1	2 – 4 – 6 – 11.6	40 – 80 – 158	11 – 65 – 100	3500

Tab. 3.1: Center of mass energy $\sqrt{s_{NN}}$ achieved or planned (LHC) at various international heavy–ion facilities.

The powerful concept of colliders is to make all incident energy available for the reaction by having the center of mass frame coincide with the laboratory frame (for mass symmetric collision systems).

3.1.2 A Short Description

A schematic view of RHIC is shown in Fig. 3.1. The AGS accelerator complex (Tandem,

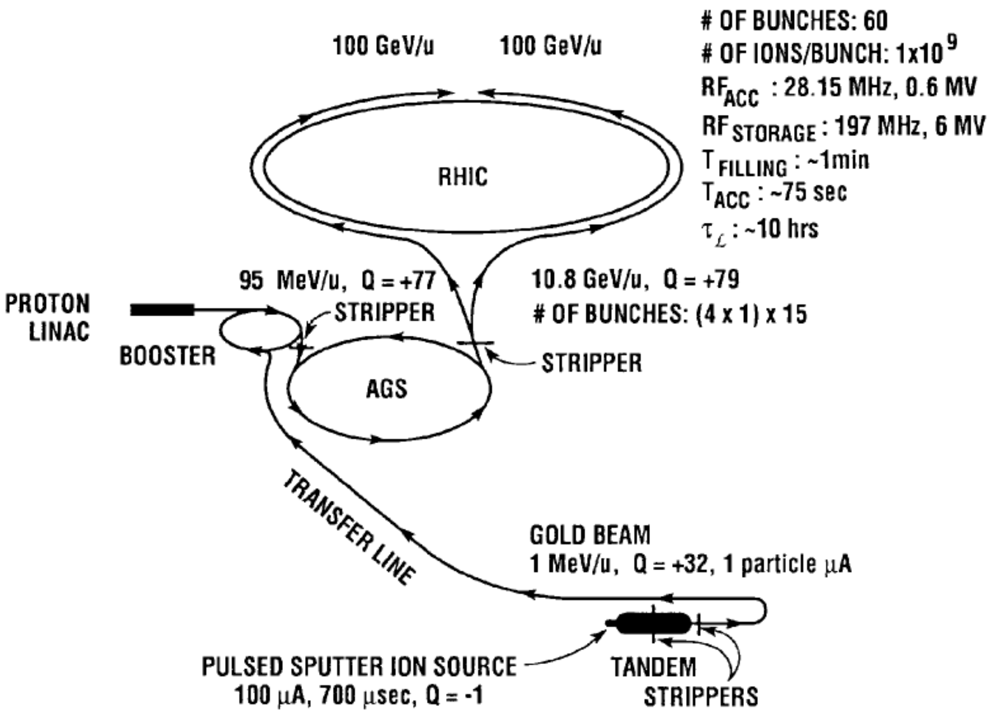

Fig. 3.1: Schematic view of RHIC

Booster and AGS) is used as a pre–accelerator of gold ions. From the AGS exit, a gold ion beam of 10.8 AGeV is directed toward the RHIC entrance where it is split into a "blue" beam and "yellow" beam. These are injected into RHIC and travel through two separate rings of 4 km circumference, clockwise and counter–clockwise. The beam storage is assured by quadrupole magnets located along the rings. The maximum energy yellow and blue beams can acquire is $E/A = 100\,\mathrm{GeV}$, which implies a nucleon velocity β_N equal to

$$\beta_N = \frac{\sqrt{(E/A)^2 - m_N^2}}{E/A} = 0.999956$$

The maximum RHIC design energy $\sqrt{s_{NN}}$ amounts to 200 GeV. It is the first time in the world that heavy ions collide at such a high center of mass energy, about ten times higher than the top SPS energy.
There are six experimental areas where beams can intersect for collision production. BRAHMS is located at the 2 o'clock hall while PHOBOS, PHENIX and STAR, the other RHIC experiments, are located at the 10 o'clock, 8 o'clock and 6 o'clock halls respectively (which leaves two locations empty).

3.1.3 Luminosity

The gold beams are designed to be divided in sixty bunches per ring, each bunch containing approximately 10^9 ions. The design luminosity $\mathcal{L}$ amounts to $2.10^{26}\,\mathrm{cm}^{-2}\mathrm{s}^{-1}$, which gives a reaction rate $R = \mathcal{L} \times \sigma \simeq 1200\,\mathrm{Hz}$, where σ is the interaction cross–section. This gives a rate per bunch $R_{bunch} \simeq 20$ Hz. Since a bunch makes $\sim 100,000$ revolutions per second, assuming it travels at the speed of light in a ring of 4 km, the interaction probability is $\sim 0.02\,\%$. Thus, the ratio between multiple collisions and single collisions is of the order of 0.02 % (the interaction probability is assumed to follow a Poisson law distribution). More details about RHIC and other experiments can be found on the dedicated web–site `http://www.bnl.gov/rhic` and in reference [96].

3.2 BRAHMS Overview

The goal of the BRAHMS experiment is to measure charged hadrons over a broad range of rapidity and momentum. BRAHMS started systematic measurements during summer and fall 2001 where identified charged particles ($\pi^{\pm}$, $K^{\pm}$ and $p\bar{p}$) have been measured over the rapidity range $0 \lesssim y \lesssim 3.6$ and momentum range 0.2 up to 25 GeV/c for the highest rapidity particles. Such measurements are only possible with high resolution detectors for tracking and particle identification (PID). This section reviews the BRAHMS detectors.

A Flexible Experiment

BRAHMS is composed of three distinct groups of detectors. The first group is devoted to the reaction characterization, namely the collision interaction point (IP) commonly called the primary vertex, and the collision centrality (cf. Sec 1.3.1). The two other groups are spectrometers which by design track charged particles and allow their identification. A schematic picture of the BRAHMS detector system is shown in Fig. 3.2. The particularity of the spec-

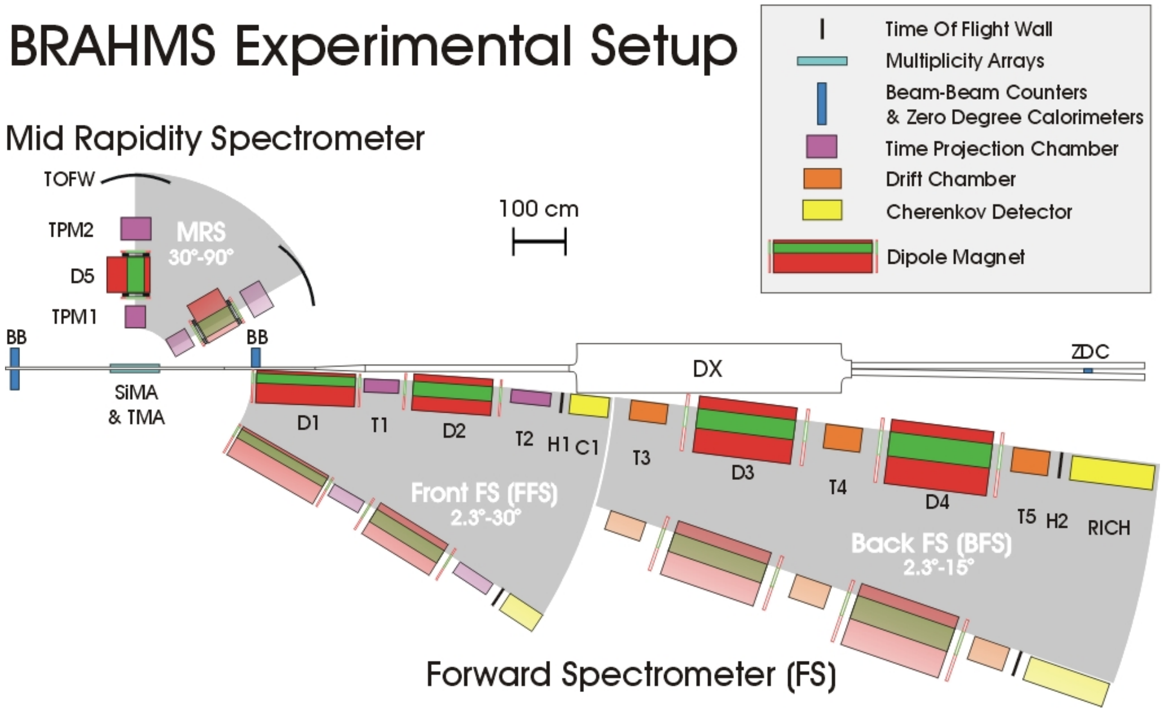

Fig. 3.2: Schematic picture of the BRAHMS detector system (top view). The spectrometer arms are independent and can rotate in the horizontal plane in order to cover a polar angle range of $\pi/2$ rad.

trometers is their capability to rotate around a vertical axis (y direction) passing through the nominal IP $(z, x) = (0, 0)$ where z is the direction of the beam line and x an axis perpendicular to z and y (cf. Appendix B). This rotation allows a coverage of the polar angle θ (angle between the spectrometer own axis and z) that amounts to nearly $\pi/2$ rad. This capability is not shared by the other RHIC experiments.

The Mid-Rapidity Spectrometer MRS

One of the spectrometers (MRS) is assigned the coverage of mid-rapidity regions. It is composed of two time projection chambers (TPC) which measure the trajectories of charged particles within the TPC active volume. Between the two TPC's, there is a dipole magnet for momentum determination, and a time–of–flight detector (TOF) for particle identification (see Fig. 3.3).

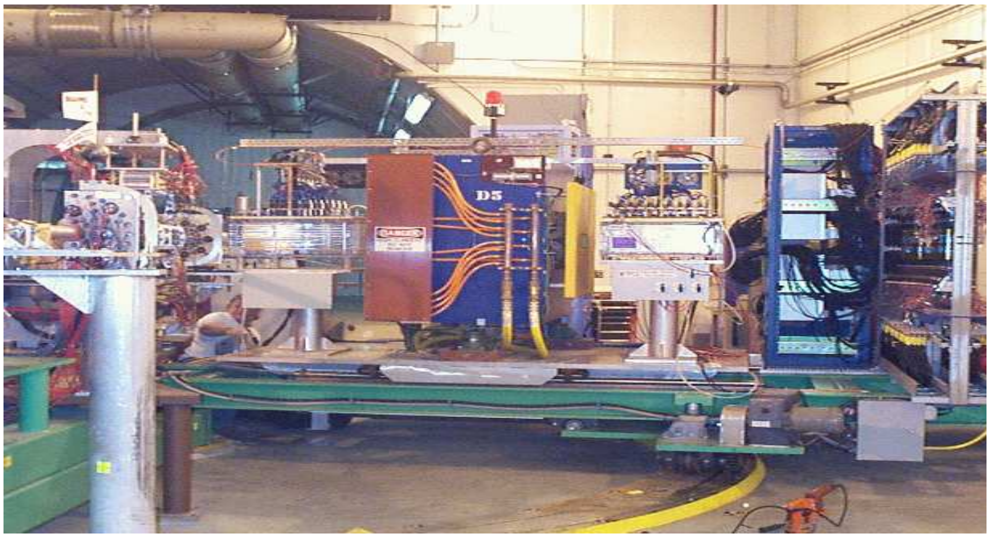

Fig. 3.3: Picture of the Mid-Rapidity Spectrometer.

The MRS can rotate from $30°$ to $90°$. The solid angle covered at e.g. $90°$ is ~ 6 msr. The close proximity of the front TPC TPM1 to the beam line can be problematic at more forward angles (around $30°$) due to high track densities. Therefore, the MRS was designed in such a way that the platform bearing TPM1, D5 and TPM2 can be moved backward to decrease the spectrometer acceptance. The data presented in this thesis were collected from spectrometer settings where the MRS was positioned at $90°$, $60°$, $52°$, $45°$, $40°$, $35°$ and $30°$.

The Forward Spectrometer FS

The forward spectrometer (FS) measures charged particles emitted at very forward angles. The FS is by design more complex than the MRS in order to cover a very broad momentum range for PID. It is composed of two independent sections, the front–forward and back–forward spectrometers (FFS and BFS). The FFS can rotate from $-2.3°$ to $-30°$. Its platform is positioned at a greater distance from the nominal IP than the MRS and presents a dipole magnet (D1) to the interaction region in order to both sweep away low momentum particles (typically below 1 GeV/c) and select only one particle charge sign at a time, depending on the magnetic field polarity applied during data taking. The rest of the FFS composition is identical to the MRS: two TPC's at the front and back of a dipole magnet, completed by a hodoscope for PID. A Čerenkov threshold counter is located behind the hodoscope to extend PID capabilities (cf. Sec 3.5.2). A picture of the FS is shown in Fig. 3.4.

Fig. 3.4: Picture of the Forward Spectrometer.

The BFS section is able to rotate from -2.3° to "only" -15° due to the limited area of the experimental hall. Its primary purpose is the identification of very high momentum particles. To achieve this goal, the FS is composed of no less than three drift chambers (DC), two dipole magnets, one hodoscope and a ring imaging Čerenkov detector at the far end of the BFS. The data presented in this thesis was collected from spectrometer settings where the FFS and BFS sections were aligned, covering the angular range $-12 \leq \theta \leq -3$ (i.e. -3°, -4°, -8° and -12°). Details on individual detectors are given below. The PID design acceptance in the transverse momentum versus rapidity space (y,$p_{\perp}$) is shown at the end of the chapter.

3.3 Reaction Characterization

The reaction characterization is a key measurement. The multiplicity/centrality determination is crucial for probing the particle and energy densities achieved at various collision impact geometry, while the primary vertex together with the start–time of all timing devices are important quantities for PID (cf. Chap. 4). Three detectors, referred to as global, are devoted to the determination of the vertex/start–time and multiplicity/centrality measurements: the beam–beam counters (BBC), the zero–degree–calorimeters (ZDC) common to all RHIC experiments, and the multiplicity arrays (MA).

3.3.1 The Beam-Beam Counters

In Fig. 3.2 is shown an object called DX which does not belong to BRAHMS but RHIC. It is a beam focusing magnet, whose purpose is to bring the beams to collisions around the nominal IP. The blue and yellow beams are steered to be very nearly parallel in the dedicated interaction zone. The distribution of primary vertex locations along z depends on the shape and length of the ion bunches. The measured width of this distribution amounts to $\sigma_z \sim 20\,\mathrm{cm}$ (cf. Chap. 4). The BBC's are designed to measure the primary vertex location along axis z. They consist of two arrays of fast Čerenkov radiators (tubes) coupled to photo–multiplier tubes (PMT) (see pictures on Fig. 3.5). The arrays are positioned at 2.19 m on each side of the nominal IP.

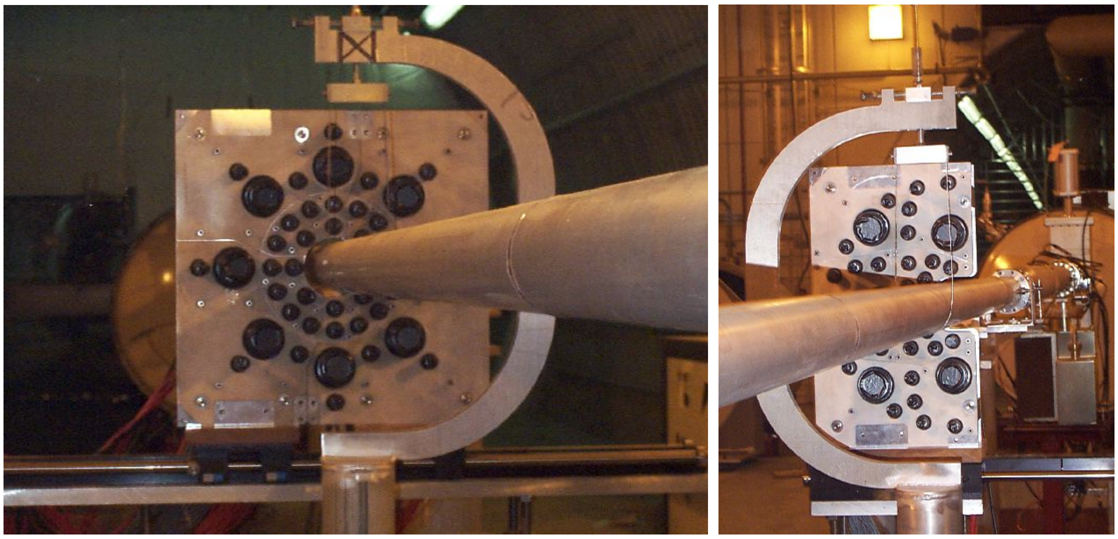

Fig. 3.5: Pictures of the beam-beam counters with the left (right) array on the left (right) panel. Note that half of the right array is missing for letting particles fly to the forward spectrometer.

Each array (left and right) is composed of two types of tubes: small tubes for a finely segmented detection and larger sized tubes which detect on average more particles at a time than small tubes. Half of the right array is missing in order to let particles fly toward the FS. The pseudo–rapidity η covered by the BBC's is $2.2 \lesssim |\eta| \lesssim 4.6$. When charged particles hit the BBC radiators, they produce Čerenkov photons if their velocity β is above c/n with $n \approx 1.5$. Detected particles have therefore a velocity $\beta \gtrsim 0.67$. BBC tube have an intrinsic time resolution of 50 ps. The vertex/start–time determination algorithm and BBC performance are described in details in Chap 4. Another source of information can be found in [97]. Table 3.2 gives the main characteristics of the BBC's.

		Tubes	Type (Hamamatsu)	Diameter (cm)	Length (cm)	Distance to beam (cm)
Left Array	ring 1	1 to 8	R3478	1.9	4.0	6.5
	ring 2	9 to 24	R3478	1.9	4.0	10.0
	ring 3	25 to 28	R3478	1.9	4.0	14.9
	ring 4	29 to 36	R3478	1.9	4.0	21.5
	ring 5	37 to 44	R2083	5.1	3.0	16.0
Right Array	ring 1	1 to 5	R3478	1.9	4.0	6.5
	ring 2	6 to 9	R3478	1.9	4.0	8.3
	ring 3	10 to 11	R3478	1.9	4.0	10.6
	ring 4	12 to 15	R3478	1.9	4.0	14.9
	ring 5	16 to 19	R3478	1.9	4.0	18.5
	ring 6	20 to 30	R3478	1.9	4.0	21.5
	ring 7	31 to 33	R2083	1.9	4.0	12.6
	ring 8	34 to 35	R2083	5.1	3.0	19.8

Tab. 3.2: Beam–beam counter characteristics.

3.3.2 Zero–Degree Calorimeters

BRAHMS owns a pair of ZDC. These are lead–tungsten calorimeters positioned at 18 m on each side of the nominal IP, behind the focusing DX magnets. The consequence of such a position is that charged particles emitted from the reaction along z cannot reach the ZDC's since they are bent away by the DX's. Only charge neutral particles, mainly spectator neutrons, are measurable by the ZDC's. A picture is shown in Fig. 3.6. The ZDC's provide both energy and time signals. Like for the BBC's, a vertex estimation along z can be estimated with a resolution $\sigma_z \simeq 2$ to 3 cm (read more on vertex in Chap. 4). The energy signal has been used to study mutual Coulomb dissociation in Au+Au collisions [98]. The neutrons measured in one calorimeter in that case show nearly no correlations with neutrons measured in the other calorimeter, which differs from inelastic collisions where both numbers are correlated since the number of spectators is the same (symmetric collisions). It should be mentioned that all RHIC experiments own their set of ZDC's built after the same model. The purpose is to have a common measurement from the four experiments as well as to provide the RHIC main control the possibility to monitor the beam intensity in the different experimental halls.

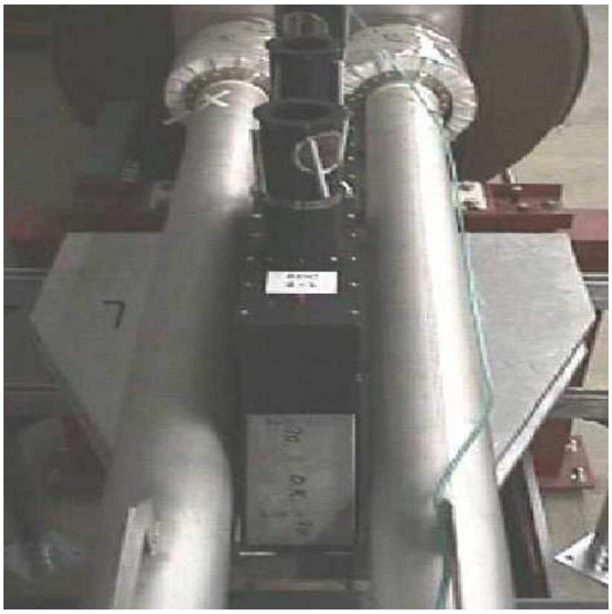

Fig. 3.6: Picture of one of the two zero–degree–calorimeters surrounded by the beam pipes.

3.3.3 Multiplicity Arrays

The multiplicity arrays (MA) measure the energy deposited by charge particles when they traverse the detector elements. Such measurement leads to charged particle multiplicities and collision centrality. The MA's are positioned around the beam–pipe (see left panel of Fig. 3.7). They consist in a two–layer cylinder of hexagonal base, with an inner part composed of silicon strip detectors (SMA) and an outer part of plastic scintillator tiles (TMA). Note that the tile coverage along the beam axis has been deliberately limited in the plane facing the MRS in order to let particles from the collision fly freely toward the spectrometer. The MA's design and software are described in great details in [99]. The pseudo–rapidity coverage is $-2.2 \lesssim \eta \lesssim 2.2$ and is therefore complementary to the BBC η acceptance. The charged particle multiplicity $dn/d\eta$ has been measured by BRAHMS at $\sqrt{s_{NN}} = 130$ and 200 GeV [100, 101].

In the right panel of Fig. 3.7 is shown the published result at $\sqrt{s_{NN}} = 200\,\mathrm{GeV}$. Event–by–

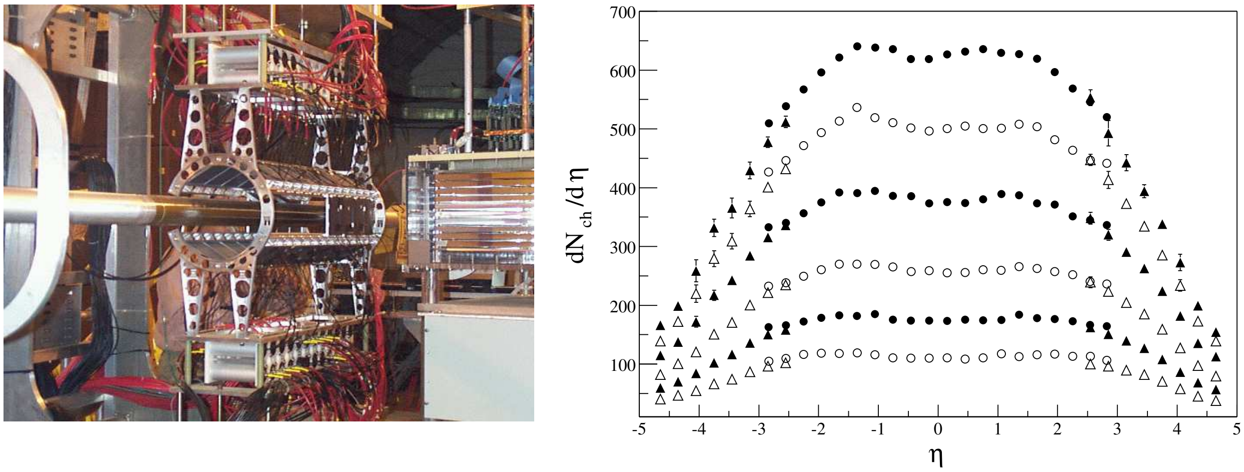

Fig. 3.7: Left: MA's picture. Right: Charged particle pseudo–rapidity density distribution at $\sqrt{s_{NN}} = 200\,\mathrm{GeV}$ [101]. Circles (triangles) are MA (BBC) measurements. Centrality classes are (from the top): 0–5%, 5–10%, 10–20%, 20–30%, 30–40% and 40–50%.

event multiplicity fluctuation analyzes have also been carried out from MA data at $\sqrt{s_{NN}} = 200\,\mathrm{GeV}$ [102, 103]. In the present analysis, the multiplicity obtained from the MA's is used to make centrality cuts. Centrality determination procedures are detailed in [99].

3.3.4 Event Trigger

The BRAHMS trigger system, or simply trigger, determines if an event can be recorded by the Data Acquisition (DAQ) or discarded. For the Au+Au 2001 run, the implemented trigger logic is only based on inputs from the global detectors, due to the relatively low event rate (the beam luminosity achieved was about 15% of the design luminosity). Table 3.3 summarizes the event trigger conditions applied during the data taking.

Trigger Id	Condition
1	BBC coincidence $N_L > 2$ AND $N_R > 2$
2	BBC coincidence $N_L > 1$ AND $N_R > 1$
3	**Multiplicity** trigger (TMA energy threshold)
4	ZDC coincidence and energy threshold
5	**Vertex** trigger (ZDC) $\rightarrow |z_{IP}| \lesssim 25\,\mathrm{cm}$
6	**Vertex** AND **Multiplicity**
7	Pulser trigger for pedestal runs
8	1 Hz synchronization trigger

Tab. 3.3: Trigger conditions used during data taking. N_L and N_R are the numbers of tubes with hits in the left and right array of the BBC's respectively.

Thus, a recorded event is characterized by a trigger word whose bits are on or off depending on which trigger condition is fulfilled (the conditions listed in Tab. 3.3 are not exclusive).

3.4 Tracking Devices

Charged particle tracking is one of the main steps for particle identification. Charged particles traversing a medium leave energy to the medium. By measuring where this energy is deposited, one can reconstruct the path of the particle through the medium. This reconstructed path is referred to as the particle track, hence "tracking" detectors. All tracking detectors utilized in BRAHMS are based on this principle. The outcome of this interaction is read out by appropriate devices in order to locate where in the reactive volume the particle interacted. These spots are called hits that, when properly combined, constitute a "local" track.

3.4.1 Time-Projection Chambers

BRAHMS has four TPC's. Two are located in the MRS (TPM1 and TPM2), the two others in the FS (T1 and T2). TPC's are designed to provide a three–dimensional measurement of charged particle trajectories with high position resolution. The BRAHMS TPC's are squared boxes positioned along the axis of the MRS and FFS outside any magnetic field. These boxes are filled with gas mixtures like Ar–CO_2 or Ne–CH_4 that are easily ionized as a charged particle passes through. Electrons created by ionization along the particle trajectory drift toward the pad–plane due to a homogeneous electrical field inside the TPC reactive volume. The pad–plane is the side of the TPC covered by read–out pads gathered in rows and strung with anode wires (see Fig. 3.8).

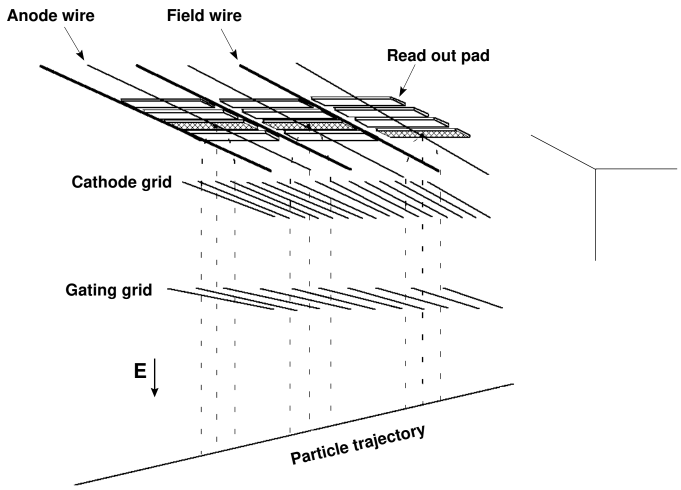

Fig. 3.8: Schematic picture of the TPC readout plane and electron drift lines.

The anode wires collect these electrons and induce a signal created by electromagnetic avalanches triggered by electron acceleration close to the wires. When the velocity v_{drift} of the drifting electrons is constant, the drift time is proportional to the drift distance. The mapping of row, pad and time leads to three–dimensional space points. Table 3.4 gives the main characteristics of the four BRAHMS TPC's. Details can be found in [30, 104, 105, 106].

3.4.2 Drift Chambers

For the BFS, BRAHMS opted for three drift chambers (DC). These are wire chambers, each of them composed of three modules with 8–10 planes arranged in 1–4 "views" (azimuthal wire orientation). Like TPC's, DC's are also gas detectors but the difference lies in the absence of

Name	L (cm)	W (cm)	H (cm)	Gas mixture 90–10%	N_{row}	N_{pads}/row	$\langle v_{drift} \rangle$ (cm/μs)	$\langle \sigma_x \rangle$ (mm)	$\langle \sigma_y \rangle$ (mm)
T1	56.0	33.6	19.8	Ar–CO_2	10 (14)	96	1.8	0.38	0.40
T2	75.5	39.6	19.8	Ar–CO_2	8 (14)	112	1.8	0.37	0.41
TPM1	36.6	38.4	20.0	Ar–CO_2	12 (12)	96	1.7	0.31	0.43
TPM2	50.0	67.7	19.8	Ar–CO_2	10 (20)	144	1.6	0.39	0.49

Tab. 3.4: Main characteristics of the four BRAHMS TPC's. L, W and H are respectively the length (z), width (x) and height (y) of the reactive volume, N_{row} the number of instrumented (total) pad rows, N_{pad}/row the number of pads per row, $\langle v_{drift} \rangle$ is the measured average electron drift velocity along the drift lines (y direction) and the $\langle \sigma \rangle$'s are the average hit position resolutions. The gas mixture is in the proportion 90%–10%.

homogeneous electrical field. Instead, electrons created by gas ionization are attracted by a set of anode and field wires. When the correspondence between drift time and drift distance to the wire has been established, each hit in a view gives a line parallel with the view direction (wires), as shown in Fig. 3.9. Since there is an ambiguity on the side of the wire the charged

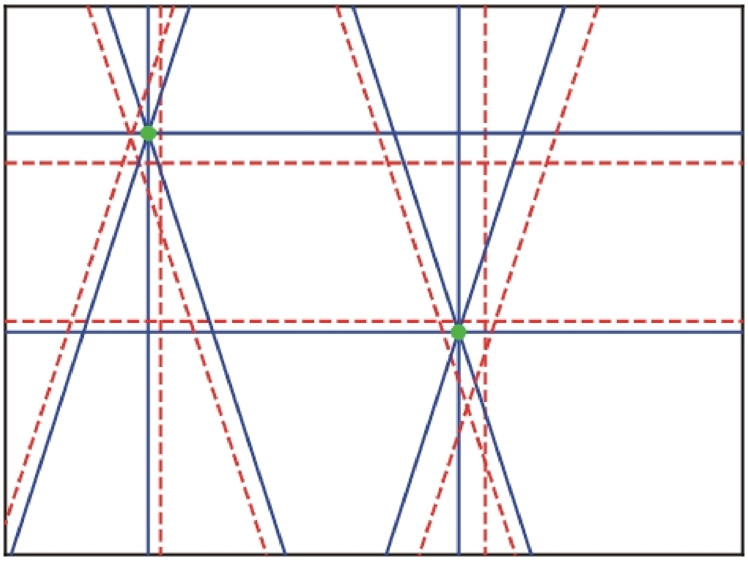

Fig. 3.9: DC tracking in an ideal situation with two tracks crossing a wire plane containing four views. The DC is shown from its front and views are x (horizontal), y (vertical), u and v (intermediate angles). Each hit gives rise to two lines before the left/right ambiguity is solved (see text). The solid lines are the true ones. The green dots, intersections between the solid lines, belong to the two particle tracks.

particle passed, at least two planes of the same view are needed. When the different views are combined, tracks can be determined by intersection of wires that were hit (see Fig. 3.9). More details on the DC design, tracking and performance can be found in [104, 107, 108].

3.4.3 Dipole Magnets

TPC's and DC's provide local tracks, i.e. straight pieces of particle trajectories. In order to determine the momentum, magnets are needed (cf. Sec. 4.3.2). BRAHMS has four dipole magnets (D2 to D5) located between tracking chambers and an extra one in front of the FFS as

mentioned in Sec. 3.2. The magnets in BRAHMS are all conventional electromagnets. Inside the magnet gaps, the magnetic field is, to a very good approximation, vertical and deflects particles in only the x direction. The magnets are placed along an arc defined by a particle of unit charge with the maximum momentum which can pass through all magnets (particles with larger momenta will not be deflected sufficiently to enter the subsequent magnet).
Magnet gap dimensions and field intensity determine the spectrometer acceptance. The field is determined by two experimental parameters: the current intensity and current polarity. Ideally, the field vector $\vec{B}$ has only one component along axis y (vertical direction). Its orientation (up or down) depends on the polarity ("A" and "B"). In the FS, an A (B) field corresponds to negatively (positively) charged particle detection. In the MRS, both charge signs are detected in a single polarity setting. This is due to the fact that there is only one magnet, and the detectors behind it are large enough to accept these particles. The experimental magnetic field has been mapped for each magnet in order to determine the excitation curve $|\vec{B}|(I)$ where I is the current in Amp. The experimental points have been fitted with a second degree polynomial. Figure 3.10 shows the excitation curves of the BRAHMS magnets. Each magnet is characterized by a maximum value of the current. Therefore, magnetic field

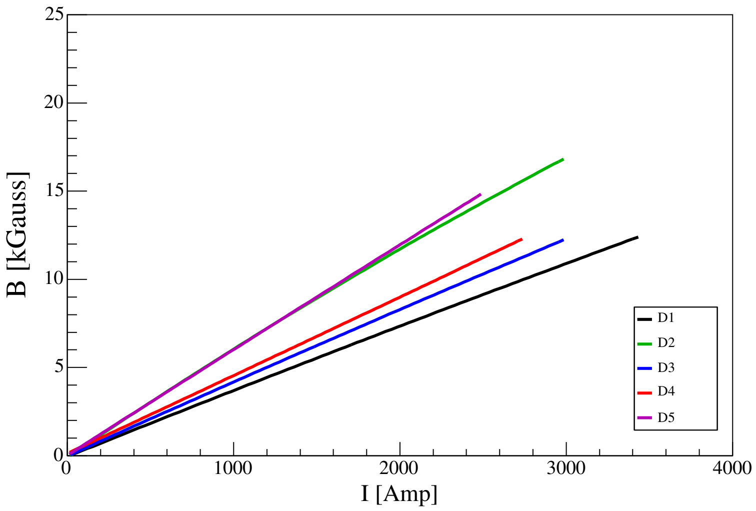

Fig. 3.10: Magnet excitation curves obtained from experimental field mappings. The fit function used is a second degree polynomial.

settings are fully determined by their polarity and the fraction of the maximum current used during data taking. Table 3.5 shows the main characteristics of the magnets and settings used during data taking.

3.5 Particle Identification Devices

PID is achieved by correlating the particle momentum (obtained from track bending inside the magnet gaps) and the time of flight (TOF) measured in the hodoscopes or the response of the Čerenkov detectors.

3.5.1 The Hodoscopes

BRAHMS has three TOF walls. One called TOFW is located in the MRS, while two hodoscopes, TOF1 and TOF2, are positioned in the FS. Each of the TOF walls consists of a

Name	Gap dim. (cm)			I_{max} (A)	B_{max} (T)	Average momentum $\langle p \rangle$ (GeV/c) per setting				
	L	W	H			1/8	1/5	1/4	1/3	1/2
D1	200	8.0	20.0	3450	1.26	p not determined				
D2	160	30.0	13.5	3000	1.68	2.0	3.0	3.5	5.0	6.5
D3	200	40.0	25.4	3000	1.22	3.0	4.5	5.5	7.2	10.0
D4	183	44.6	32.1	2750	1.19	3.0	4.5	5.5	7.2	10.0
						164	350	500	700	1000
D5	76.2	35.0	10.0	2500	1.45	0.30	0.35	0.40	0.45	0.55

Tab. 3.5: Characteristics of the BRAHMS magnets. I_{max} is the maximum current intensity value. MRS current settings are in *Amp* (not fractional like for the FS).

row of rectangular scintillator slats wrapped in aluminum foil for guiding light, and dark tape for light insulation. Ideally, slats are positioned in the hodoscope frame so that dead zones, i.e. areas of non detection between slats, are minimized. Each scintillator slat is coupled to a PMT at each end (top and bottom) that provides an energy signal, and a time signal which is used as a stop signal for TDC devices (cf. Chap. 4). In Fig. 3.11 is shown a schematic picture of TOF1.

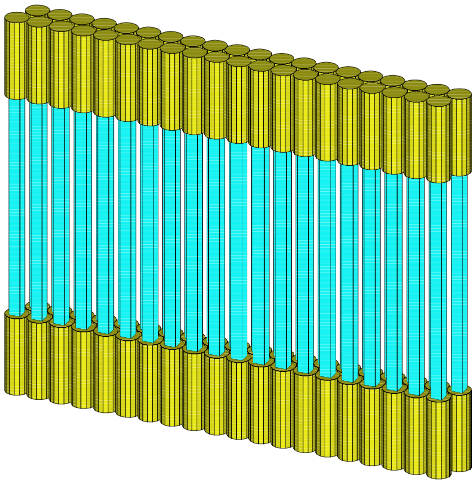

Fig. 3.11: The hodoscope TOF1. Only scintillator slats (blue) and PMT's (yellow) are drawn.

Charged particle detection using scintillators is based on the physics of scintillation. A charged particle traversing a scintillating medium excites the atoms along its path. These atoms deexcite by producing a light. The intensity of the produced flash of light has a sharp increase but slower decrease, which makes scintillators well suited to timing measurements. In first approximation, the energy deposited per unit of length dE/dx is proportional to dI/dx where I is the intensity of the produced light. The light propagates through the slat at an effective speed lower than c due to the index of refraction $n > 1$. It is eventually collected by the PMT's which amplify the signal and transmit it to the data acquisition system (DAQ). This process is illustrated in Fig. 3.12.
Charged particles above $\beta \sim 0.9$ are minimum ionizing particles (MIP). This means that the amount of energy deposited through the ionization process of the scintillating material (ΔE) is at its lowest. Moreover, it depends very little on the particle momentum p for particles carrying the same charge fraction Z ($\Delta E \sim Z^2$). This implies that ΔE, although used for

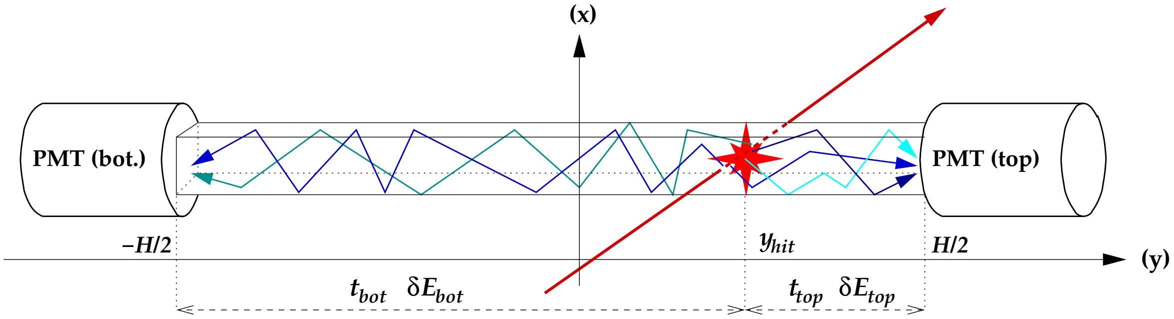

Fig. 3.12: Scintillation in a TOF slat due to the passage of a charged particle.

particle identification for low momentum particles (not MIP's), cannot discriminate particle masses for momenta above the minimum ionization momentum. However, for these particles, identification can be achieved via a timing procedure. In BRAHMS, determining the time of flight of the detected particles requires a "start–time" device (BBC's) and a stop–time measurement provided by the hodoscopes. The TOF PID procedure and performance are explained in details in Chap. 4. The main characteristics of the BRAHMS hodoscopes are given in Tab. 3.6.

Name	Distance from IP (m)	N_{slat}	Slat dim. (cm) L	W	H	Material (bicron)	σ_t (ps)	p_{max} (GeV/c) π/K	K/p
TOF1	8.7	40	1.00	1.00	20	BC420	65	3.8	6.5
TOF2	18.6	32	1.00	1.50	40	BC420	65	5.8	9.7
TOFW	4.3	125	1.27	1.25	22	BC404	65	2.5	4.3

Tab. 3.6: Characteristics of the BRAHMS hodoscopes. σ_t is the nominal time resolution of each tube, p_{max} is the nominal PID capability in a 3σ cut assuming the overall TOF resolution equals 75 ps, i.e. the maximum momentum below which the particle can be identified (to be compared with the experimental values in Chap. 4).

3.5.2 The Čerenkov Detectors

The FS has two Čerenkov detectors in order to extend the PID capability to high momentum particles. The detection is based on the Čerenkov effect (after the Russian physicist P. A. Čerenkov), i.e. radiated light during the passage of a charged particle through a medium of index of refraction $n > 1$, when the particle velocity β is greater than c/n (speed of light in the medium). The latter condition implies a momentum threshold p_{th} (that depends on the particle type) above which particles can be observed. More details are given in Chap. 4.

The Threshold Detector C1

In the FFS, a threshold detector is located behind TOF1. It consists of a box with radiator gas (C_4F_{10}), two mirrors and 32 ($2 \times 2 \times 8$) PMT's. In the left panel of Fig. 3.13 is shown a schematic picture of C1. The mirrors are located in the back plane of the gas vessel. Their orientation is $\pm\, 45\,^\circ$ in order to reflect the Čerenkov light to PMT's, where photo–electrons are created. Their flux is amplified and the signal is transmitted to the electronics. The number of photons that produced photo–electrons can be estimated via proper calibrations. C1 is

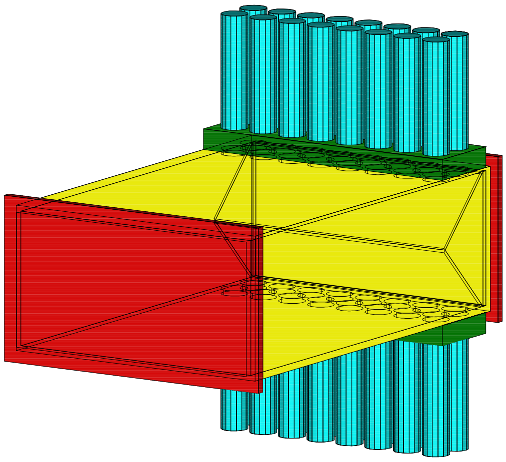


Fig. 3.13: Left: the Čerenkov detector C1. Right: the Ring Imaging Čerenkov detector RICH.

used for pion identification due to the relatively low pion momentum threshold and high kaon threshold (cf. Tab. 3.7). The TOF1 PID can be extended for kaons if pions with a positive C1 signal are vetoed.

The Ring Imaging Čerenkov RICH

RICH is a ring imaging Čerenkov detector and is positioned behind TOF2 at the end of the BFS ($\sim 20\,\mathrm{m}$ from the nominal IP). Its PID is based on the same physical principle as C1 but its design is different. RICH has a focusing mirror at the back of the gas vessel. Therefore, the incident light cone becomes a ring at a plane located at a distance equal to the focal distance of the mirror. The ring radius is determined by the momentum and mass of the particle (cf. Chap. 4). In order to have a good ring resolution, the focal plane is highly segmented, it bears 80 PMT's, each divided in four pixels (320 pixels). A picture is shown in the right panel of Fig. 3.13. RICH is primarily designed for high momentum particles. The momentum thresholds are similar to that of C1 (cf. Tab. 3.7).

	N_{tube}	Gas	n	p_μ	p_π	p_K	p_p
C1	32	C_4H_{10}	1.00138	2.01	2.65	9.39	17.85
RICH	4×80	C_4H_{10}	1.00202	1.66	2.19	7.76	14.75

Tab. 3.7: Characteristics of the BRAHMS Čerenkov detectors. The p's are the momentum thresholds of the listed particles.

3.5.3 BRAHMS Design Acceptance

For a given spectrometer setting (angle and field), the acceptance is rather small ($\sim 6\,\mathrm{msr}$ in the MRS and $0.5\,\mathrm{msr}$ in the FS). The force of BRAHMS is to map out the particle phase–space by collecting data with many different spectrometer settings. Such a map is given in Fig. 3.14 for pions, kaons and protons, with a distinction between the acceptance coverage of the different PID detectors. By design, the BRAHMS spectrometers can identify pions

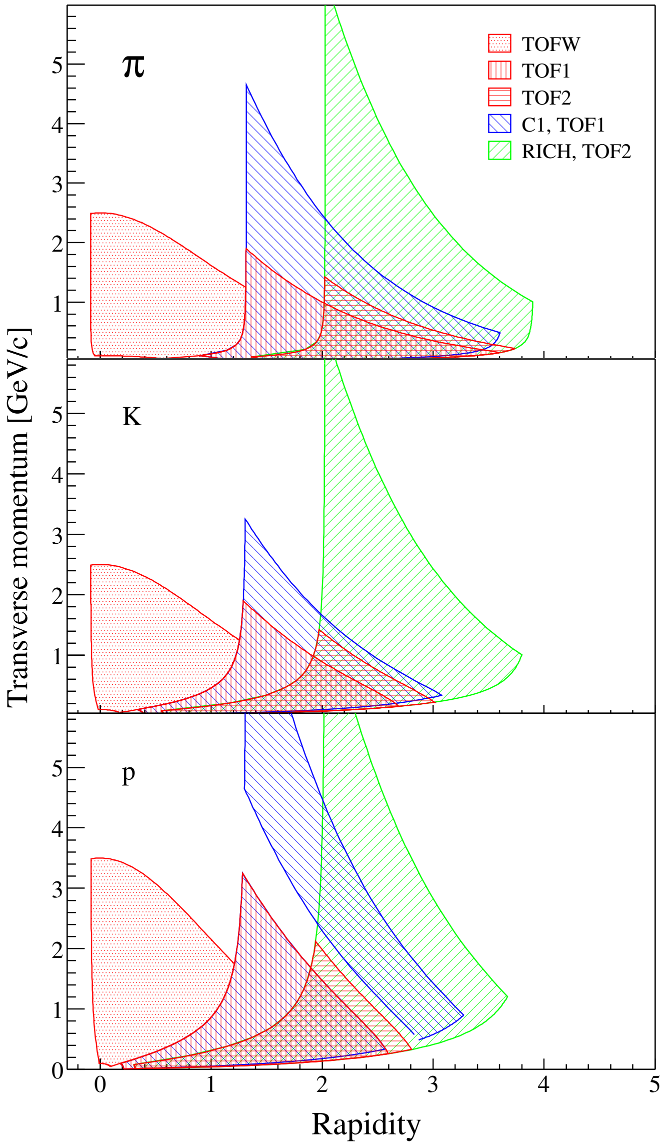

Fig. 3.14: BRAHMS design acceptance for pions, kaons and protons. The individual PID detector acceptances are highlighted with different fill styles.

and kaons over the rapidity range $-0.1 < y < 3.8$ by combining data from all spectrometer settings. At mid–rapidity, the momentum limit below which kaons and pions can be separated is 2.5 GeV/c if the TOFW resolution is 75 ps (2σ cut around the expected time of flight). This implies that the transverse momentum p_T limit for pion and kaon identification in the MRS decreases with increasing rapidity. It is also true in the FS with TOF1 and TOF2. However, the additional Čerenkov information extends the PID capability up to ~ 6 GeV/c (RICH) at $y \sim 2.2$ and ~ 1.5 GeV/c at $y \sim 3.5$. In the following chapters, data from the hodoscopes and the RICH are presented and discussed. Figure 3.14 must be compared to the experimental results discussed in Chap. 6 and 7.

♣♣♣♣♣♣

Chapter 4

Particle Identification

Among the RHIC experiments, BRAHMS has the unique capability to identify charged particles over a broad range of rapidity and momentum, using time of flight and Čerenkov techniques. This chapter describes how the "raw" information from the detectors is converted to particle four–momenta.

4.1 Basic Principles and Requirements

BRAHMS measures the momentum of charged particles which traverse the spectrometers, together with their time of flight (TOF). Additional Čerenkov information is provided in the FS. By combining the momentum and the corresponding TOF or Čerenkov signal appropriately, one can determine the particle mass. Indeed, the momentum p is given by the following equation:

$$p = \gamma m \, \beta c = \frac{m\beta c}{\sqrt{1-\beta^2}} \tag{4.1}$$

with m the particle mass, $\beta = v/c = L/ct$ the particle velocity, L and t the flight path and corresponding TOF. In BRAHMS, L is in the order of a few meters (~ 4 to $20\,\mathrm{m}$) with TOF's ranging between $\sim 14\,\mathrm{ns}$ (MRS) to $60\,\mathrm{ns}$ (full FS) for the fastest particles.

In Sec. 4.3.1 is briefly reviewed how time projection chambers (TPC) measure track segments. The momentum is deduced by matching track segments inside magnet gaps (Sec. 4.3.2).

4.1.1 Time of Flight

In BRAHMS, TOF means time of flight between the collision vertex and the scintillator slats of the hodoscopes. Since the interaction point (IP) changes on an event by event basis, so does the start–time, which is the time when the main trigger of the data acquisition system (DAQ) gives time devices (TDC) the order to start "counting time". The latter stop counting when 1- a stop–time is triggered by a signal issued by electronic devices called discriminators, or 2- after a fixed time (timeout) when no signals were sent by discriminators. Discriminators react to analog pulses induced by charged particles passing through the scintillator slats and amplified by photomultiplier tubes (PMT), if the amplitude of the signals is above a threshold

(150 mV). Each PMT is linked to a TDC channel than can be stopped independently[1]. A scheme is shown in Fig. 4.1.

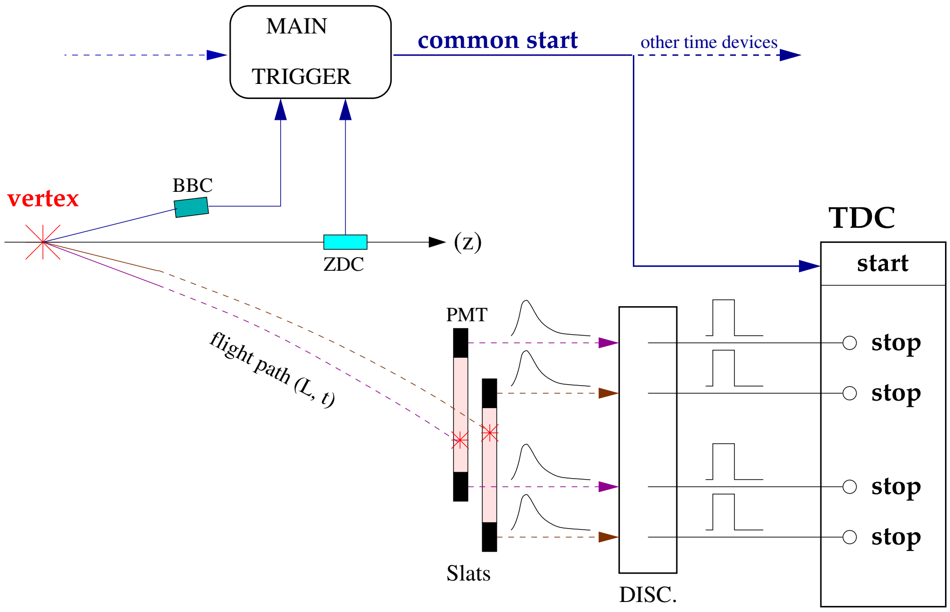

Fig. 4.1: Time of flight technique. Time devices (TDC) start counting until the discriminators (DISC) send a logical signal if the original analog signals fulfill certain conditions (see text).

Figure 4.1 does not show all details of the start-time logic, the signals from the slat PMT's are in reality discriminated twice, a first time inside the cave, a second time in the Fast Electronic Hut outside the cave in order to refresh the discriminated signals transported through the delay lines. However, this figure provides a rough illustration of the timing procedure. The measured quantities (TDC output) are given by the following equations (for a given slat):

$$t_{top} = TOF + t_{top_\perp} + HW_{top} - t_{start} \quad (4.2)$$

$$t_{bot} = TOF + t_{bot_\perp} + HW_{bot} - t_{start} \quad (4.3)$$

where subscripts *top* and *bot* refer to the top and bottom tubes of the slat, subscript $\perp$ to the effective time it takes for the light to travel from the track intersection with the slat to the PMT's, and HW to all effects introduced by delay cables, electronics (discriminators), etc. The primary vertex and start–time are estimated with the beam–beam counters. Calibration and construction procedures are described in Sec. 4.2. For the stop–time, hodoscope hits are first matched to spectrometer tracks (Sec. 4.4.1). The following step consists of calibrating the hodoscope data in order to remove hardware effects from the raw time signal. The hodoscope calibration and PID determination are described in Sec. 4.4.2 and 4.4.3 respectively. As can also be seen from Fig. 4.1, each slat has two PMT's leading to two measurements containing the particle TOF. This design is explained when hodoscope calibrations are presented.

Once the particle velocity β and momentum p are known, the correlation between these variables reveals the particle mass. Figure 4.2 shows expectation curves for different particle masses.

[1]In a high background environment, the stop–time signal and track pointing to the corresponding slat can be uncorrelated. Data are therefore selected in such a way that uncorrelated track–TOF combinations are minimized (Sec. 4.4.1 and 4.4.2).

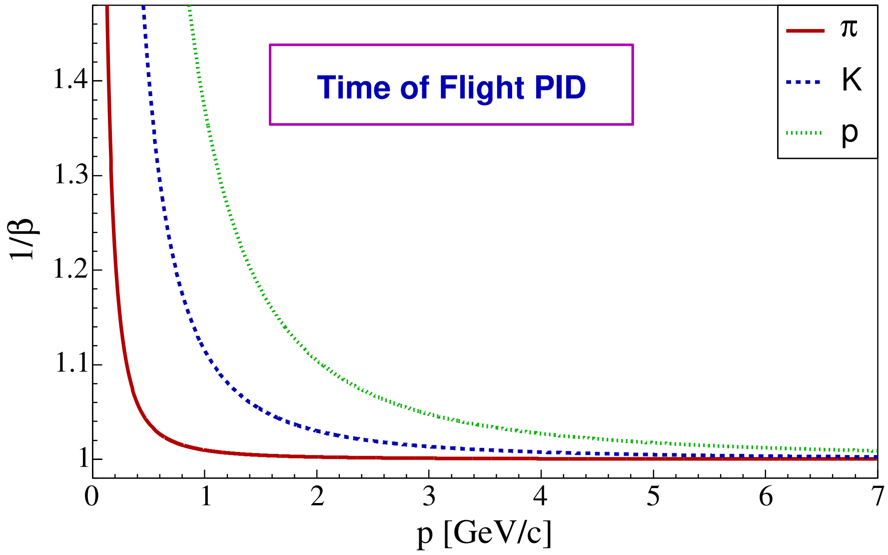

Fig. 4.2: Expected TOF PID curves ($1/\beta$ vs p) for pions, kaons and protons, based on Eq. 4.1.

4.1.2 Čerenkov Effect

It has been known since 1934 [109] that a charged particle traversing a medium of index of refraction $n > 1$ emits electromagnetic radiation if its velocity β is greater than the speed of light in the medium c/n. The emission angle θ_c of the radiated light along the particle path is constant, it is given by the equation :

$$\cos\theta_c = \frac{1}{n\beta} \tag{4.4}$$

Therefore, the light emitted by one charged particle belongs to a cone of angle θ_c. The Čerenkov effect is illustrated in Fig. 4.3.

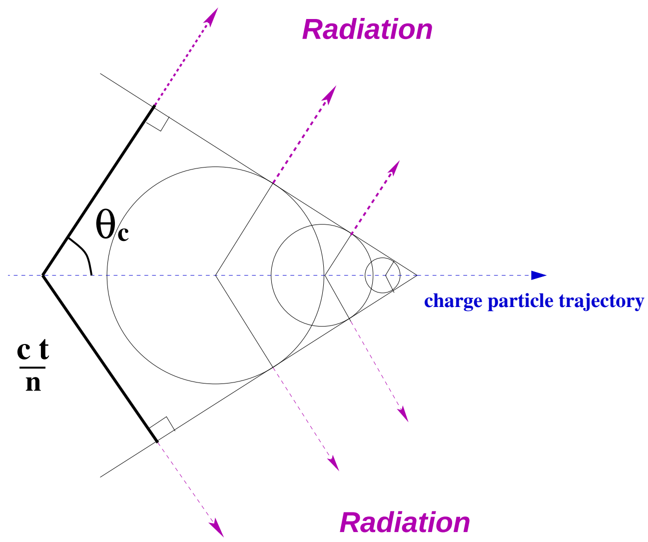

Fig. 4.3: Čerenkov effect. A charged particle of velocity $\beta > c/n$ emits light at a well defined angle θ_c along its path through the medium.

Charged particles produce Čerenkov light above well defined momentum thresholds p_{th}, given by the equation:

$$p_{th} = \frac{m}{\sqrt{n^2 - 1}} \tag{4.5}$$

The momentum threshold p_{th} depends on the particle mass m and the index of refraction n. Figure 4.4 shows the correlation between θ_c and the particle momentum p for different particle types.

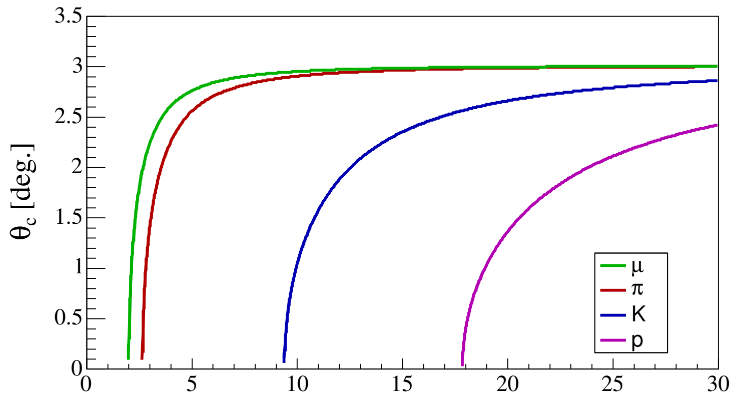

Fig. 4.4: Čerenkov angle versus particle momentum with $n = 1.00138$.

The Čerenkov effect is very powerful for identifying high momentum particles. The RICH detector was used for the data presented in this thesis. Section 4.5 describes how PID was achieved by using the Čerenkov light focusing technique which is the design concept of the RICH.

4.2 Collision Vertex and Start–Time

Collision vertex and start–time are measured by the beam–beam counters (BBC's). These detectors, consisting of two arrays of Čerenkov radiators coupled to PMT's and located from each side of the nominal interaction point (IP), need first to be calibrated. Raw data consist of hits (one per tube) containing information in the form of integers. Those are called ADC, which in the case of the BBC's are related to the number of particles hitting the radiators, and TDC digits related to the stop–time. Calibrations consist of converting these integers into the corresponding physical quantities.

4.2.1 Beam-Beam Counter Calibrations

An exhaustive study of the BBC's can be found in [97]. This section describes the main calibrations performed for the data presented in this thesis, they are listed in Tab. 4.1:

Pedestal Calibrations

The BBC PMT's deliver signals to the DAQ if charged particles produced photons inside the BBC radiators. The analog to digital converter (ADC) is an electronic device that converts these signals into integers ranging between 0 and 2048, 4096 or more depending on the device. To each BBC tube corresponds an ADC spectrum which sharply rises around an ADC value

Calibration Type	Purpose
ADC pedestal	ADC spectrum alignment
ADC gain	Conversion ADC digits to number of particles
TDC gain	Conversion TDC digits to times
Time delay	Time offset removal between tubes
Slewing correction	Removal of energy dependence in time signal

Tab. 4.1: BBC calibrations prior to vertex and start–time determination.

called pedestal. The pedestal reflects low amplitude electronic noise and corresponds to the "zero volt" of the ADC (null pulse amplitude). This means that pedestals are ADC offsets and they can differ from spectrum to spectrum. In practice, pedestal are characterized by a narrow distribution (see Fig. 4.5).

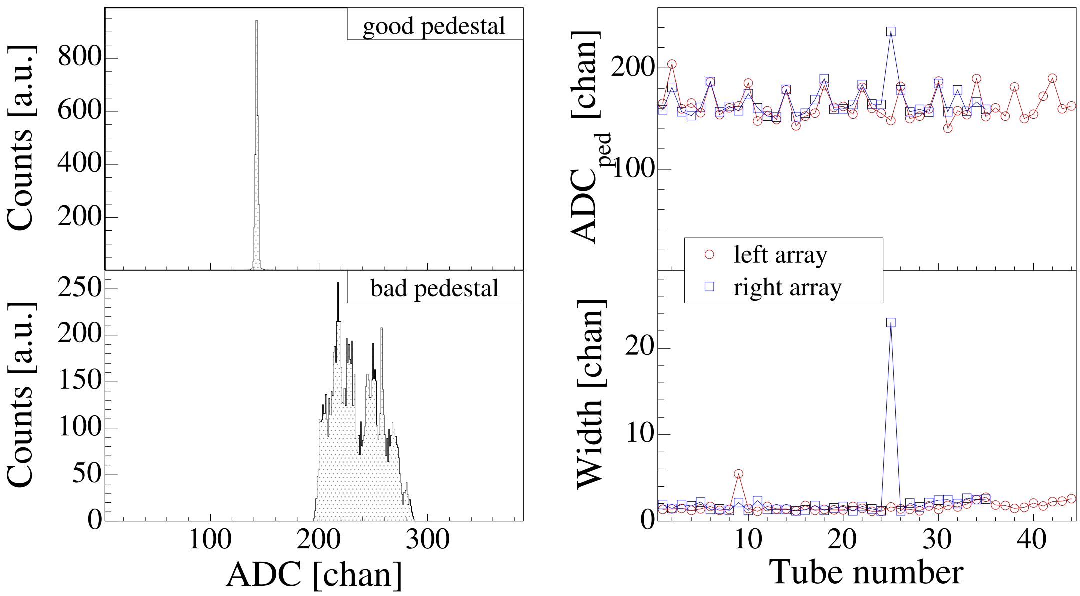

Fig. 4.5: BBC pedestal calibration with a typical pedestal (top left), a noisy pedestal (bottom left), a pedestal summary (top right) and a summary of pedestal width (bottom right).

In order to have a common start for all ADC spectra, pedestals must be evaluated and subtracted. Special runs are devoted to the measurement of pedestals. To each BBC tube corresponds a one dimensional histogram filled with ADC pedestal data. Since the pedestals are assumed to originate from random noise, they are fitted to a Gaussian, whose mean and width are stored in the BRAHMS database. Figure 4.5 illustrates this procedure. Bad pedestals like the one shown in the bottom left panel of Fig. 4.5 are indicators of electronic drift or other malfunction. They are tagged by assigning them a special calibration constant so that data from corresponding tubes are not used in the analysis. The knowledge of these bad calibrations is essential when detector efficiency and acceptance are to be calculated.

TDC Gain Calibration

BBC PMT's also deliver signals used for time determination. The time to digital converter (TDC) is the electronic device converting these signals to integers ranging between 0 and e.g.

4096. These data have to be converted to a time unit (nanosecond). The goal of the TDC gain calibration is to determine the conversion factor of the TDC device. Like for the ADC data, each BBC tube is associated to an electronic TDC unit. It is important for all procedures dealing with time (TOF PID or primary vertex determination) that TDC devices are linear. In practice, special data runs are also devoted to TDC gains. An electronic pulser triggers the TDC device every 10 ns for each unit connected to a BBC tube (the time step depends on the pulser used). This gives TDC spectra a "comb" shape: each peak corresponds to a pulse at a precise time (see Fig. 4.6). The peak positions (in TDC digits) are plotted as a function of the time the corresponding pulses were emitted (the error on the time interval between two pulses can be neglected), as illustrated on Fig. 4.6.

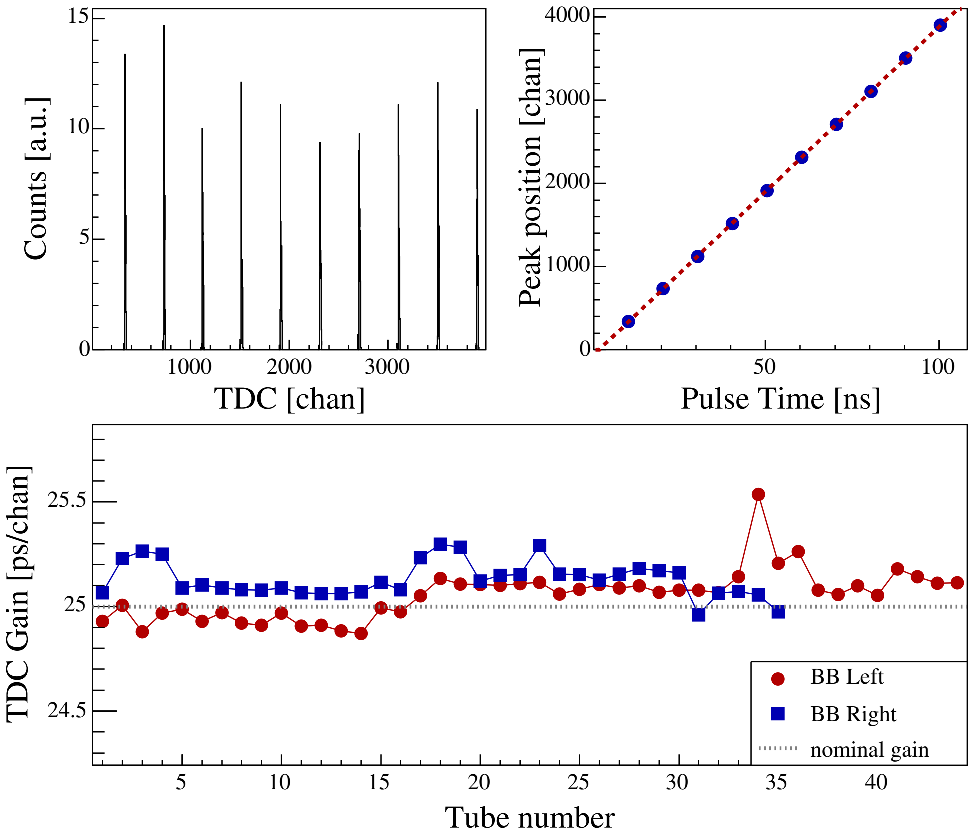

Fig. 4.6: BBC TDC gain calibration, with a typical comb shape TDC spectrum of a single TDC unit (top left), a fit of the peak positions versus pulse time (top right) and a summary of the TDC gains (bottom).

The profile in the top right panel, which demonstrates the TDC linearity, is fitted with a linear function. The inverse of the slope of this function is the TDC gain. The summary plot in the bottom panel reveals some deviations from the nominal gain (25 ps/chan).

ADC Gain Calibration

The ADC converts the amplitude of the PMT signal into digits whose values primarily depend on the number of particles that hit the radiators. Figure 4.7 illustrates how an ADC spectrum is obtained. The peak positions are also dependent on the energy gain of the tube, mainly related to the applied high-voltage (HV). Because tubes differ in gain, particle peaks are not located at the same values from spectrum to spectrum. The goal of the ADC gain calibration

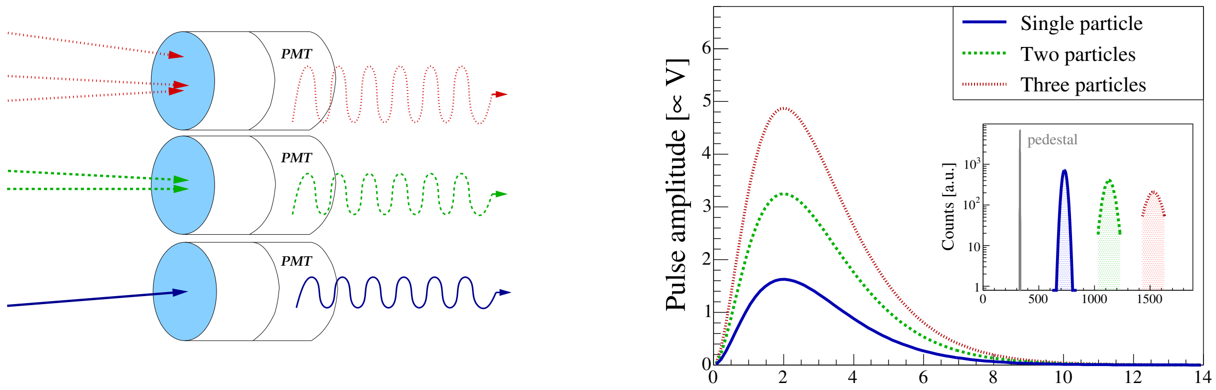

Fig. 4.7: Raw signal conversion. Depending on the number of particles hitting a tube, the corresponding ADC spectrum shows a succession of peaks.

is to find a factor for converting the ADC values into a number of particles for each spectrum. An example of raw spectrum (ADC digits pedestal–subtracted) is shown in the top left panel of Fig. 4.8 (the gap in the middle of the distribution is due to the dual ranged ADC devices used).

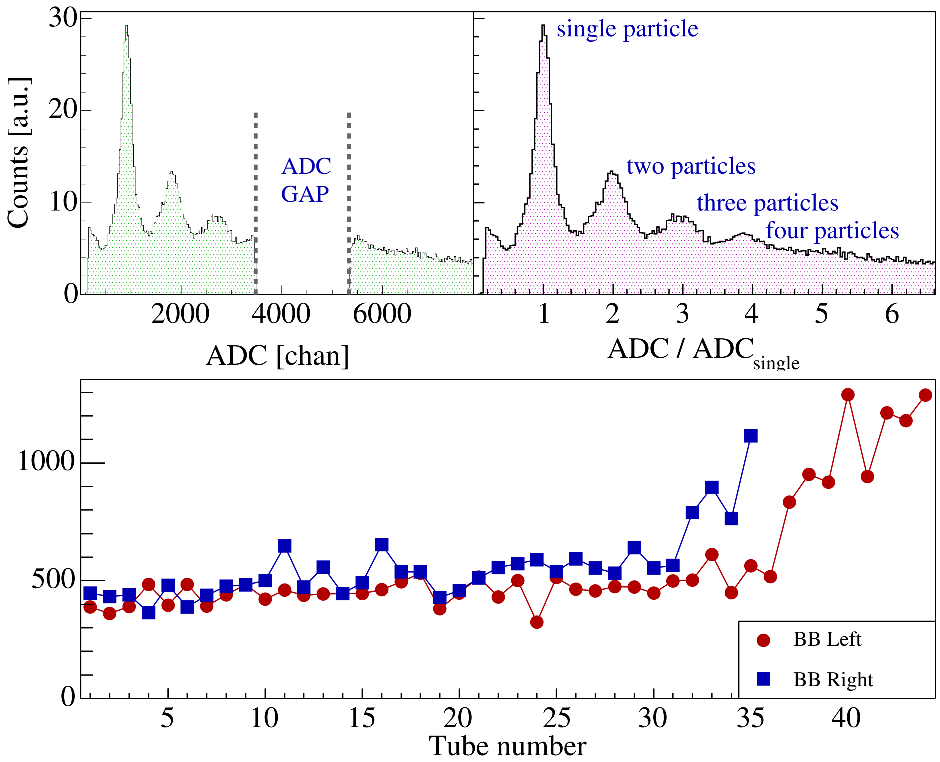

Fig. 4.8: BBC ADC gain calibration.

Without a software threshold, the highest peak would correspond to pedestal signals, mixed up with very low ADC signals. A threshold of ten times the pedestal width above the pedestal is applied in order to rule them out. The ADC gain is determined by finding the mean ADC digit of the single particle peak. Note that it is necessary to select events that are not dominantly central, otherwise multiple particle peaks would be populated to the detriment of the single particle peak. Once histograms are filled, the top of the single particle peak is fitted with a Gaussian function, although one can argue that these peaks are not Gaussian-like. But as far as the ADC calibration is concerned, only a reasonable estimation of the peak location is needed. The top right panel of Fig. 4.8 shows the same ADC spectrum converted after gain calibration ($n_{part} = ADC/ADC_{single}$). The bottom panel is a summary of ADC gains for all BBC tubes (the non-linearity of the small tubes is discussed in [99, 97]). When ADC signals are calibrated, one can obtain particle distributions from the BBC. The one presented in Fig. 4.9 is not normalized but reveals the geometry of the BBC arrays. Tubes are positioned on rings of different radii.

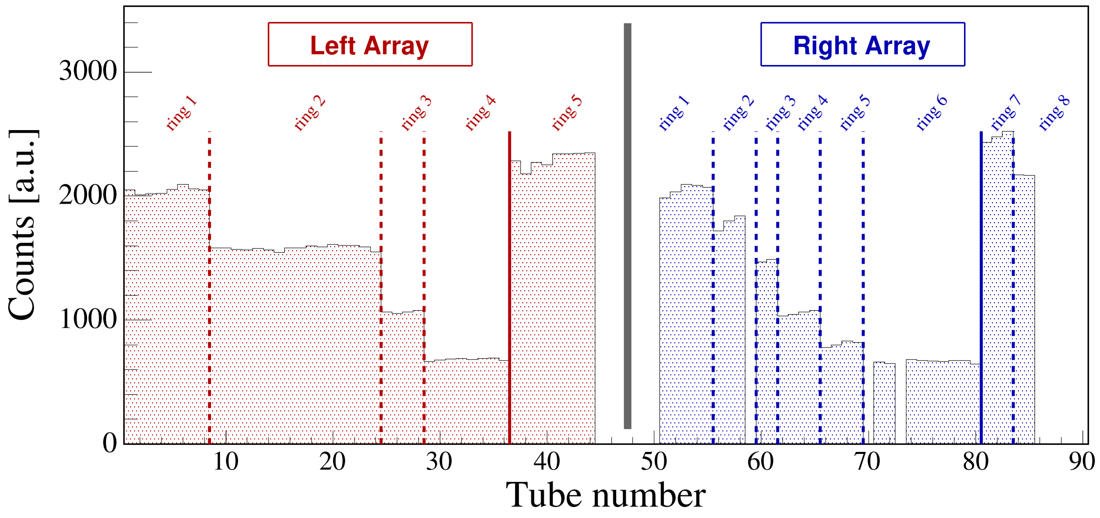

Fig. 4.9: BBC hit distribution. A BBC raw digit is a hit if its calibrated ADC is above 0.7.

Note how uniform the hits are distributed in each ring (a couple of tubes are missing in the right array due to bad pedestals). The closest tubes to the beam line detect more particles than outer tubes. Big tubes, although not very close to the beam line, are also among the most effective. This is due to their larger geometrical acceptance.

Time Calibration

As mentioned before, the time signal related to a charged particle detection is provided by the TDC measurement. For a BBC tube i in a given event, the measurement (in nanosecond) follows Eq. 4.6:

$$tdc_i = tof_i + t_{off,i} + t_{slew,i} - t_{start} \tag{4.6}$$

where t_{start} is the start–time, tof_i the particle time of flight (from its vertex to tube i), $t_{off,i}$ and $t_{slew,i}$ the time offset, delay and energy dependence of the TDC measurement (it is implicitly assumed that the collision occurs at the time origin $t = 0$).

• Time Offsets:

Most of the particles detected by the BBC tubes are pions traveling at a speed close to the speed of light. Therefore, their TOF's from the collision vertex to the tubes (of a given array) are approximately equal (the different tube locations on each BBC array can be neglected). Consequently, time spectra obtained from tubes of a given BBC array show no significant difference. In practice, there are time offsets between these spectra, i.e. a constant time difference Δt_{ij} between spectra of tube i and j. These offsets are due to various factors like different delay cable lengths, temperature variations, etc, they are a property of the hardware chain between the tubes and the TDC device. It is essential to remove these offsets since the vertex and start–time resolution can be affected if offsets remain.

A reference tube is chosen in each BBC array, preferably a big tube whose hit probability is greater than that of small tubes. In each event, the hit of the reference tube is selected if

$$|ADC/ADC_{single} - 1| < 0.1 \quad (4.7)$$

$$10\,\text{chan} < TDC_{ref} < 3500\,\text{chan} \quad (4.8)$$

Condition 4.7 implies that only single hits are selected. It prevents the corresponding time from being affected by the slewing effect of the reference tube. Condition 4.8 is used in order to select hits with valid times (mainly excludes TDC overflows). For all other tubes i of a given array, histograms are filled with time differences $t_i - t_{ref}$ (where the common start-time t_{start} cancels out event by event). The top panel of Figure 4.10 shows typical histograms. The

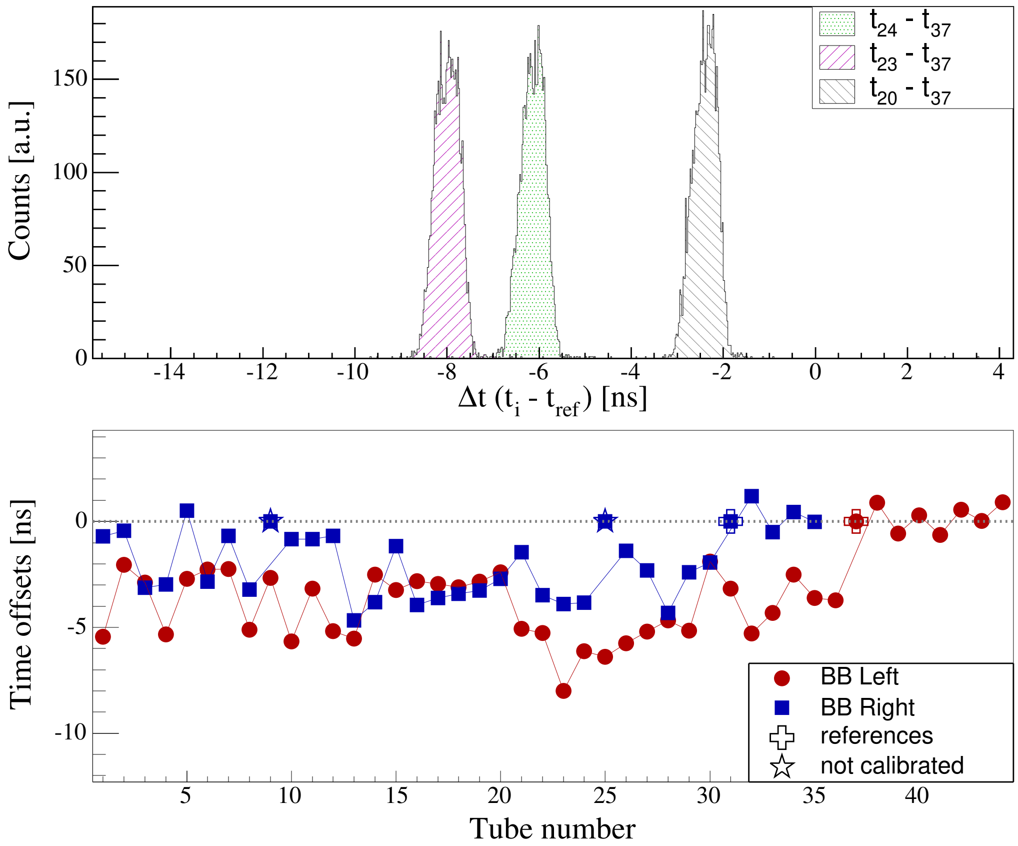

Fig. 4.10: BBC Time offset calibration. Top panel: examples of time differences; Bottom panel: time offset summary.

mean value of the peak is deduced from a Gaussian fit and is used as the time offset between tube i and the reference tube. A summary is presented in the bottom panel of the figure. As can be seen, offsets can be as large as a few nanoseconds while the intrinsic time resolution of each tube is in the order of 50 ps.

Slewing Correction

The time offset calibration is refined by the slewing correction. The slewing effect manifests itself as an ADC dependence of the TDC signal and originates from the triggering mode of the discriminators (leading edge triggering), illustrated in Fig. 4.11.

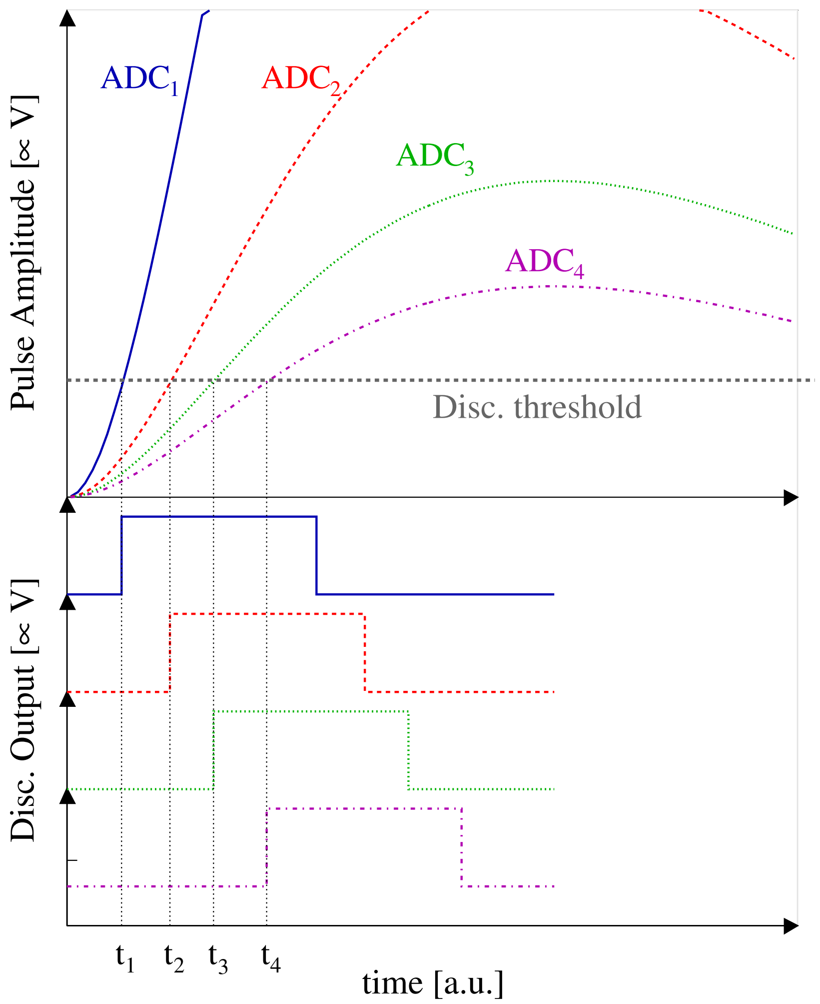

Fig. 4.11: Slewing effect caused by the discriminator threshold and leading edge triggering mode.

As can be seen from Fig. 4.11, the smaller the pulse amplitude (and consequently the ADC value), the later the discriminator triggers, i.e. the larger the TDC. The goal of the correction is to quantify and remove the TDC dependence on the ADC. For the BBC's, it is done by using a profile method for each pair (tube i, tube$_{\rm ref}$) of a given array. The reference hit is selected like for the time offsets (conditions 4.7 and 4.8). Profiles are filled with time differences $\Delta t_i = tdc_i - tdc_{ref} - t_{\mathit{off},i} = t_i - tdc_{ref}$ versus $\langle E_i \rangle$, where $\langle E_i \rangle$ and $t_{\mathit{off},i}$ are the ADC and time offset of tube i previously calibrated. A typical profile is shown in the top panel of Fig. 4.12. The empirical fit function used to describe the slewing behavior is

$$\Delta t_i = t_i - t_{ref} = a + \frac{b}{\sqrt{\langle E_i \rangle}} + \frac{c}{\langle E_i \rangle} \tag{4.9}$$

where t means calibrated time and a, b and c are the calibration parameters to be determined.

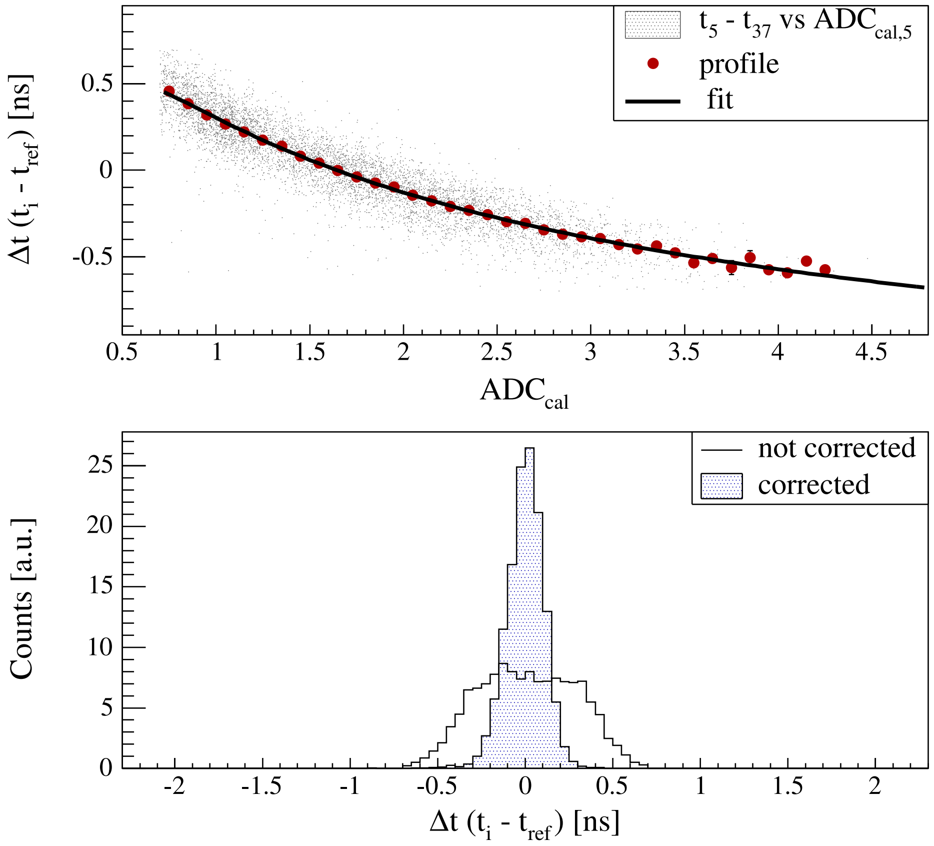

Fig. 4.12: BBC slewing correction.

The fit is shown in the top panel of Fig. 4.12. For each tube, the set of parameters a, b and c is stored in the BRAHMS database[2]. When the raw time information tdc_i from tube i is read out in an event, the calibrated time t_i is constructed by subtracting time offset and slewing effect:

$$t_i = tdc_i - t_{off,i} - \left(a + \frac{b}{\sqrt{\langle E_i \rangle}} + \frac{c}{\langle E_i \rangle} \right) \tag{4.10}$$

In the bottom panel is shown Δt for PMT's 5 and 37 of the left array, before and after slewing correction. Note that this procedure implies that each BBC array is calibrated w.r.t. one reference tube per array. It means that there remains some overall offset between both arrays. This is taken care of when the "raw" vertex calculated from the BBC's is compared to TPM1 tracks. Moreover, one can now ask about the slewing correction of the reference tubes. There are two options: they can either be left without correction since there are only two tubes among many or some other reference hit from another detector can be used (like ZDC hits). Such improvements are under investigation.

4.2.2 Vertex and Start–Time Determination

This section describes how the collision start-time and primary vertex are reconstructed from the calibrated BBC data. These quantities are crucial for the rest of the analysis (TOF PID,

[2]For the reference tube, all parameters are set to 0.

event and track selection, acceptance correction, spectrum normalization, etc).

The primary vertex and start–time are calculated according to the following equations:

$$t_{start} = \frac{1}{2}\left[\left(\frac{D - z_{\mathit{off}}}{c}\right) - \langle t_L\rangle - \langle t_R\rangle\right] \tag{4.11}$$

$$z_{vtx} = \frac{c}{2}\left[\langle t_L\rangle - \langle t_R\rangle\right] - z_{\mathit{off}} \tag{4.12}$$

Their derivation is detailed in Appendix D. The quantities $\langle t_{L,R}\rangle$ are the average (calibrated) times measured in the left and right arrays respectively:

$$\langle t\rangle = \frac{\sum_i (tdc_i - \mathit{off}_i - slew_i)}{n_{hits}} \tag{4.13}$$

z_{off} is the vertex offset along the beam axis, originating from the overall time offset between the left and right arrays, D is the distance between left and right arrays (219 cm). For each array, hits are selected according to the conditions

$$\langle E_i\rangle > 0.7 \text{ particles} \tag{4.14}$$

$$10 < TDC_i < 3500 \tag{4.15}$$

Condition 4.14 ensures that “real” particles are selected (the single particle peak has a width of 0.1 particle after a fit to a Gaussian, therefore the lower cut of 0.7 excludes hits with ADC’s below $1 - 3\sigma$ particles). Condition 4.15 rules out hits with overflow TDC digit (abnormally long times). Once selected, hits are sorted in three groups: small tube hits, big tube hits, fastest tube hits (in the latter case, there are only two hits, one left and one right). This sorting leads to three vertices (z_{st}, z_{bt} and z_{ft}) and start-time estimations (the algorithm remains the same, although the third method does not require building a time average). In a first pass, for each array and each group of hits, calibrated times $t_i = tdc_i - \mathit{off}_i - slew_i$ are summed and averaged over the number of hits of the sum

$$\langle t_L\rangle_1 = \frac{\sum_{i,L} t_i}{n_L} \tag{4.16}$$

$$\langle t_R\rangle_1 = \frac{\sum_{i,R} t_i}{n_R} \tag{4.17}$$

In a second pass, individual times t_i are compared to the average of first pass $\langle t\rangle_1$. If a time difference $|t_i - \langle t\rangle_1|$ is greater than 0.5 ns, hit i is rejected (a window of 0.5 ns is large enough to keep the efficiency and time average confidence high). The remaining hits are used to construct a final time average $\langle t_L\rangle$ and $\langle t_R\rangle$. Using Eq. 4.12, Figure 4.13 shows the vertex distribution obtained by the three groups of tubes, before the offset z_{off} is determined. These distributions are slightly shifted toward the positive z’s. It is clearly demonstrated on Fig. 4.14 which shows the difference between TPM1 tracks and the three vertex estimations along the z axis of plane $x = 0$.

Vertex Efficiency and Resolution

The vertex determined by the small tubes shows the best resolution because a large number of tubes contribute to its construction (time averages are better determined). The width reported on Fig. 4.14 is a combination between the vertex and tracking resolution. It fluctuates

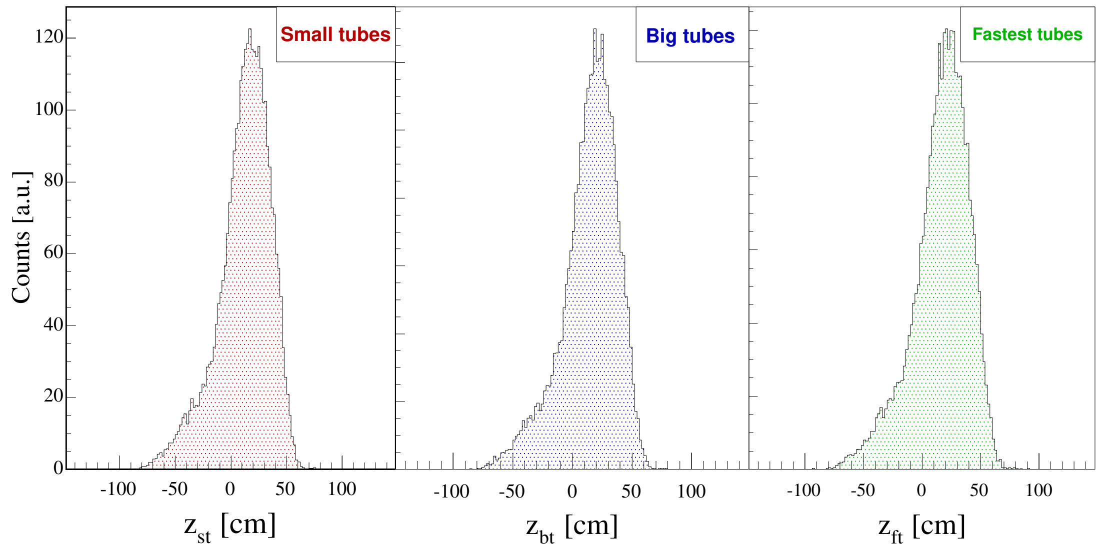

Fig. 4.13: BBC vertex distribution determined by the small tubes (left panel), big tubes (middle) and the fastest tubes (right).

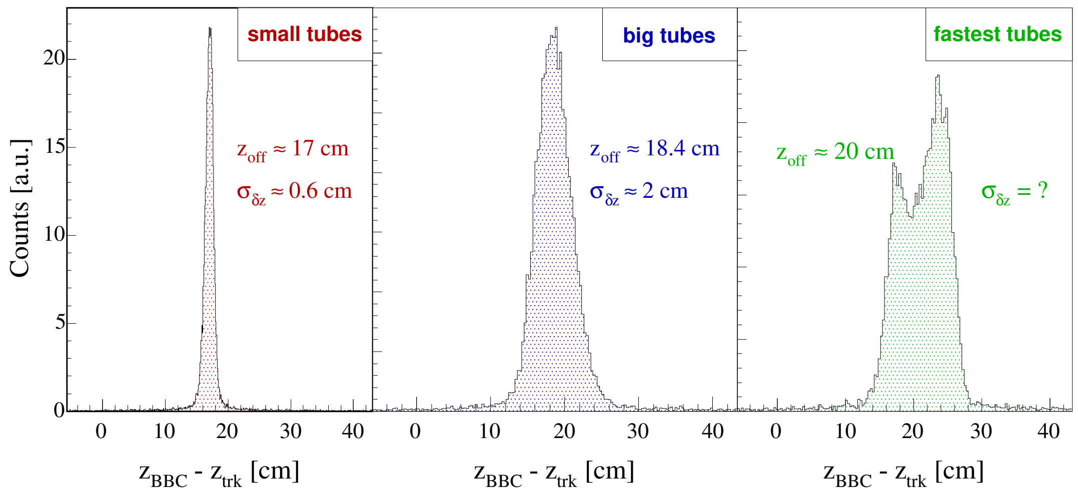

Fig. 4.14: BBC vertex offset determined with the help of TPM1 tracks.

little with time and ranges between 0.55 cm to 0.8 cm, depending on the MRS position[3] as long as central events are selected. Figure 4.15 shows the variation of ΔZ (top panel) and $\sigma_{\Delta Z}$ (bottom panel) with the number of small tubes used. As the events become peripheral,

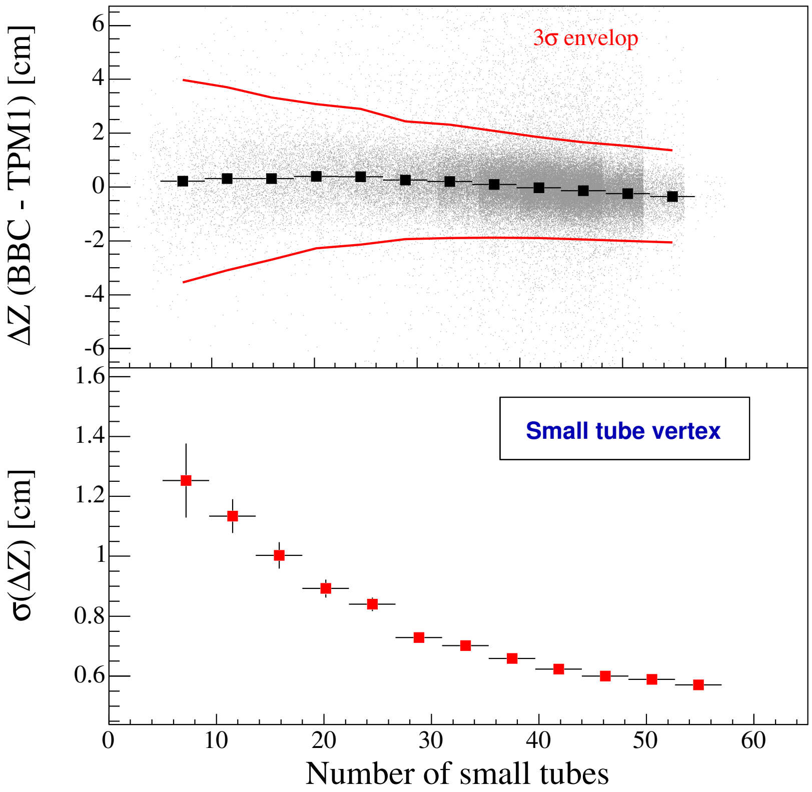

Fig. 4.15: Small tube vertex resolution as a function of the number of tubes used. The solid lines delimit a 3σ region.

fewer tubes contribute to the vertex reconstruction. At the same time, the track density decreases. Therefore, the vertex uncertainty increases while statistical fluctuations on the track intersection are more important. Note also the small variation of ΔZ. Ideally, the mean $\langle \Delta Z \rangle$ should be equal to 0. This is due to the slewing correction. Indeed, parameter a of Eq. 4.9 does not depend on the ADC, it is therefore an extra time offset (asymptotic limit of the fit function). Consequently, a is not estimated with the best confidence since the ADC range of the small tubes is not broad enough. Therefore, when time averages are constructed, there could be small differences depending on the combination of tubes used in the summation. In order to remove this effect, the vertex offset could be calculated as a function of centrality. Alternatively, the slewing correction procedure can be improved: if it is done before the time offset calibration, one can ignore a during this step, parameters b and c are enough to describe the relative shape of the slewing. The final time offset would include all offsets at the same time.

The “big tube” vertex resolution is also quite stable around 2cm. The number of big tubes (left + right) is 14, while the total number of small tubes is 65. Their dynamical range is also larger than that of the small tubes but are known to have a poorer intrinsic time resolution.

[3]he uncertainty of the track intersection with axis z depends on the spectrometer angle with the beam line.

These properties lead to a worse resolution but still acceptable (the ZDC vertex resolution amounts to $\sim$ 2 to 3 cm).

Regarding the fastest tube method, there are two visible peaks. It might be that conditions 4.14 and 4.15 are not stringent enough since this particular vertex requires only two tubes, one in each array, with the assumption that the detected particles travel at the speed of light (fastest tubes mean that the lowest TDC values in each array are selected). The double peak could be explained if the lowest TDC value always originates alternatively from two tubes of one of the arrays. The non optimal slewing correction would therefore be the cause. This effect is under investigation but the "fastest tube" vertex is almost never used.

The three different resolutions impose a simple quality scale for the choice of the event vertex: if all three methods provide a vertex estimation in an event, the "official" event vertex is z_{st}. If only z_{bt} and z_{ft} could be estimated, then z_{bt} is the "official" event vertex. Figure 4.16 shows how often the different vertex methods are used in an ordinary Au + Au run. The right

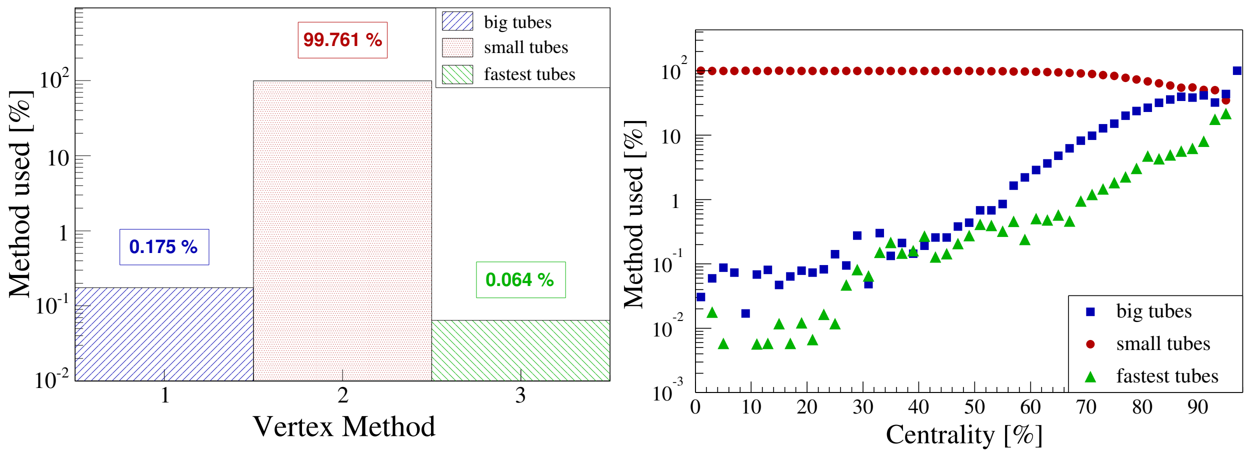

Fig. 4.16: BBC vertex method statistics averaged over all triggers and centralities (left) and versus centrality (right).

panel of Fig. 4.16 shows the centrality dependence of the vertex method used. As expected, the efficiency of the small tube method decreases as the events become more peripheral since fewer particles happen to hit the small tubes. At the same time, the other two methods are solicited more and more, big tubes have more chance to detect particles than small tubes and the last method always works as long as the BBC's detect particles respecting conditions 4.14 and 4.15. Note that requiring a centrality estimation limits the vertex distribution to roughly $|z_{vtx}| < 50$ cm (multiplicity array acceptance).

4.3 Particle Tracking

After a brief review of the TPC local tracking (the DC tracking is explained elsewhere [108]), this section describes how the particle momentum is determined by matching track segments inside magnet gaps, using basic geometrical principles. The particle flight path length is then estimated by straight extrapolations (outside the regions with no magnetic field) to the primary vertex at one end and to the hodoscope plane at the other end.

4.3.1 Local Tracking

The BRAHMS tracking chambers measure pieces of charged particle trajectories that consist of sets of points called track hits. The local tracking is by definition the construction of these points and the subsequent linear fit leading to straight three dimensional segments in the chamber.

Tracking with Time Projection Chambers

A TPC row consists of read–out pads. Rows and pads cover the (x, z) plane of a TPC. The y information is obtained from the drift of secondary electrons created by the passage of a charged particle ionizing the TPC gas. The signal of these electrons (ADC) is distributed over more than one pad and time bin. The raw TPC data are called TPC sequences, illustrated in Fig. 4.17. The TPC tracking algorithm starts first by scanning pads and rows and grouping sequences into clusters. Figure 4.18 shows how a cluster looks in the (pad, time, ADC) space. When two tracks are close, clusters can overlap. The second step is therefore the deconvolution of such clusters into two or more clusters. The process is illustrated in Fig. 4.19. The next step is the conversion of the deconvoluted clusters into TPC hits containing space position, variance on this position and cluster ADC sum (or energy loss). The final step consists of carefully grouping hits together via an algorithm called “track follow finder” and fitting them in order to get a three dimensional line. These steps are described in [30, 105]. Figure 4.20 summarizes this algorithm.

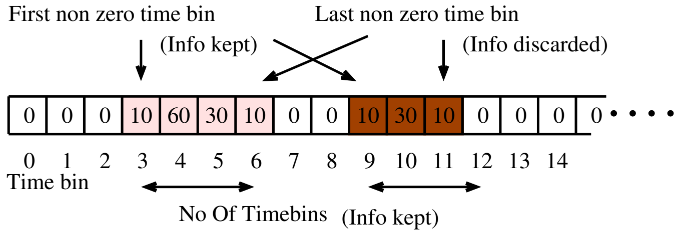

Fig. 4.17: For a given row and pad, a TPC segment is a set of time bins with non zero ADC values (zeros are removed).

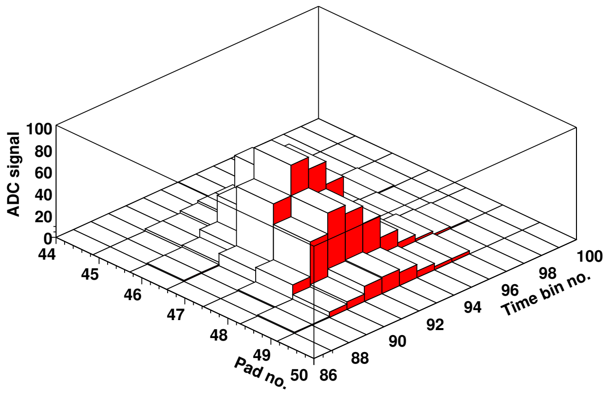

Fig. 4.18: A TPC cluster.

Figures 4.17 to 4.20 show ideal cases. In practice, a TPC needs some calibrations before going through these tracking steps. The main calibrations are :

pad status	:	noisy or dead pads are identified and ruled out during tracking
time correction	:	the drift velocity in the pad–rows closest to the sides of the TPC shows some non–linearities that are corrected
drift velocity drift	:	gas pressure changes make the drift velocity fluctuate with time

An example of drift velocity fluctuation with time is shown in Fig. 4.21 for TPM2.
Figure 4.22 shows the average number of tracks per event for the top 20% central events, as a function of spectrometer setting. It also shows the stability of the spectrometer with time (the event range consists of several runs).

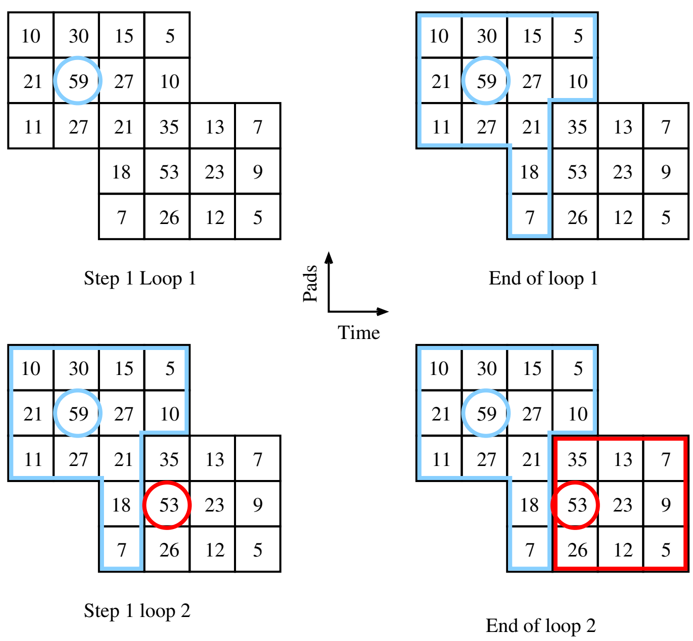

Fig. 4.19: TPC cluster deconvolution. The numbers are the ADC values. The big cluster (top left) is finally deconvoluted into two clusters (bottom right). See [30] for details on the deconvolution algorithm.

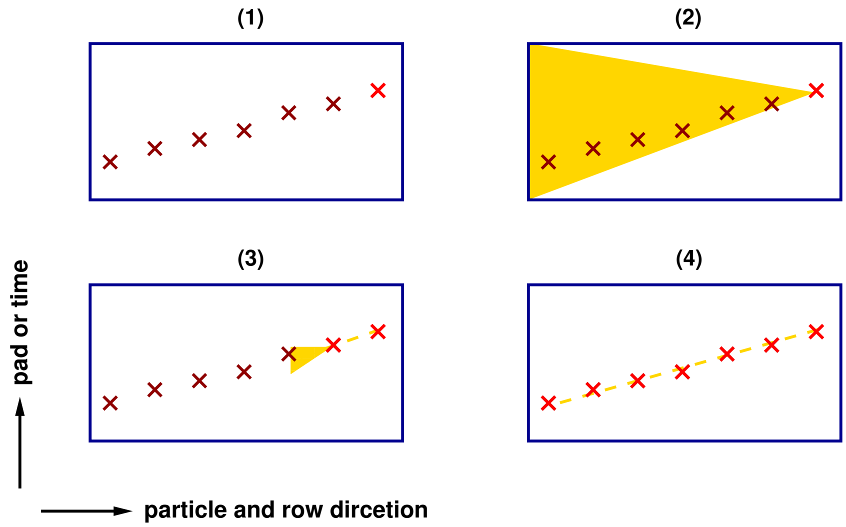

Fig. 4.20: TPC track "follow" finder algorithm. The search process starts from the back of the TPC and is conducted in a limited area in each row (see [30]).

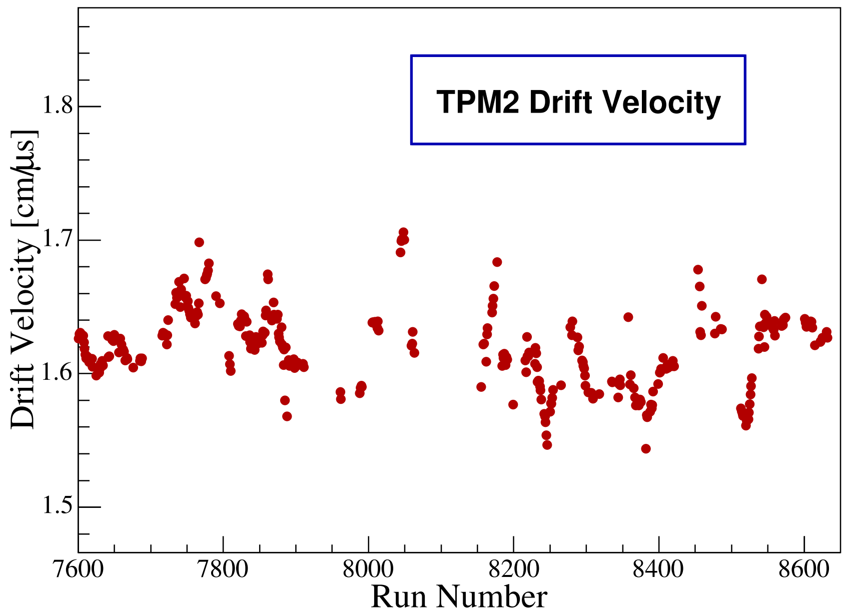

Fig. 4.21: Measured TPM2 drift velocity as a function of run number. The fluctuation are due to changes of the TPC gas pressure.

4.3.2 Momentum Determination

Basic Principles

To determine the particle momentum, BRAHMS utilizes the combination of a tracking chamber at the front of a dipole magnet and a tracking chamber at its back. Figure 4.23 is an illustration of the geometrical framework. The momentum determination algorithm is based on the formula

$$\vec{p} = q\vec{B} \times \vec{\rho} \tag{4.18}$$

where $\vec{p}$ is the momentum of the particle, q its electrical charge, $\vec{B}$ the magnetic field and $\vec{\rho}$ the curvature of the particle trajectory due to the action of the field. For each dipole magnet, the field acts in a squared gap. The axis of the field is parallel to the vertical axis of the gap (y) while the current polarity governs the direction of the field vector $\vec{B}$ (up or down). The longitudinal axis of the gap is z whereas x is the direction along its width. Since the particle trajectory inside the gap is a helix of axis y, its projection on the plane (x, z) is a circle (see Fig. 4.23).

If $\vec{p} = \vec{p}_{xz} + \vec{p}_y$, Eq. 4.18 projected to the (x, z) plane becomes

$$p_{xz} = qB_y\, r \tag{4.19}$$

since $\vec{\rho} = \vec{r} + \vec{y}$. In principle, $\vec{B}$ is uniformly distributed inside the magnet gap and has only one component B_y. This configuration implies that the field has no action on the particle in the y direction. In practice, B_y (or simply B) does not exactly vanish at the edges of the gap. Therefore, the magnetic field has been measured as a function of z (and x for second order

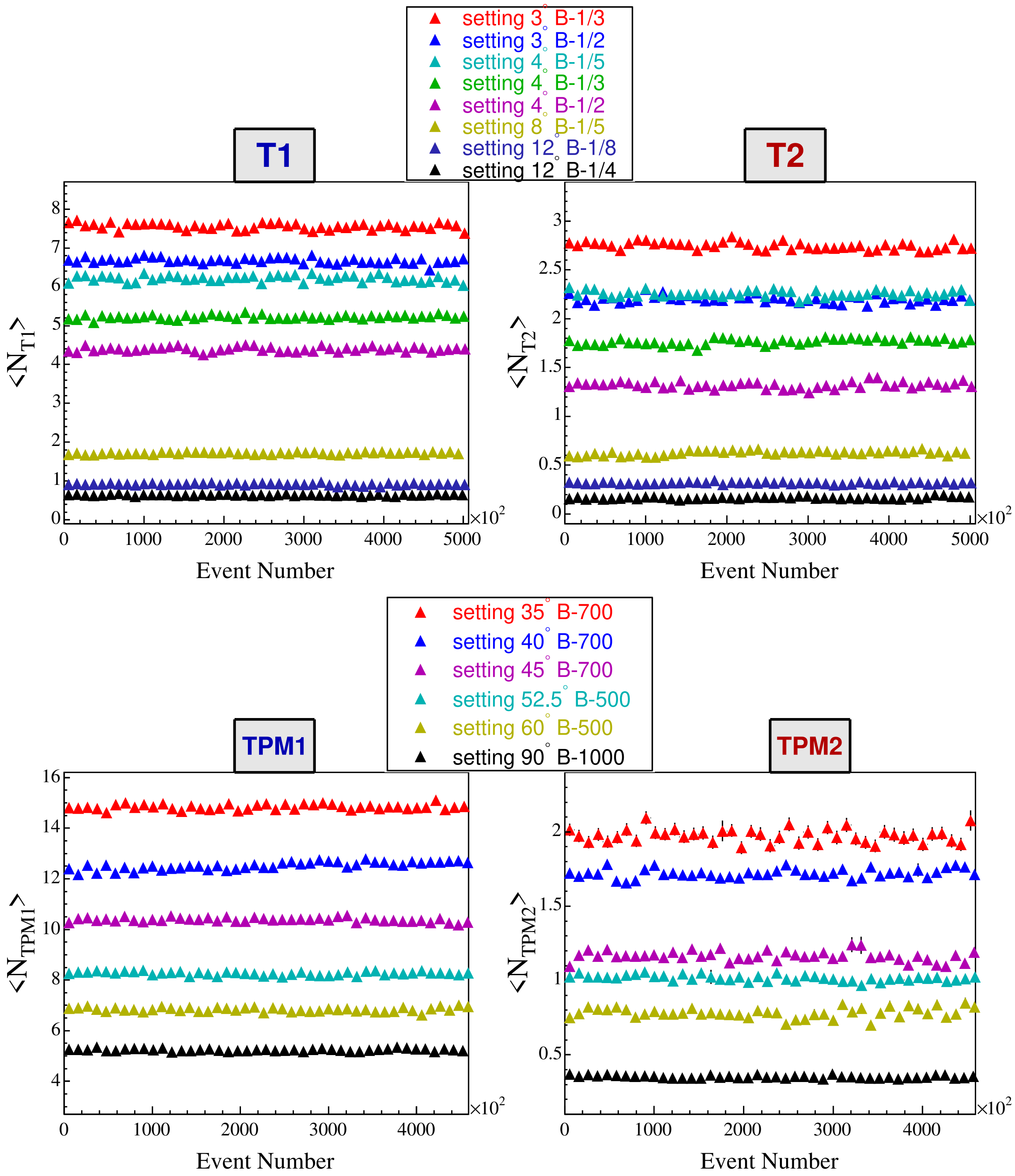

Fig. 4.22: Average number of TPC tracks per event (20% most central) for different spectrometer settings. The FS (MRS) TPC's are shown in the top (bottom) panels, respectively.

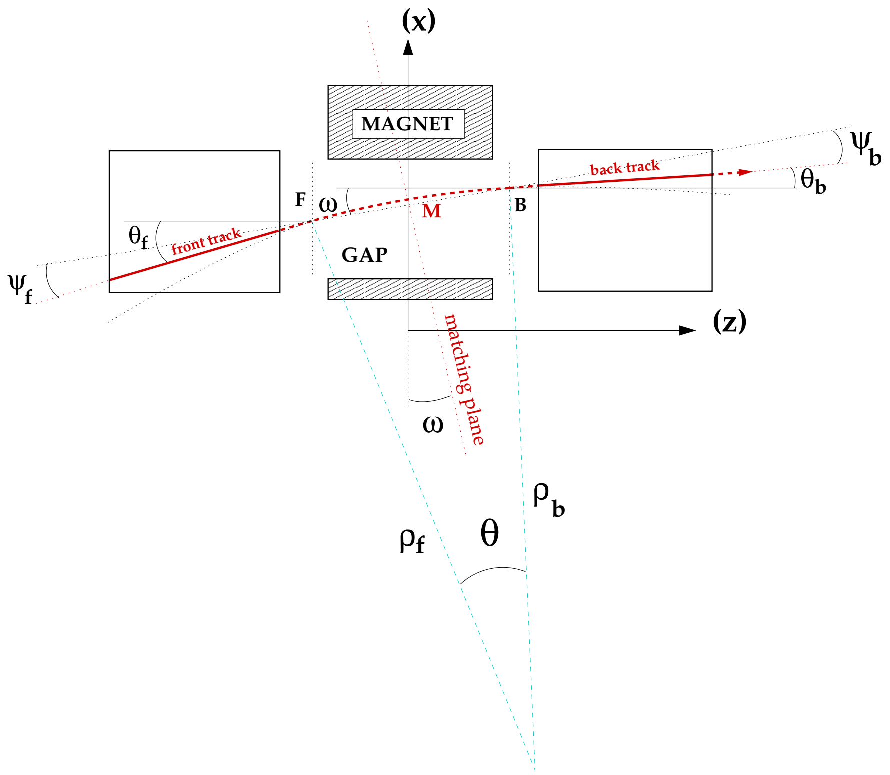

Fig. 4.23: Top view of a charged particle trajectory. The relative scale between magnet and tracking chambers is not respected for clarity.

deviations, although this is not used here) in order to calculate the following integral:

$$
\begin{aligned}
I &= \int_{-\infty}^{+\infty} B(z)\, dz && (4.20)\\
&\equiv 2B\, z_{eff} && (4.21)\\
&= B\Delta L && (4.22)
\end{aligned}
$$

where z_{eff} is the z coordinate of the edge planes of the gap, with $z_{eff} > z_{gap}$, and $\Delta L = 2z_{eff}$. Figure 4.24 illustrates the effective edge approximation.

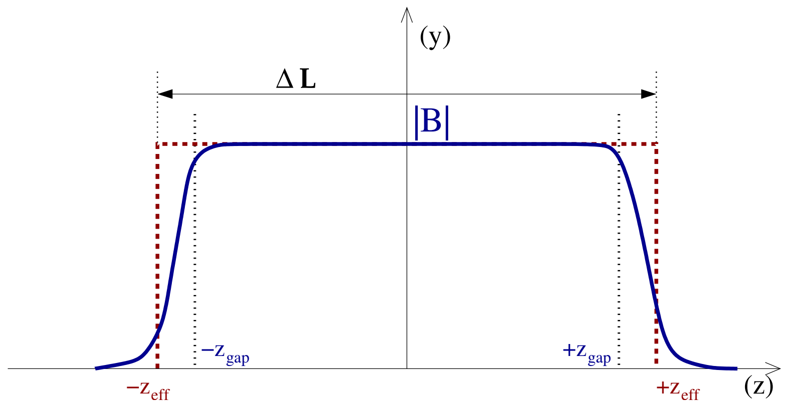

Fig. 4.24: Magnetic field intensity along the longitudinal axis of the magnet gap (solid blue line) and effective approximation (red dashed line). Both integrals are equal.

This integral appears in the equation used for momentum estimation. Indeed, using the notation of Fig. 4.23, if θ_f (θ_b) is the angle between the direction of the front (back) track and the z axis, ω the angle between the z axis and the line linking point F to B, and l the length of segment $[FB]$, it follows that

$$\theta_f = \omega + \psi_f = \omega + \theta/2 \tag{4.23}$$

$$\theta_b = \omega - \psi_b = \omega - \theta/2 \tag{4.24}$$

$$\Delta L = l\cos\omega \tag{4.25}$$

$$r = \frac{l}{2\sin\theta/2} \tag{4.26}$$

Therefore, after some trigonometry, it follows that

$$r = \frac{\Delta L}{2\sin\left(\frac{\theta_f-\theta_b}{2}\right)\cos\left(\frac{\theta_f+\theta_b}{2}\right)} = \frac{\Delta L}{\sin\theta_f - \sin\theta_b} \tag{4.27}$$

Finally, the momentum component p_{xz} is given by the following equation

$$p_{xz} = \frac{q\,B\Delta L}{\sin\theta_f - \sin\theta_b} \tag{4.28}$$

where the integral 4.22 is revealed explicitly and justifies the effective edge approximation. The full momentum is completed thanks to the slope α_y of the track direction (cf. Fig. 4.25). Using Pythagoras's rule $p^2 = p_{xz}^2 + p_y^2$ with the fact that there is no field action along the y direction and that $|p|$ and $|p_{xz}|$ are *constant*, it follows

$$p = \frac{p_{xz}}{\sqrt{1-\alpha_y^2}} \tag{4.29}$$

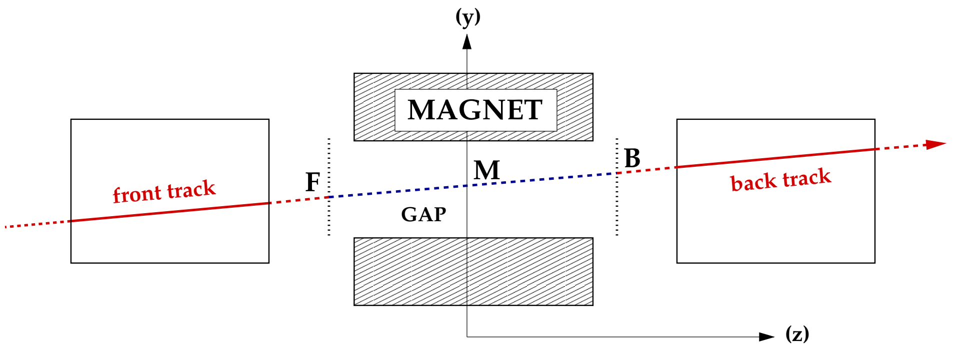

Fig. 4.25: Side view of a particle trajectory.

Matching parameters

In a central Au + Au collision event, many local tracks are reconstructed in the tracking chambers. Matching a pair of front and back tracks therefore requires some criteria. From the previous equations, three matching parameters can be deduced. The first one is given by Eq. 4.23 and 4.24: when the front and back tracks match with each other, $\Delta\psi = \psi_f - \psi_b = \theta/2 - \theta/2 = 0$. The other matching parameters are related to the y axis. Since the field has no effect along this direction, the front and back tracks must have the same slope α_y. Therefore, the second criterion is $\Delta\alpha_y = \alpha_{y,f} - \alpha_{y,b} = 0$. Moreover, a matching plane is defined for each pair of front and back tracks: its origin is the center of segment $[FB]$ and its base vectors are $(\vec{u}_n, \vec{u}_y)$ with $\vec{u}_n$ a unit vector normal to segment $[FB]$ and $\vec{u}_y$ the unit vector along y. The intersections of the front and back track lines with this plane are calculated (giving points P_f and P_b) and the quantity $\Delta y = P_{f,y} - P_{b,y}$ is equal to zero for matching tracks (point M on Fig 4.23 and 4.25).

In summary, front and back tracks are perfectly matched if

$$\Delta\psi = 0 \tag{4.30}$$
$$\Delta\alpha_y = 0 \tag{4.31}$$
$$\Delta y = 0 \tag{4.32}$$

Experimentally, due to the finite tracking resolution, geometrical imperfections and field approximations, the matching conditions are more loose. Figure 4.26 shows the distributions $\Delta\psi$, $\Delta\alpha_y$ and Δy for [T1–D2–T2]. The three histograms show a clear signal on top of a com-

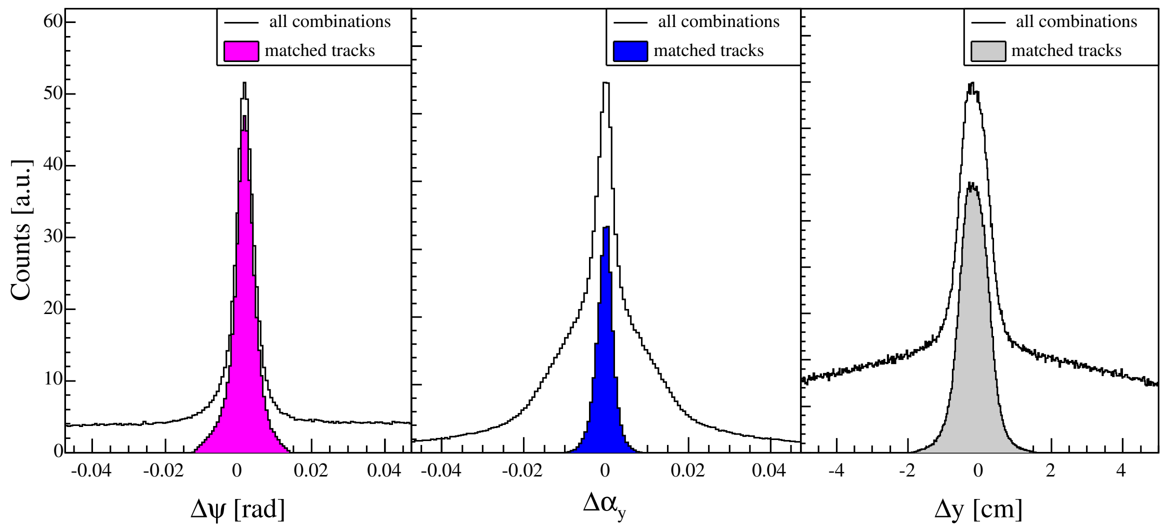

Fig. 4.26: Distributions of the three matching observables in the FFS. The signal is visible on top of a combinatorial background. Matched tracks (filled histograms) fulfill condition 4.33 (see text).

binatorial background. Since small offsets are present for the reasons cited above, a first pass is needed to evaluate offsets and widths for each run. Although distributions are not Gaussian–like due to multiple scattering, they are fitted to a Gaussian in a first approximation. In a second pass, pairs of tracks are selected according to the following elliptical cut:

$$\left(\frac{\Delta\psi - \Delta\psi_{off}}{\sigma_{\Delta\psi}}\right)^2 + \left(\frac{\Delta\alpha_y - \Delta\alpha_{off}}{\sigma_{\Delta\alpha_y}}\right)^2 + \left(\frac{\Delta y - \Delta y_{off}}{\sigma_{\Delta y}}\right)^2 < n_\sigma^2 \tag{4.33}$$

with σ the width of each distribution (evaluated by fitting the signal with a Gaussian function) and $n_\sigma = 3$ (user's cut). It is interesting to check how the matching parameters evolve with time. Figure 4.27 shows this evolution as a function of the run number for the MRS. It reveals a few noticeable facts : the quantity $\Delta\psi$ is rather stable in width and offset. The parameters

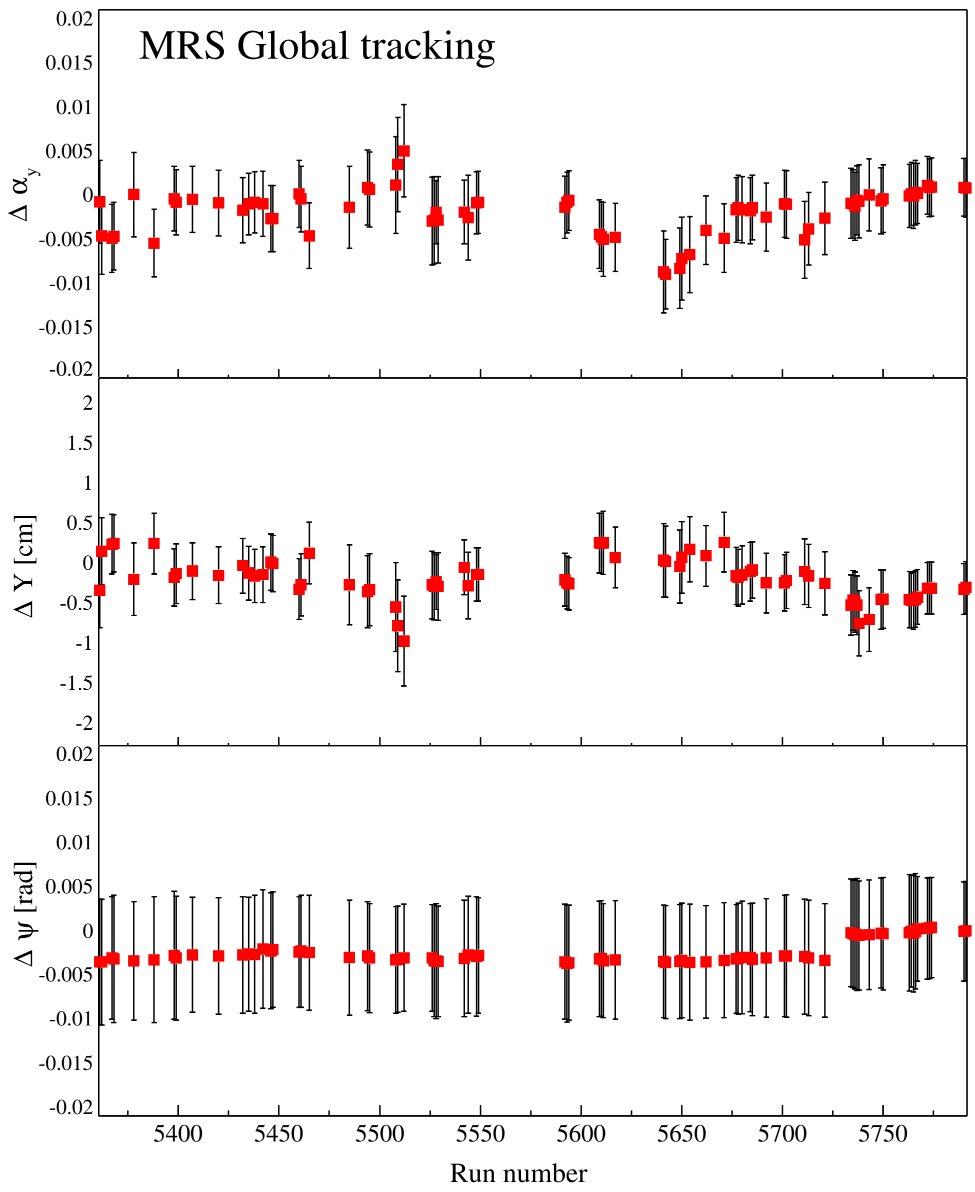

Fig. 4.27: Time evolution of the matching parameters in the MRS. Error bars are the widths given by the fit.

$\Delta\alpha_y$ and Δy are not as stable as $\Delta\Psi$ but are anti–correlated. Nevertheless, their respective width does not change. This is explained by the TPC drift velocity fluctuations. It is therefore necessary to investigate and evaluate matching parameter offsets and widths on a run by run basis before matching cuts are applied.

Ghost tracks

The drawback of such a matching procedure is the creation of "fake" tracks or "ghost" tracks which occurs when uncorrelated tracks happen to fall within the user's cuts. In that case, there can be two or more front tracks matching a single back track (the opposite can also happen but is more rare, the number of back tracks is usually much smaller than the number of front tracks). For such groups of multiple matchings, matched tracks are tagged according to the quality of the matching. Each of them is assigned a confidence level according to the following equation :

$$\chi^2 = \left[\left(\frac{\Delta\psi - \Delta\psi_{off}}{\sigma_{\Delta\psi}} \right)^2 + \left(\frac{\Delta\alpha_y - \Delta\alpha_{off}}{\sigma_{\Delta\alpha_y}} \right)^2 + \left(\frac{\Delta y - \Delta y_{off}}{\sigma_{\Delta y}} \right)^2 \right] / \, 3 \tag{4.34}$$

In a given group of multiple matchings, the one with the smallest χ^2 is considered as a real matching whereas the others are ghost candidates. Figure 4.28 shows the number of matched tracks per event before and after ghostbusting. All events with more than one matched track are generally contaminated. The "ghostbusting" process aims at eliminating fake track contamination.

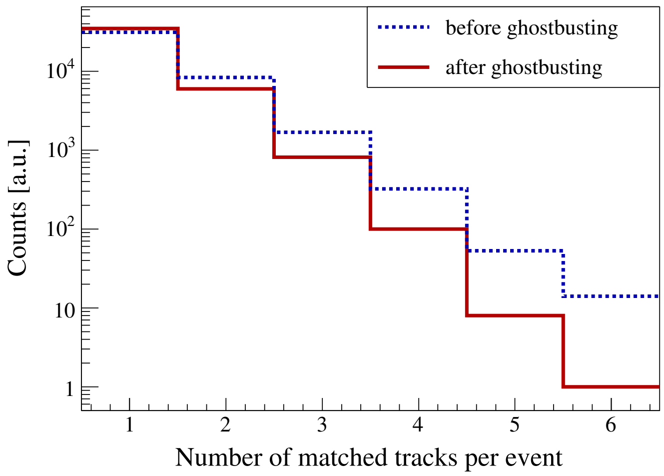

Fig. 4.28: Track ghostbusting in the MRS.

Finally, Figure 4.29 shows examples of momentum distributions obtained from this procedure for the MRS, FFS and BFS. The difference between the FS and the MRS is striking: the dynamical range is much broader in the FS but at the same time, only one charge sign is detected for a given field polarity. In the FFS (D2 momenta), some particles have the opposite charge sign but in relatively low amount. Most of these particles are rejected if the matched tracks are required to "swim back" through D1 without hitting the magnet gap sides. It means that they are mainly created inside D1 by scattering and are thereby considered as background tracks.

Advanced matching in the FS

In the FS, once the local track matching is done, another level of matching takes place in order to build full FS tracks. The first and easiest step is done in the BFS. Indeed, local tracks in T4 are shared by D3 and D4 matched tracks. Therefore, these two groups of matched tracks are matched by checking which ones share the same T4 tracks. Since some prior ghostbusting was applied independently to both groups, there is no ghost track creation when matching these two groups. Resulting tracks are called BFS tracks. Figure 4.30 illustrates the BFS matching.

The second and last step consists of matching BFS and FFS tracks. There are two possibilities. If matched tracks in D3 were obtained from the combination [T2–D3–T4], the same principle is applied since the D2 and D3 matched tracks have T2 in common. In the case D3 matched tracks were obtained with [T3–D3–T4], a geometrical matching similar to the local track

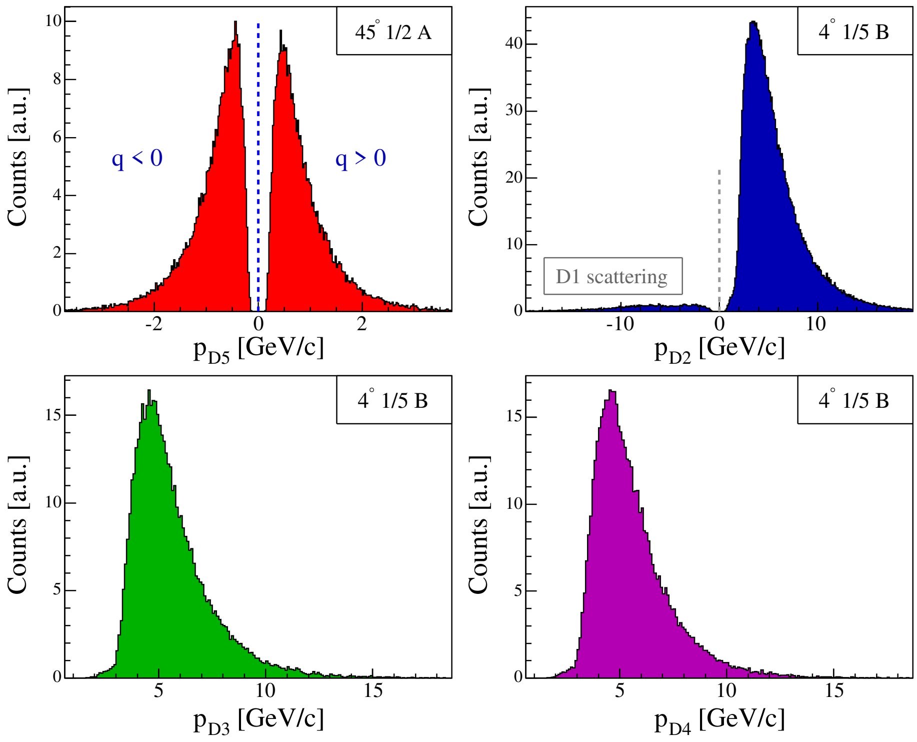

Fig. 4.29: Momentum distributions from all BRAHMS magnets. Top left: D5, top right: D2, bottom left: D3, bottom right: D4.

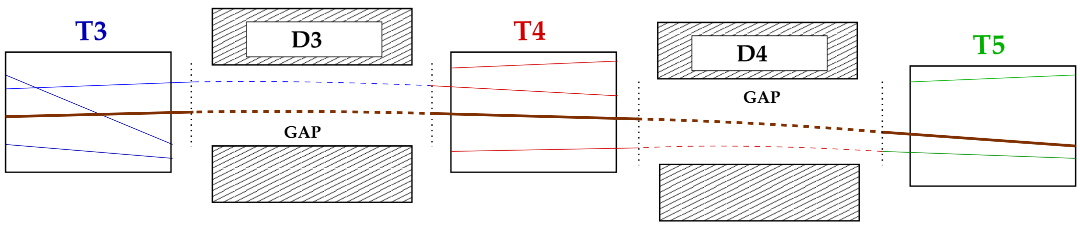

Fig. 4.30: Drawing illustrating the matching between D3 and D4 matched tracks in the BFS, done via T4 tracks.

matching procedure is performed between T2 and T3. But here, there is no magnet in between, therefore the matching condition is

$$\left(\frac{\Delta x - \Delta x_{off}}{\sigma_{\Delta x}}\right)^2 + \left(\frac{\Delta y - \Delta y_{off}}{\sigma_{\Delta y}}\right)^2 + \left(\frac{\Delta \alpha_x - \Delta \alpha_{x,off}}{\sigma_{\Delta \alpha_x}}\right)^2 + \left(\frac{\Delta \alpha_y - \Delta \alpha_{y,off}}{\sigma_{\Delta \alpha_y}}\right)^2 < n_\sigma^2 \quad (4.35)$$

with Δx and Δy the differences along (x) and (y) between the intersection of the T3 track line, with a plane containing the middle point of the T2 track segment, and the latter (this plane is normal to the z axis of T2). $\Delta\alpha_x$ and $\Delta\alpha_y$ are the slope differences along axes (x) and (y). When multiple matchings occur, the same χ^2 principle as before is applied, with the corresponding matching variables.

4.3.3 Particle Flight Path

Track Vertex

The determination of the particle path length needs an estimation of the track origin (or track vertex). In BRAHMS, track vertex means the track line intersection with a "vertex" plane, defined below. Strictly speaking, real track vertices cannot be measured in BRAHMS, unless particles decay inside a tracking chamber[4]. This information is eventually be used for selecting primary particles. Figure 4.31 illustrates the procedure for FS and MRS tracks. The planes

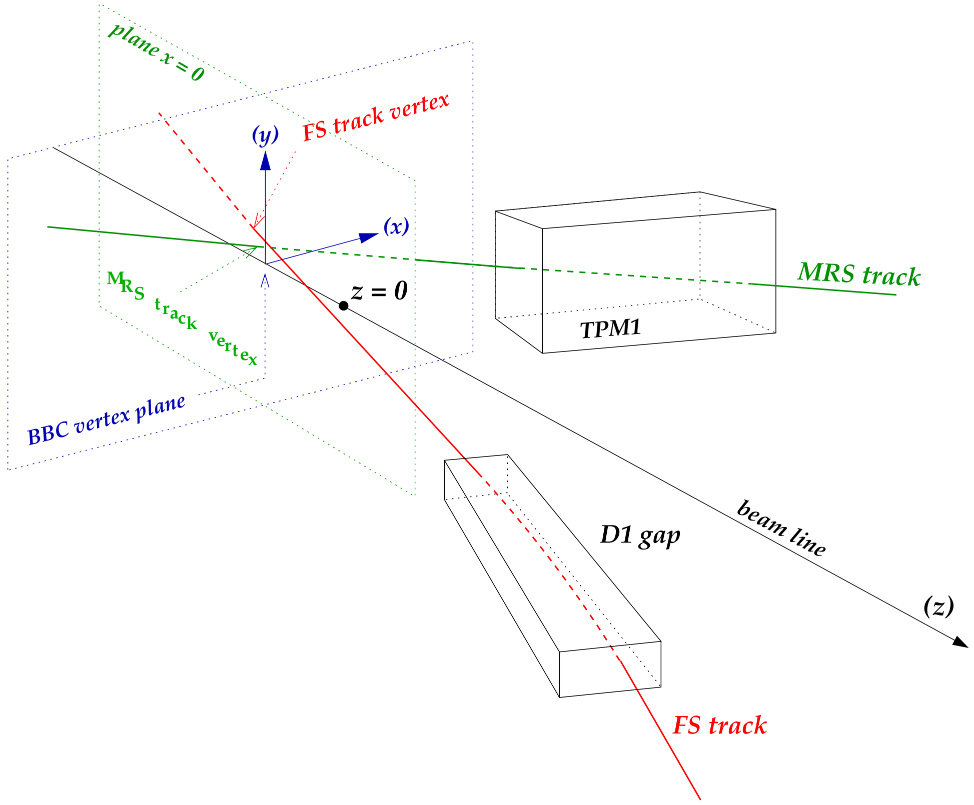

Fig. 4.31: Track projection to primary vertex planes. The intersection point is used as the track vertex. For FS tracks, the plane is $z = z_{BBC}$. For MRS tracks, the plane is $x = 0$.

are $x = 0$ for MRS tracks and $z = z_{BBC}$ for FS tracks. It is a natural choice since the MRS rotates with the angular range $30\,°$– $90\,°$ whereas the FS covers $\theta = 2.3\,°$– $30\,°$. In the MRS, this implies that the x position of the track vertex is fixed to $x = 0$ but at the same time, the coordinates in y and z are directly comparable to the vertex location obtained from the BBC's $(z_{BBC}, 0, 0)$.

In the FS, the situation is different. The BBC vertex is by construction defined along axis (z) only. Unfortunately, trying to evaluate a z coordinate for FS track vertices (e.g. by calculating the closest point of the track line to the beam line) is useless, the track angles θ relative to the beam axis are so small that the uncertainty on z is big (roughly proportional to $1/\sin\theta$). However, FS track vertices are defined on a plane transverse to the beam line. This prevents from dealing with such angle effect. Note that projecting FS tracks to the primary vertex

[4] But even in this case, since the local tracking algorithms lead to straight lines within the whole volume of the chamber, deviations from straight lines, characteristic of a decay topology, cannot be reconstructed.

plane requires the knowledge of their momentum since D1 is in front of T1. The momentum is used to calculate the trajectory inside the D1 gap. The slope and the intersection of the trajectory at the front plane of D1 are used to extend the track path straight to the vertex plane. A typical track vertex estimation is shown on Fig. 4.32.

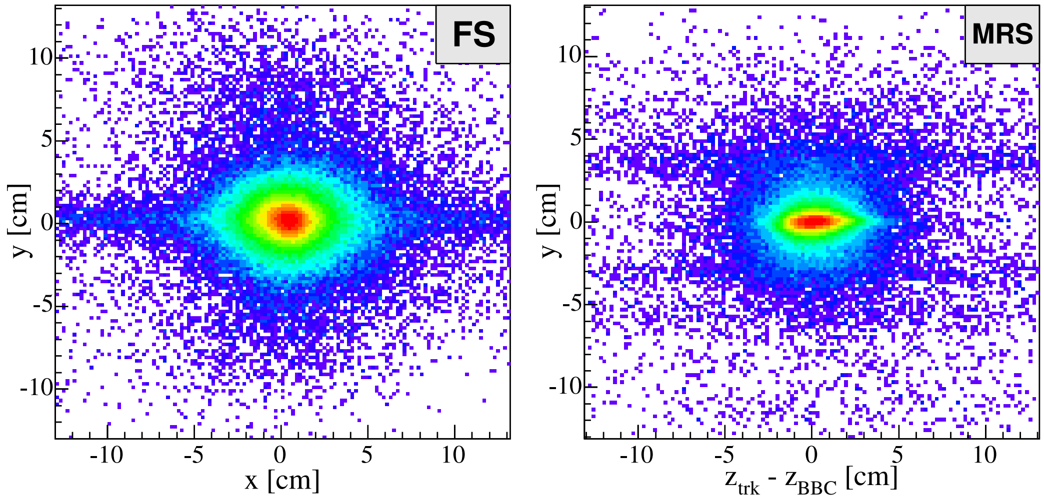

Fig. 4.32: Track extrapolation to primary vertex planes. The contour level scale is logarithmic. In both the FS (left) and the MRS (right), tracks are distributed around the collision point with a maximum at the primary vertex location, surrounded by a scattered background of secondary tracks.

Track End Point

The knowledge of the track length is only useful for the TOF PID. The other end of the track is therefore the track line intersection with a plane defined by the hodoscope axes. In the MRS, TOFW slats are grouped in six panels arranged on a circle arc. In each panel, slats are positioned on the same line. Tracks are extrapolated from TPM2 to TOFW panel planes (see Fig. 4.33). The intersection point with the (x, y) plane of the intersected slat as well as the

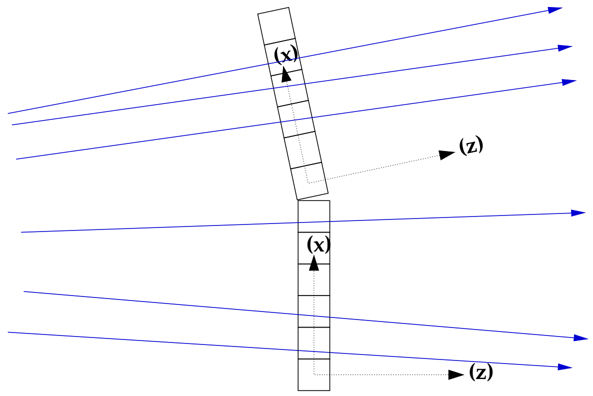

Fig. 4.33: Track line extrapolation to TOFW slats in the MRS. Panels stand on a different line unlike slats in each panel.

slat index number are kept for track–TOF hit matching.

In the FS, the track extrapolation is more complex. Slats with odd and even indices are not on the same line. Therefore, an FS track can intersect zero, one or two slats (see Fig. 4.34). When two slats are intersected, the path lengths inside the slat volumes are compared. The longest path determines the best slat candidate.

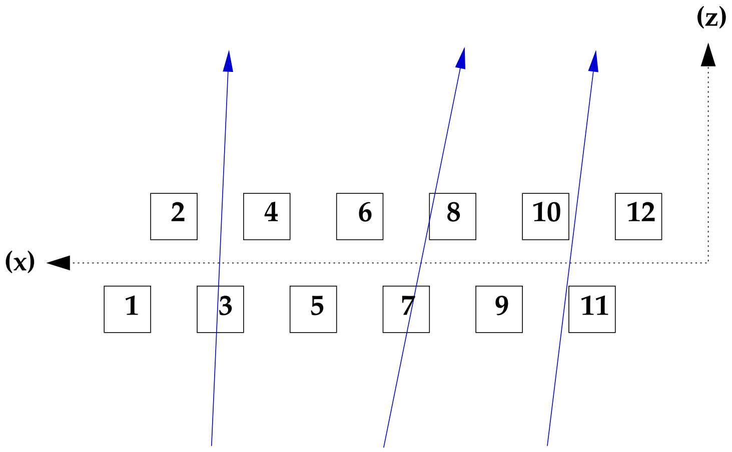

Fig. 4.34: Track line extrapolation to hodoscope slats in the FS (TOF1 and TOF2) seen from top. Lines can cross zero, one or two slats. Since the incident angle of "good" FS tracks on the hodoscope plane is close to 90 °, the probability to hit one slat only is by far the highest (see text).

Although the primary vertex location changes event by event, the track length between the spectrometer front planes and the hodoscope slats is approximately constant. An example is shown in Fig. 4.35 where the special slat arrangement in TOF1 is recognized (double peak) whereas a single peak is visible for MRS tracks.

Unfortunately, the track length resolution cannot be rigorously investigated without a simulation reproducing the experimental resolutions of the detectors, especially due to the track vertex as defined in the previous section. The track length resolution goes into the error on the particle velocity β. Nevertheless, an empirical approach is used when the PID resolution is investigated (Sec. 4.4.3).

4.4 The Time of Flight PID

TOF PID is done by first matching TOF hits to tracks whose momenta are known. Only tracks that survived the ghostbusting step are considered. Slats intersected by selected tracks are inspected to check if they contain valid TOF hits. Once hits are matched to tracks, ADC and TDC calibrations can be performed. The ADC (or energy loss) calibration is useful for selecting minimum ionizing particles (MIP) by applying an energy threshold that rules out very low ADC hits. The TDC calibration, unlike for the BBC's, leads to "absolute" particle time of flight. From there, PID can be done by using Eq. 4.1.

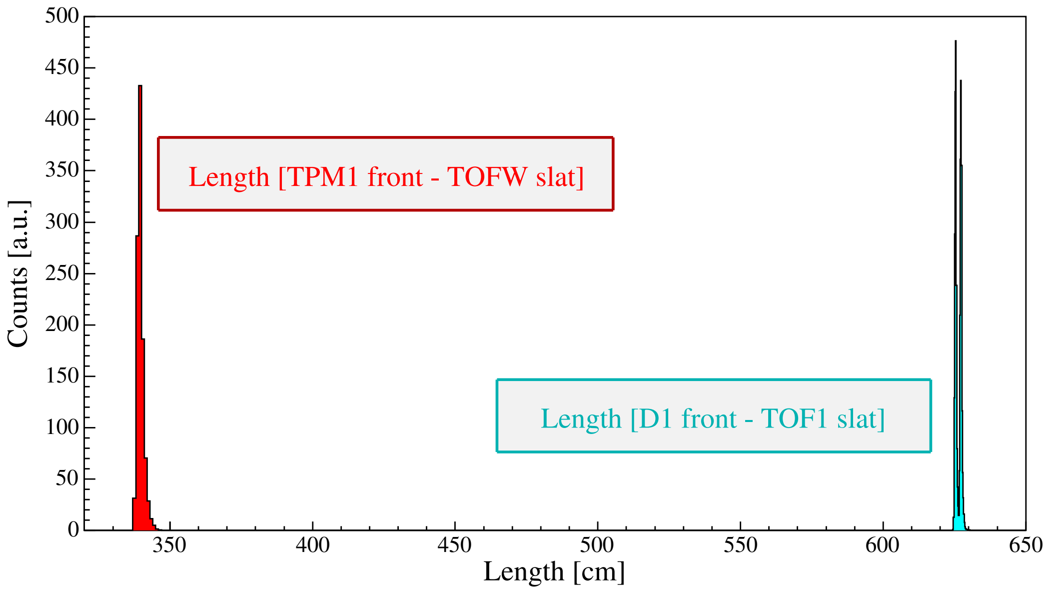

Fig. 4.35: Track path length between spectrometer front planes and intersected hodoscope slats. The double peak structure for FFS tracks reflects the slat positioning in TOF1.

4.4.1 Matching TOF hits and Tracks

The purpose of this matching is twofold: PID and background removal for TOF calibration. The matching is done by investigating hits in slats intersected by tracks. A TOF hit is defined by four digits. Each slat has a bottom and a top PMT's, each of them producing ADC and TDC signals. In order to correlate TOF hits with tracks, the top and bottom ADC digits of each hit are imposed a threshold $ADC_{ped} + 10 \times PED_{width}$ while the TDC digits are restricted to the range $[10, 4000]$, insuring that pedestal hits are rejected. In the MRS, if a slat associated to an MRS track does not have a valid hit, the neighboring slats are checked. If valid hits are present, the selection is done by imposing the condition $\Delta x = |x_{track} - x_{hit}| < 1.2\,\text{cm}$ where x_{hit} is defined as the middle of the slat along axis x of the hodoscope plane (1.2 cm, which is the slat width, is large enough to take into account the track extrapolation uncertainty). Multiple matchings can be introduced (two tracks sharing the same hit). This is discussed below.

In the FS, the procedure is more complex since an FFS or BFS track can be associated to two slats. Several passes are necessary. They are summarized in Tab. 4.2.

	1 slat candidate	2 slat candidates s_1 (best) and s_2
1st pass	matched if valid hit, else 2nd pass	both saved if valid hits in both, else 2nd pass
2nd pass	check neighboring slats ala MRS	if no hit in s_1 but hit in s_2, s_2 becomes s_1 if neither hit in s_1 nor s_2, 3rd pass
3rd pass		check neighboring slats à la MRS

Tab. 4.2: Track–TOF hit matching in the FS.

Figure 4.36 shows the distribution $\Delta x = x_{track} - x_{hit}$ obtained for all hodoscopes (left panels). The track uncertainty is visible in the difference between the slat number the matching hit belongs to, and the slat number the track points to (right panels).

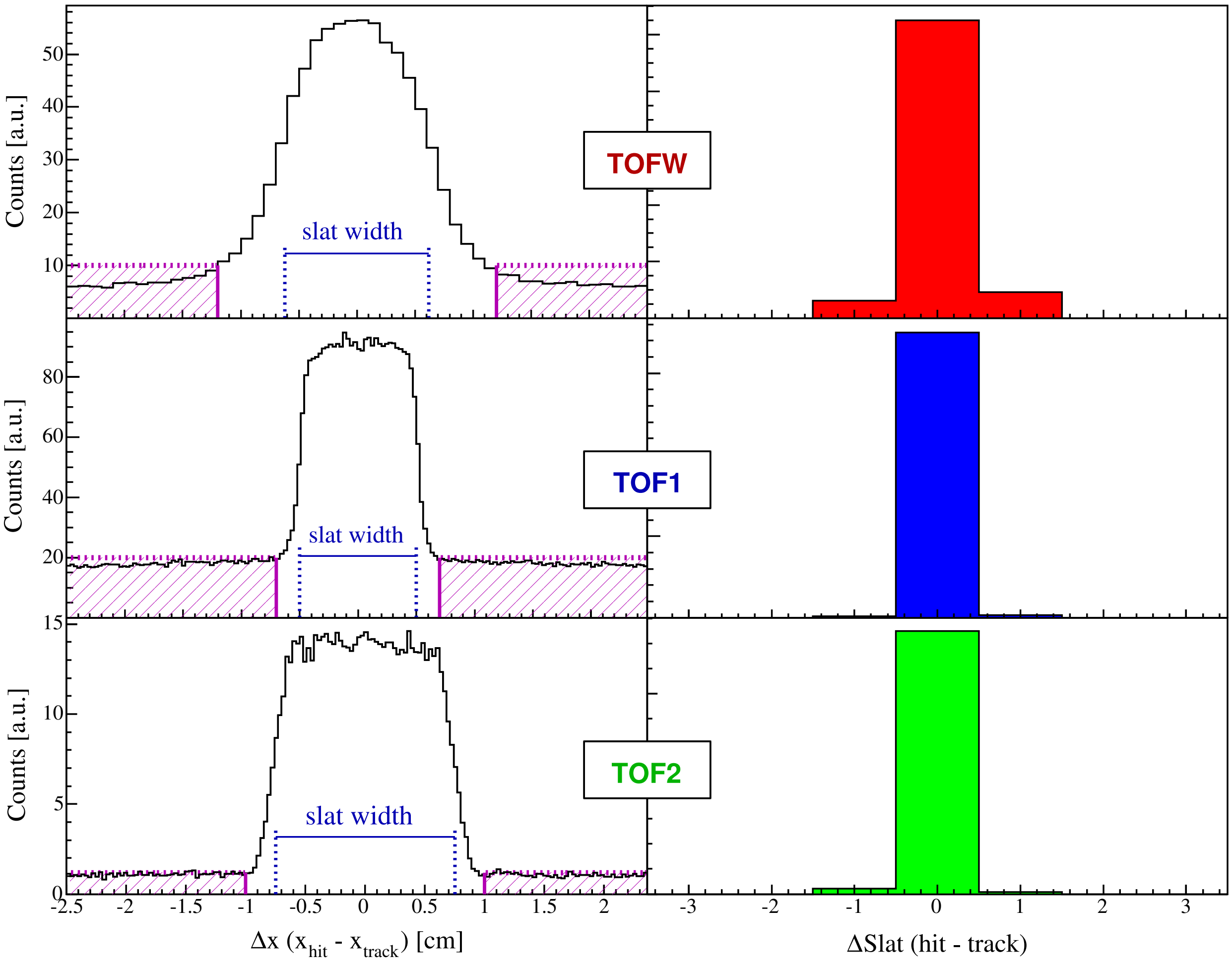

Fig. 4.36: Track TOF hit matching distributions in the MRS (top), FFS (middle) and BFS (bottom). The left panels show the difference between the hit positions and the track intersection along axis x of the hodoscopes. Hashed areas are rejected combinations. Selected areas are wider than slat widths due to track extrapolation uncertainties. The right panels show the difference between the slat index of the TOF hit and the index of the slat intersected by the track (matchings only).

Note that the TOFW histogram (MRS) is the sum of all panels. However, the selection cut is done for each panel. Depending on the TOF hit and track density, the level of combinatorial background differs. Another matching procedure (along y) will be applied when the TOF hit position along this axis is available after some calibrations.

Multiple hits

It can happen that two or more tracks are matched to the same TOF hit. The probability of such an event depend on the track density which is correlated to the spectrometer position. Figure 4.37 shows the ratio between multiple and single matchings as a function of slat and spectrometer setting. For TOF1, the multiple matchings do not constitute more than $\approx 5\%$ of the total number of matchings, with a fast drop as the FS angle increases. In the BFS, the density of tracks reaching TOF2 is lower than FFS tracks intersecting TOF1, a maximum of 1% only has been noticed. In the MRS, no more than 2% of the tracks share the same TOF

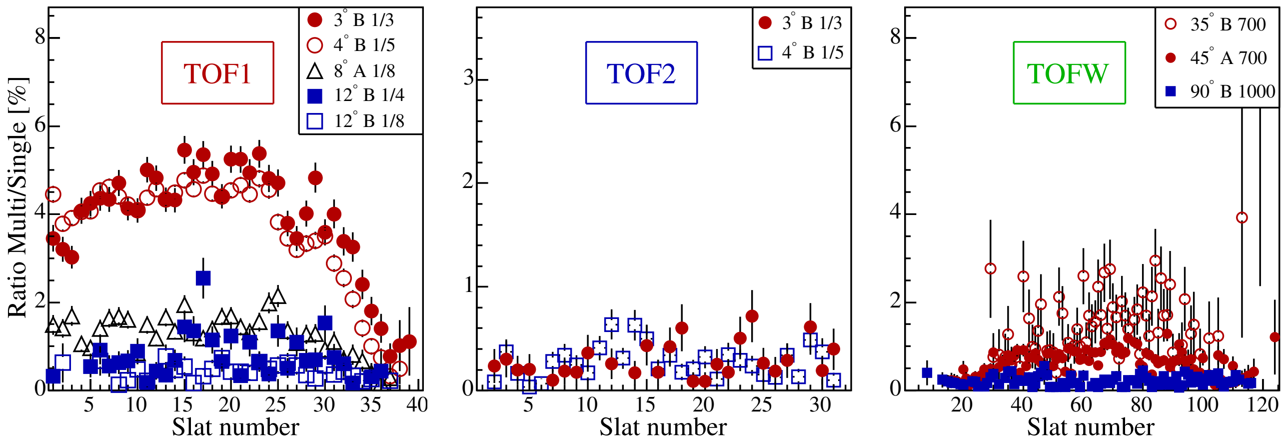

Fig. 4.37: Ratio between multiple and single matching distributions as a function of slat indices and spectrometer settings (0–20% central events).

hits. These multiple matchings are not removed but tagged and saved with the rest of the data. They are not included in the hit sample used for TOF calibrations.

Finally, Figure 4.38 shows TOF hit distributions before and after matching as a function of slat. As can be seen, the matching procedure rule out a lot of background hits. The TOF–

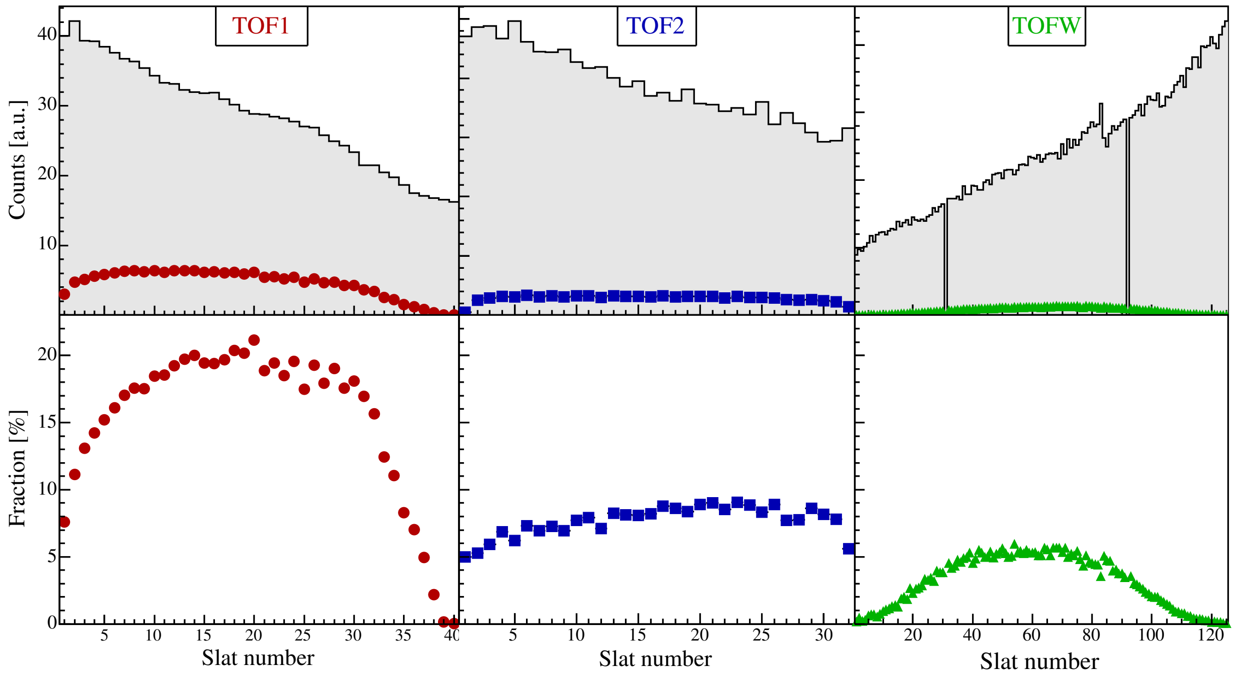

Fig. 4.38: Hit distributions in TOF1 (left), TOF2 (middle) and TOFW (right). The markers show hits matching global tracks.

track matching is therefore necessary for the quality of the TOF calibration. Moreover, the track information is needed for timing calibration, which is crucial for particle identification.

4.4.2 Hodoscope Calibrations

The hodoscope calibration is done in four steps (pedestals and TDC gains excluded, they are similar to the BBC procedure). They are listed in Tab. 4.3.

Calibration Type	Purpose
ADC gain	Conversion of ADC digits to average MIP energy loss
Relative Delay	Removal of delay between bottom and top PMT's
Time offset	"Absolute" time offset removal
Slewing correction	Removal of energy dependence in time signal

Tab. 4.3: Hodoscope calibrations prior to PID.

Energy deposited

The goal of the ADC gain calibration is the conversion of the ADC data to a number of particles à la BBC's. However, in the case of the hodoscopes, the raw signal originates from a different physical process (cf. Sec. 3.5.1 and Fig. 3.12).

The intensity of the collected light is related to the energy that the charged particle deposited inside the medium. Although slats are wrapped to prevent external sources of light from polluting the signals, there is always some electronic noise in PMT's, amplifiers and cables producing a low voltage converted to ADC data. Some electronic devices called discriminators are used to ignore signals below a certain voltage (see Fig. 4.39). Since detected particles are mainly MIP's, the energy dE deposited within a distance dx through the medium varies little with momentum. A typical MIP ADC spectrum has a Landau shape due to Landau fluctuations in the number of excited atoms inside the scintillator. Since dE/dx is proportional to Z^2, Z being the charge number of the particle, ADC data cannot be used for identifying particles of charge $Z = \pm 1$ (e.g. pions and kaons). However, it is used for track selection (above a certain ADC threshold). Figure 4.40 illustrates the procedure applied to TOF1.

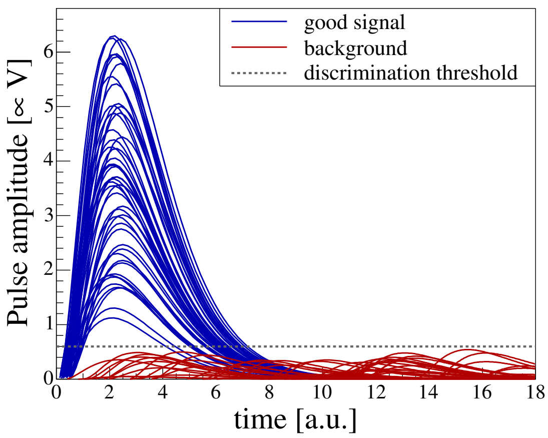

Fig. 4.39: Discrimination of background signals.

Figure 4.40 shows a first order calibration. Indeed, since the slat height is not negligible ($\sim$ 20 cm for TOF1 and TOFW, 40 cm for TOF2), light propagating from the hit location to the PMT's undergoes an intensity attenuation. The intensity of the light collected by the PMT's follows the equations

$$I_{top} = I_\circ \, exp\left[-(H/2 - y_{hit})/L_{att}\right] \tag{4.36}$$

$$I_{bot} = I_\circ \, exp\left[-(H/2 + y_{hit})/L_{att}\right] \tag{4.37}$$

with $I_\circ$ the initial light intensity, H the height of the slats and L_{att} the attenuation length, property of the scintillating material. Hence, the ADC spectrum of a given top or bottom PMT of a slat has a dependence on the hit position along the slat y axis. A good estimation of

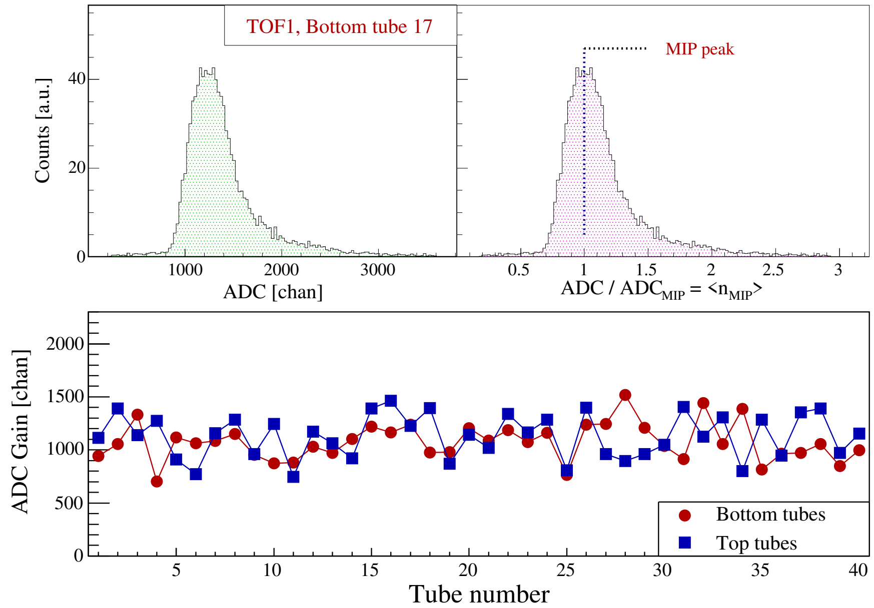

Fig. 4.40: ADC Gain calibration, with a raw ADC spectrum (top left), calibrated (top right) and a summary for all top and bottom PMT's. Only good matched tracks have been used.

this position is given by the crossing of the associated track. Figure 4.41 shows the attenuation effect in a TOF1 slat. Given equations 4.36 and 4.37, the attenuation effect is removed by

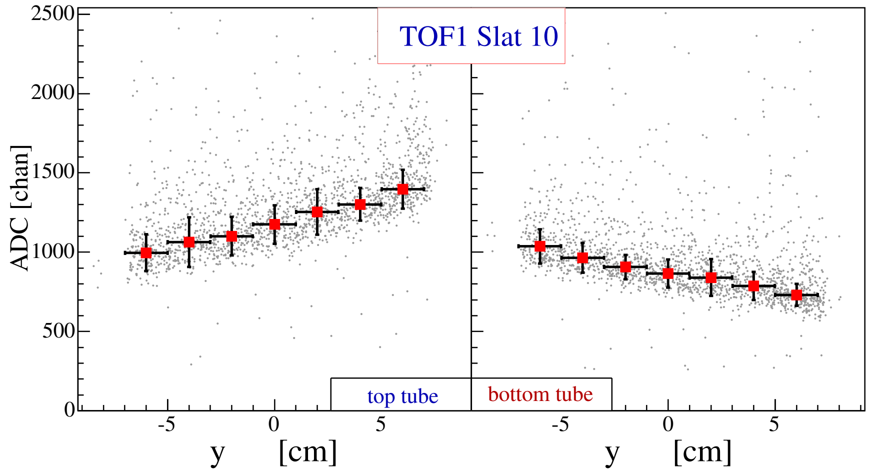

Fig. 4.41: Correlation between ADC data and hit y positions along the slat, reflecting the energy loss attenuation through the scintillator.

calculating the geometrical average of the top and bottom PMT signals:

$$\langle n_{MIP} \rangle = \sqrt{\langle n_{MIP} \rangle_{top} \times \langle n_{MIP} \rangle_{bot}} \tag{4.38}$$

The result can be seen on Fig. 4.42 which shows the geometrical average $\langle n_{MIP} \rangle$ as a function of the y position of the hit along the slat. The multiple matchings observed in Fig. 4.37 are revealed by the calibrated ADC data. Indeed, if two or more tracks match a hit, the energy loss or average number of MIP's $\langle n_{MIP} \rangle$ must be on average larger than 1. Figure 4.43 shows the calibrated energy loss for multiple matchings. As expected, the main peak is located at a

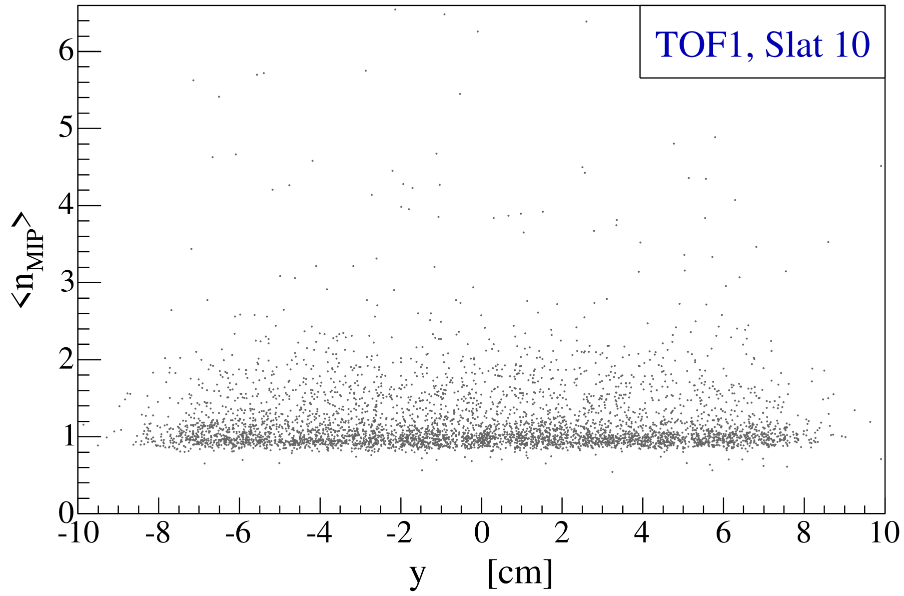

Fig. 4.42: Geometrical average of the calibrated ADC of the top and bottom PMT's as a function of the hit position along the slat.

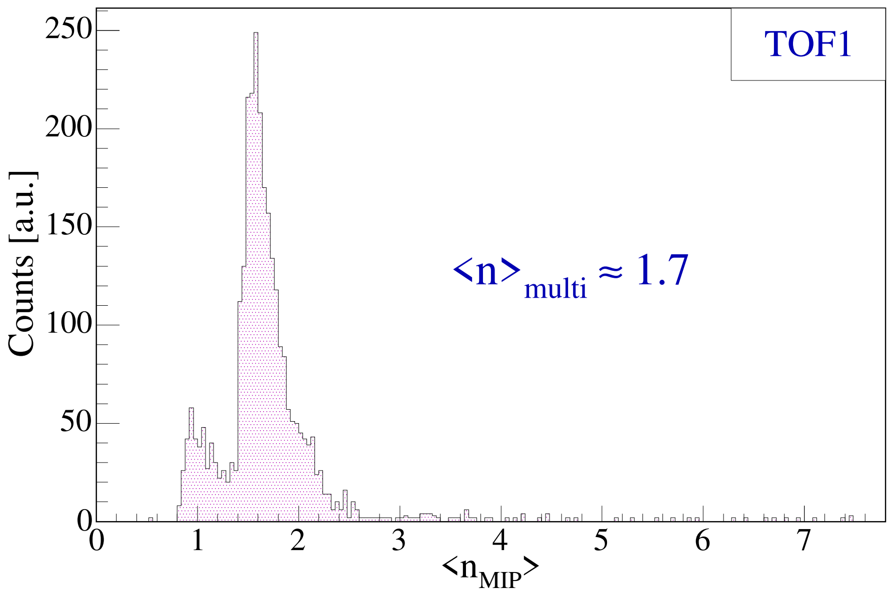

Fig. 4.43: Calibrated ADC of hits matching more than one track.

value greater than 1. However, there is a secondary peak at exactly 1. A possible explanation could be that the hits are matched with tracks that are either "ghosts" that could not be removed from ghostbusting, or tracks of uncertain direction, in which case they point to the wrong slat. It has been checked that for a given spectrometer setting, although the number of multiple matchings increase with the track density, the ratio between the height of the two main peaks remains constant. This would indicate that the geometrical uncertainty on the track direction is the most probable explanation.

PMT's Relative Offset : a New Matching Condition

The ADC gain calibration is used during all subsequent steps in order to select hits according to the following condition:

$$\langle \delta E \rangle \equiv \langle n_{MIP} \rangle > 0.5 \tag{4.39}$$

For the rest of the TOF calibration, the focus is on the TDC data. This section describes a calibration that leads to another condition for hit selection. Indeed, using notations of Fig. 3.12, the light propagation from the hit to the top (bottom) PMT takes a certain time $t_{top_\perp}$ ($t_{bot_\perp}$). Therefore, a correlation exists between the hit position y_{hit} and these times. If t_{top} and t_{bot} are the measured TDC digits, it follows that

$$t_{top} = \mathit{tof} + t_{top_\perp} + \mathit{off}_{top} + \mathit{slew}_{top} - t_{start} \tag{4.40}$$
$$t_{bot} = \mathit{tof} + t_{bot_\perp} + \mathit{off}_{bot} + \mathit{slew}_{bot} - t_{start} \tag{4.41}$$

where tof is the particle time of flight, t_{start} the common TDC start-time, $t_\perp$ the propagation time from the TOF hit to the PMT, off and slew the time offset and slewing effect. If one ignores the slewing effect and subtracts Eq. 4.40 to Eq. 4.41, then

$$t_{bot} - t_{top} = (t_{bot_\perp} - t_{bot_\perp}) + \left(\mathit{off}_{bot} - \mathit{off}_{top}\right) \tag{4.42}$$
$$\Delta t = \Delta t_\perp + \Delta_{\mathit{off}} \tag{4.43}$$

The scintillator used for the hodoscope slats is a highly homogeneous medium: the speed of the light traveling through is approximately constant within most of the scintillator slat. It is therefore called the effective speed of light c_{eff}. Given the slat height H, PMT's are connected at $y = \pm H/2$. Consequently:

$$t_{bot_\perp} = (H/2 + y_{hit})/c_{\mathit{eff}} \tag{4.44}$$
$$t_{top_\perp} = (H/2 - y_{hit})/c_{\mathit{eff}} \tag{4.45}$$
$$\Delta t = \frac{2}{c_{\mathit{eff}}} y_{hit} + \Delta_{\mathit{off}} \tag{4.46}$$

In practice, y_{hit} is given by the track–slat intersection along y (y_{track}). The calibrations of c_{eff} and Δ_{off} are based on profiles where Δt is correlated to y_{track} for each slat. Figure 4.44 illustrates the procedure. The bottom right panel of Fig. 4.44 shows how important the time offset between the top and bottom PMT's of a slat can be. At the same time, it is obvious that the effective speed of light cannot be determined with a high accuracy due to changes of the T2 drift velocity, unless the latter is well calibrated on a run by run basis. But since c_{eff} is a property of the scintillating material, a constant can be assigned to all slats and all runs. To prove such a statement, the same calibration is done to TOF2 with T5 tracks. By design, drift chambers are not affected by drift velocity change. Since TOF2 slats are made with the

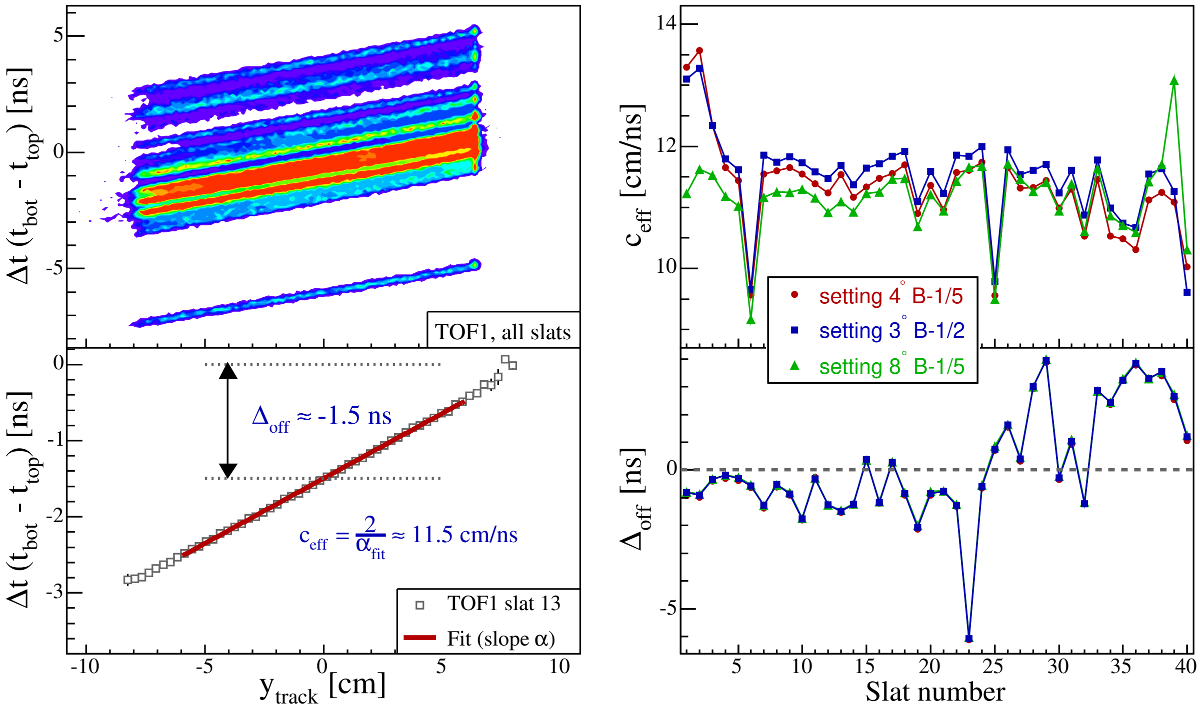

Fig. 4.44: Calibration of the effective speed of light and time offset between bottom and top PMT's in TOF1. The top right panel shows c_{eff} for three different spectrometer settings. Differences between settings are an artifact due to small changes of the T2 drift velocity.

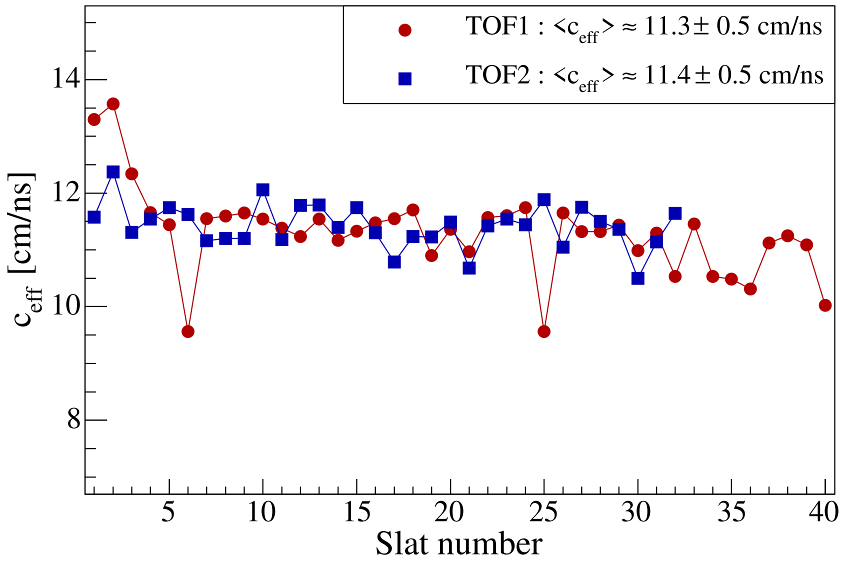

Fig. 4.45: TOF1 and TOF2 effective speed of light average. The average over the slat is very close to what is measured in TOF2 since slats are made of the same material (cf. Tab. 3.6).

same material, c_{eff} amounts to the value observed in TOF1. Figure 4.45 demonstrates the last statement.

In TOFW, the effective speed of light is $\sim 13.4\,\mathrm{cm/ns}$ (slats are made of a different scintillating material). The most important point of this calibration is the delay removal between the bottom and top PMT's on a slat by slat basis. The knowledge of c_{eff} and Δ_{off} leads to a new track–hit matching condition $|y_{track} - y_{hit}| / \sigma_{\Delta y} < n$ with $n = 3$ (user's cut). Figure 4.46 shows Δy distributions for all hodoscopes.

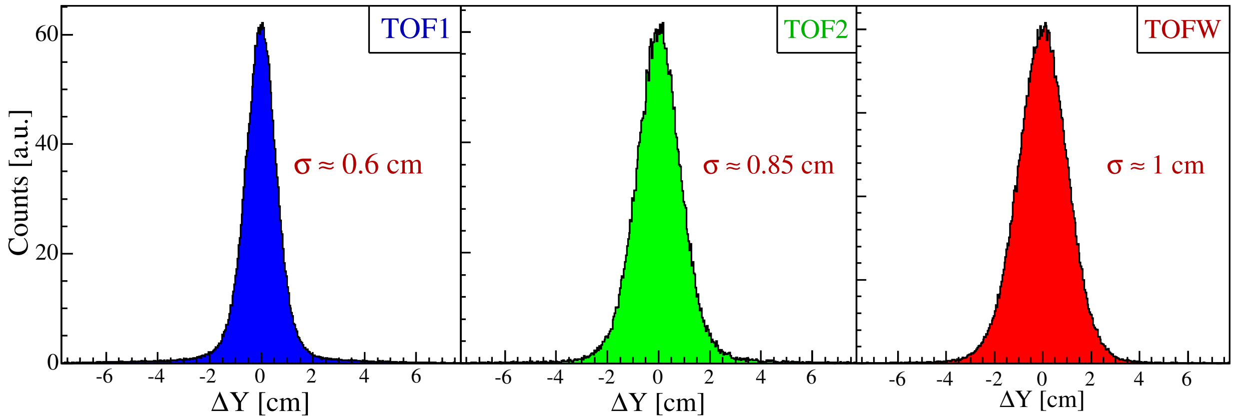

Fig. 4.46: Δy track - hit after relative delay and effective speed of light calibrations.

Time Offset

While time offsets between BBC tubes were calibrated relatively to an arbitrary time reference, the hodoscope time offsets are "absolute", i.e. the corrected TDC measurement leads to the particle TOF from the collision vertex to the hodoscope. Since BRAHMS is a collider experiment, it is almost impossible to remove time offsets by solely investigating raw time spectra due to the primary vertex and start–time spreads. The strategy is to use the track information: since most of detected particles are pions, an expected time of flight is calculated given the flight path L, the momentum p and the mass m_π:

$$t_{calc} = \frac{L}{c}\,\frac{\sqrt{p^2 + m_\pi^2}}{p} \tag{4.47}$$

The calculated time t_{calc} is compared to the experimental one, derived from Eq. 4.41 and 4.40. Ignoring the slewing effect, it follows that

$$tof + \sum_{bot}^{top} (t_{off} + t_\perp) = \frac{1}{2}\,(t_{top} + t_{bot}) + t_{start} \tag{4.48}$$

The term $\sum t_\perp$ is a constant and equal to H/c_{eff} (cf. Eq. 4.44 and 4.45). It can be safely included in $\sum t_{off}$, from now on called off_{slat}. Replacing tof by t_{calc} leads to

$$\mathit{off}_{slat} = \frac{1}{2}\,(t_{top} + t_{bot}) + t_{start} - t_{calc} \tag{4.49}$$

Histograms are filled with this quantity and fitted with a Gaussian function whose mean value is the time offset. Figure 4.47 shows time offsets as a function of slat in all hodoscopes.

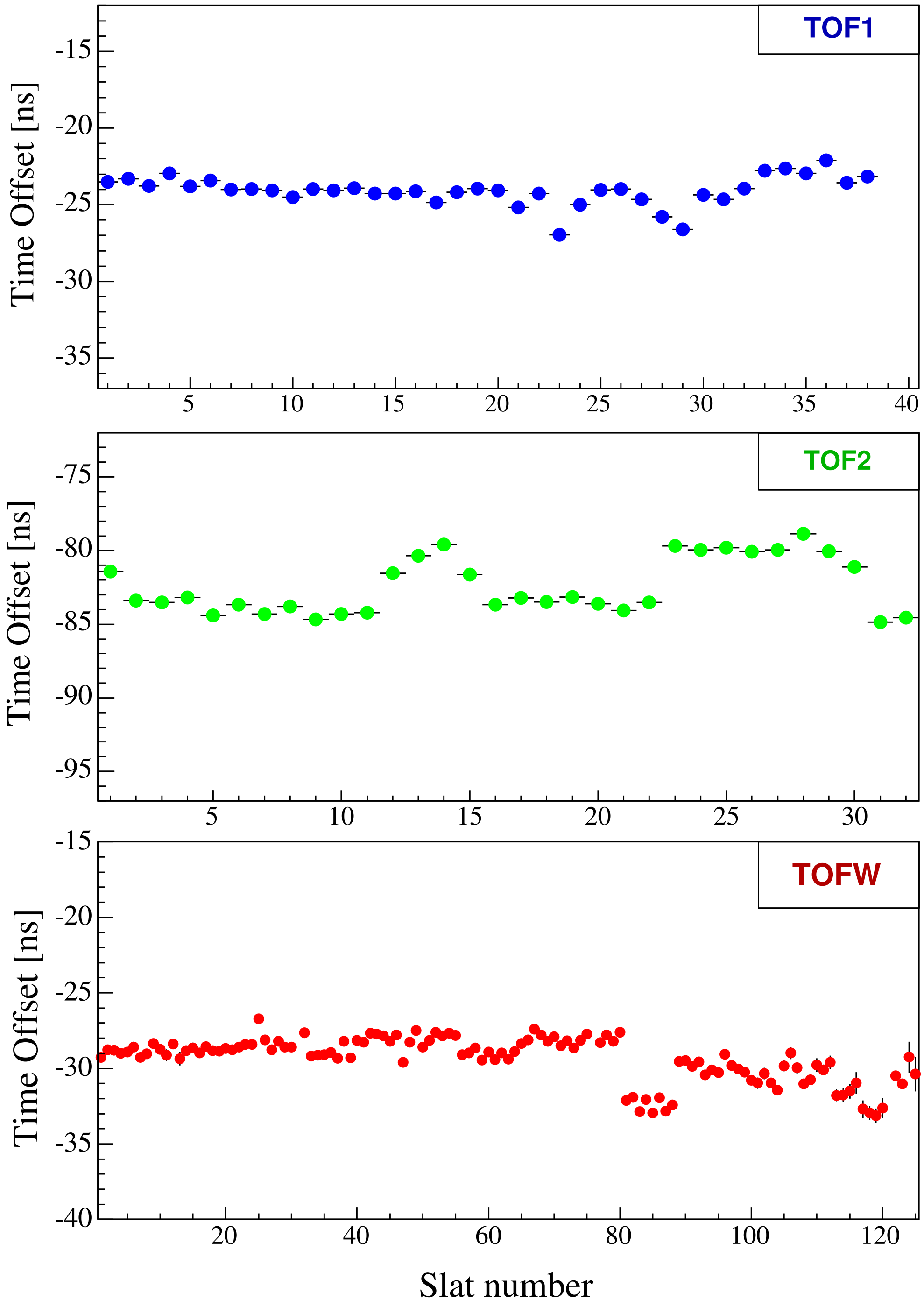

Fig. 4.47: Time offsets as a function of slat.

Slewing Correction

The TOF slewing correction algorithm is different from that of the BBC's. The profile procedure is complicated by the terms $t_\perp$. The slewing cannot be averaged between the top and bottom PMT's because the top and bottom analog pulses can have different amplitudes and therefore cross the discriminator threshold at slightly different times. Therefore, constructing a profile procedure for each PMT requires an accurate estimation of $t_\perp$ (either top or bottom). To remedy this difficulty, the slewing correction utilizes a minimization procedure based on the MINUIT package. The slewing effect is described as follows :

$$slew_{slat} = dt + \frac{1}{2}\sum_{top}^{bot} \frac{s}{\sqrt{ADC}} \tag{4.50}$$

There are therefore three parameters: s_{top}, s_{bot} and dt. The minimization is done for each slat on the following function:

$$\frac{\frac{1}{2}\left(t_{top} + t_{bot}\right) + t_{start} - \mathit{off}_{slat} - slew_{slat}}{t_{calc}} \tag{4.51}$$

The numerator of function 4.51 is ideally equal to t_{calc}. The result of this procedure is shown on Fig. 4.48 where the particle TOF is correlated to the calibrated ADC before and after slewing correction.

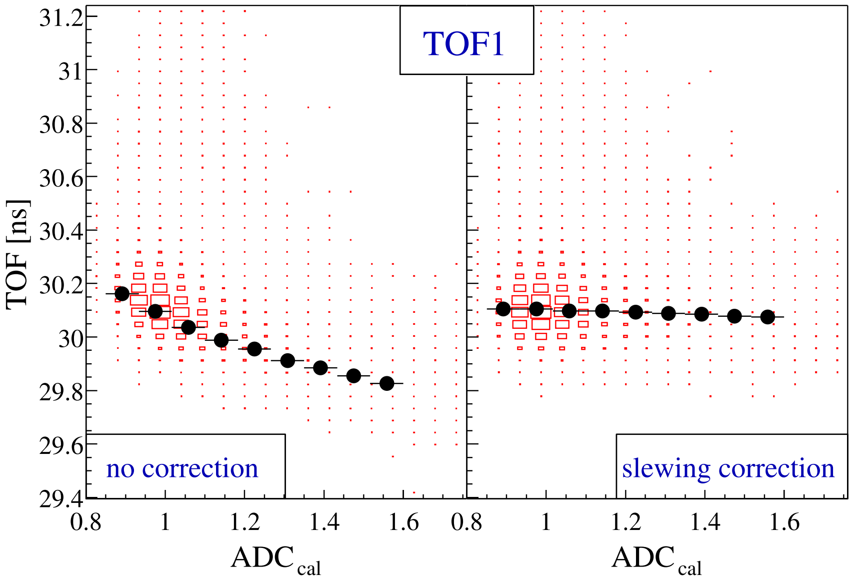

Fig. 4.48: Slewing correction in TOF1.

The remaining energy dependence visible in the right panel of Fig. 4.48 (black markers) is an artifact of the fit due the non uniform distribution of slow particles.

4.4.3 Particle Identification

The particle flight times are now fully determined. Using Eq. 4.1, the ability to identify particles is investigated by examining first how β correlates with p. The PID quality strongly depends on momentum, time and track path length resolutions. Due to the primary vertex/start–time and track vertex procedures, it can also be improved by eliminating secondary tracks produced far from the primary vertex, multiple TOF hits and uncorrelated track–TOF hit pairs. Figure 4.49 shows β vs p scatter plots with different quality cuts.

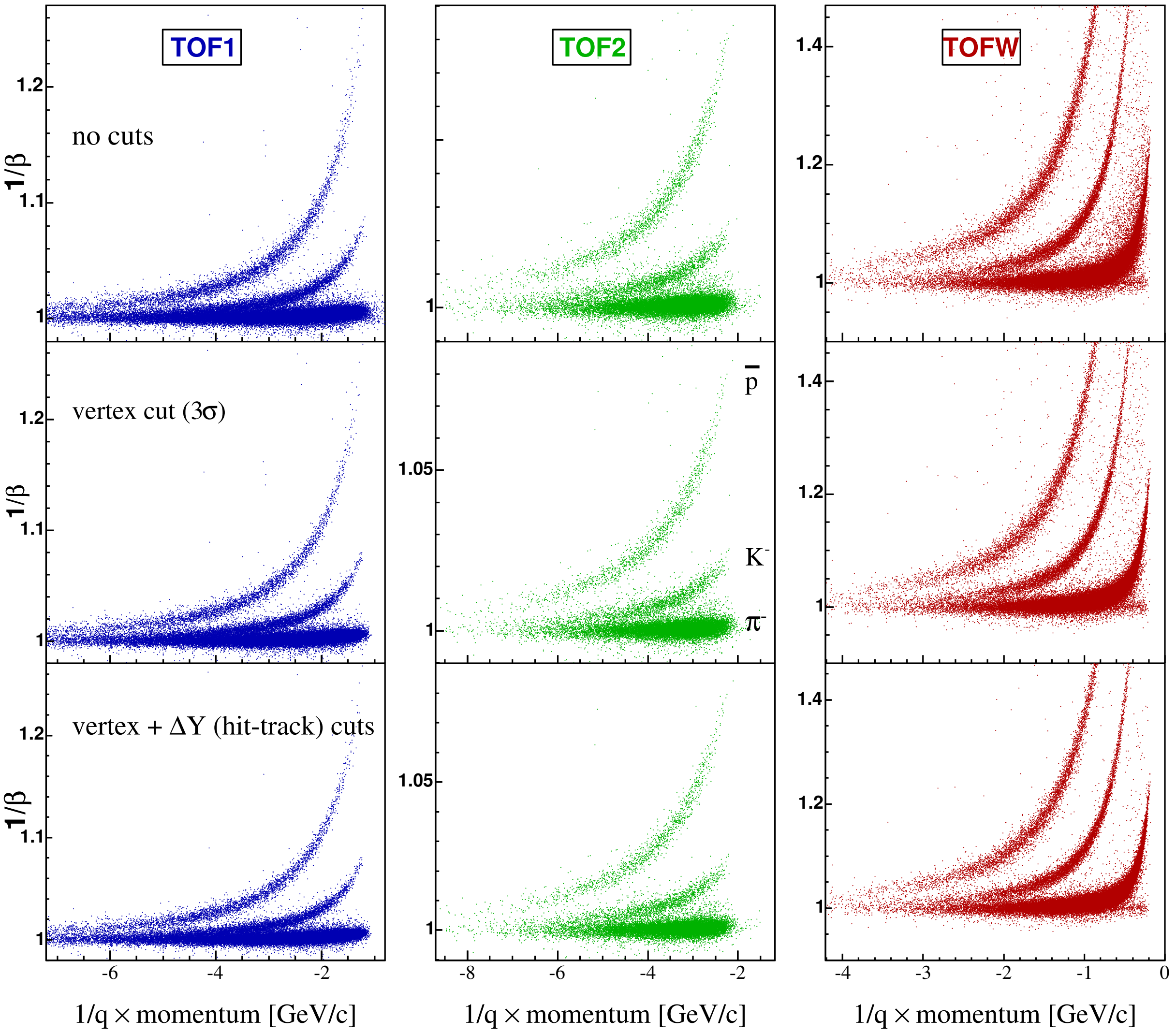

Fig. 4.49: Particle velocity versus momentum with different quality cuts. Note that $1/\beta$ and momentum ranges are different in the FS and MRS.

As can be seen from this figure, pions, kaons and protons are clearly separated until a momentum limit which is determined according to the PID resolution (see below). Figure 4.50 shows particle mass squared m^2 distributions from different spectrometer settings and momentum ranges. As expected, the m^2 resolution in the FS is better at relatively large angles ($\theta > 8°$) where the track density is lower. The same behavior is noticed in the MRS.Figure 4.51 shows the achieved TOF resolution in TOF1 as a function of slat for a few selected settings. Note that it is only a rough estimation. Indeed, the experimental measurement is in fact β, which primarily depends on L, t_{start}, t_{bot} and t_{top}. Since the vertex distribution is broad, so is the

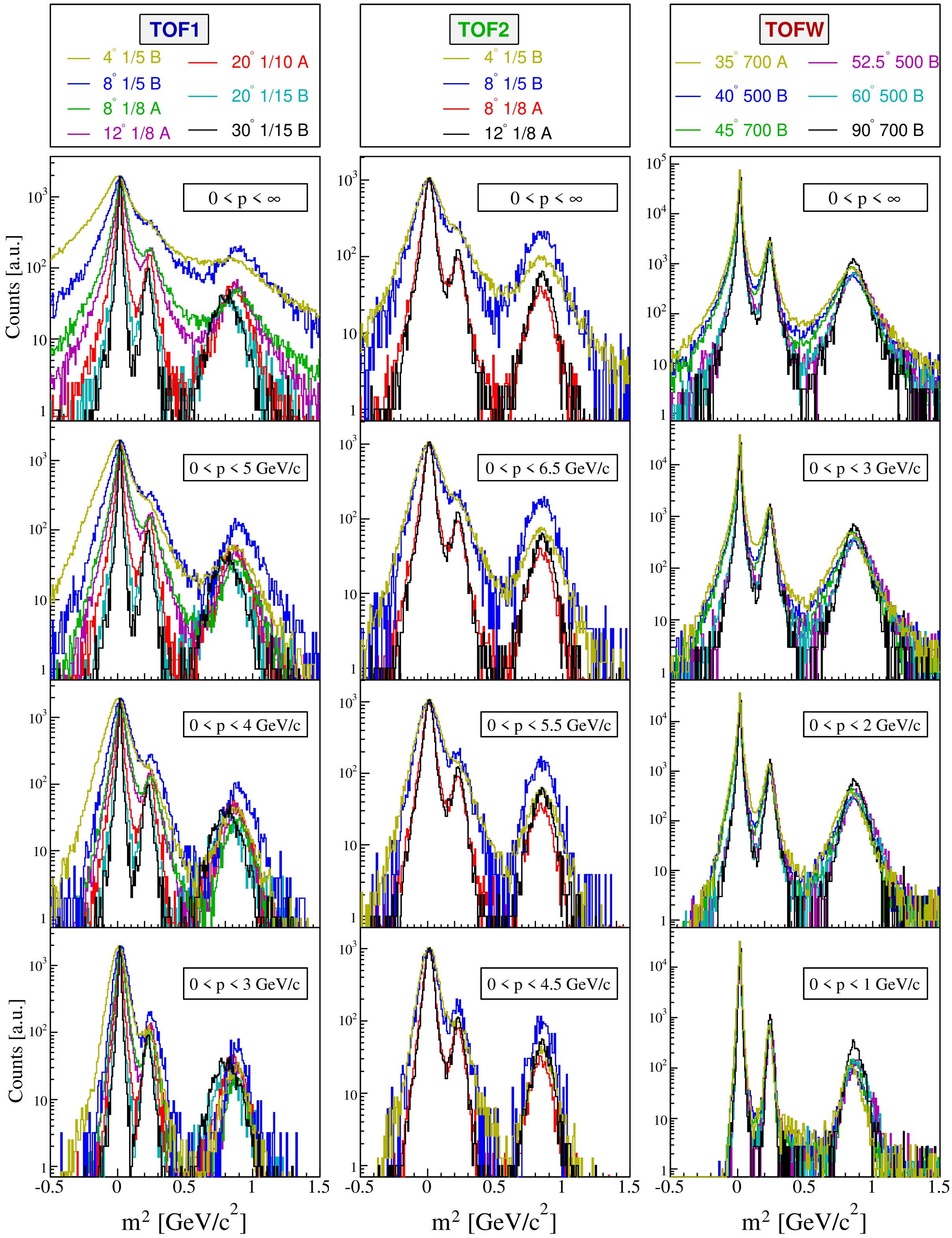

Fig. 4.50: Mass squared m^2 distributions as a function of spectrometer setting and momentum. Each colored distribution corresponds to particles from a setting with a given momentum range. Distributions were normalized according to the height of the pion peak. Field settings are detailed in Tab. 3.5.

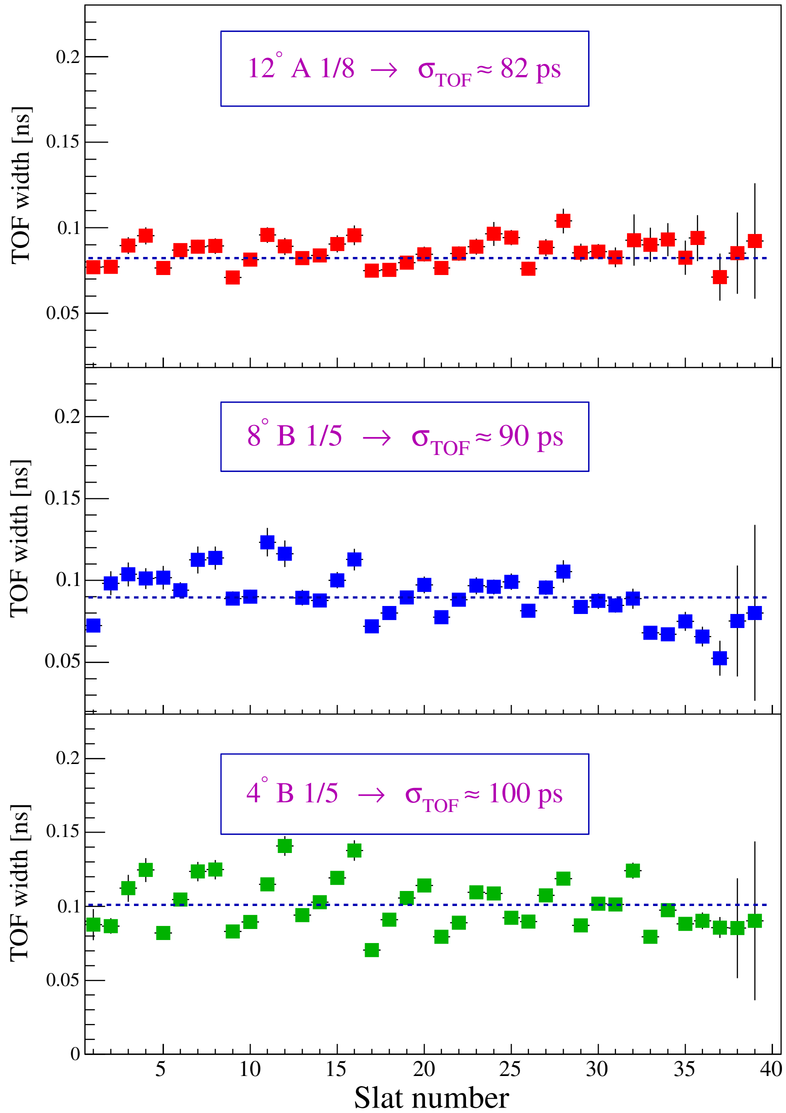

Fig. 4.51: TOF resolution as a function of slat in TOF1 for three different spectrometer settings. The resolution is better as the spectrometer angle increases (lower track density).

TOF distribution. Figure 4.51 shows the width of the time distribution evaluated by fixing the flight distance to 9 m without momentum cut (the distributions are dominated by pion velocities close to the speed of light). The dashed lines are zero polynomial fits.

It is also clear that the PID quality is momentum dependent. In order to quantify the PID resolution, the equation expressing the mass squared as a function of p and β is differentiated w.r.t. p and β. It then follows from error propagation that

$$\left(\frac{\sigma_{m^2}}{m^2}\right)^2 = 4\frac{\sigma_p^2}{p^2} + 4\gamma^4\,\frac{\sigma_\beta^2}{\beta^2} \tag{4.52}$$

If $\sigma_t \equiv \sigma_\beta^2/\beta^2$, $\sigma_p^2/p^2 = p^2\sigma_{ang} + (1 + m^2/p^2)\,\sigma_{mult}^2$ where σ_{ang} depends on track angular resolution and field setting, σ_{mult} takes into account multiple scattering (cf. [110]), Eq. 4.52

becomes (using $\gamma = E/m$)

$$\sigma^2_{m^2} = 4\left[m^4p^2\sigma^2_{ang} + m^4\left(1+\frac{m^2}{p^2}\right)\sigma_{mult} + (m^2+p^2)^2\sigma^2_t\right] \tag{4.53}$$

The m^2 versus p distributions are first sliced into narrow momentum intervals. Each slice is fitted with a Gaussian function in order to evaluate the slice width. The latter is plotted as a function of momentum and fitted with Eq. 4.53. An illustration of the resulting fits is given in Fig. 4.52.

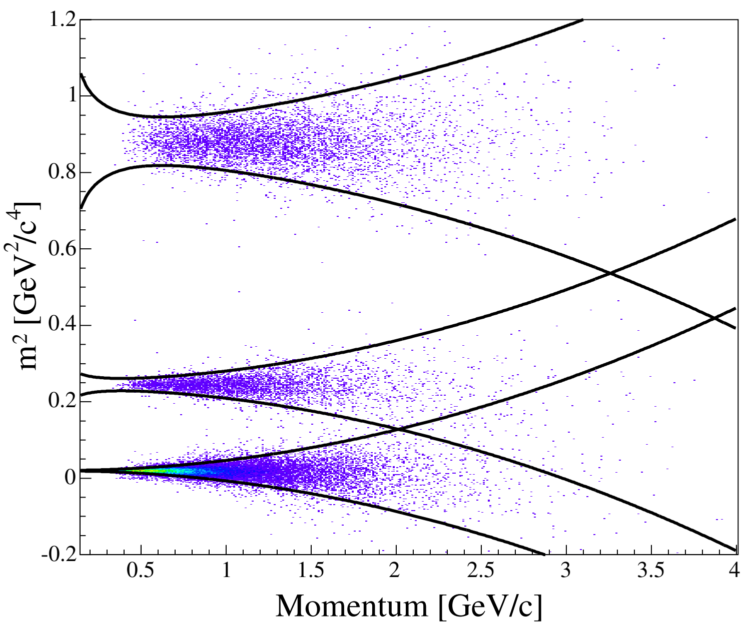

Fig. 4.52: Example of m^2 versus p resolution obtained by a simultaneous fit using Eq. 4.53. The data set is 90°B 1000 (MRS). The curves delimit a 2σ area.

The parameters σ_{ang}, σ_{mult} and σ_t are tabulated in Tab. 4.4 (FFS), 4.5 (BFS) and 4.6 (MRS).

FFS Setting	4°1/5	8°1/5	8°1/8	12°1/4	12°1/8
$\sigma_{ang} \times 10^2$	1.2	0.9	1.0	0.8	0.9
$\sigma_{mult} \times 10^2$	0.0	0.0	1.2	0.0	1.7
$\sigma_t \times 10^3$	3.7	3.1	2.9	2.9	3.0

Tab. 4.4: PID resolution parameters in the FFS.

The parameter σ_{mult} is often equal to 0 in the FS. This is due to the absence of low momentum particles in the data sets, unlike in the MRS.

4.5 RICH or the High Momentum PID

The RICH detects charged particles above a momentum threshold given in Tab. 3.7. The detection is based on the focusing of light cones into rings on a focal plane consisting of

BFS Setting	$4\,°1/5$	$8\,°1/5$	$8\,°1/8$	$12\,°1/4$	$12\,°1/8$
$\sigma_{ang} \times 10^2$	0.8	0.5	0.7	0.4	0.4
$\sigma_{mult} \times 10^2$	0.0	0.0	0.0	0.0	0.0
$\sigma_t \times 10^3$	1.8	1.6	1.6	1.6	1.5

Tab. 4.5: PID resolution parameters in the BFS.

MRS Setting	$90\,°350$	$90\,°1000$	$60\,°500$	$52.5\,°500$	$45\,°700$	$40\,°500$	$40\,°1000$	$35\,°700$
Polarity A								
$\sigma_{ang} \times 10^2$	3.1	0.01	1.4	0.9	1.3	1.7	1.1	1.1
$\sigma_{mult} \times 10^2$	2.7	2.9	2.2	2.4	1.8	2.5	1.3	2.1
$\sigma_t \times 10^3$	6.2	5.8	6.4	6.4	7.5	8.8	8.8	8.6
Polarity B								
$\sigma_{ang} \times 10^2$	3.1	1.5	1.6	1.6	0.8	1.5	1.2	1.9
$\sigma_{mult} \times 10^2$	2.6	0.7	2.3	2.2	1.8	2.4	1.0	2.2
$\sigma_t \times 10^3$	6.0	6.6	6.5	6.4	7.8	8.6	8.2	8.5

Tab. 4.6: PID resolution parameters in the MRS.

PMT's. When correlated to the momentum, ring radii allow particle identification up to high momentum limits. It is also possible to use the RICH as a particle veto in certain cases. The RICH is described in details elsewhere [111]. This section only reviews the PID algorithm and performance.

4.5.1 Light Focusing

When a charged particle above momentum threshold emits light inside the RICH gas of refractive index $n = 1.00202$, the light is focused on the spherical mirror and reflected to the PMT plane oriented at twice the mirror focal angle ($2 \times 9\,°$) and located at a distance equal to the mirror focal length (150 cm). Figure 4.53 shows the light focusing geometry.

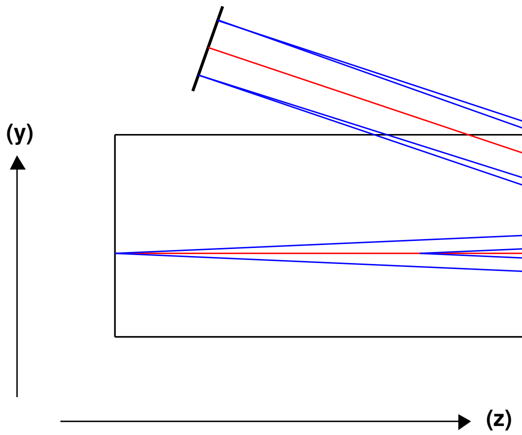

Fig. 4.53: Light focusing in the RICH. The track path is drawn in red (but it is not physically reflected to the image plane), sample photon paths are shown in blue.

The high segmentation of the image plane allows the construction of photon rings. Each PMT pixel can induce an ADC signal whose value depends on the number of photons detected. With a proper ADC pedestal calibration, hits are selected if their ADC digit is above a threshold of 3.5 times the pedestal width above pedestal. Fired pixels are then investigated by the ring finding algorithm described in Fig. 4.54.

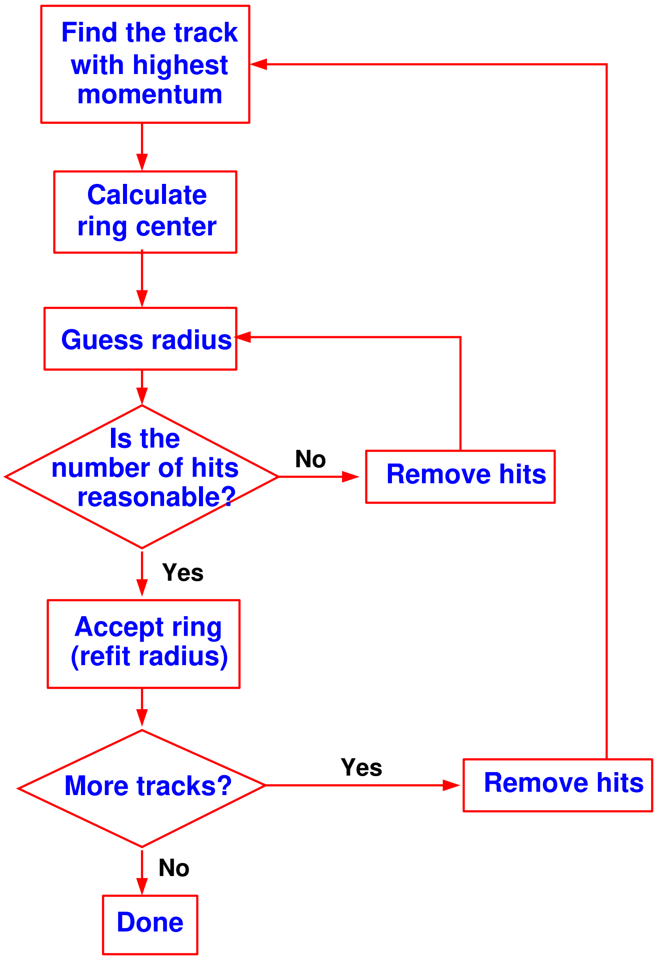

Fig. 4.54: RICH PID algorithm diagram.

This algorithm works if the intersection of the reflected track line with the focal plane is within the pixel area. The left panel of Fig. 4.55 shows these intersection points in a typical run. A ring is shown in the right panel of Fig. 4.55 where the black box areas are proportional to the magnitude of the ADC value. Once rings are measured, the PID is done by utilizing the following equations:

$$\theta_c = \arctan \frac{r}{L_{foc}} \tag{4.54}$$

$$\frac{1}{\beta} = \frac{\sqrt{p^2 + m^2}}{p} = n \cos \theta_c \tag{4.55}$$

where L_{foc} is the focal length of the spherical mirror. Hence, there exists a direct relation between the ring radius r, the momentum p and the mass m.

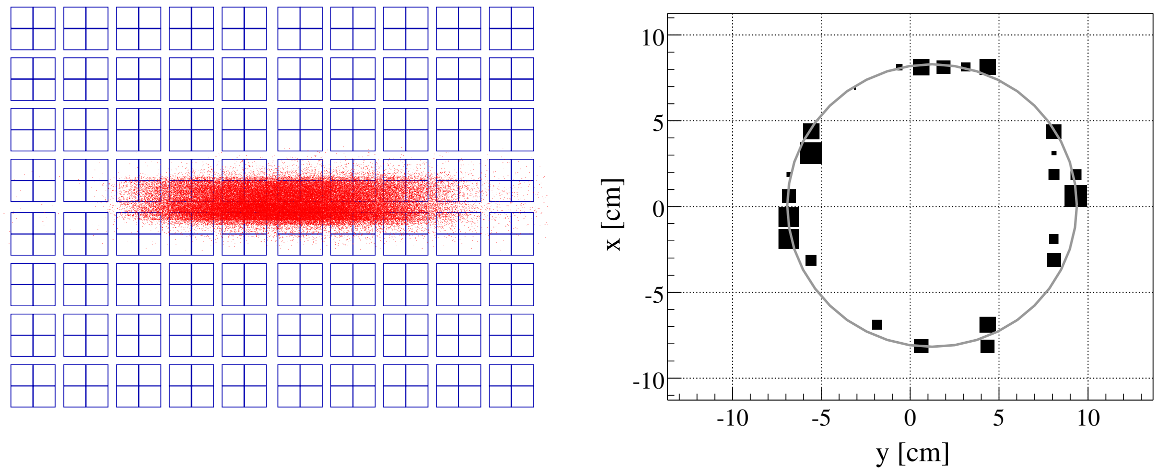

Fig. 4.55: Ring centers defined as the reflected track line intersection with the pixel plane (left) and a typical ring (right).

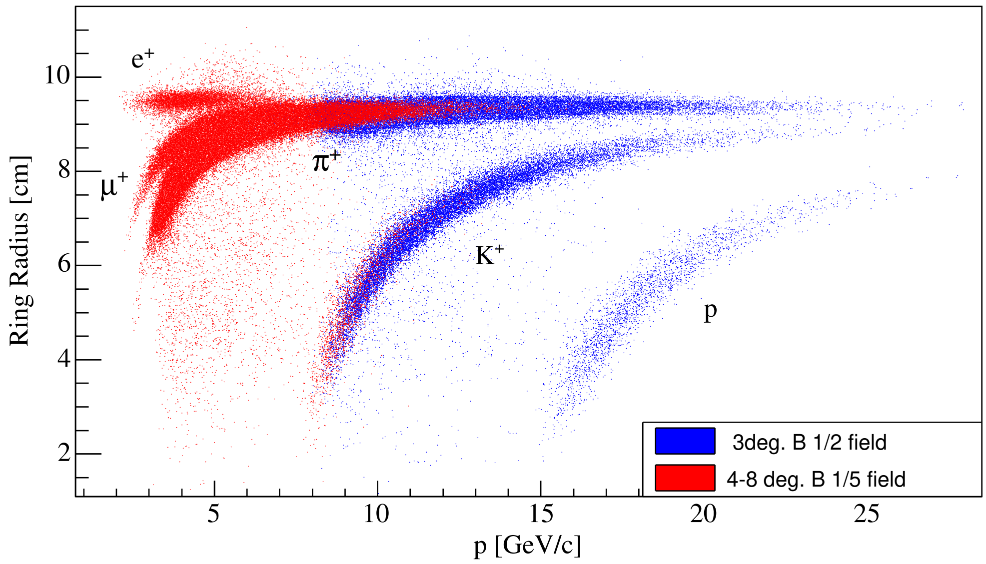

Fig. 4.56: RICH ring radius versus momentum.

4.5.2 PID Performance

Figure 4.56 shows such a correlation for two different field settings (low and high field). It shows an excellent separation between pions and kaons up to $\sim 25\,\mathrm{GeV/c}$. In the low momentum region, muons and electrons can also be identified up to $\sim$ 4-5 GeV/c. Figure 4.57 shows the mass squared distributions obtained from the RICH. In the low field setting, the RICH

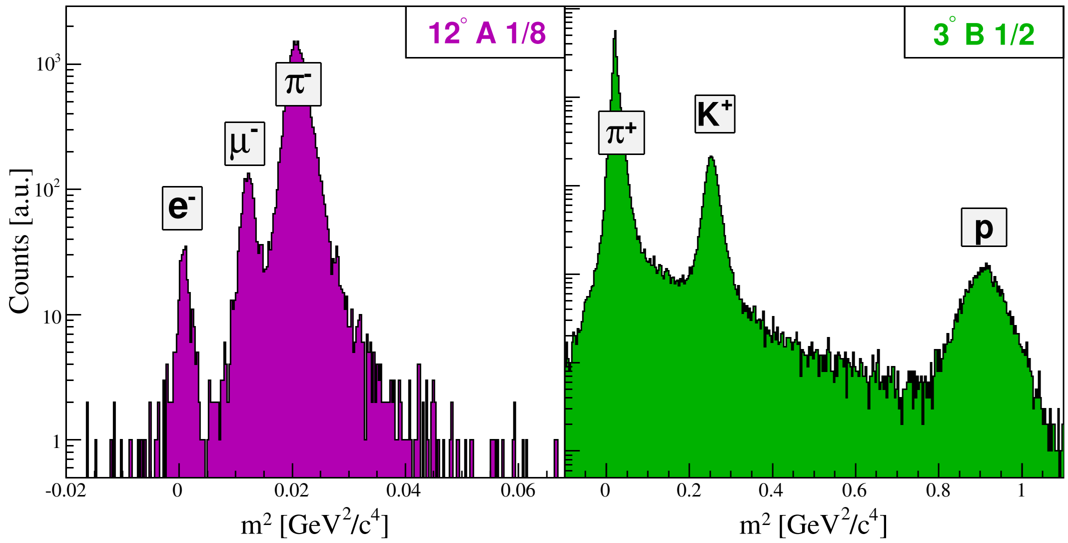

Fig. 4.57: RICH mass squared distributions obtained from two different data sets.

identifies e, μ and π but not kaons and protons. Those are positively identified when the field is high enough for measuring particles above Čerenkov threshold. At the same time, the muon and electron separation is not evident if $|p| \gtrsim 4 - 5\,\mathrm{GeV/c}$. Note also the background. It corresponds to uncorrelated track–radius combinations. The background contamination is evaluated when particle spectra are constructed. This topic is described in the next chapter.

♣♣♣♣♣♣

Chapter 5

Particle Spectra

This chapter describes the many steps necessary to construct normalized spectra. The emphasis is on spectra of charged pions and kaons. Particle spectra are built by combining data sets that are collected at various angle and field settings. From each set, data are first selected and corrected for various experimental biases, before being combined with other sets in order to form spectra at well defined rapidity intervals as a function of transverse momentum. These analysis steps are:

$\rightarrow$ Data selection (events, tracks and PID)
$\rightarrow$ Corrections (detector efficiency, geometrical acceptance, secondary reactions)
$\rightarrow$ Normalization (data set combining and weighting)

5.1 Event Selection

5.1.1 Centrality and Trigger

The selected events are trigger 6 events, as defined in Sec. 3.3.4 and Tab. 3.3. This trigger is based on an energy threshold in the tile multiplicity array (TMA) corresponding to the $\sim 20\%$ most central events, and a beam–beam vertex restriction consisting of a narrow time difference between left and right arrays, corresponding to $|vtx| \lesssim 25\,\mathrm{cm}$. Trigger 6 events have not been down–scaled during data collection, meaning that all events fulfilling the trigger condition have been recorded. The centrality distribution of such events is shown in Fig. 5.1. The distribution is rather flat from 0% to $\sim 20\%$ and drops rapidly for more peripheral events due to the trigger definition, as expected from the TMA energy requirement. The centrality slices 0–5%, 5-10% and 10–15% contain approximately the same number of events, the difference between the most central class (0–5%) and the 10–15% class amounts to $\sim 5\%$. It shows that the centrality determination has a minimum relative error of 5% when trigger 6 events are selected. The analysis concentrates on the top 5% events only.

5.1.2 Collision Vertex

A cut on the location of the collision vertex must also be done. This selection is defined as a $\pm 3\sigma$ cut around the mean difference between the independent ZDC and BBC vertex measurements. It is motivated by the fact that requiring a good correlation between both measurements assures that well defined events in terms of vertex but also TDC start-time are selected. Figure 5.2 illustrates the vertex consistency cut. The number of events with

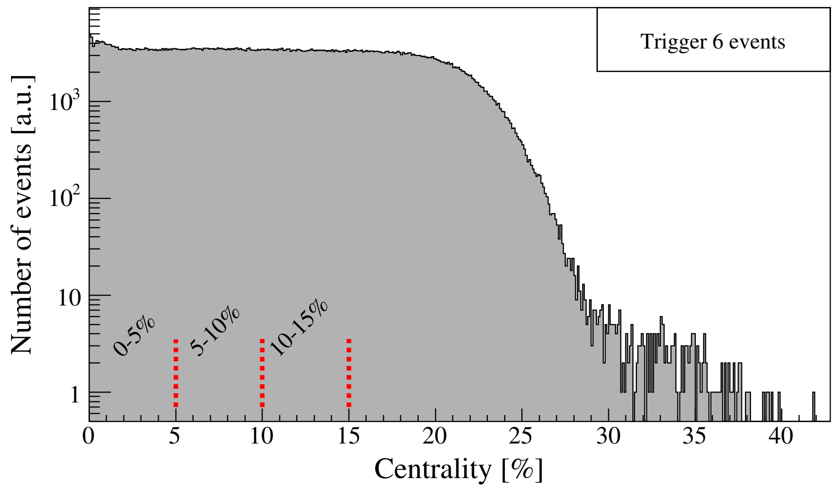

Fig. 5.1: Centrality distribution of trigger 6 events.

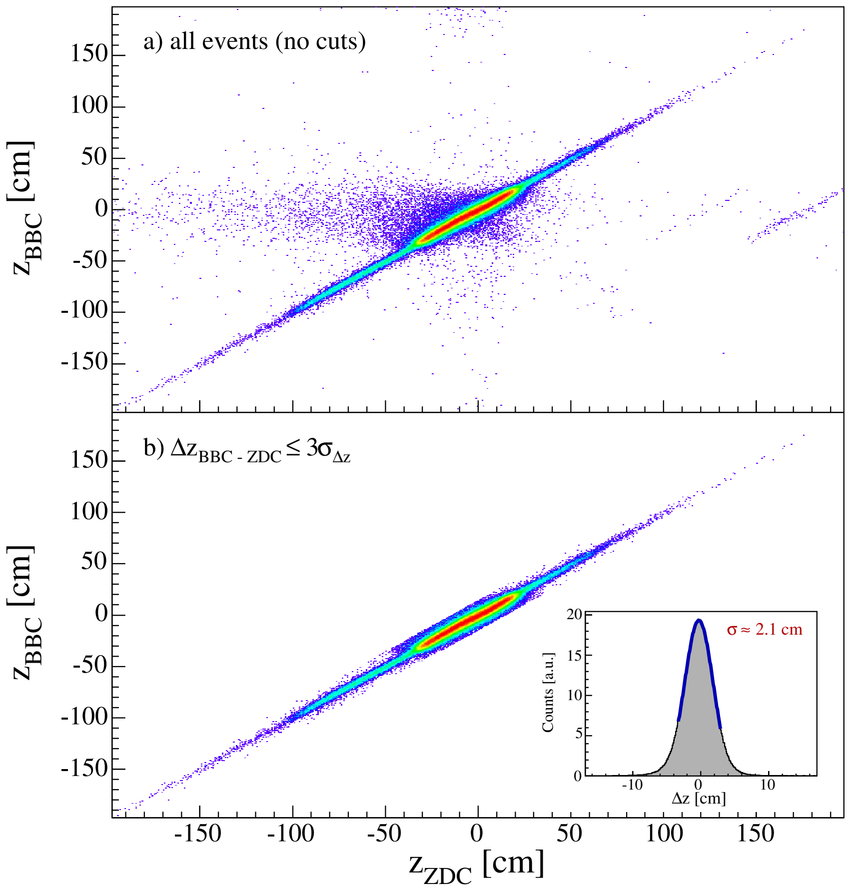

Fig. 5.2: Correlation between the BBC and ZDC vertex measurements. The top panel shows all events, the bottom panel shows the effect of a 3σ cut based on a Gaussian fit on the vertex difference (small panel).

inconsistent vertex measurements, rejected by this cut, amounts to 1% of the total number of events. A final cut has been applied to the vertex distribution itself: only events with $|vtx| < 20\,(15)$ cm for the FS (MRS) analysis are kept due to an efficiency decrease of the trigger 6 beyond these limits. This cut is also motivated by the spectrometer acceptance correction, as explained in Sec. 5.4.3. The difference between the MRS and FS is due to a larger acceptance of the FS. The effect of this cut is shown on Fig. 5.3.

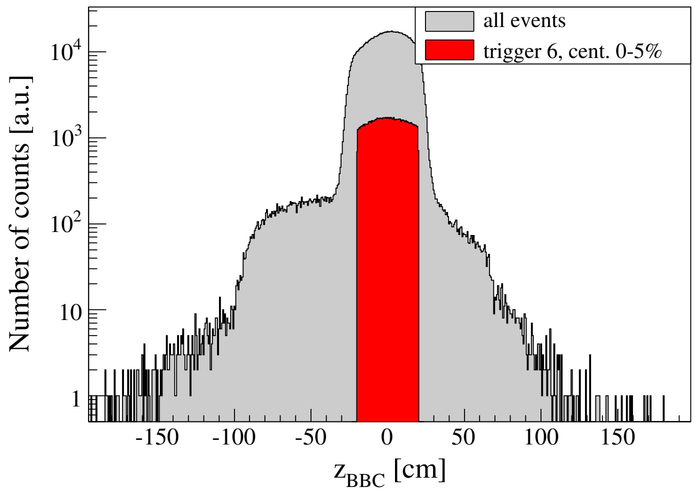

Fig. 5.3: Vertex distribution as measured by the BBC with and without a 0%–10% centrality cut and a user cut of [-20 cm, -20 cm]

5.2 Track Selection

The track selection aims at removing background tracks or tracks too close to the magnet sides. The selection is done by introducing magnet fiducial cuts, checks of momentum status and track vertices.

5.2.1 Cuts in the Magnet Gaps

Magnet fiducial cuts forbid a volume around the physical magnet gap where the confidence on track combination is low due to track direction uncertainties, especially along the y direction because the drift velocity close to the TPC edges is not perfectly uniform. A width of 1 cm is removed from the gap sides – x and y axes of the magnet gap – uniformly along the longitudinal axis z (in the local coordinate system of the magnet). This forbidden volume is taken into account when spectrometer acceptance corrections are calculated. Figure 5.4 illustrates typical fiducial cuts in D5. As seen in Fig. 5.4, some of the rejected tracks are within the selection area. This is because the fiducial cut is applied along the whole volume. Therefore, some tracks already rejected close to the front plane of D5 and transported geometrically to the magnet back plane fall within the selection area.

As mentioned in Sec. 4.3.2, trajectories of tracks that survived track ghostbusting (cf. Fig. 4.28) and fiducial cuts are extrapolated from T1 to the entrance plane of D1 (facing the collisions) by using the track momentum and D1 field, because there is no tracking device at the front

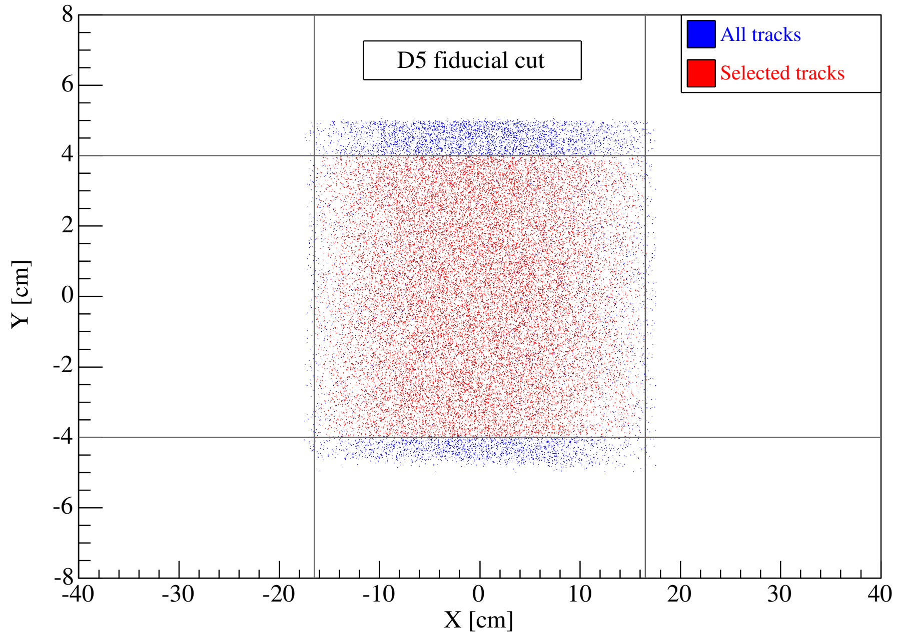

Fig. 5.4: Magnet fiducial cuts in D5. Dots are track intersections with the effective edge back plane of D5.

of D1. Tracks are not selected for the analysis if they intersect the magnet gap sides. The relative fractions of tracks removed by such cuts are tabulated in Tab. 5.1 and 5.2 for a few spectrometer settings.

FS setting	12 °A 1/8	12 °B 1/4	8 °B 1/5	4 °B 1/5	3 °B 1/3	3 °B 1/2
D2 ghost (%)	0.17	0.13	1.54	0.38	2.15	1.55
D2 fiduc. cuts (%)	3.91	7.84	8.42	9.48	10.23	10.53
D1 swim status (%)	10.87	8.76	11.62	7.32	8.38	8.20

Tab. 5.1: Fraction of tracks removed by the different magnet cuts in the FFS. The ghost track fraction is evaluated with tracks within the matching parameter cuts (cf. Sec. 4.3.2). The fiducial cut fraction is evaluated w.r.t. tracks that survived the ghostbusting. The fraction of tracks extrapolated back through D1 and that hit the magnet sides, are calculated w.r.t. tracks that survived all D2 cuts.

As can be seen from Tab. 5.1, the fraction of tracks removed from the D2 fiducial cuts is growing with decreasing spectrometer angle and increasing magnetic field. The status check in D1 also implies a stringent cut. In the MRS, the D5 fiducial cut removes $\sim 20\%$ of tracks regardless of the setting while the ghost track removal is more important as the spectrometer angle decreases (track density dependence).

MRS setting	90 °B 1000	60 °B 500	45 °A 700	35 °A 700	30 °B 700 (back)
D5 ghost (%)	0.18	0.52	1.12	1.49	0.48
D5 fiduc. cuts (%)	22.05	21.66	22.43	19.55	21.17

Tab. 5.2: Fraction of tracks removed by the different magnet cuts in the MRS.

The total fraction of tracks removed is quite large due to the small geometrical acceptance of the magnets compared to that of the tracking device. Moreover, the width of the fiducial cuts is 1 cm from the sides in both the x and y directions of the magnets. Therefore, the fraction of the magnet volume outside the fiducial cuts is 24.6% of the total magnet volume for D5, 10.4% for D4, 12.5% for D3 and 20.5% for D2 (no fiducial cuts in D1).

5.2.2 Track Vertex Selection

A fraction of the particles detected by the spectrometers come from sources other than the primary collisions. By comparing the track vertex (as defined in Sec. 4.3.3) with the primary vertex, it is possible to reject most of these secondary particles. Figure 5.5 shows the selection procedure. For both FS and MRS, a peaked distribution of track intersections centered around

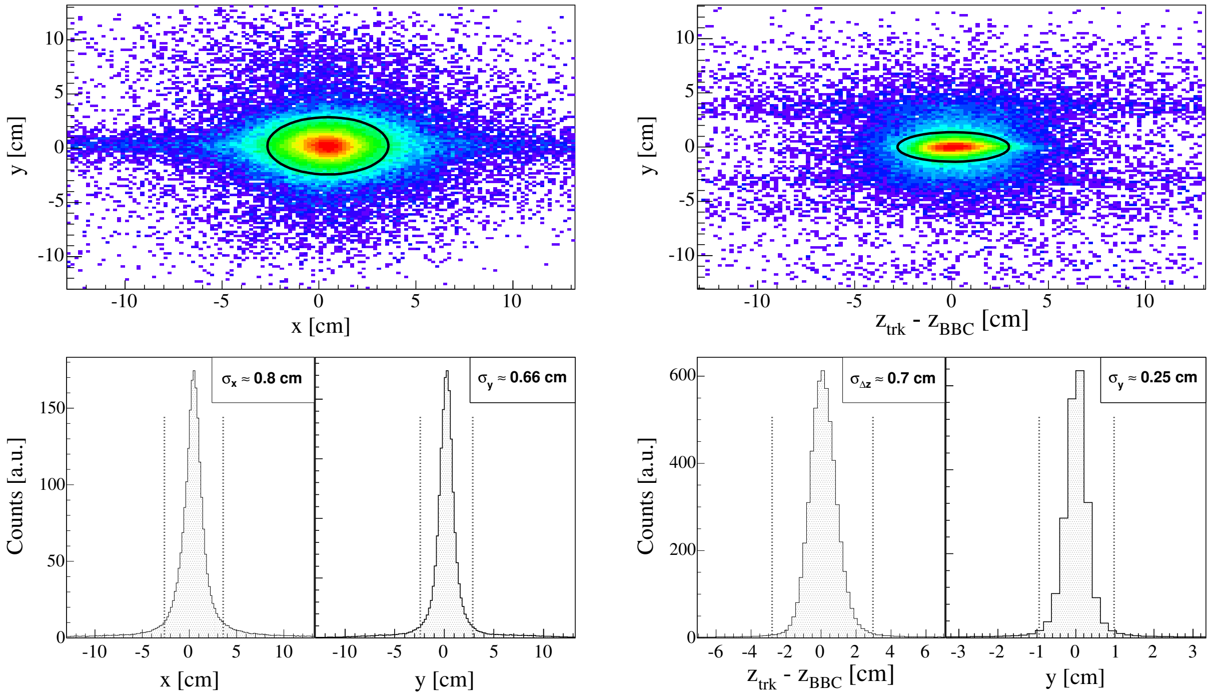

Fig. 5.5: Intersection of particle track lines with primary vertex planes in the FS (left), and MRS (right). A 4σ cut is applied (elliptical cut).

the collision vertex is obtained. The projections on the axes are fitted with Gaussian functions whose means (x_{off}, Δz_{off}, y_{off}) and widths (σ_x, $\sigma_{\Delta z}$, σ_y) are used to apply a two dimensional elliptical cut, based on the inequalities

$$\left(\frac{x - x_{off}}{\sigma_x}\right)^2 + \left(\frac{y - y_{off}}{\sigma_y}\right)^2 \leq n_\sigma^2 \quad \text{(FS cut)} \tag{5.1}$$

$$\left(\frac{\Delta z - \Delta z_{off}}{\sigma_{\Delta z}}\right)^2 + \left(\frac{y - y_{off}}{\sigma_y}\right)^2 \leq n_\sigma^2 \quad \text{(MRS cut)} \tag{5.2}$$

where x, y, z refer to the laboratory frame, the subscript *off* means offset (these offsets are mostly present along the y axis due to TPC drift velocity fluctuations) and n_σ is the user cut, set to 4 for this analysis. Note also that the cut is applied on a run by run basis in order to minimize the effect of the fluctuations in y.

5.3 PID Cuts

Once particle tracks are selected, PID cuts are applied in order to select pions and kaons over the broadest momentum range that the PID resolution allows. In the MRS, PID cuts are based on the m^2 resolution achieved by TOFW. In the FS, beside the TOF PID, the RICH is used in two ways: positive K and π identification, and π veto to improve kaon selection in H2, as explained below.

5.3.1 Time of Flight

Two methods have been investigated for the MRS. One is based on the PID resolution presented in Sec. 4.4.3. The other consists of applying a fixed cut in the m^2 distributions. In both cases, particles with momenta $|p| > 2\,\mathrm{GeV/c}$ were ignored as this is the limit of the PID capabilities. Figure 5.6 shows how both methods compare on two different data sets ($90\,^\circ$ and $35\,^\circ$) where the PID performance are slightly different because of a larger background at $35\,^\circ$. In the momentum dependent selection, the selection is based on Eq. 4.53 and parameters tabulated in Tab. 4.6. Curves drawn in Fig. 5.6 correspond to a 2σ cut around the mean mass squared as a function of momentum. At $90\,^\circ$ the difference in the number of pions (kaons) amounts to 5.5% (5%). Considering that a 2σ cut around the mean of a Gaussian function represents 95.5% of its integral, the background introduced by the fixed m^2 cut represents 1% (0.5%). At $35\,^\circ$ the difference is 8% (6%), implying a background of 3.5% (1.5%). Other MRS settings are in–between these two cases. The apparent asymmetry of the kaon sample is due to pion contamination at relatively high momentum (the π and K 2σ areas overlap above 1.7 GeV/c at $35\,^\circ$). It is estimated by reflecting the clean half of the kaon distribution and calculating the quantity $\left(N_{\frac{1}{2}real} - N_{\frac{1}{2}ref}\right)/N_{tot}$. It amounts to less than 1% (4%) at $90\,^\circ$ (35°) for both procedures. In conclusion, the momentum dependent cut is preferred in general because less background is introduced, and the method takes into account the momentum dependent resolution of the PID. Note also the crossing of the curves at $p \sim 1.7\,\mathrm{GeV/c}$ for the $35\,^\circ$ setting. Particles between this momentum limit and 2 GeV/c do not affect the final results.

In the FS, a momentum dependent 2σ cut was applied to TOF1 and TOF2 data where PID was possible (low field settings), based on parameters listed in Tab. 4.4 and 4.5. The momentum limit is 3(4.5) GeV/c for TOF1 (TOF2). The m^2 distributions obtained from these cuts are shown in Fig. 5.7 for a couple of settings. The $3\,^\circ$ and $4\,^\circ$ settings have been in general ignored due to a large background in the hodoscope except low momentum pions in TOF2 at $4\,^\circ$.

5.3.2 Čerenkov

As could be seen before, TOF PID is only possible to relatively low momentum. Higher momentum particles are identified with the RICH. Figure 5.8 shows the selection (delimited by solid curves) . The dashed curves are the expected ring–radius vs momentum. correlation for pions and kaons.
The expectation curves are defined by the following equation:

$$r = L\,\tan\left[\cos^{-1}\frac{1}{n}\sqrt{1+\frac{m^2}{p^2}}\right] \tag{5.3}$$

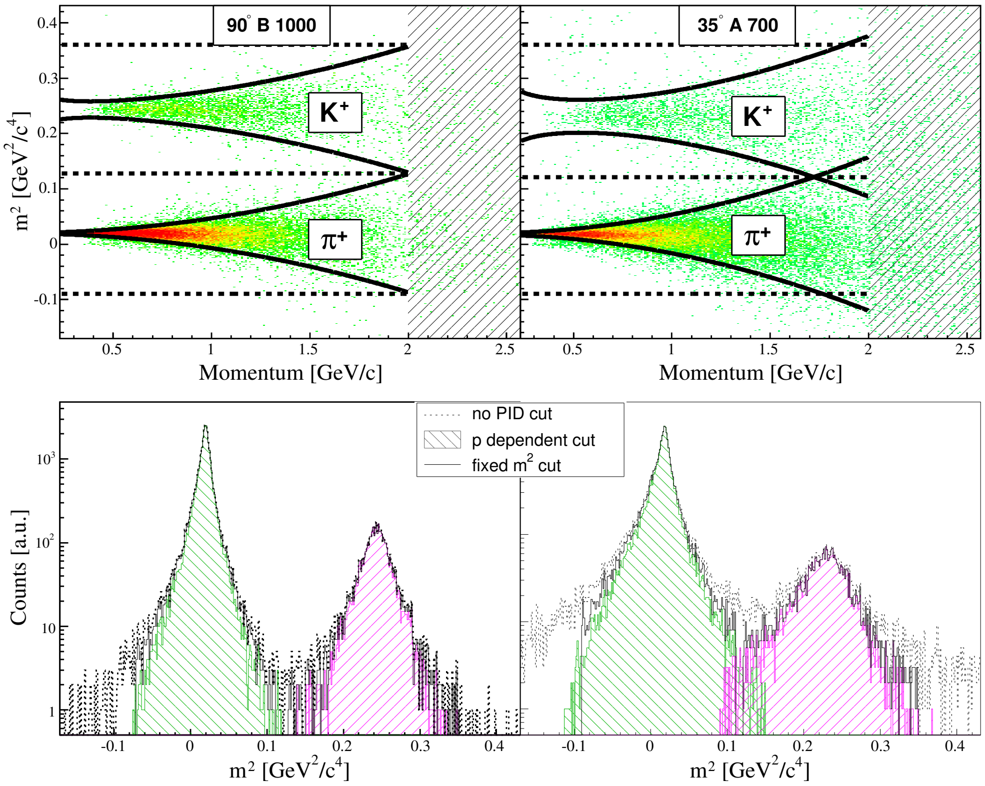

Fig. 5.6: Pion and kaon selection in the MRS at 90 ° (left) and 35 ° (right). The momentum dependent curves delimit a 2σ area around the mean mass squared.

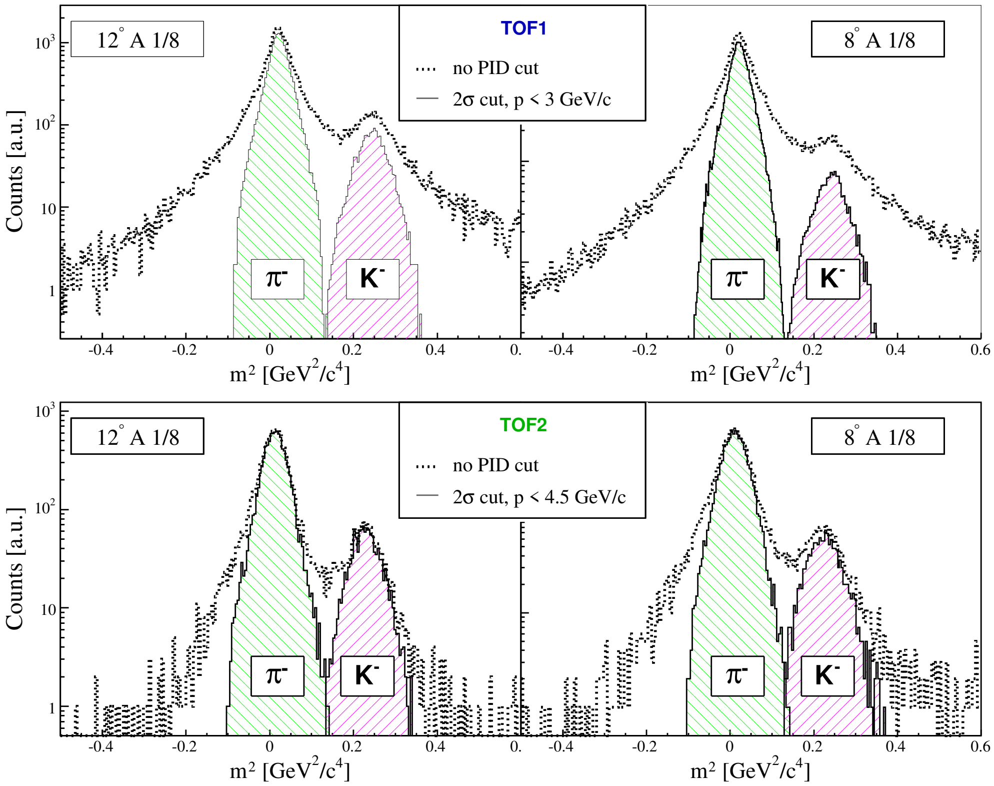

Fig. 5.7: Pion and kaon selection in the FS at 12 ° (left) and 8 ° (right). The selected particles are restricted to a momentum dependent cut of 2σ around the mean mass squared. The upper momentum limit is 3 (4.5) GeV/c in the FFS (BFS), upper and lower panels respectively.

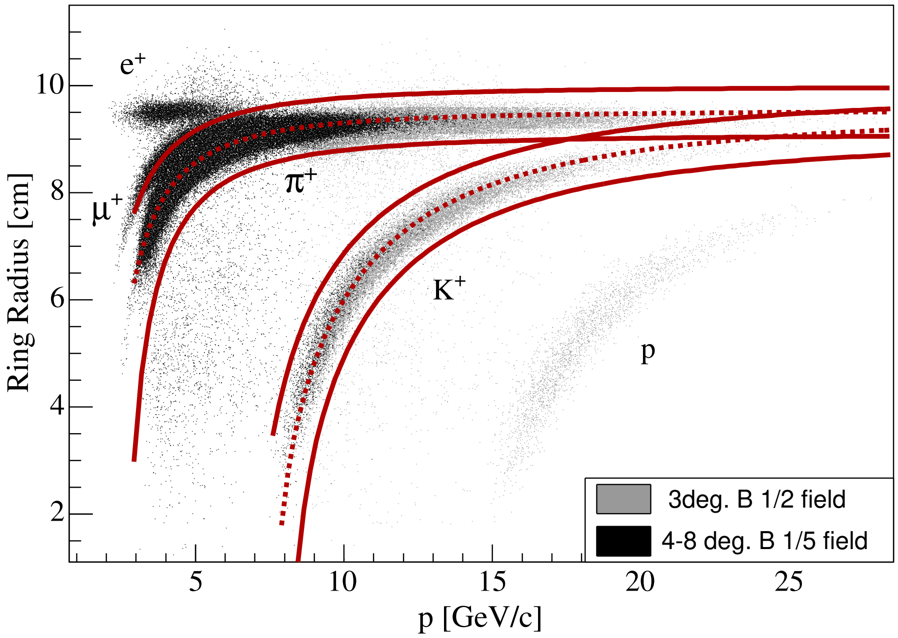

Fig. 5.8: RICH PID selection. Solid curves are defined by Eq. 5.4 and 5.5 (see text). The dashed lines are expected ring radius–momentum correlations.

where r is the ring radius, L the focal length of the spherical mirror, n the index of refraction of the gas, m the mass of the particle and p its momentum. The calculation of the selection envelop is based on the following equations:

$$r_+ = L \tan\left[\cos^{-1}\frac{1}{n}\sqrt{1+\frac{m^2}{(p+\delta p)^2}}\right] + \delta r \tag{5.4}$$

$$r_- = L \tan\left[\cos^{-1}\frac{1}{n}\sqrt{1+\frac{m^2}{(p-\delta p)^2}}\right] - \delta r \tag{5.5}$$

The ring radius is assumed to have an uncertainty $\delta r = 0.45\,\mathrm{cm}$. The values for δp are 0.4 and 0.6 GeV/c for pions and kaons respectively. They "mimic" the RICH PID resolution but rather consist of guesses of the PID performance. The method can be further improved by introducing resolution parameters that depend on the track momentum and the number of photons of Čerenkov rings. Figure 5.9 shows the mass squared (m^2) measured by the RICH before and after this cut is applied.

The RICH particle selection applied to the data presented in this thesis is little contaminated by the background seen in Fig. 4.57. The background has been estimated as a function of momentum, as can be seen in Fig. 5.10. It is found that the background falling inside the PID cut is less than 1% over the entire momentum range, and decreases with increasing momentum. The RICH is also used to extend the kaon selection in TOF2. Indeed, since the RICH can reasonably identify low momentum $e/\mu/\pi$, these particles can be vetoed in the H2 data. This allows a clearer identification of kaons, below a momentum limit of 7 GeV/c (see Fig. 5.11). One should keep in mind that a small fraction of kaons decay between TOF2 and RICH into charged muons and pions (total branching ratio of $\sim 90\%$). However, the procedure requires also that the particle velocity measured in TOF2 is consistent with that of kaons (2σ cut

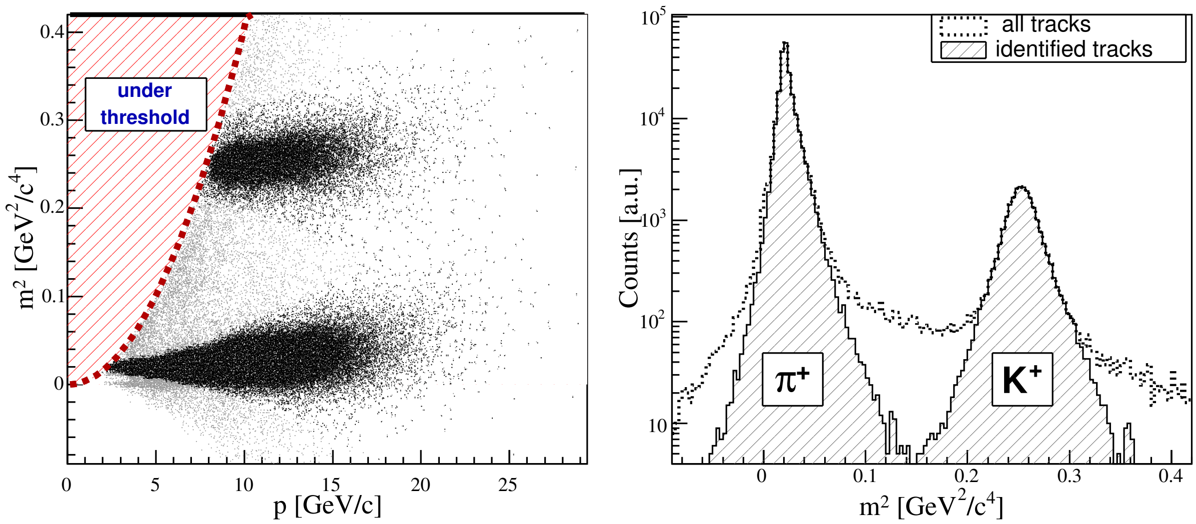

Fig. 5.9: RICH mass squared: versus track momentum (left) and projected mass squared distribution (right). Fully identified particles are shown in black whereas all tracks associated with a RICH ring are represented in gray.

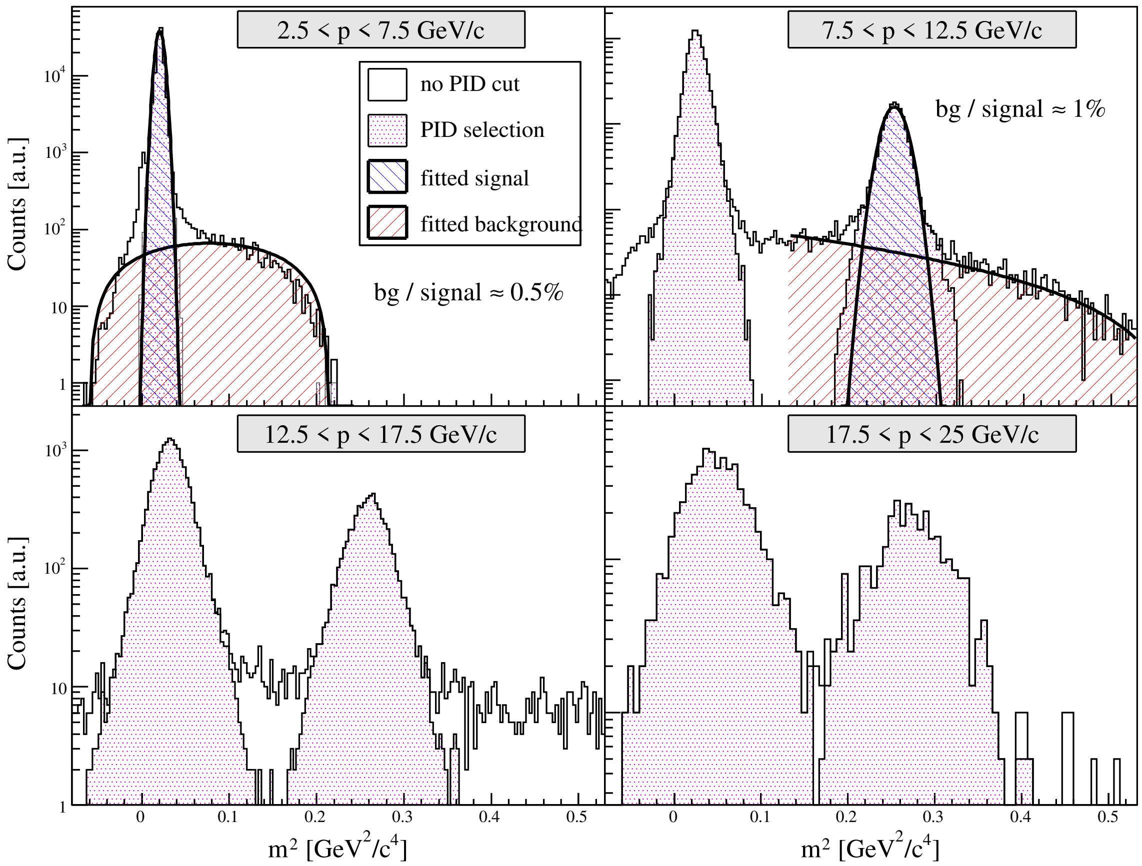

Fig. 5.10: Background estimation in the RICH. The background has been fitted with a second degree polynomial. The background falling inside the PID cut is less than 1% in the low momentum regions and decreases as the momentum increases.

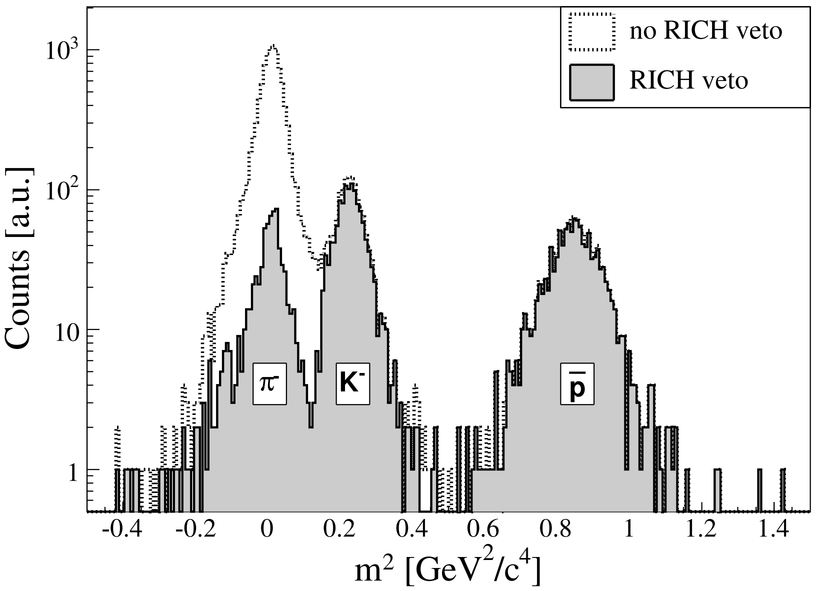

Fig. 5.11: Kaon identification in TOF2 by vetoing pions, muons and electrons in the RICH.

around the expected velocity). This ensures that if a vetoed particle comes from the decay of a kaon between TOF2 and RICH, the parent kaon is still identified by TOF2 if the consistency check of the particle velocity is positive. In Fig. 5.11, the remaining pion peak seen after veto is populated with pions below RICH momentum threshold or missed by the RICH (inefficiency). The latter is discussed in the next sections.

5.4 Data Correction

Constructing particle spectra requires data corrections of many kinds. The corrections applied to the data presented in this thesis are :

→ Detector efficiency ϵ_{det}
→ Spectrometer acceptance correction $\mathcal{C}_{acc}$
→ Other corrections (particle decay $\mathcal{C}_{dk}$, multiple scattering $\mathcal{C}_{ms}$)

Correction factors can be spectrometer setting dependent (e.g. acceptance) or only momentum dependent (e.g. particle decay). However, for each spectrometer setting, a correction map is constructed in the (p_T, y) space so that the data are corrected for each cell in this space, according to the following equation:

$$data_{corr}(p_T, y) = data_{raw}(p_T, y) \times \mathcal{C}orr \quad (5.6)$$

$$\mathcal{C}orr = \frac{\mathcal{C}_{acc} \times \mathcal{C}_{dk} \times \mathcal{C}_{ms}}{\epsilon_{det}} \quad (5.7)$$

Normalization follows data correction, this is described in Sec. 5.5.1.

5.4.1 Tracking Efficiency

For this analysis, two types of efficiency have been investigated: the tracking and PID efficiencies. The factor ϵ_{det} has been split into two factors: $\epsilon_{track} \times \epsilon_{PID}$. The tracking efficiency has been studied by using embedding of simulated tracks into a set of experimental tracks in the MRS and FFS [112]. The method is briefly described below. An alternative method has been developed for the FS tracking [107]: the efficiency of a tracking device is studied by a reference track constructed using track segments seen in possible tracking chambers except the one under study.

Track Embedding

The track embedding method has been used for the TPC's. The underlying concept is as follows: simulated tracks with well defined momentum and identity are digitized, meaning that the hit characteristics on a detector plane is made to look like raw TPC data (TPC sequences). It is then inserted to real TPC data. The tracking software is used normally and studies are made of how often simulated tracks could be found, as a function of the number of hits in the TPC. The reconstructed tracks are compared to the simulated input track as follows: to each track is associated a cylinder with a radius of 0.4 cm centered on the track so that the overlap volume between the simulated track cylinder and other cylinders is calculated. If a track has an overlap volume greater than 60% of the simulated track cylinder, the latter is considered as successfully reconstructed. Figure 5.12 shows the resulting MRS track reconstruction efficiency as a function of the number of TPC hits for pions and kaons. The efficiency curves turn out to be linear and decrease as the number of hits increase. Using them as is implies no momentum dependence. The latter has been studied in [112] and related to multiple scattering. Note that these efficiency curves are used regardless of the event centrality (since the number of TPC hits is related to the event centrality).

Reference Track Method

The reference track approach consists of the construction of a reference track using $N-1$ tracking detectors and checking whether tracking detector N contains a track segment that can be matched to the reference track. For this N^{th} detector, the resulting efficiency is defined as

$$\epsilon = \frac{N_{match}}{N_{ref}} \tag{5.8}$$

A detailed study of the reference track construction and of the efficiency estimation can be found in [107]. In substance, the reference track is constructed by matching track segments in x and y in the same way tracks are matched for momentum reconstruction (cf. 4.3.2), e.g. if the T1 tracking efficiency is studied, the reference track is constructed by matching T2 to T3 tracks, T3 to T4 tracks and T4 to T5 tracks. It is important that the user's cuts applied during track matching for momentum calculation, out of the efficiency calculation context, correspond to the matching cuts used for the reference track for efficiency estimations, i.e. if a 3σ cut around the matching parameters was applied for momentum determination, the same cut has to be applied when the reference track is constructed. Reference [107] contains a study of the sensitivity to the user's cuts and of the resulting background contamination. Once the reference track is made, it is extrapolated to the middle plane of T1 whose track segments are compared in position and slope with the extrapolated track. This procedure has been applied for each data set and studied as a function of the event centrality and horizontal track position and slope (x axis of the tracking detector). Note that this procedure is particle type independent. Figure 5.13 shows the efficiency estimated for different FS settings as a function of momentum for the top 5% central events.

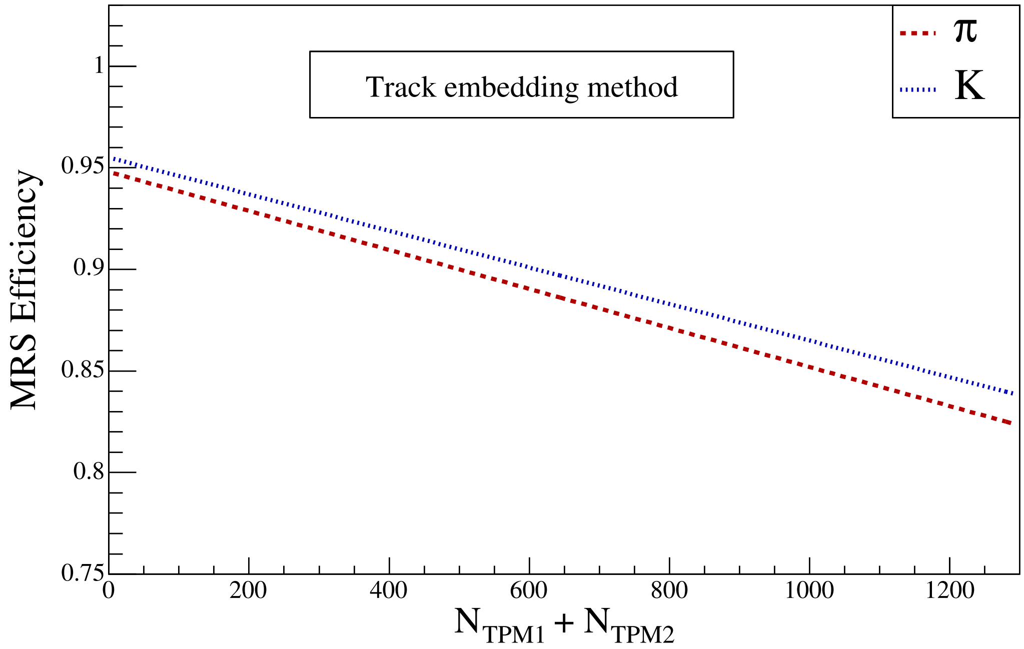

Fig. 5.12: MRS global tracking efficiency estimated by the track embedding method (see text and [112]).

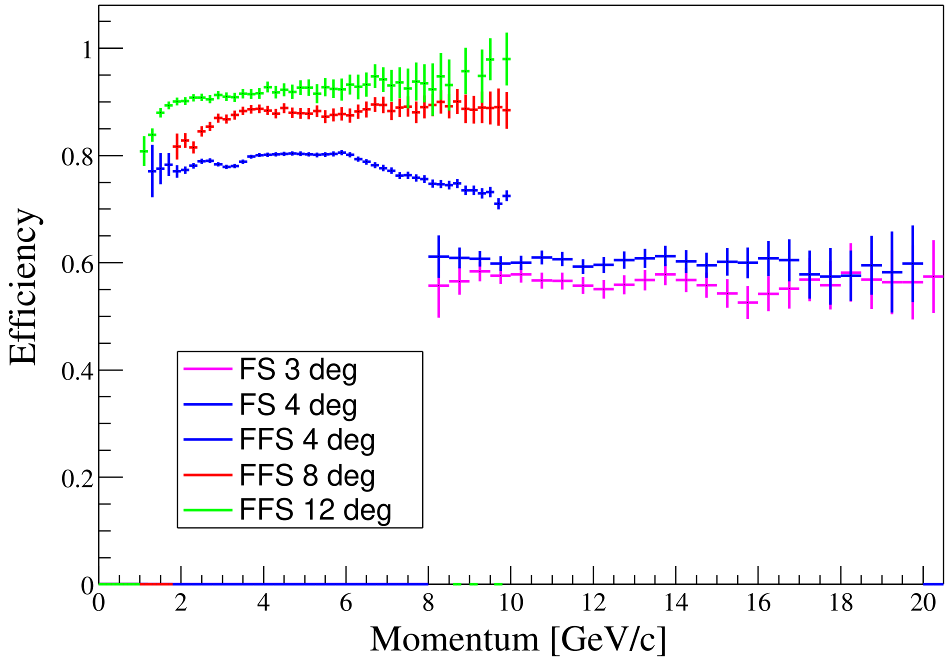

Fig. 5.13: FS tracking efficiency estimated by the reference track method (see text and [107]).

5.4.2 PID Efficiency

Hodoscopes

The hodoscope efficiency is related to the the way slats are stacked. In the MRS, TOFW slats are positioned on the same line in each panel. Such positioning introduces edge effects, i.e. tracks passing through close to slat edges, thereby depositing very little energy, or even in the wrapping material, in which case no signal is detected. In the FS, TOF1 and TOF2 have two stacks of slats, as seen before. The advantage is to remedy the effect present in the MRS and to give room to the PMT's. However, a few tracks can traverse the hodoscope without hitting any slats. In order to estimate the overall slat efficiency, the distribution of hits associated to valid tracks is divided by the distribution of the number of times valid tracks intersect slats. It is illustrated for TOF1 in Fig. 5.14. In the MRS, due to low track statistics hitting the outer panels of TOFW, the calibration of the corresponding slats is not optimal. These panels are not considered in this analysis. The remaining slats show a constant efficiency that amounts to $\sim 93\%$. TOF2, due to little background, is the most efficient hodoscope with a constant efficiency of $\sim 98\%$.

Another correction is added due to the presence of multiple hits (cf. Fig. 4.37) since two tracks associated to the same hit are ignored in this analysis. The fraction of multiple hits estimated in Sec. 4.4.1 is underestimated for the reason that only fully reconstructed tracks were considered. However, particle tracks which could not be fully determined have to be taken into account. A preliminary analysis showed that the fraction of multiple hits in TOF1 at $4\,^\circ$ is twice higher if T2 track segments that were not selected for momentum determination are also matched to TOF hits (see [113]). This correction is not yet available.

RICH Efficiency

Ideally, the RICH efficiency should be estimated with a simulation reproducing the response of this detector. Since it is not yet fully implemented, the efficiency is evaluated by using identified pions in TOF2. The efficiency is not mass dependent but solely depends on β. There are at least two drawbacks inherent to this procedure: one is the pion decay between TOF2 and RICH (see Sec. 5.4.4), the other is the limited PID momentum range common to TOF2 and RICH. Only pions between 2 and 4.5 GeV/c can be used. The estimated efficiency is shown in Fig. 5.15. It is assumed in this analysis that the RICH efficiency is constant above a momentum of 2.8 GeV/c for pions. The corresponding value for kaons (at equal β) is therefore ~ 9.9 GeV/c.

5.4.3 Acceptance Correction

Figure 5.16 shows raw $p_\perp$ spectra of identified π^+ (RICH PID) from three data sets without acceptance correction nor normalization. As can be seen, the raw spectra show significant discrepancies with each other (acceptance edges, slopes). The goal of the acceptance correction is to remove the geometrical bias introduced by the small phase–space coverage of the spectrometers. By definition, the geometrical acceptance is the ratio $\mathcal{A}cc$ between the distribution of particles that could be tracked throughout the spectrometer and the input distribution (Eq. 5.9). This ratio is calculated in the ($p_\perp$,y) space.

$$\mathcal{A}cc = \frac{\text{detected particles}}{\text{all particles}} \tag{5.9}$$

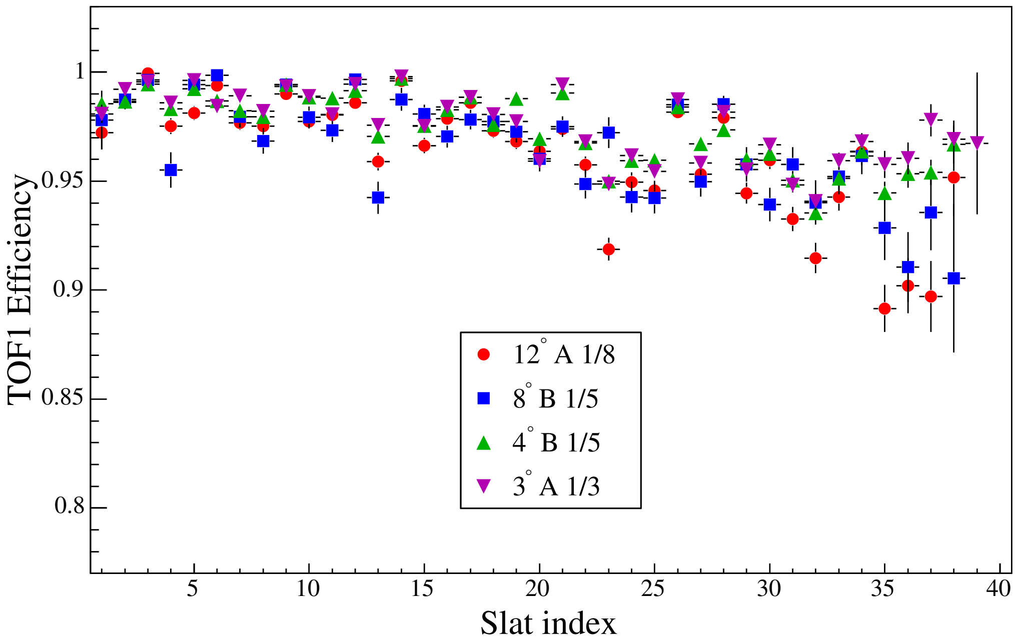

Fig. 5.14: Efficiency of associating a TOF hit to a valid track in TOF1. The efficiency is slightly dependent on the slat position, which reflects in fact the momentum distribution influence.

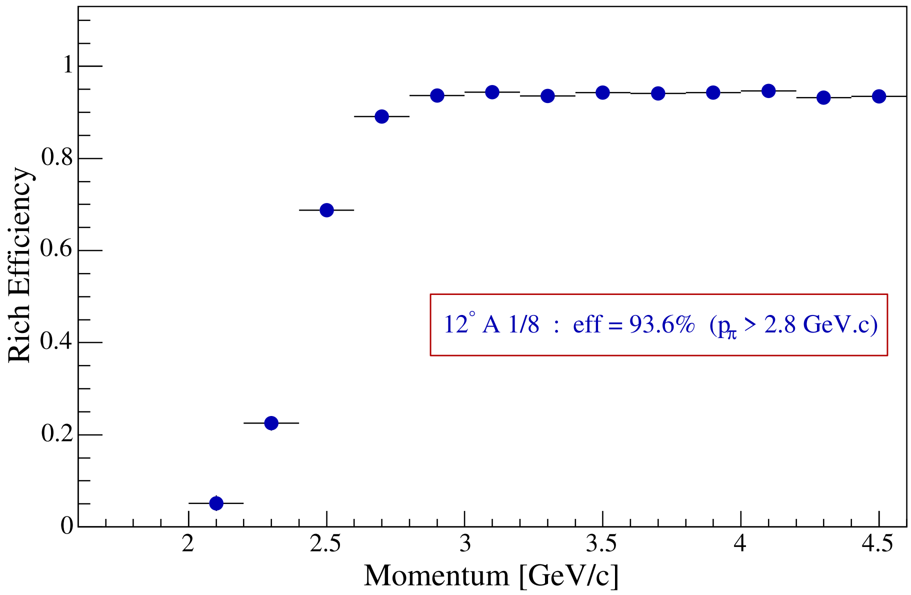

Fig. 5.15: RICH detection efficiency estimation, using pions identified in TOF2. The efficiency is very low close to threshold but increases rapidly from 0.1 to 0.93 in only 1 GeV/c increase in momentum.

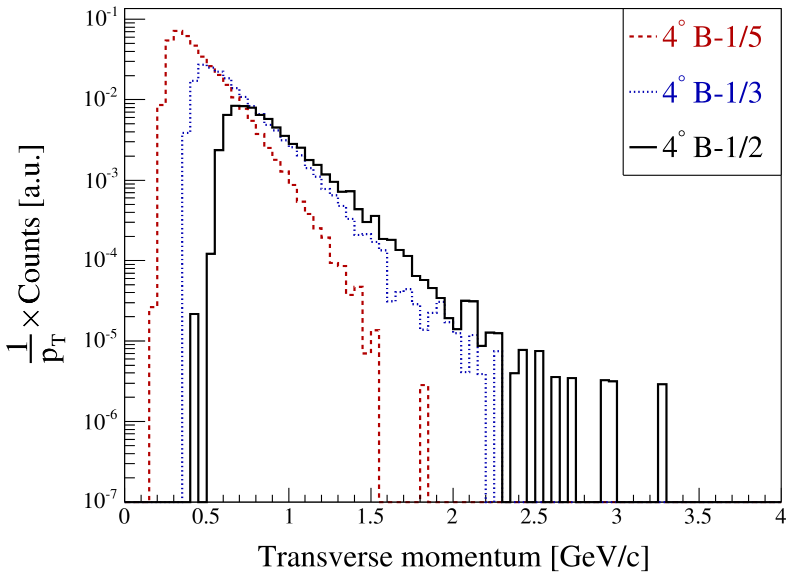

Fig. 5.16: Raw transverse momentum distributions of positive pions for three different magnetic field settings at $\theta_{FS} = 4\,^{\circ}$.

For a given spectrometer, a particle is accepted if it could be tracked until the PID detector, in the same fashion as what is done with real data.

Acceptance Simulation

The procedure used for this analysis is to simulate the response of the spectrometers for given position and magnetic field settings: a particle distribution is sent through the spectrometer where all physics processes are switched off, except for energy loss through material[1] in order to track the particles through the spectrometer. Simulations are performed with a package called `brag`, based on GEANT3, which reproduces the BRAHMS spectrometer properties. The input distribution contains only pions of a given electrical charge sign (depending on the simulated magnetic field setting). To avoid redoing long simulations for kaons, the pion calculations are utilized with the pion mass replaced by the kaon mass to evaluate y, $p_\perp$ or m_T for a correct kaon acceptance mapping. A picture of the `brag` simulation is shown in Fig. 5.17. Momenta of input particles are uniformly distributed within a momentum range broader than the range where PID is achieved. Particles are also chosen in a given azimuthal angle range $\Delta\phi < 2\pi$ but broad enough so that the spectrometer aperture lies within this range. Idem with θ. The magnitude of the input distribution is then rescaled by a factor $2\pi/\Delta\phi$ before acceptance is calculated[2]. The acceptance factor is therefore

$$\mathcal{A}cc\,(y, p_T) = \frac{\text{accepted particles}}{\text{thrown particles}} \times \frac{\Delta\phi}{2\pi} \tag{5.10}$$

The number of particles thrown within the phase–space $\Delta\phi\Delta\theta\Delta p$ is 15,000,000 for each spectrometer setting.

[1]Energy losses though material have practically no effect on particle momenta at so high momentum ranges (MIP).

[2]Particles produced in heavy ion collisions are uniformly distributed in ϕ over a large set of events.

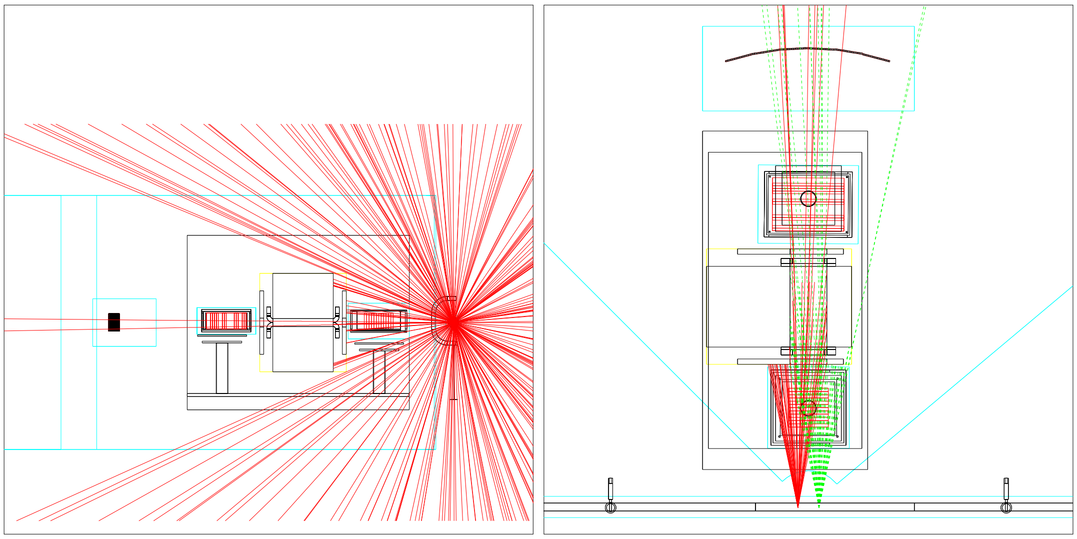

Fig. 5.17: Simulation for acceptance correction, with a side (top) view of the MRS in the left (right) panel. Only a small fraction of the incident particles reach TOFW via TPM1, D5 and TPM2. Note also the effect of the vertex position on the acceptance (see discussion in text).

Other Geometrical Biases

Apart from the global geometry of the spectrometer, there exists some specific detector geometries that cannot be neglected at the simulation level. The TPC's have inactive rows, TPM2 has an asymmetric readout plane. These effects are taken care of by a software designed to convert GEANT tracks to TPC tracks. The hodoscopes have invalidated slats (bad calibrations). Those are therefore disabled in the simulation when the particle selection is based on a TOF PID like in the MRS. The DC tracks are fully digitized and track segments are reconstructed ala real data. The local tracks are combined using the standard global tracking software. Likewise, magnet fiducial cuts applied to real data are used in the simulation.

Collision vertex

The spectrometer acceptance slightly differs from one event to the next due to the changing vertex location. Figure 5.18 illustrates this effect. To minimize this bias, the vertex range ($\pm$ 20 cm for the FS and $\pm$ 15 cm for the MRS) is divided into bins of 5 cm. An acceptance map is constructed for each vertex bin. The data are also treated in the same way. Since the experimental vertex distribution is not uniform even in the selected range of $|vtx| < 20\,(15)$ cm for FS (MRS) data, an overall event normalization would bias the results. This method takes into account the variation of the number of events with the vertex location (see Sec. 5.5.1). The chosen bin width (5 cm) is a compromise between statistical errors (too small bins would imply few tracks per vertex bin and therefore large statistical uncertainties) and the dependence of the acceptance on the vertex position (too large bins would hide this acceptance effect). An example of K and π acceptance map is shown on Fig. 5.19 (FS setting 3° B–1/2). Three remarkable points:

1- the data (black boxes) and the simulation (colored histogram) nicely overlay,
2- the acceptance magnitude is not constant in $p_\perp$
3- the acceptance edges have a lower magnitude

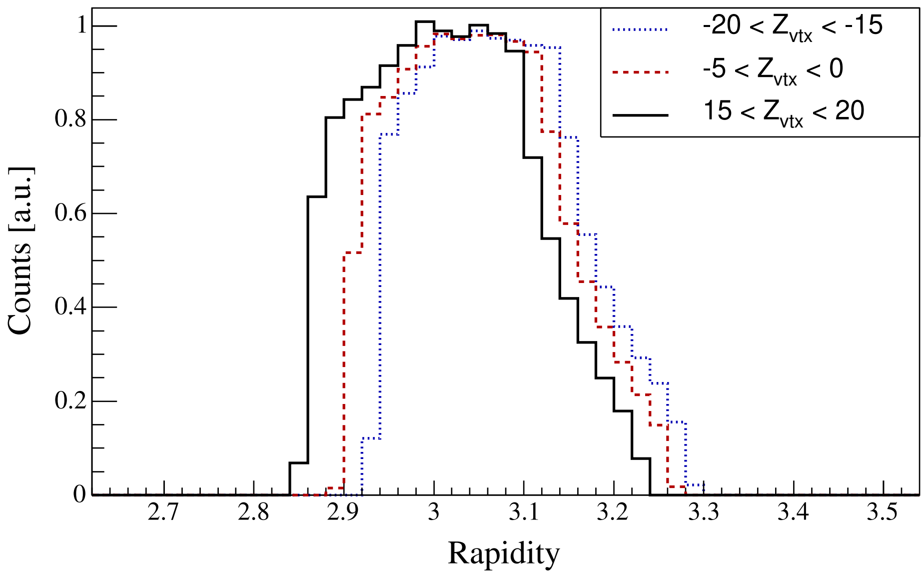

Fig. 5.18: The spectrometer acceptance is vertex dependent.

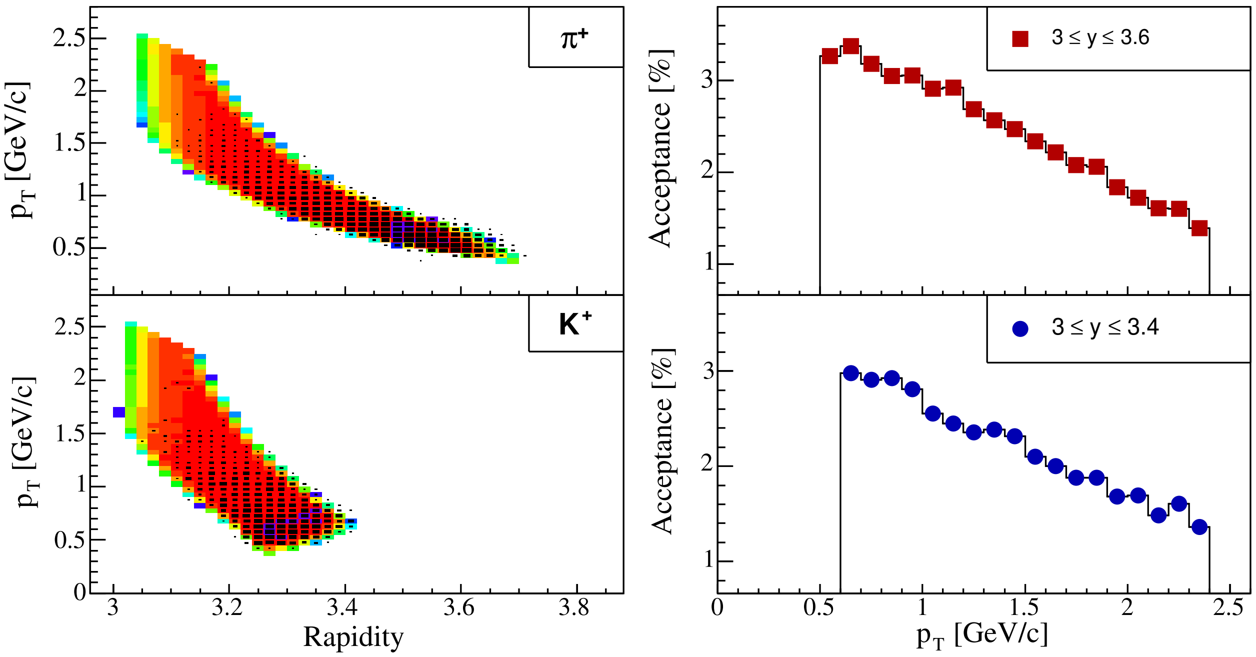

Fig. 5.19: π and K acceptances in $(p_\perp, y)$ of the FS setting 3° B–1/2. The black boxes are real data whereas the color contours are acceptance maps. The panels on the right show averaged projections of the maps on the $p_\perp$ axis within the given rapidity ranges. It represents the fraction in % of accepted particles.

The second point is important: the slope of the raw spectra changes after FS acceptance correction. In the MRS, the acceptance is constant except at very low p_T. The third point is taken care of by removing edges below half of the average acceptance in the MRS and 1/3 in the FS. In Fig. 5.20 are plotted acceptance maps of all settings.

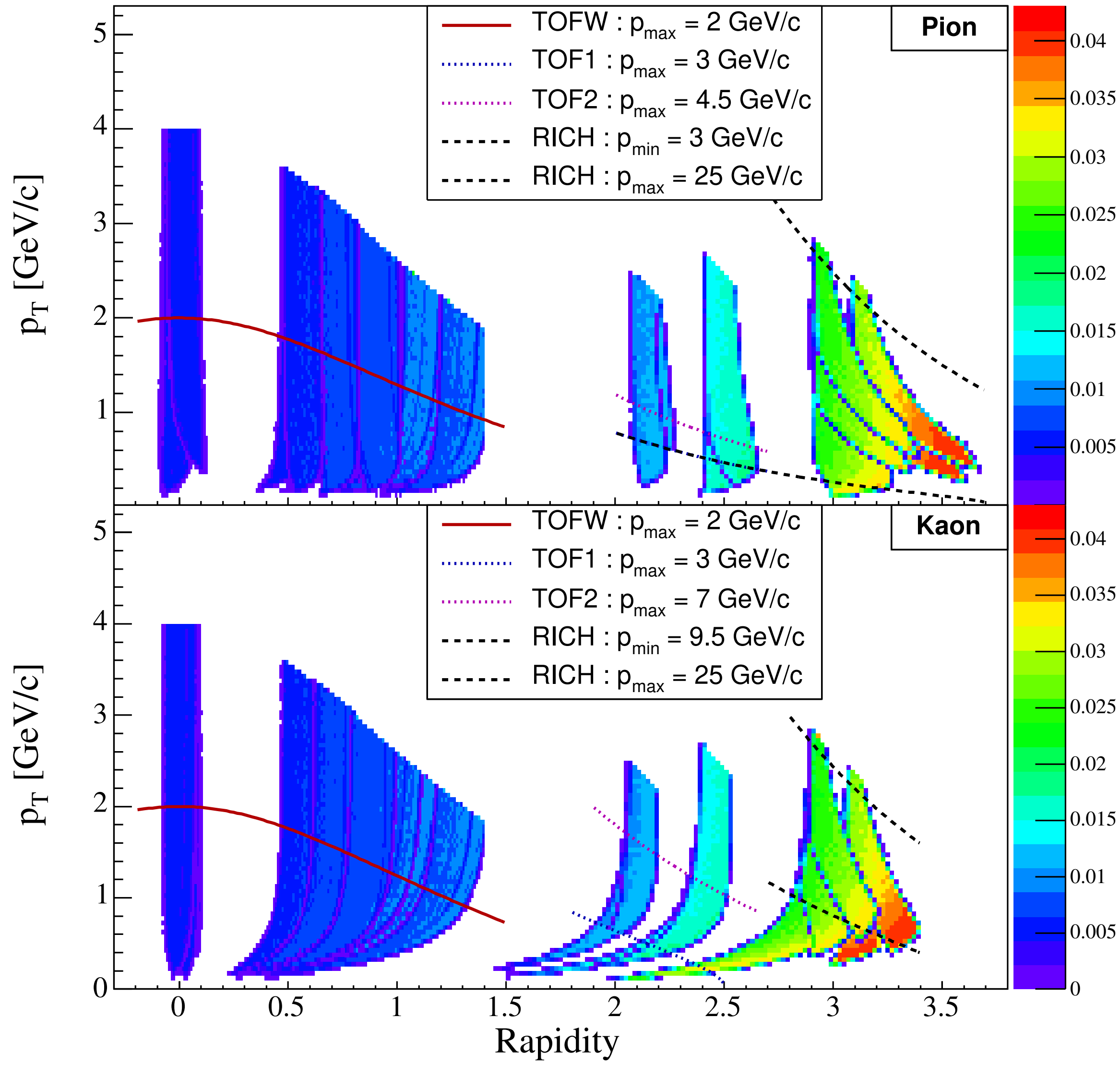

Fig. 5.20: π and K acceptance maps for all spectrometer settings (vertex bin 0–5 cm). The isomomentum lines represent PID limits.

The color contours represent the acceptance magnitude $\mathcal{A}cc$. The isomomentum lines indicate where PID limits are reached. Note that the low momentum limit in the RICH is about 1 GeV/c above threshold in order to avoid identification inefficiency. Figure 5.21 represents the relative statistical error introduced by the procedure. In all settings, it is at most $\sim$ 4%, depending on the (p_T, y) cell (edges excluded). When projections are made over rapidity intervals, the error is lowered by summing.

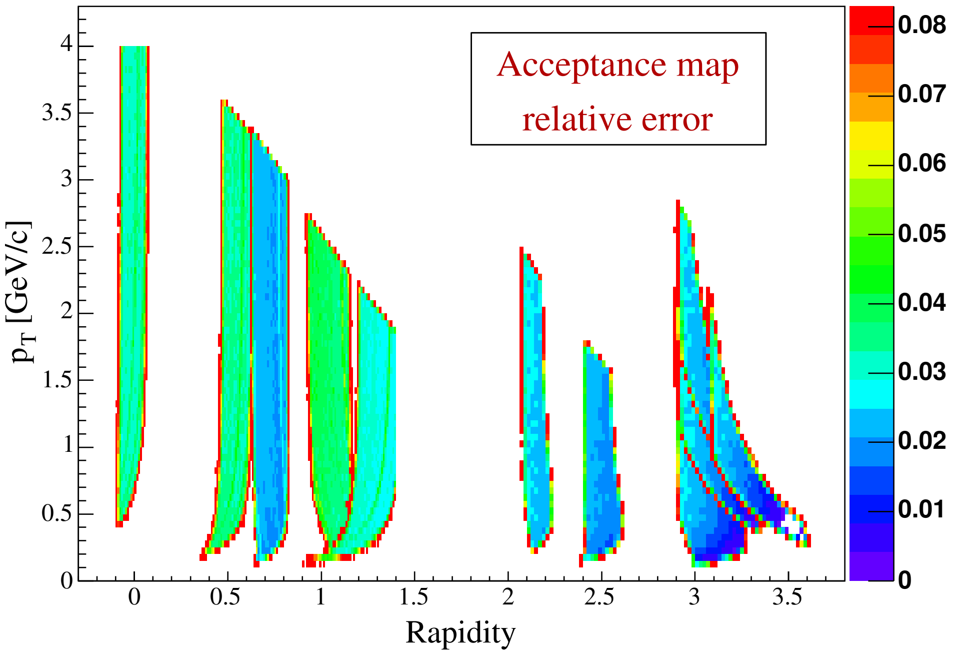

Fig. 5.21: Acceptance map relative statistical error. The error is at most $\sim 4\%$ in each (p_T, y) cell, edges excluded.

5.4.4 Secondary Reactions

Two types of secondary reactions are taken into account in this analysis. One is multiple scattering which is the effect of repeated elastic Coulomb scatterings that can deflect particles in and out of the acceptance. The other type is pion and kaon weak decay and has a larger effect. In order to evaluate their effect, `brag` was used with and without these effects. Unlike the acceptance correction, particle tracks were fully digitized, reconstructed and selected ala real data (fiducial cuts, matching cuts and PID cuts were applied). The motivation is that a kaon (pion) can decay before e.g. the hodoscope but still be identified as a kaon (pion) due to little momentum and flight path change of the leading daughter particle (muon). Figure 5.22 shows the kaon multiple scattering correction and decay in the MRS at 90° and 40° as a function of momentum. As can be seen, the corrections are independent of the spectrometer setting. They were fitted with the following function

$$\mathcal{C}orr^{-1} = a - b\,\exp\left(-c\,p\right) \tag{5.11}$$

The parameters a, b and c are listed in Tab. 5.3 for all spectrometers.
The parameters have been found to be independent of the spectrometer angle. However, correction maps are constructed in the way acceptance maps are: the momentum dependence of the correction is converted into a (p_T, y) dependence in the form of two-dimensional histograms for each spectrometer setting. These histograms have of course the same binning as the acceptance maps so that they can be multiplied with each other cell by cell in (p_T, y).

5.5 Last Steps before Particle Spectra

Remember that each data set has been divided into vertex bins of 5 cm. Therefore, each data set is first treated in order to remove the vertex dependence. The following step consists of

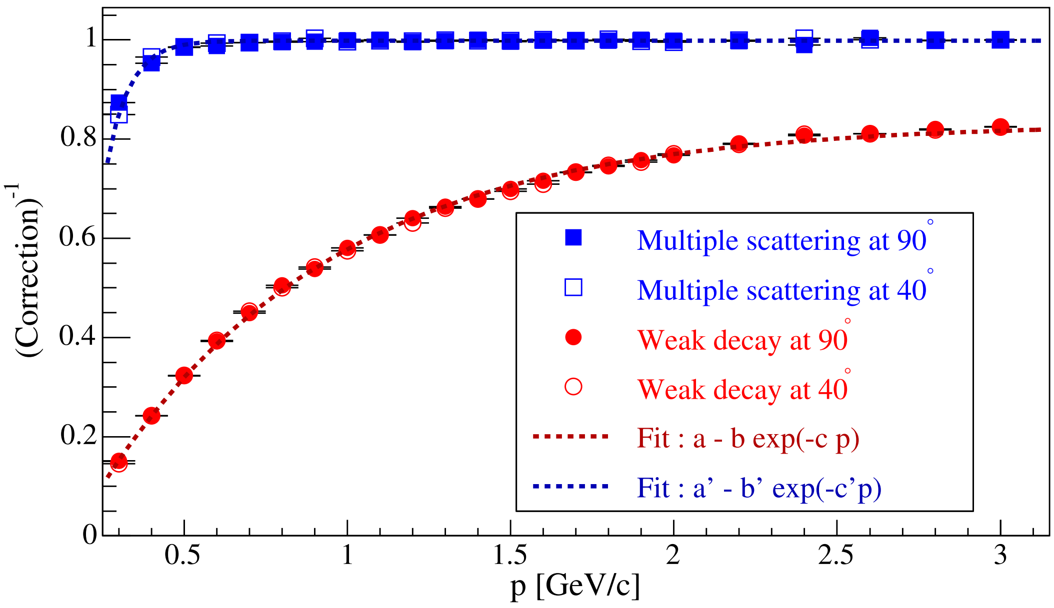

Fig. 5.22: Kaon multiple scattering and weak decay effects in the MRS. No dependence on spectrometer setting was found.

	MRS		FFS		FS	
Pions	Decay	M. Scatt.	Decay	M. Scatt.	Decay	M. Scatt.
a	0.986		1.000		0.993	
b	0.437	ignored	0.250	ignored	1.130	ignored
c	2.671		0.689		1.535	
Kaons	Decay	M. Scatt.	Decay	M. Scatt.	Decay	M. Scatt.
a	0.986	0.998	0.9409		0.9092	
b	0.437	10.546	0.6748	ignored	0.723	ignored
c	2.671	14.199	0.3179		0.2259	

Tab. 5.3: Decay and multiple scattering fit parameters (using Eq. 5.11). Multiple scattering is neglected in most cases, the main correction is from the decay correction.

combining sets together by constructing a weighted average. Finally, normalized differential yields in the (p_T, y) space are binned along the rapidity axis in order to construct particle spectra by projecting each rapidity bin to the p_T axis.

5.5.1 Data Set Correction and Normalization

As mentioned before, pion or kaon data and corresponding acceptance and correction maps are two–dimensional histograms in (p_T, y) (the histogram binning is $b_{p_T} = 50\,\mathrm{MeV}$, $b_y = 0.01$ in the MRS and $b_{p_T} = 50\,\mathrm{MeV}$, $b_y = 0.02$ in the FS). The acceptance and correction histograms are merged according to the following equation:

$$\mathrm{CORR}|_{v,p_T,y} = \frac{\mathcal{C}orr|_{p_T,y}}{2\pi N_{ev}(v)\,\mathcal{A}cc|_{v,p_T,y} \times b_{p_T} \times b_y} \tag{5.12}$$

where subscript v identifies the vertex bin and $N_{ev}(v)$ the corresponding the number of events. Therefore, the 2D–histogram CORR contains all correction and normalization for vertex bin

v. Then, for each data set characterized by a spectrometer angle and a magnetic field, all vertex bins are summed up as follows:

$$\mathrm{DATA}|_{p_T,y} = \sum_v \mathrm{DATA}|_{v,p_T,y} \tag{5.13}$$

$$\left(\mathrm{CORR}|_{p_T,y}\right)^{-1} = \sum_v \left(\mathrm{CORR}|_{v,p_T,y}\right)^{-1} \tag{5.14}$$

where the sum is running over the vertex bin v. The last term is then inversed for each (p_T, y) cell, so that the normalized and corrected differential yield reads

$$dN|_{p_T,y} = (\mathrm{DATA}|_{p_T,y}) \times (\mathrm{CORR}|_{p_T,y}) \tag{5.15}$$

5.5.2 Combining Data Sets

Combining data sets is necessary in order to cover enough p_T range at each rapidity bins. Following reference [30], index s is used to identify a given spectrometer setting. The average normalized differential yield becomes:

$$\langle dN|_{p_T,y}\rangle = \frac{\sum_s dN|_{s,p_T,y} \times W|_{s,p_T,y}}{\sum_s W|_{s,p_T,y}} \tag{5.16}$$

where the weight $W|_{s,p_T,y}$ is defined as

$$W|_{s,p_T,y} = \frac{1}{\mathrm{CORR}|_{s,p_T,y}} \tag{5.17}$$

to ensure that (p_T, y) cells with large corrections carry low weights. With these definitions, Eq. 5.16 can be rewritten

$$\langle dN|_{p_T,y}\rangle = \left(\sum_s \mathrm{DATA}|_{s,p_T,y}\right) \times \left(\sum_s \frac{1}{\mathrm{CORR}|_{s,p_T,y}}\right)^{-1} \tag{5.18}$$

i.e. a form that conserves the statistical distribution $\mathrm{DATA}|_{s,p_T,y}$. Other choices for the weights would not give this factorized form and hence not the straight sum of contributing counts. In this form, weights W's can be interpreted as an effective number of events. When the resulting yield is zero in a cell, there can be two explanations: either the correction factor is zero, in which case the cell was excluded from the acceptance from the beginning, or there was no particle (data) in the cell. In the latter case, the measurement is still valid (as well as the weight factor) and keeping zero cells is important when cells are averaged over to make projections to the p_T axis. A discussion on the subject can be found in [30]. The present analysis derives from the procedures implemented in this reference. Another discussion about the way corrections are applied can also be found. In substance, because of the relatively low statistics of most spectrometer settings, it has been chosen to apply corrections on average instead of doing it track by track. In the present analysis, track by track and momentum averaged correction methods agree thanks to the relatively high pion statistics (compared with the proton statistics in [30]). However, since the kaon statistics is in the order of the proton statistics, the average method has been preferred for coherence. Errors are discussed in Sec. 6.4

Figure 5.23 shows the kaon and pion normalized differential yields after setting averaging. The color contours are logarithmic.

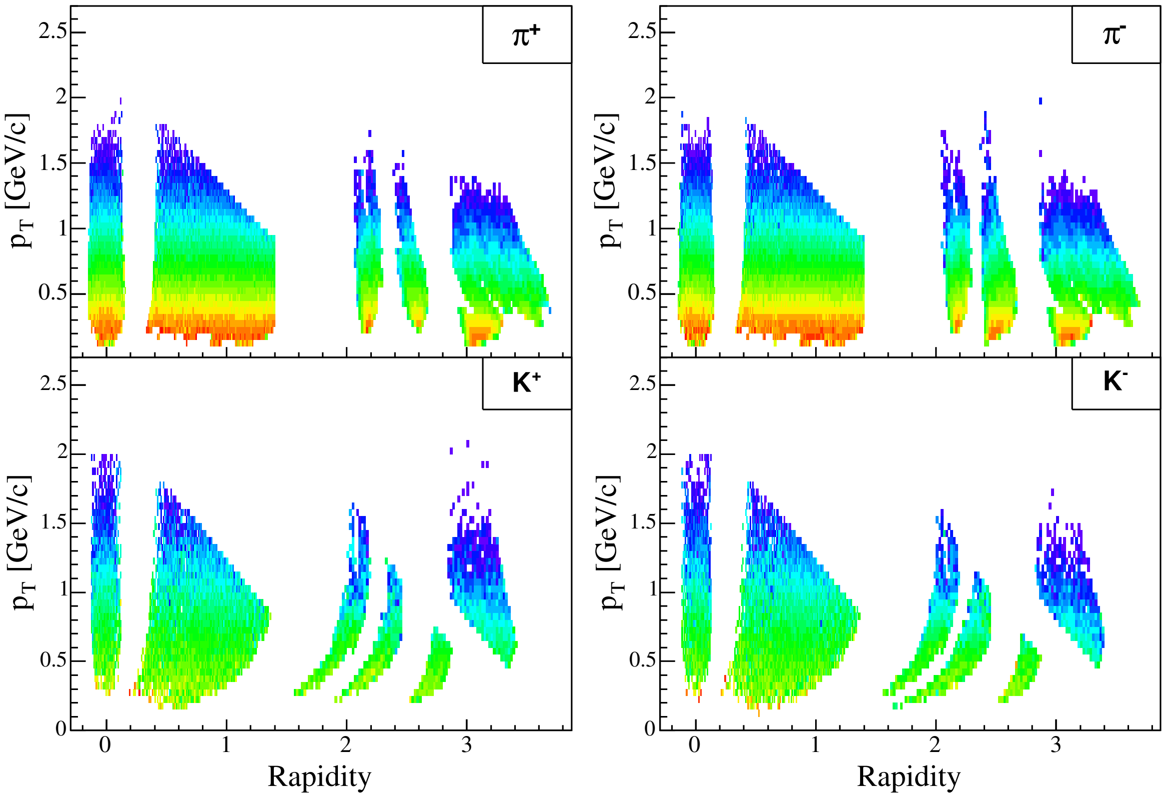

Fig. 5.23: Kaon and pion normalized yields after all data sets were corrected and combined.

5.5.3 Projection to Normalized Particle Spectra

From histograms shown in Fig. 5.23, particle spectra are constructed by first chopping the rapidity axis into intervals of width $\Delta y = 0.1$ or 0.2, depending on the available statistics. A p_T spectrum at a given rapidity y is the averaged projection over the rapidity bins that the rapidity interval Δy contains, according to the following equations:

$$N(p_T) = \left(\sum_y \sum_s \mathrm{DATA}|_{s,p_T,y} \right) \times \left(\sum_y \sum_s \frac{1}{\mathrm{CORR}|_{s,p_T,y}} \right)^{-1} \tag{5.19}$$

with $y - \Delta y/2 \leq y \leq y + \Delta y/2$ and

$$\frac{1}{2\pi p_T} \frac{d^2N}{dp_T dy}(p_T) \equiv \frac{N(p_T)}{p_T \Delta y} \tag{5.20}$$

where p_T in the denominator is the center of the histogram bin. Figure 5.24 shows an example of such a projection. The procedure is applied to all rapidity intervals where enough p_T coverage is achieved. The obtained results are presented in the next chapter.

♣♣♣♣♣♣

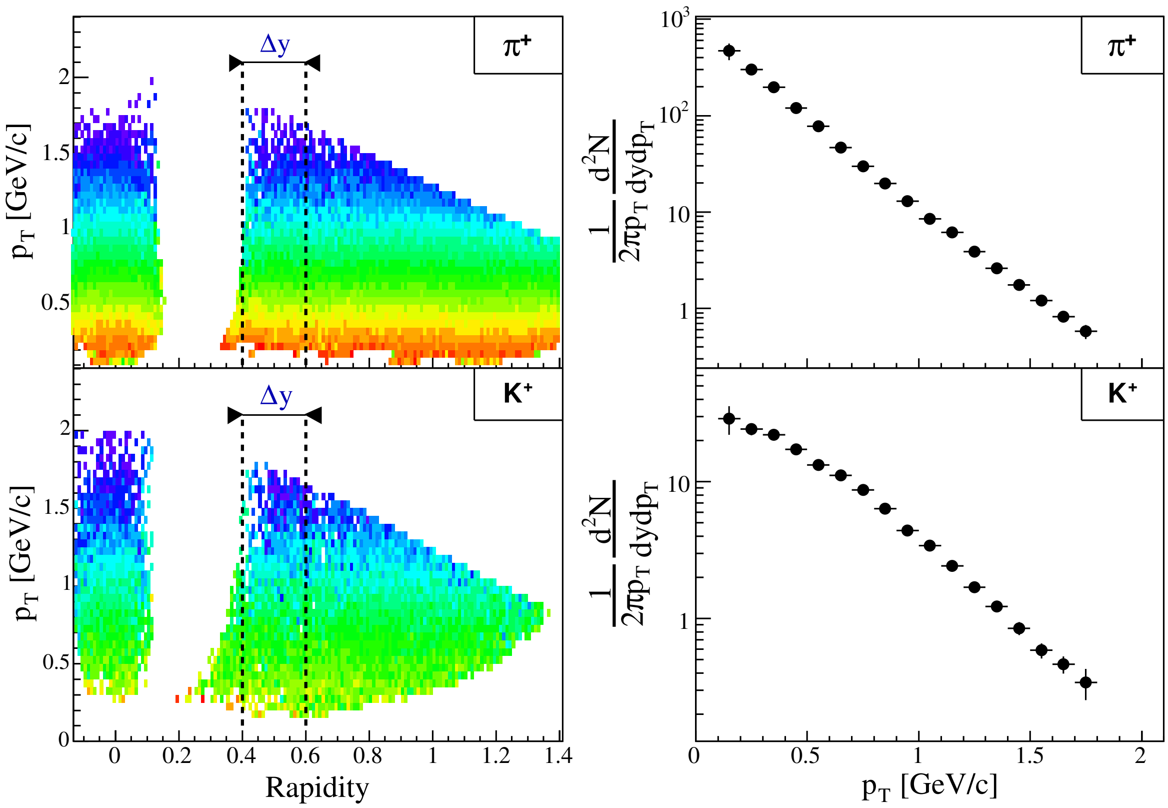

Fig. 5.24: Averaged projection of data within interval Δy to the p_T axis. The histograms in the right panels are normalized particle spectra.

Chapter 6

Results

Normalized particle spectra are investigated from rapidity -0.1 to rapidity 3.6 for the top 5% central events. The invariant yields are deduced from extrapolation to uncovered acceptance regions. The choice of the fitting function is discussed, as well as sources of systematic errors. All results are tabulated at the end of the chapter.

6.1 Normalized Particle Spectra

Normalized particle spectra from the top 5% central collisions of the reaction Au+Au at $\sqrt{s_{NN}} = 200\,\mathrm{GeV}$ are presented as a function of rapidity. The rapidity intervals are shown in Fig. 6.1. Filled gray areas are phase–space regions not covered in this analysis. The MRS

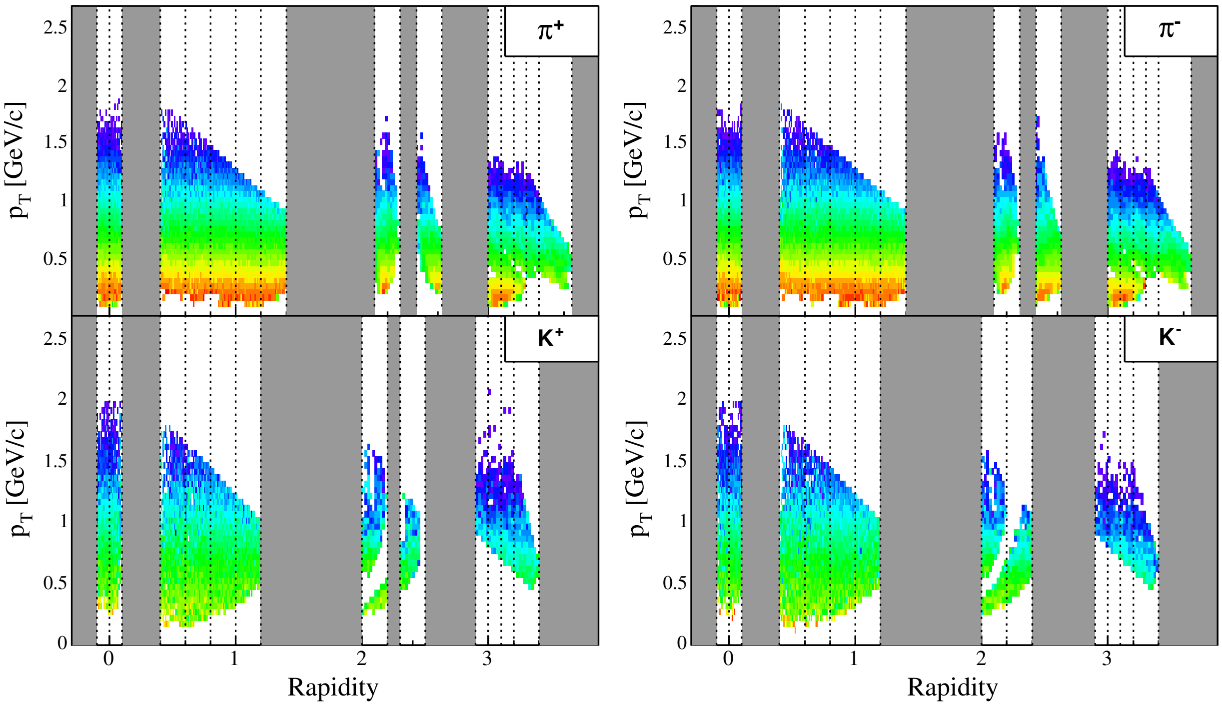

Fig. 6.1: Rapidity selection. A difference between K^+ and K^- exists at $y \sim 2.3$ due to a spectrometer setting that was not applied for positive kaons.

covers rapidities from -0.1 to 1.4 (1.2) for pions (kaons). The FS, by combining FFS and BFS settings, covers from $y = 2.1$ (2.) to 2.6 (2.5) and 3.0 (2.9) to ~ 3.65 (3.4). The relatively broad p_T coverage around y $\sim$ 2.3 is possible by using the RICH as a direct pion identifier. The error originating from discrepancies between data sets covering the same phase space is discussed in Sec. 6.4. Note also that the presented spectra are inclusive, i.e. no attempt was done in order to disentangle pions from resonance decays to primary pions due to absence of resonance studies as a function of rapidity at RHIC. Similarly, kaons from ϕ, Ω or K^* decays are not discussed since no estimation of their yields is yet available as a function of rapidity. A possible estimation would be given by calculations from an event generator filtered by the GEANT simulation discussed in the precedent chapter, although this estimation would remain model dependent. Alternatively, one can assume that the yields of strange resonances investigated at mid–rapidity by the STAR or PHENIX experiments scale with kaon yields as a function of rapidity[1].

Figure 6.2 shows pion transverse mass $m_T - m_\pi$ spectra as a function of rapidity for the top 5% central events. The error bars are statistical. The spectra show a remarkable similarity in

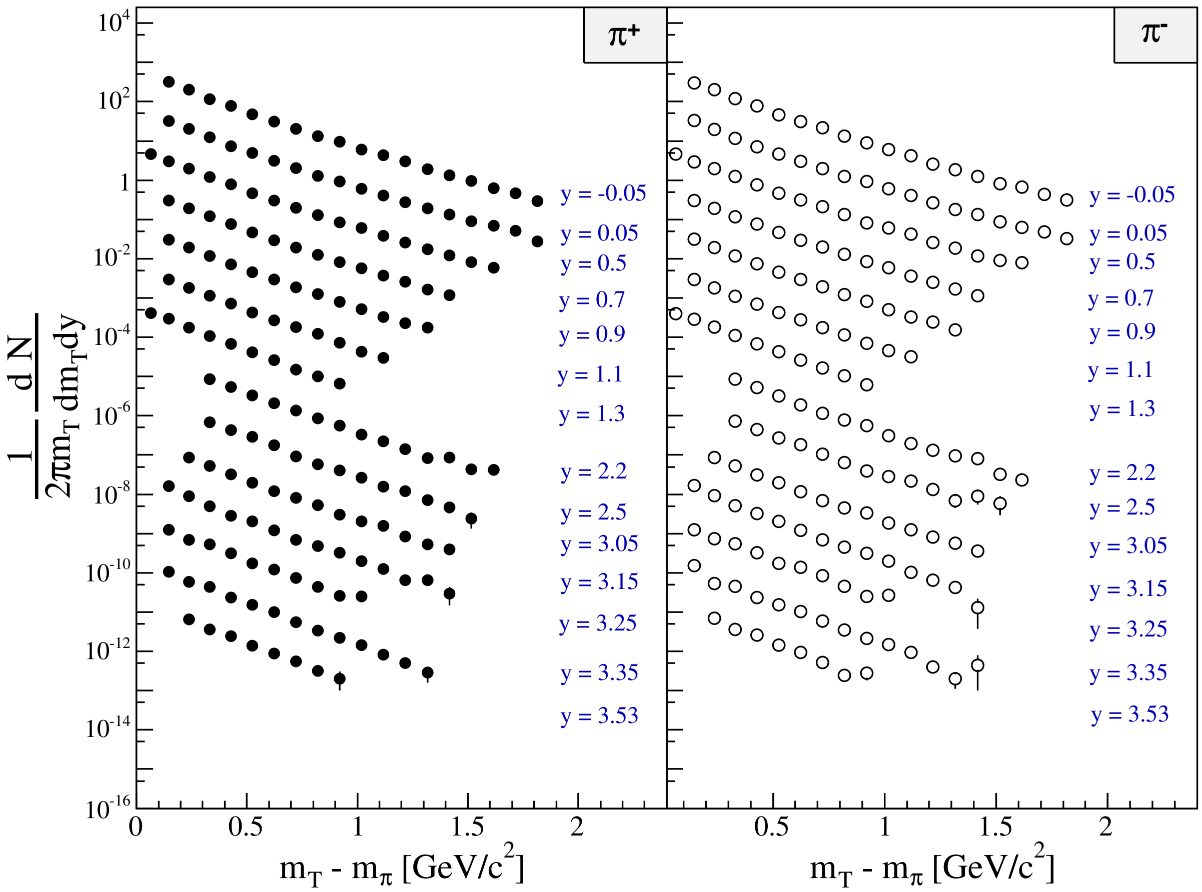

Fig. 6.2: Normalized pion transverse mass spectra as a function of rapidity. The magnitude of spectra have been rescaled by 10^0, 10^{-1}, 10^{-2}, etc, from the top to the bottom. Errors are statistical. The marker size can be larger.

shape at all rapidities for both π^+ and π^-. The m_T range covered depends on magnetic field

[1] In reference [85], it is shown that the ratio $\langle\phi\rangle / \langle K^-\rangle$ as a function of $\sqrt{s_{NN}}$ is constant at ~ 0.13.

settings, thus some discrepancies between ranges covered at different rapidity intervals.

Figure 6.3 shows kaon spectra at the selected rapidities. Again, no strong differences in

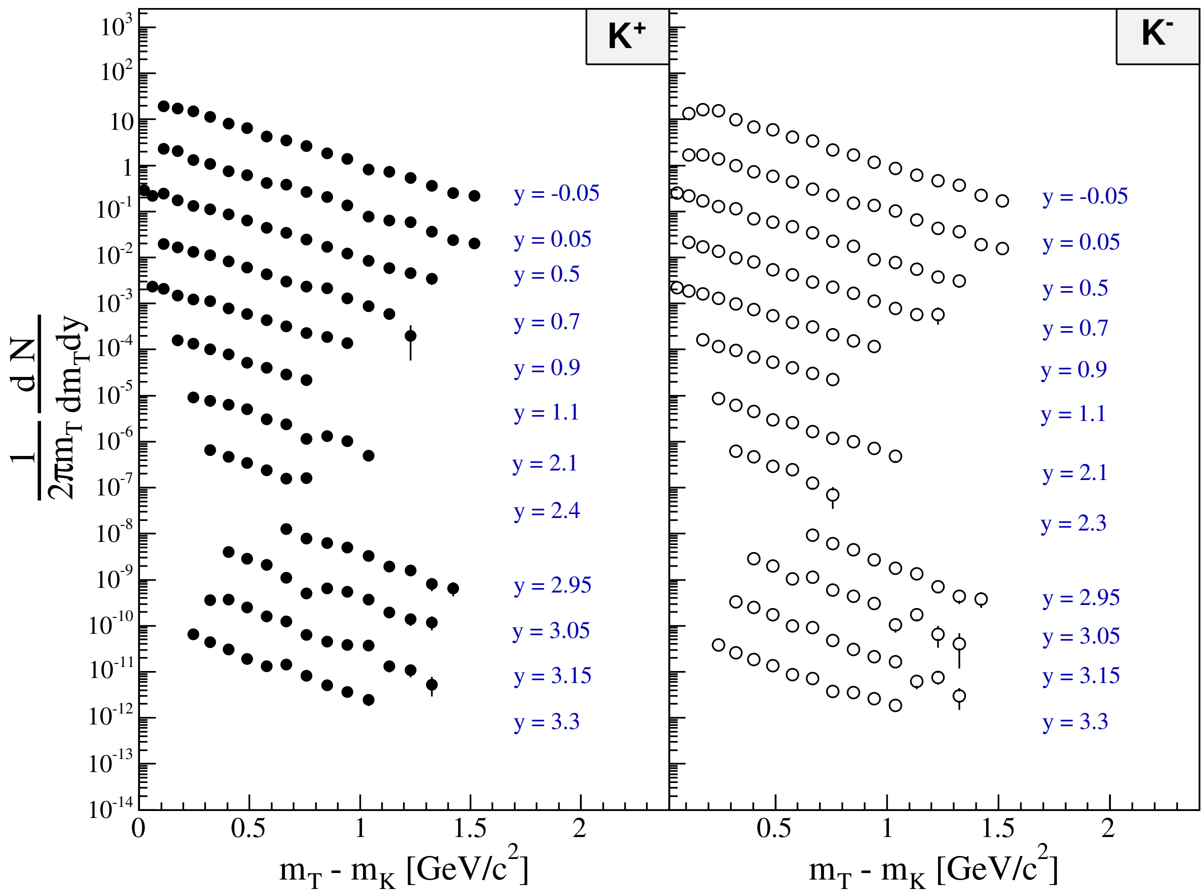

Fig. 6.3: Normalized kaon transverse mass spectra as a function of rapidity. Scale factors have been applied like in Fig. 6.2.

the spectral shape are qualitatively visible between spectra. The next section describes how spectral features are quantified.

6.2 Extracting Spectral Information

Once particle spectra are constructed, yields are evaluated at each rapidity interval by integrating the covered p_T or m_T range and extrapolating to regions outside the acceptance. Remember that the differential yield at a given rapidity y, if described by function $f(m_T)$, reads

$$\frac{1}{2\pi m_T}\frac{d^2N}{dm_T dy} = f(m_T) \tag{6.1}$$

where m_T can be changed by p_T without any modification. Therefore, the integrated yield at a given rapidity y is

$$\frac{dN}{dy} = \int_m^\infty 2\pi\, m_T \left(\frac{1}{2\pi m_T}\frac{d^2N}{dm_T dy}\right) dm_T = 2\pi \int_m^\infty m_T\, f(m_T)\, dm_T \tag{6.2}$$

In practice, integrated yields over the full p_T or m_T range depend on the choice of $f(m_T)$. Since the extrapolated yield outside the acceptance (in particular at low p_T) depends on the choice of the fit function, a systematic error is introduced. The fit function is chosen so that it can fit all spectra with a good confidence level. The systematic errors are discussed in Sec. 6.4.

6.2.1 Fit Function

The most common fit functions are listed in Tab. 6.1. The T parameters in the denominators

Name	Formula
Boltzmann in m_T	$B \times m_T \times \exp\left[-(m_T - m)/T\right]$
Exponential in p_T	$A_p \exp\left[-p_T/T_{\text{eff}}\right]$
Exponential in m_T	$A_m \exp\left[-(m_T - m)/T_{\text{eff}}\right]$
Power law in p_T	$C(1 + p_T/p_0)^{-n}$
Sum of two exponentials	$D_1 \exp\left[-(m_T - m)/T_1\right] + D_2 \exp\left[-(m_T - m)/T_2\right]$

Tab. 6.1: Most common fit functions describing charged particle spectra.

of the exponential functions are called the inverse slope parameter or effective temperature of the particle source. Coefficients A to D are normalization factors from which integrated yields can be deduced (see Appendix E). The Boltzmann function describes the particle distribution emitted from a classical thermalized source at temperature T, i.e. when particles in the source are moving randomly (stochastic motion) according to classical statistical laws[2]. The other listed functions are empirical functions. They are used without solid theoretical bases but turn out to describe spectra better than the theoretical ones in some cases (as will be evident in the next section). They can be seen as effective distributions, i.e. experimental distributions are the result of several contributions, each of them following a different statistical law.

In the following sections, only three functions are discussed in details, the exponential function in m_T, the sum of exponential functions in m_T and the power law in p_T. The Boltzmann function is ruled out because a first attempt showed that it was not adequate.

6.2.2 Fitting Spectra

In practice, fits are done in ROOT [114] by using the minimum χ^2 method. Note that the integral of the function is used as a fit parameter for a correct error treatment. Indeed, the normalization parameters can be analytically expressed (cf. Appendix E):

$$A_m = \frac{1}{2\pi}\frac{dN/dy}{T(T+m)} \quad \text{(single expo.)} \tag{6.3}$$

$$D_1 = \frac{1}{2\pi}\frac{dN/dy - N_2}{T_1(T_1+m)} \quad \text{(sum of 2 expo.)} \tag{6.4}$$

$$D_2 = \frac{1}{2\pi}\frac{N_2}{T_2(T_2+m)} \quad \text{(sum of 2 expo.)} \tag{6.5}$$

$$C = \frac{(n-1)(n-2)}{2\pi p_0^2}\frac{dN}{dy} \quad \text{(power law)} \tag{6.6}$$

[2]Since mesons are bosons, one can use the Bose–Einstein statistics but the Boltzmann statistics is a good approximation.

Figure 6.4 shows the three test functions applied to pion data in the MRS and the FS. The spectra are all expressed in p_T for coherence. The exponential function in m_T in this repre-

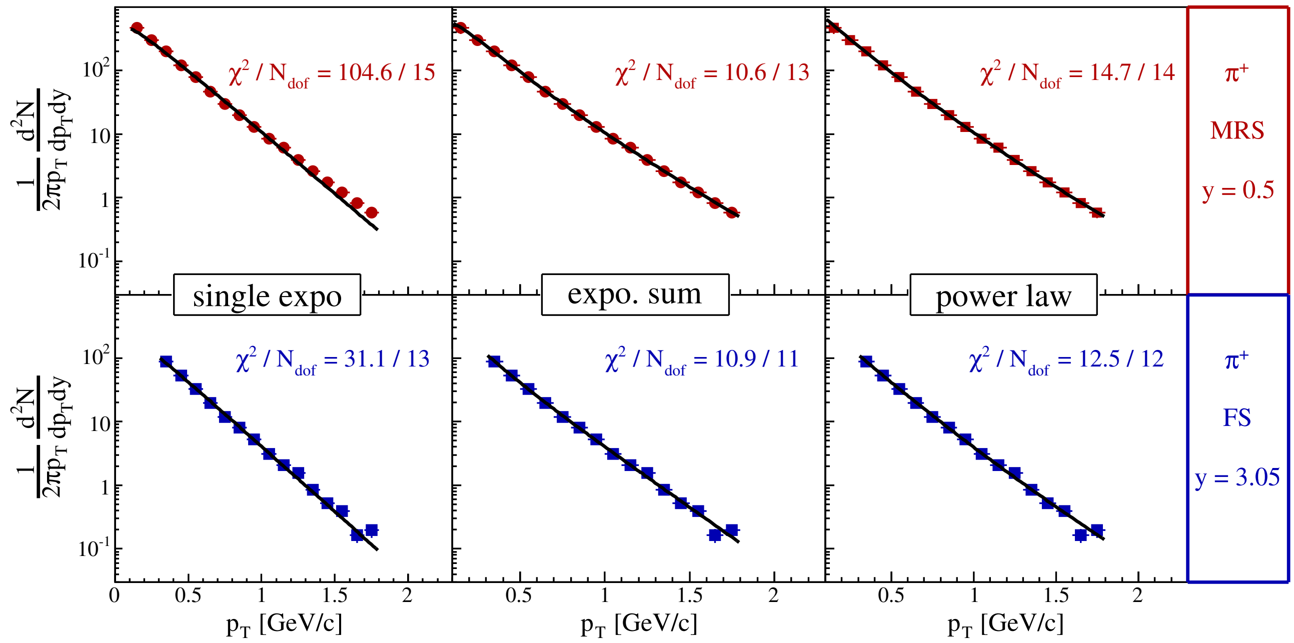

Fig. 6.4: Fit tests of pion spectra at two different rapidities. On the top (bottom) panels is shown an MRS (FS) spectrum ($y = 0.5\,(3.05) \pm 0.1\,(0.05)$). In both cases, the sum of exponential functions and the power law are equally good at describing spectra, unlike the single exponential.

sentation becomes

$$\exp\left[-\left(\sqrt{p_T^2+m^2}-m\right)/T_{\rm eff}\right] \tag{6.7}$$

Both the sum of exponential functions and power law give a good description of the spectra within the fit range, at mid–rapidity and most of the high rapidity intervals (see power law results in Tab. 6.7). In contrast, the single exponential poorly describes MRS spectra, and FS spectra when there is a good low p_T coverage. This deviation from a simple exponential is due to the strong "contamination" of pions from resonance decays at low p_T. The extrapolated yields deduced from the fits are:

Function	MRS ($y = 0.5$)	FS ($y = 3.05$)
Single exponential	271.5 ± 2.2	117.1 ± 1.4
Exponential sum	287.9 ± 3.2	130.1 ± 6.0
Power law	297.8 ± 3.3	129.3 ± 2.7

The extrapolated yield of the single exponential is systematically $\sim 10\%$ lower than the other extrapolations. Indeed, this fit underestimates the differential yield of the low p_T bins. This is visible in Fig. 6.5 that shows the same data as Fig. 6.4 but where each bin content has been multiplied by the normalization factor $2\pi\, p_T$ in order to have the (non invariant) differential yield d^2N/dp_Tdy.

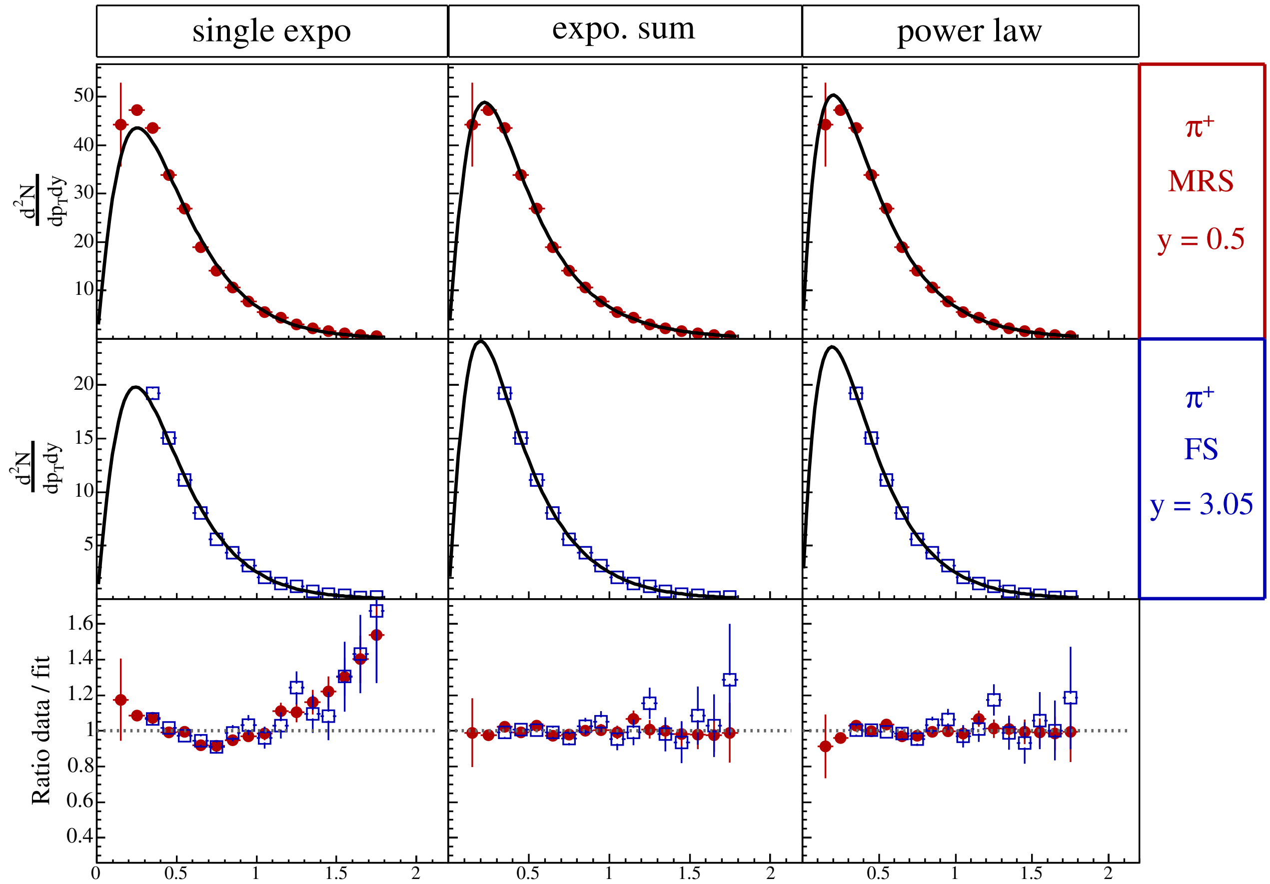

Fig. 6.5: Same as Fig. 6.4 but multiplied by $2\pi\, p_T$. The single exponential fit fails at describing the lower p_T region.

At high rapidities, the effect is less visible due to a worse coverage of the low p_T region. Regarding the difference between the exponential sum and the power law fits, it decreases as the rapidity increases. Nevertheless, the confidence level of sum of exponential fit becomes worse at high rapidities, the fit fails sometimes to separate the two a priori distinct exponential contributions. The power law fit has shown a rather stable behavior, in the sense that all spectra could be fitted with this function. Therefore, in the rest of the chapter, if not explicitly mentioned, extrapolated pion yields are those estimated by the power law fit. In the top panel of Fig. 6.6 are shown all fitted pion spectra. Results are listed in Tab. 6.7.

Kaon spectra are subject to less ambiguities. They are best described by the single exponential in m_T (power law and exponential sum fail to describe kaon spectra). The kaon results discussed further are therefore solely based on the single exponential fit. The fits are shown in the bottom panel of Fig. 6.6, and results listed in Tab. 6.8.

6.3 Results

In this section are presented results obtained from the fits discussed in the previous section. The focus is on the rapidity dependence of particle yields and other spectral features. The analysis focuses on the top 5% central events only.

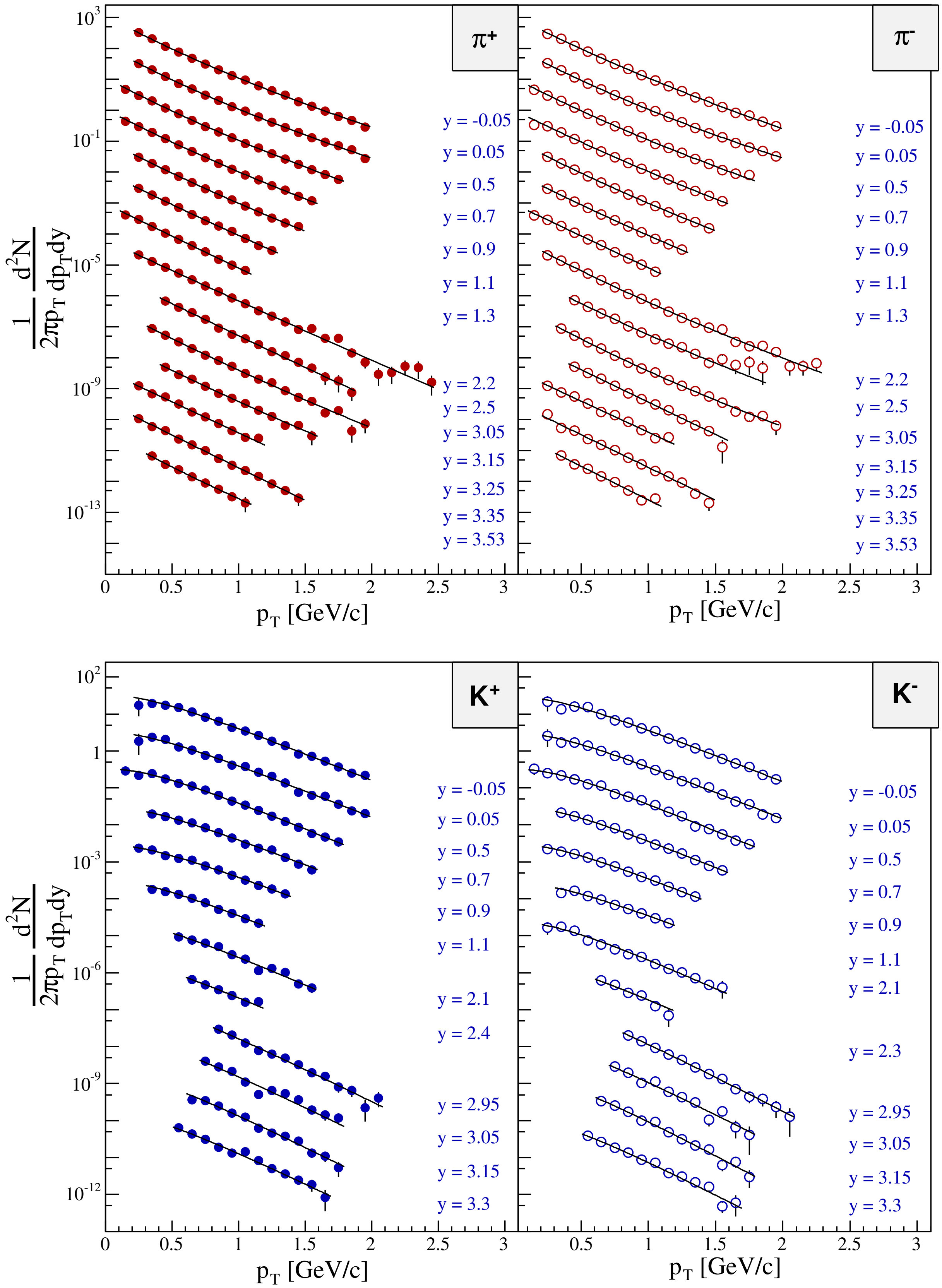

Fig. 6.6: Power law fits to pion spectra (top) and exponential fit to kaon spectra (bottom). Spectra have been scaled by 10^0, 10^{-1}, 10^{-2}, etc, from the top to the bottom.

6.3.1 Spectral Slopes and Mean Transverse Momentum

The pion and kaon slope parameters are obtained from the single exponential fit. It has been mentioned in the previous section that this fit poorly describes the overall shape of the pion spectra. Nevertheless, it is still valuable to select a p_T range common to all pion spectra, fit it with this function and study the systematic of the extracted slope with rapidity. The inverse slope parameter systematic is shown in Fig. 6.7.

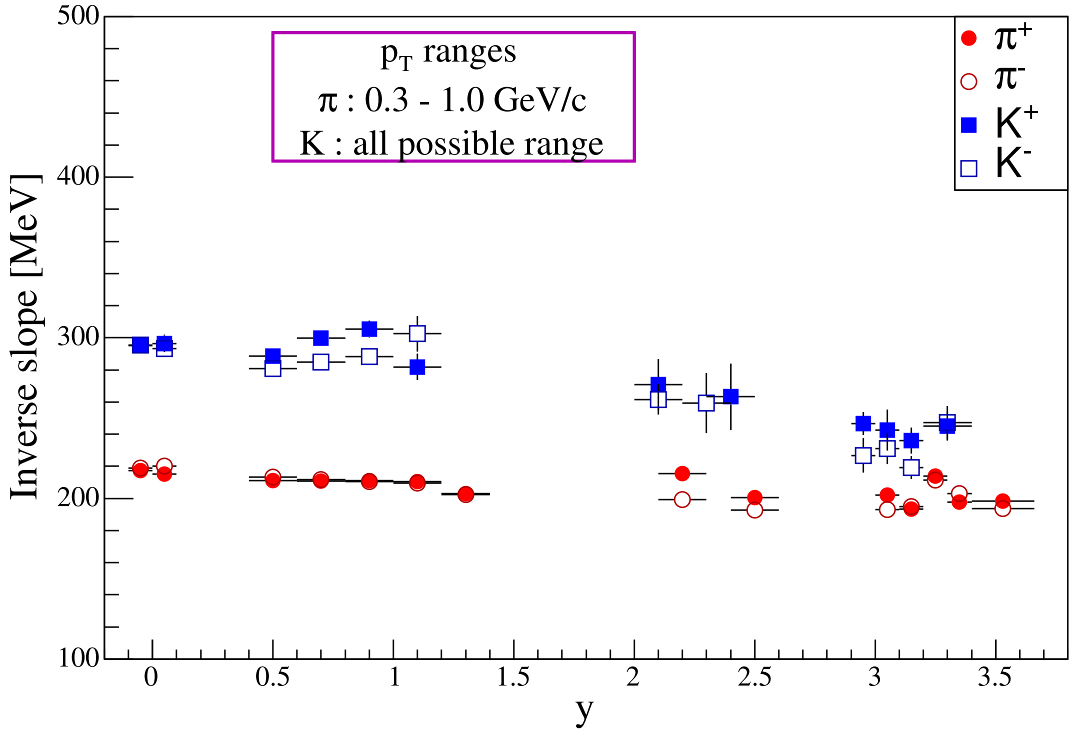

Fig. 6.7: Inverse slope parameter as a function of rapidity. The p_T range for pions is common to all spectra. Error bars are statistical.

The pion slopes have a remarkably small rapidity dependence. The difference between the two extremes is $\sim 20\,\text{MeV}$, so 10% of the estimated slopes. Kaon slopes show a stronger rapidity dependence. The mid–rapidity values ($0 \leq y \leq 1.1$) amount to $\sim 300\,\text{MeV}$ but start dropping as $y \gtrsim 2$. They finally reach values as low as $\sim 230\,\text{MeV}$ at $y \gtrsim 3$. The decrease therefore amounts to $\sim 25\%$ from mid–rapidity to the highest rapidities. Such a systematic can be interpreted as a smooth decrease of collective transverse flow as the rapidity increases. Together with the proton data of reference [30], a blast–wave analysis could be carried out in order to quantify the transverse flow systematic with rapidity.

Figure 6.8 shows the mean transverse momentum $\langle p_T \rangle$ of pions and kaons as a function rapidity. Using Eq. 6.1, this quantity is defined as follows:

$$\langle p_T \rangle = \frac{\int_0^\infty p_T \frac{d^2N}{dp_T dy}\, dp_T}{\int_0^\infty \frac{d^2N}{dp_T dy}\, dp_T} = \frac{\int_0^\infty 2\pi\, p_T^2\, f(p_T) dp_T}{\frac{dN}{dy}} \tag{6.8}$$

where $f(p_T)$ is the power law for pions (the other fit functions give the same results) and the single exponential for kaons.

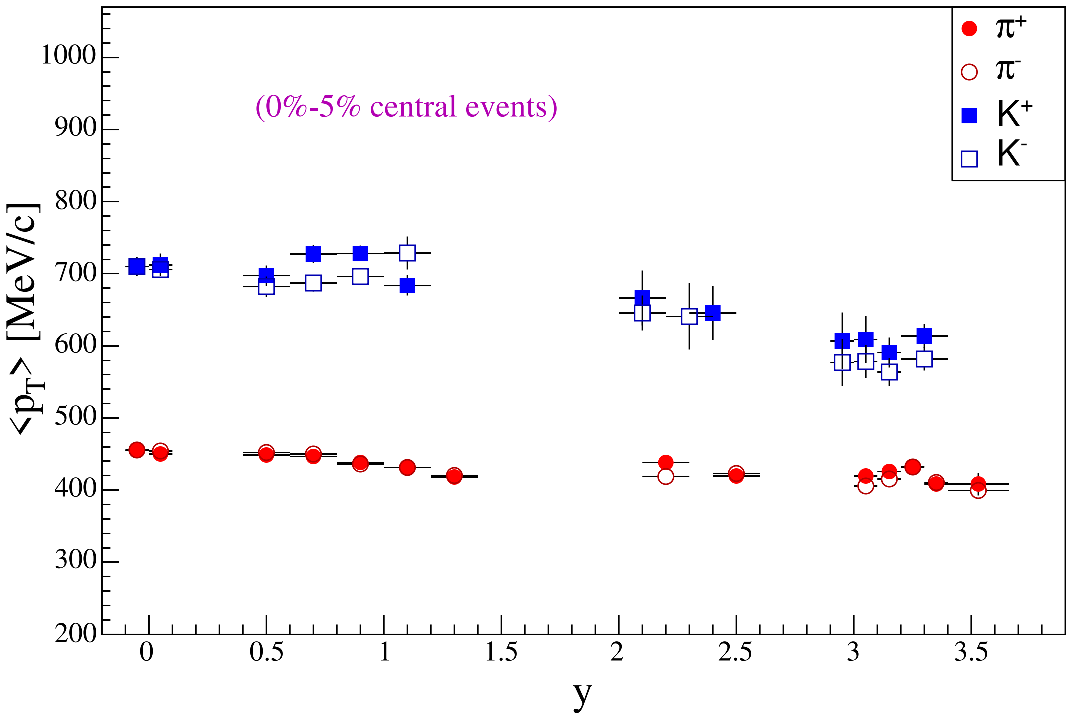

Fig. 6.8: Mean transverse momentum as a function of rapidity.

The correlation exhibits the same trend as seen in Fig. 6.7. The pion mean transverse momentum varies little with rapidity from $\sim 460\,\mathrm{MeV/c}$ at mid–rapidity down to $420\,\mathrm{MeV/c}$ at $y > 3$ (less than 10% difference) while kaons drop from $\sim 710\,\mathrm{MeV/c}$ to $\sim 580\,\mathrm{MeV/c}$. Also remarkable is the equality between spectral features of positive and negative particles of the same kind. This indicates that sources of particles and anti–particles have similar characteristics at all rapidities covered in this analysis.

6.3.2 Extrapolated Yields

Particle yields as a function of rapidity are calculated by extrapolating the fit functions to the full p_T range. The results are shown in Fig. 6.9. Both kaon and pion multiplicities show a maximum at mid–rapidity and decrease more and more rapidly with increasing rapidity (bell–shape). Negative and positive pions are equally distributed within the statistical errors, dN/dy amounts to ~ 300 at $y = 0$ and drops to ~ 90 at $y \approx 3.5$, i.e. a decrease of more than 2/3. Kaons are redrawn in the bottom panel of Fig. 6.9 for better visualization. It is found that $dN/dy(K^-)$ are systematically lower than $dN/dy(K^+)$ at all rapidities. At $y < 1$, positive (negative) kaon yields amount to ~ 47 (44) while high rapidity yields are in the order or 18 (10). The drop between these two extremes $\sim 62\%$ (77%).

Although the present data do not cover the whole rapidity range, there is enough rapidity coverage to estimate the total integral after reflection of the data around $y = 0$ (since Au+Au is a mass symmetric system). This is done by fitting the rapidity density distribution by an even function. Figure 6.10 shows three different estimations. The first one (top) is based on a Gaussian fit whose mean is fixed to $y = 0$, the second fit (middle) uses a sum of two Gaussian functions placed symmetrically with respect to mid–rapidity (both Gaussian functions have

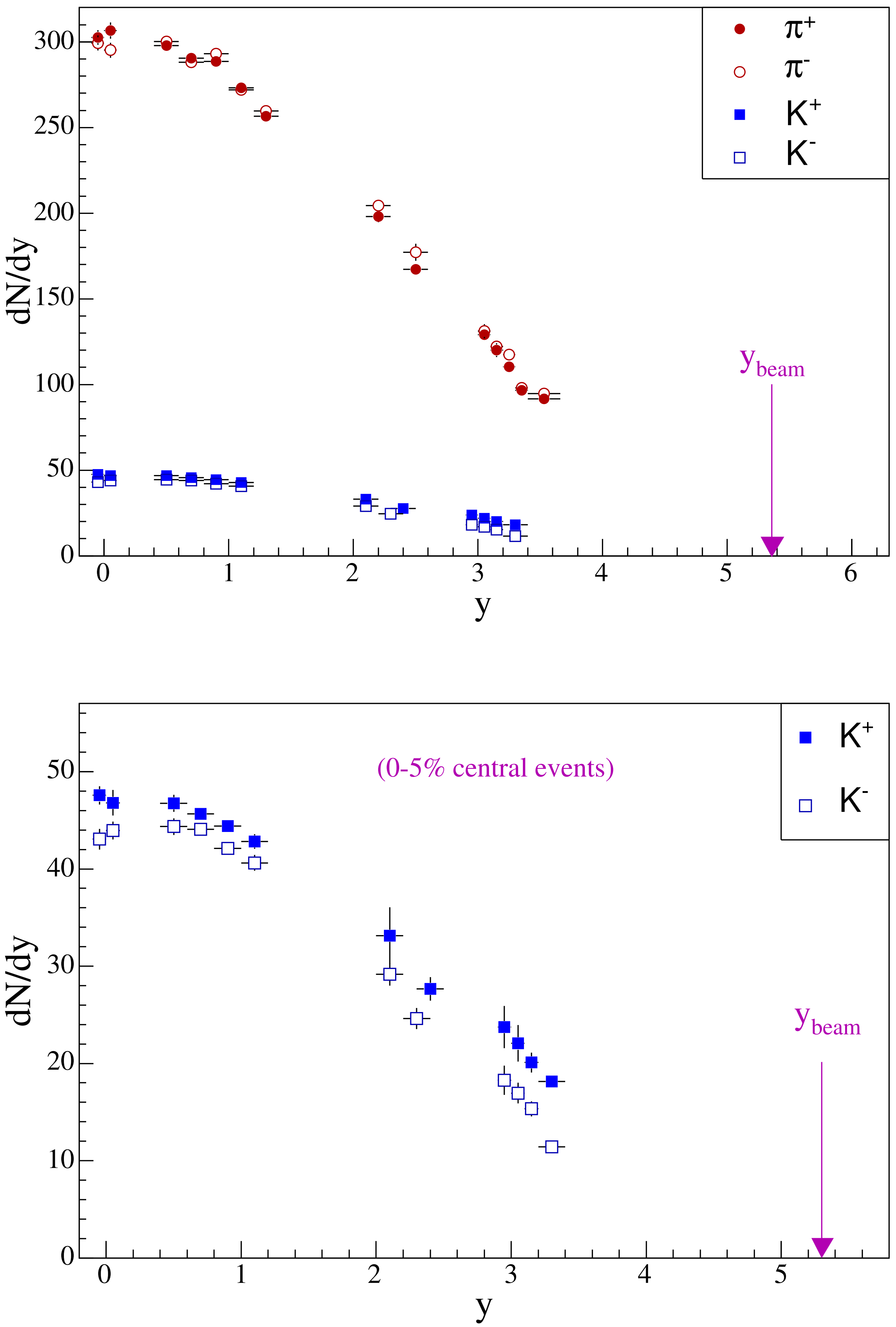

Fig. 6.9: Pion and kaon rapidity densities as a function of rapidity. Error bars are statistical.

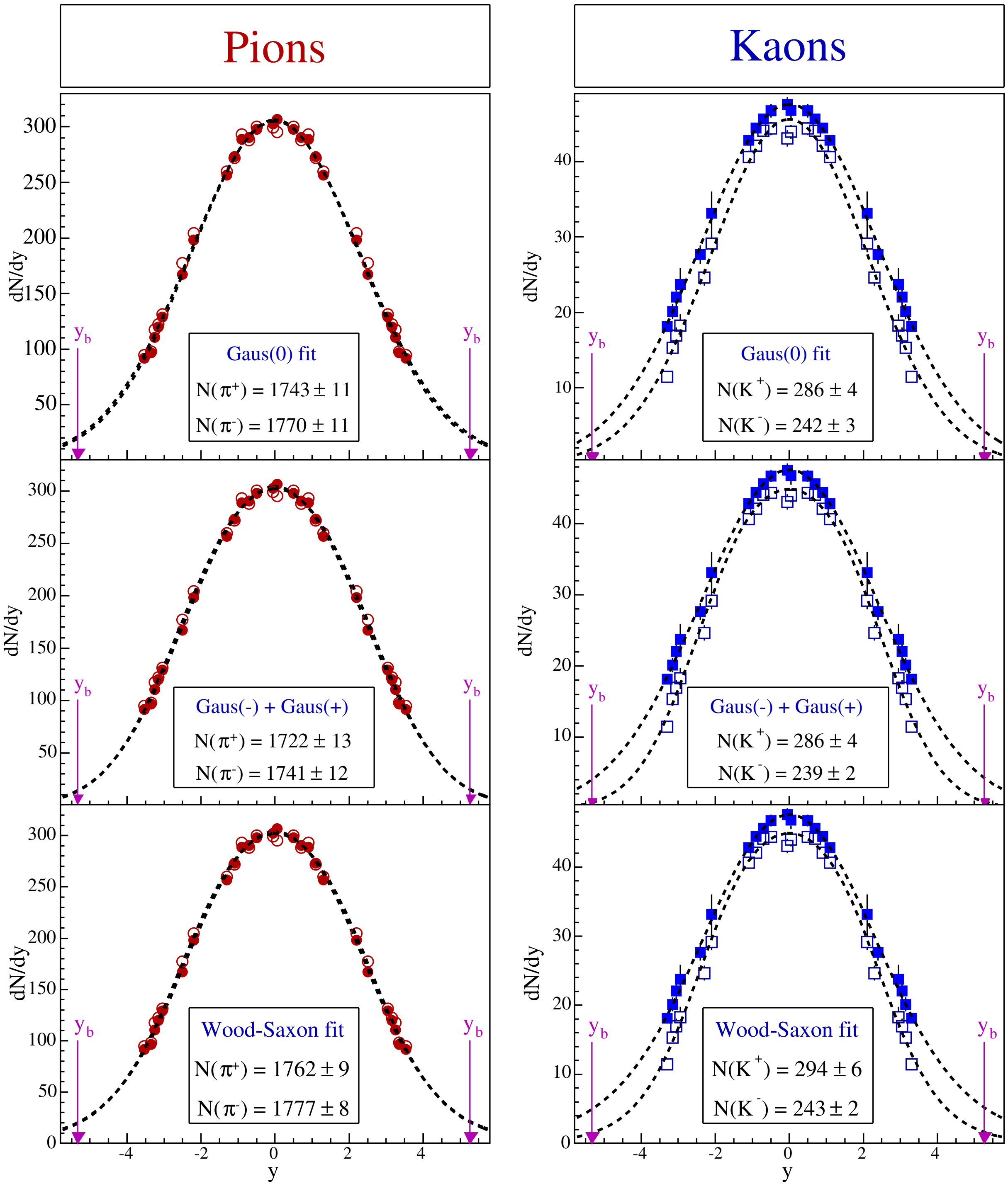

Fig. 6.10: Fits of pion and kaon rapidity distributions: single Gaussian (top), symmetric sum of Gaussian (middle) and symmetrized Wood-Saxon (bottom). Only measured data points are fitted. Including reflected data points in the fit do not change the results. Fits are equally good in terms of χ^2/N_{dof} ($\sim$ 0.6 and 1 for positive and negative particles respectively in all three cases).

the same width and opposite means) that is referred to as “Gaussian sum” in the rest of the thesis, the last one (bottom) consists of a symmetrized Wood–Saxon function:

$$\text{Gaussian:}\quad \frac{N}{\sigma_y\sqrt{2\pi}}\,\exp\left(-y^2/2\sigma_y^2\right) \tag{6.9}$$

$$\text{Sum of Gaussian:}\quad \frac{N}{2\sigma_y\sqrt{2\pi}}\,\left\{\exp\left[-(y+y_0)^2/2\sigma_y^2\right] + \exp\left[-(y-y_0)^2/2\sigma_y^2\right]\right\} \tag{6.10}$$

$$\text{Wood–Saxon:}\quad a/\left\{1 + \exp\left[(y-y_0)/\sigma_y\right] + \exp\left[-(y+y_0)/\sigma_y\right]\right\} \tag{6.11}$$

where N is the total yield (set as a parameter when possible), σ_y the rapidity width and y_0 the (positive and negative) mean rapidity. For the Wood-Saxon fit, it is not possible to analytically derive the normalization factor a. In order to evaluate the statistical error on the total yield, each data point has been randomly moved within the corresponding statistical error (according to a Gaussian distribution). At each throw, the Wood-Saxon fit has been processed and the integral calculated in ROOT has been stored in a histogram. After 5000 throws, the histogram has shown a Gaussian distribution whose mean and width are the values tabulated in Tab. 6.2. There is good agreement between the different fits, only $\sim 2\%$ (3%)

	Single Gaussian		Gaussian sum			Wood-Saxon		
	N	σ_y	N	y_0	σ_y	N	y_0	σ_y
π^+	1743±11	2.28±0.02	1722±13	1.22±0.09	1.81±0.12	1762±9	2.35±0.16	1.06±0.08
π^-	1770±11	2.33±0.02	1741±12	1.27±0.08	1.81±0.11	1777±8	2.44±0.16	1.06±0.09
K^+	286±4	2.42±0.06	286±4	0.02±3.57	2.42±0.25	294±6	1.59±1.81	1.48±0.54
K^-	242±3	2.12±0.04	239±2	1.19±0.13	1.60±0.21	243±2	2.24±0.26	0.96±0.16

Tab. 6.2: Total yield estimation and fit parameters. Errors are statistical.

difference at most is noticed for pion (kaon) yields. Note that there was no requirement that dN/dy should be zero at the beam rapidity. Moreover, the integrals have been calculated from $y = -\infty$ to $+\infty$. Restricting integrals to the range $|y| < 5.36$ (beam rapidity) reduces yields by at most 2%. Errors remain unaffected. Note also that fitting measured data points or measured + reflected data points does not significantly affect the results (less than 2%).

6.3.3 Particle Ratios

From particle yields, ratios are derived where rapidity intervals are common between kaons and pions. The rapidity dependence of ratios quantifies differences and similarities of particle sources (see discussion in Chap. 7).

Like–particle Ratios

Figure 6.11 shows like–particle ratios as a function of rapidity. These ratios are defined as $dN/dy(-)\,/\,dN/dy(+)$. The dashed lines represent ratios between the fit functions obtained in the previous section. As can be seen, the pion ratio is consistent with unity along the covered rapidity range. The fits hint toward a slight increase with rapidity, which would not be surprising because of isospin conservation (see Chap. 7). The kaon ratio behaves differently. While the ratio is constant from mid–rapidity to $y \approx 1.1$ and amounts to ~ 0.94, a drop occurs around $y \approx 2$, described by the last two fits. The kaon ratio decreases down to ~ 0.6 at the highest rapidity ($y = 3.3$). Such a behavior is discussed in Chap. 7.

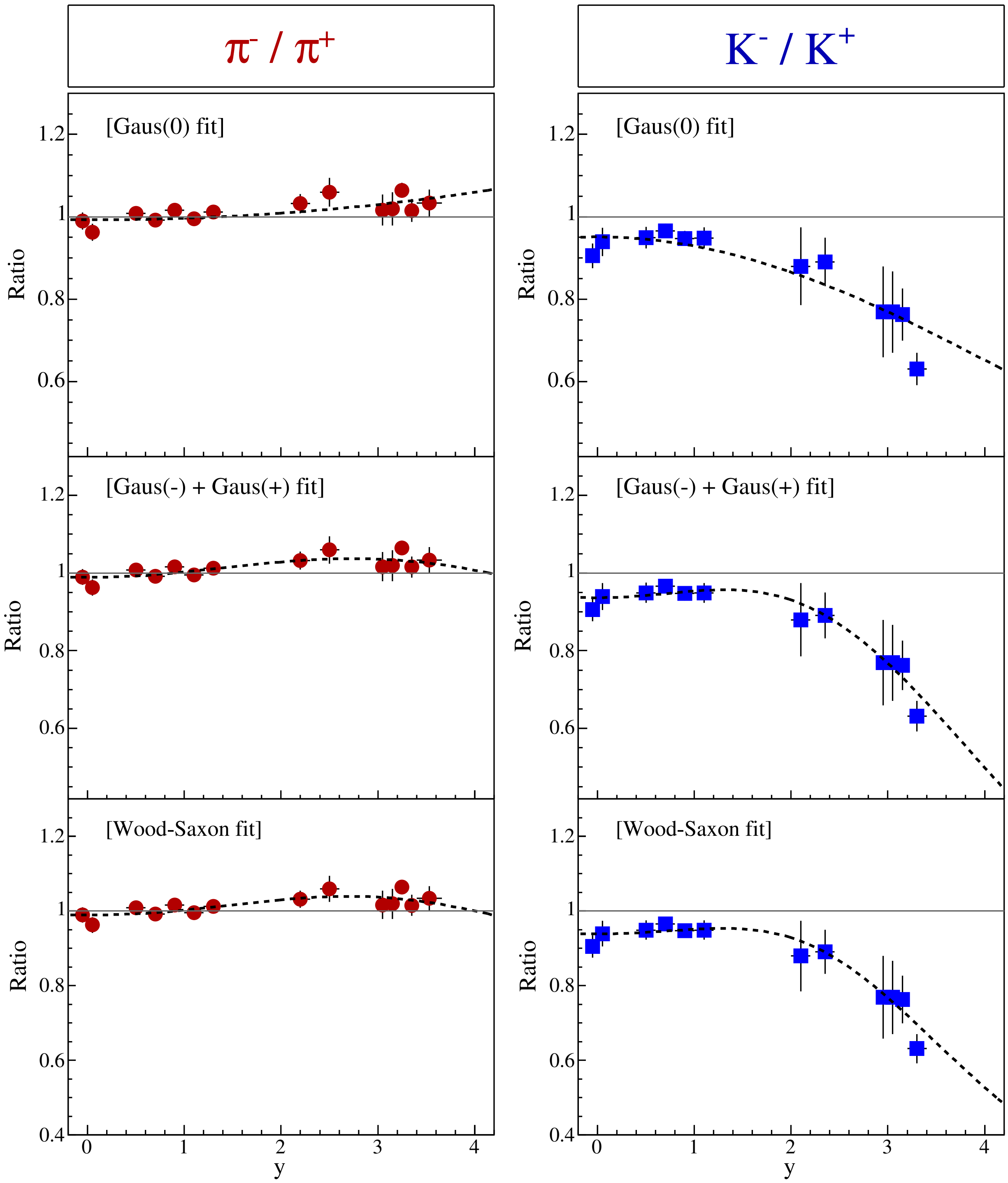

Fig. 6.11: Like–particle ratios as a function of rapidity. The dashed lines are ratios between fits obtained in the previous section. The solid line is to mark the difference with unity.

Kaon to Pion Ratio

The kaon to pion ratio is shown in Fig. 6.12 as a function of rapidity. At $y \approx 2$ and $y \approx 3.3$, kaon and pion rapidity intervals slightly differ. Therefore, an interpolation has been made between the kaon points in order to calculate a value at $y = 2.2$, where pion data exists, and between the pion points so as to compare with the kaon rapidity density at $y = 3.3$. Both positive and negative ratios show the mid–rapidity plateau structure already seen in the like–particle ratios. In this region, they amount to ~ 0.156 and 0.147 respectively. As the rapidity increases, the positive ratio remains constant within the statistical errors although dN/dy fit ratios tend to increase at $y \gtrsim 2$ up to ~ 0.17 whereas the negative ratio drops significantly and reaches ~ 0.10 at $y = 3.3$. In Chap. 7 is detailed a comparison with lower energy experiments. The statistical model "predictions" at $\sqrt{s_{NN}} = 200\,\mathrm{GeV}$ are also discussed, together with calculations from parton cascade models.

6.4 Systematic Errors

Ideally, a detailed Monte–Carlo study of all steps (from PID to final spectra) would give an estimation of the final systematic errors. Since it could not be achieved due to lack of time, systematic errors are evaluated from the data. Following reference [30], the errors are divided into two categories:

→ Error introduced by fitting spectra and extrapolating yields,
→ Error on the normalization of settings measuring the same phase–space.

6.4.1 Error from Fit

The stability of the fit has been studied by:

→ varying the fit range (increased lower limit by 1 bin and decreased upper limit by 1 bin, alternatively),
→ varying the p_T bin size,
→ removing edge bins from the rapidity interval (alternatively),
→ fitting with other fit functions that could describe the spectra (sum of exponentials for pions and exponential in p_T for kaons).

The average systematic error introduced by the fit is then estimated as

$$\sigma_{fit} = \sqrt{\sum_i (x - x_i)^2} \tag{6.12}$$

where x_i is the extrapolated dN/dy after variation i and x is the original result. Results are listed in Tab. 6.3.

y	-0.05	0.05	0.50	0.70	0.90	1.10	1.30	2.20	2.50	3.05	3.15	3.25	3.35	3.53
π^-	1.2%	0.9%	1.1%	1.4%	0.9%	0.8%	1.7%	2.8%	3.8%	4.3%	4.2%	3.0%	4.8%	3.1%
π^+	1.5%	1.5%	0.9%	1.2%	0.9%	0.5%	1.5%	3.4%	2.9%	2.6%	6.5%	3.4%	3.9%	3.4%

Tab. 6.3: Estimated systematic errors of pion fits. The high rapidity data are more sensitive to small variations (see text).

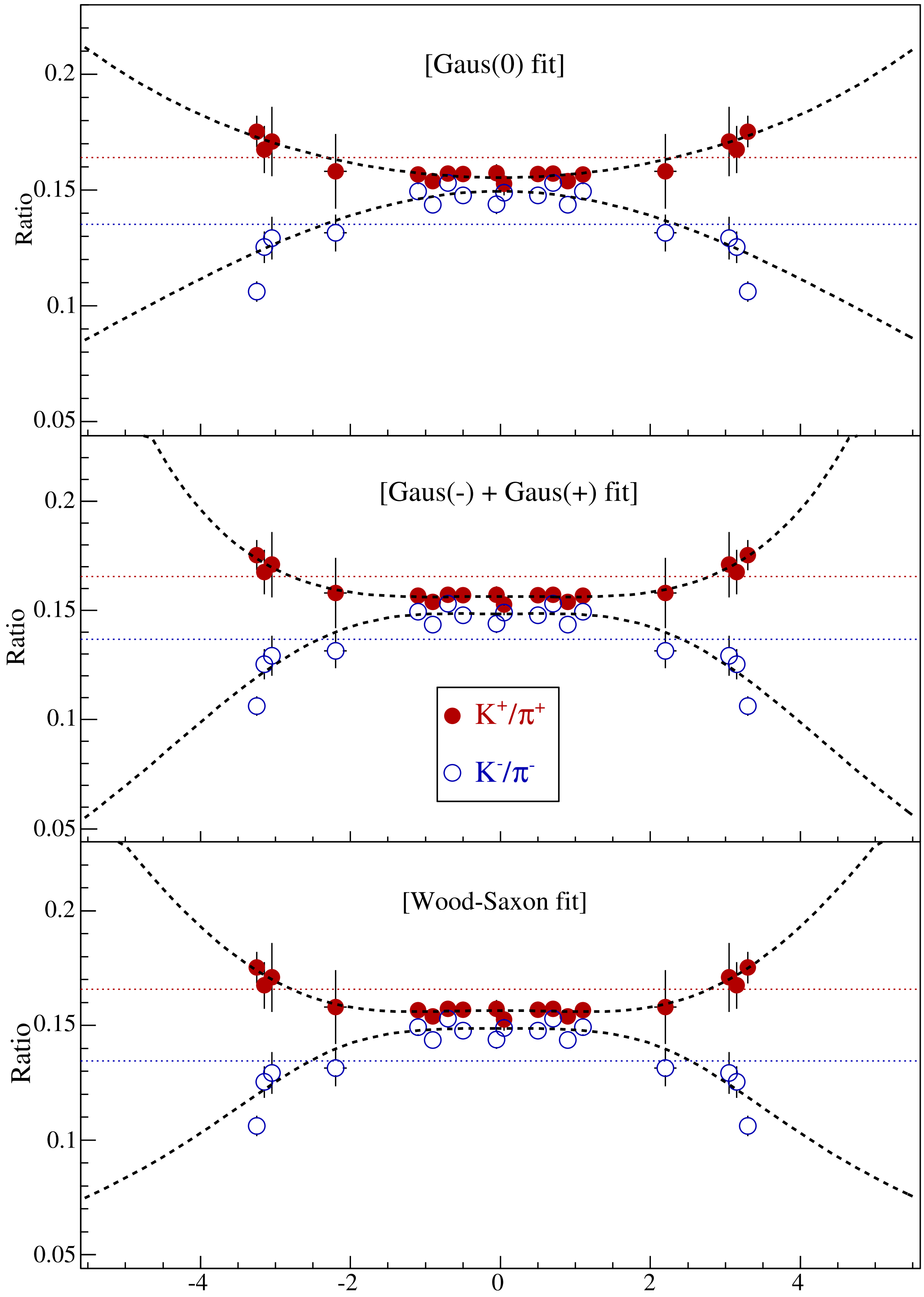

Fig. 6.12: Kaon over pion ratio as a function of rapidity. The dashed lines are ratios of fits like in Fig. 6.11 and 6.10. The dotted lines are estimated 4π ratios.

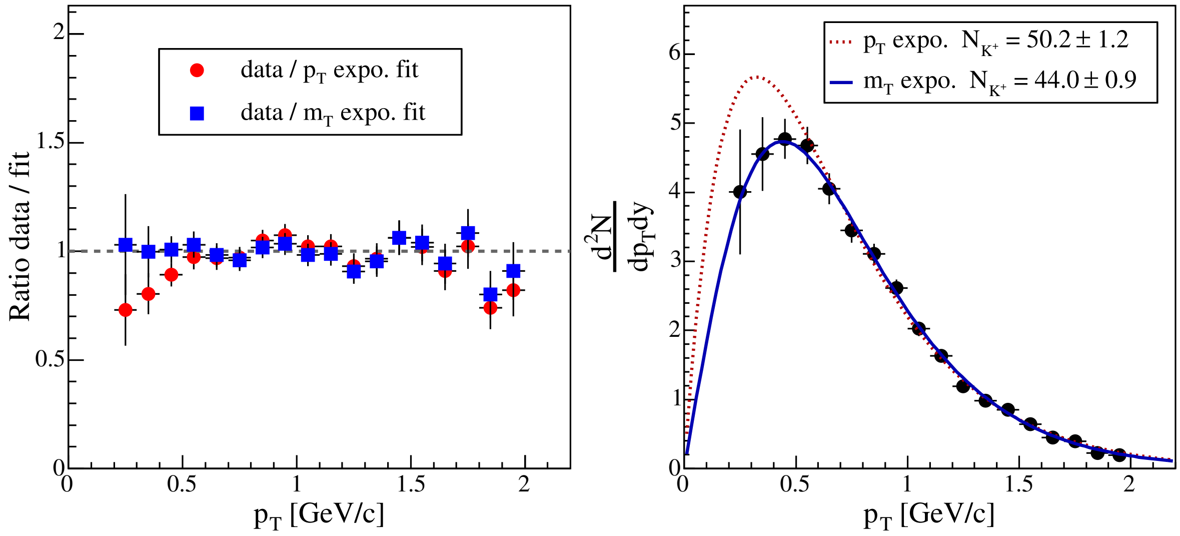

Fig. 6.13: Comparison between exponential in p_T and m_T fits on kaon data (MRS data).

As can be seen from Tab. 6.3, the errors on the FS data are systematically larger than the MRS errors. This is due to the better low p_T coverage of the MRS, which constrains the fits more effectively. Kaon fitting systematic errors are shown in Tab. 6.4.

y	-0.05	0.05	0.50	0.70	0.90	1.10	2.10	2.30 (2.40)	2.95	3.05	3.15	3.3
K^-	1.6%	1.0%	0.8%	0.4%	0.3%	0.5%	3.0%	4.0%	4.0%	5.3%	2.4%	5.6%
K^+	2.5%	2.9%	0.8%	0.5%	1.7%	1.4%	4.8%	5.6%	3.3%	4.8%	5.3%	4.4%

Tab. 6.4: Estimated systematic errors of kaon fits.

The errors on kaon data tabulated in Tab. 6.4 are evaluated without taking into account the yield estimation from exponential in p_T fits. These errors are increased by a factor ranging between 2 and 4 (rapidity dependent) when this fit is included in Eq. 6.12. Figure 6.13 shows the ratio between data and fits, and the difference in yield extrapolation at low p_T. In the MRS, the low p_T coverage allows to disregard the p_T fit. This is not obvious for high rapidity data where the lowest p_T bin is often too high to rule out the exponential in p_T but the relatively smooth dependence of the slope parameter with rapidity (Fig. 6.7) gives confidence that the exponential in m_T is a better choice and therefore that the yield extrapolation from a pure exponential in p_T fit can be excluded from the error estimation.

6.4.2 Error From Discrepancies between Data Sets

Particle spectra are often obtained by the combination of several data sets that cover the same phase–space or so. In order to evaluate the systematic error introduced by discrepancies between data sets, spectra are constructed for each of them within the common acceptance. Yields are then calculated by counting particles in the overlapping region. This leads to different measurements of the same quantity $dN/dy|_{s,acc}$. A weighted average over the individual measurements and corresponding χ^2 are derived:

$$\langle Y_{acc} \rangle = \left\langle \frac{dN}{dy} \right\rangle_{acc} = \frac{\sum_s w_s \times dN/dy|_{s,acc}}{\sum_s w_s} \tag{6.13}$$

with weight w_s defined as $w_s = 1/\sigma_s$ so that large statistical errors carry less weight, and

$$\chi^2_{measured} = \sum_s \frac{\left(\langle Y_{acc}\rangle - dN/dy|_{s,acc}\right)^2}{\sigma_s^2} \tag{6.14}$$

The number of degrees of freedom is equal to $N_{sets} - 1$. When $\chi^2_{measured}/N_{dof} \gg 1$, the statistical errors are not enough to explain the difference between settings. A systematic error that scales with the statistical error is added so that the reduced χ^2 in the considered phase–space region becomes 1. It reads:

$$\chi^2 = \sum_s \frac{\left(\langle Y^+\rangle - Y_s^+\right)^2}{\sigma^2_{Y_s^+}(1+\alpha^2)} + \sum_s \frac{\left(\langle Y^-\rangle - Y_s^-\right)^2}{\sigma^2_{Y_s^-}(1+\alpha^2)} \tag{6.15}$$

where $Y^{+(-)}$ is the positive (negative) pion or kaon dN/dy. This equation is used for the MRS data sets where both charge signs are detected in each setting. For FS data sets, only negative or positive particles are considered in the modified χ^2. Requiring that $\chi^2/N_{dof} = 1$ determines the scale factor α. The systematic error is then $\sigma = \alpha \times \sigma_{stat}$. The resulting systematic error depends on the yield in the covered range, i.e. it scales with the yield. The total systematic error originating from data set comparison is therefore scaled with the total yield of the corresponding rapidity interval as follows

$$\sigma_{scaled} = \alpha\, \sigma_{stat} \left(\frac{dN/dy_{tot}}{dN/dy|_{acc}}\right) \tag{6.16}$$

(although the total yield only gives a rough scale factor due to error on the extrapolation that led to it). The total systematic error is then defined as $\sigma^2_{syst} = \sigma^2_{fit} + \sigma^2_{scaled}$, assuming that errors from fitting and from combining data sets are independent. Note that only a limited p_T range at each rapidity interval is common to FS data sets, which do not include the most populated bins (low p_T). Therefore, the assumption is that the scaling is valid for the whole range. In Tab. 6.5 and 6.6 are listed the relevant quantities that lead to the final systematic errors.

6.4.3 Other Sources of Systematic Errors

Some sources of systematic errors do not depend on rapidity, like errors introduced by track matching in the magnets, PID procedures, or efficiency estimations. For example, the tracking efficiency estimated by the track embedding and reference track methods discussed in Sec. 5.4.1 disagree by up to 10% in the FS. Another main source of systematic error is the particle yield extrapolation at low p_T. In order to verify the behavior of the fit functions, transverse momentum spectra calculated by the event generator HIJING [10] have been fitted with the three test functions within p_T ranges corresponding to the experimental acceptance. HIJING spectra are not a priori described by these functions. The extrapolated yields have been compared with yields calculated by HIJING. The difference found are not significant (in the order of 1%) for the fit functions chosen in this analysis.

	Rapidity	p_T range [GeV/c]	dN/dy_{acc} weighted	χ^2/N_{dof}	α	$\sigma_{scaled}\,/\,(dN/dy_{tot})$
π^+	-0.05	0.7–1.9	64.2 ± 1.8	53.6 / 11	3.1	8.4%
π^-		0.7–1.8	63.3 ± 1.4	50.3 / 11		6.8%
π^+	0.05	0.7–2.0	64.2 ± 1.1	35.2 / 9	3.0	4.9%
π^-		0.7–1.7	62.0 ± 2.4	44.0 / 9		11.8%
π^+	0.50	0.3–1.6	197.0 ± 2.2	62.6 / 3	6.1	6.9%
π^-		0.3–1.7	201.7 ± 2.5	14.4 / 3		7.8%
π^+	0.70	0.5–1.5	93.3 ± 1.6	14.6 / 6	2.2	3.9%
π^-		0.5–1.5	92.9 ± 1.6	14.8 / 6		3.7%
π^+	0.90	0.8–1.3	35.4 ± 1.3	61.2 / 9	3.9	14.7%
π^-		0.8–1.3	35.3 ± 1.2	68.9 / 9		13.3%
π^+	1.10	0.5–1.1	87.8 ± 1.3	117.1 / 9	5.7	8.7%
π^-		0.5–1.0	88.8 ± 1.4	147.6 / 9		8.9%
π^+	1.30	0.2–1.1	177.9 ± 2.3	147.2 / 4	8.9	11.7%
π^-		0.4–1.1	101.9 ± 1.4	91.9 / 4		12.7%
π^+	2.20	0.8–1.2	17.4 ± 0.6	76.6 / 4	4.2	15.3%
π^-		0.8–1.2	16.5 ± 0.4	51.4 / 4	3.4	9.6%
π^+	2.50	0.5–0.9	39.0 ± 1.3	2.1 / 2	< 1	3.1% (σ_{stat})
π^-		0.5–0.9	36.9 ± 0.5	165.1 / 3	7.35	10.4%
π^+	3.05	1.0–1.5	5.4 ± 0.3	11.8 / 2	2.2	13.8%
π^-		1.0–1.6	6.1 ± 1.1	1.2 / 2	< 1	17.8% (σ_{stat})
π^+	3.15	1.0–1.6	4.1 ± 0.2	11.1 / 2	2.1	11.5%
π^-		0.7–1.8	3.9 ± 0.2	10.7 / 2	2.1	13.7%
π^+	3.25	0.7–1.2	17.6 ± 0.4	31.0 / 1	5.5	13.9%
π^-		0.7–1.2	18.1 ± 0.4	81.8 / 1	9.0	21.4%
π^+	3.35	0.7–1.1	14.1 ± 0.5	23.7 / 2	3.3	11.6%
π^-		0.7–1.1	14.9 ± 0.5	30.7 / 2	3.8	12.3%
π^+	3.53	0.4–0.7	20.9 ± 0.6	6.4 / 1	2.3	6.6%
π^-		0.4–0.7	22.1 ± 1.2	9.9 / 1	3.0	15.6%

Tab. 6.5: Estimated systematic error from pion data set comparison.

	Rapidity	p_T range [GeV/c]	$\frac{dN}{dy_{acc}}$ (weighted)	χ^2/N_{dof}	α	$\frac{\sigma_{scaled}}{dN/dy_{tot}}$	
K^+	-0.05	0.8–1.6	15.9 ± 1.1	27.3 /10	1.3	9.4%	
K^-		0.7–1.7	16.1 ± 0.8	8.4 /10	< 1	5.0%	(σ_{stat})
K^+	0.05	0.7–1.7	19.7 ± 0.7	45.3 / 8	2.2	7.6%	
K^-		0.7–1.5	18.5 ± 0.7	6.2 / 8	< 1	3.8%	(σ_{stat})
K^+	0.50	0.5–1.5	28.7 ± 0.9	2.5 / 3	< 1	3.1%	(σ_{stat})
K^-		0.5–1.5	27.2 ± 0.9	0.9 / 3	< 1	3.3%	(σ_{stat})
K^+	0.70	0.8–1.1	7.9 ± 0.6	1.7 / 6	< 1	7.6%	(σ_{stat})
K^-		0.8–1.1	7.2 ± 0.6	13.6 / 6	1.2	10.3%	
K^+	0.90	0.6–1.3	19.1 ± 0.5	5.9 / 7	< 1	2.6%	(σ_{stat})
K^-		0.6–1.2	16.9 ± 0.6	8.5 / 7	1.0	3.5%	
K^+	1.10	0.6–1.1	14.8 ± 0.6	17.3 / 4	3.0	12.6%	
K^-		0.6–1.1	14.0 ± 0.5	23.3 / 4		10.9%	
K^+	2.10	0.8–1.6	10.0 ± 1.1	$\ll 1$	< 1	11.8%	(σ_{stat})
K^-		0.8–1.5	5.9 ± 0.3	0.3 / 1	< 1	5.2%	(σ_{stat})
K^+	2.40	0.5–0.9	11.3 ± 0.5	1.7 / 1	< 1	4.4%	(σ_{stat})
K^-	2.30	0.4–0.8	11.9 ± 0.4	20.8 / 2	3.1	11.2%	
K^+	2.95	1.0–2.0	2.7 ± 0.2	3.8 / 1	1.7	12.1%	
K^-		1.0–1.7	2.1 ± 0.3	$\ll 1$	< 1	16.8%	(σ_{stat})
K^+	3.05	0.7–1.8	6.8 ± 0.3	22.9 / 1	4.7	20.8%	
K^-		0.7–1.6	5.0 ± 0.2	13.4 / 1	3.5	18.0%	
K^+	3.15	0.7–1.3	5.7 ± 0.2	10.1 / 2	2.0	9.2%	
K^-		0.7–1.3	4.0 ± 0.2	2.1 / 2	< 1	4.9%	(σ_{stat})

Tab. 6.6: Estimated systematic error from kaon data set comparison. The multiplicity at the highest rapidity interval ($y = 3.3$) has been obtained with only one data set. The systematic error is set to 20%.

	y interval	fit range	dN/dy	$\langle p_T \rangle_{\mathrm{fit}}$ (MeV/c)	χ^2/N_{dof}	$(dN/dy)^{\mathrm{counting}}_{\mathrm{fitrange}}$	$(dN/dy)^{\mathrm{fit}}_{\mathrm{fitrange}}$	Fraction
π^+	$-0.10 \leq y \leq 0.00$	$0.2 \leq p_T \leq 2.0$	302.5 ± 4.3	455.1 ± 3.7	27.7 / 15	229.6	227.6	75.9%
π^-			299.4 ± 4.4	455.3 ± 4.1	20.5 / 15	226.7	227.1	75.7%
π^+	$0.00 \leq y \leq 0.10$	$0.2 \leq p_T \leq 2.0$	306.6 ± 4.8	450.0 ± 4.2	15.7 / 15	229.4	220.1	74.8%
π^-			295.1 ± 6.7	453.9 ± 3.9	25.4 / 15	224.4	221.3	75.7%
π^+	$0.40 \leq y \leq 0.60$	$0.1 \leq p_T \leq 1.8$	297.8 ± 3.7	448.7 ± 4.0	14.7 / 14	266.8	271.0	89.5%
π^-			300.3 ± 3.8	452.3 ± 4.1	26.3 / 14	268.1	273.5	89.2%
π^+	$0.60 \leq y \leq 0.80$	$0.1 \leq p_T \leq 1.7$	290.4 ± 2.8	446.2 ± 3.8	13.7 / 13	257.9	263.8	88.9%
π^-		$0.2 \leq p_T \leq 1.6$	288.0 ± 2.4	449.7 ± 3.6	9.6 / 12	249.8	262.0	86.7%
π^+	$0.80 \leq y \leq 1.00$	$0.2 \leq p_T \leq 1.5$	288.6 ± 2.0	438.0 ± 2.6	12.8 / 10	213.5	213.5	74.0%
π^-			293.1 ± 2.1	436.1 ± 2.7	12.3 / 10	215.7	215.7	73.6%
π^+	$1.00 \leq y \leq 1.20$	$0.1 \leq p_T \leq 1.3$	273.3 ± 3.1	431.0 ± 5.6	17.9 / 9	246.8	244.6	90.4%
π^-		$0.2 \leq p_T \leq 1.3$	272.0 ± 2.7	431.4 ± 4.2	4.5 / 8	198.4	198.2	72.9%
π^+	$1.20 \leq y \leq 1.40$	$0.1 \leq p_T \leq 1.1$	256.6 ± 1.8	418.1 ± 3.8	20.3 / 7	224.2	226.4	87.4%
π^-			259.7 ± 2.1	420.5 ± 3.4	16.2 / 7	225.6	229.5	86.9%
π^+	$2.10 \leq y \leq 2.30$	$0.2 \leq p_T \leq 2.4$	198.2 ± 3.5	438.1 ± 5.4	40.5 / 19	151.5	150.2	77.4%
π^-		$0.2 \leq p_T \leq 2.3$	204.5 ± 2.9	423.2 ± 10.0	48.6 / 18	149.4	151.0	73.0%
π^+	$2.40 \leq y \leq 2.60$	$0.3 \leq p_T \leq 2.1$	167.2 ± 3.3	419.5 ± 6.4	30.5 / 15	97.0	97.4	57.3%
π^-		$0.4 \leq p_T \leq 1.9$	177.2 ± 4.9	405.4 ± 7.2	24.3 / 12	75.8	74.6	42.6%
π^+	$3.00 \leq y \leq 3.10$	$0.3 \leq p_T \leq 2.0$	129.0 ± 2.7	419.3 ± 5.4	21.7 / 16	73.4	73.4	56.9%
π^-		$0.3 \leq p_T \leq 2.1$	131.1 ± 4.1	405.4 ± 7.2	11.1 / 15	71.0	71.3	54.2%
π^+	$3.10 \leq y \leq 3.20$	$0.4 \leq p_T \leq 1.6$	120.0 ± 4.0	425.7 ± 10.5	17.2 / 9	50.7	51.0	42.2%
π^-			122.3 ± 2.6	415.6 ± 5.9	14.2 / 9	51.5	51.7	42.1%
π^+	$3.20 \leq y \leq 3.30$	$0.2 \leq p_T \leq 1.2$	110.4 ± 1.2	432.5 ± 6.1	44.3 / 7	83.7	81.4	75.9%
π^-			117.5 ± 1.6	432.1 ± 5.5	60.0 / 7	87.4	86.7	74.4%
π^+	$3.30 \leq y \leq 3.40$	$0.2 \leq p_T \leq 1.5$	96.5 ± 1.9	408.6 ± 10.7	26.3 / 10	70.2	71.1	72.7%
π^-		$0.2 \leq p_T \leq 1.6$	98.0 ± 1.6	410.5 ± 4.9	50.9 / 11	76.6	72.7	78.1%
π^+	$3.40 \leq y \leq 3.66$	$0.3 \leq p_T \leq 1.1$	91.6 ± 2.6	408.1 ± 10.7	14.1 / 5	49.0	49.0	51.8%
π^-			94.7 ± 1.6	399.3 ± 4.5	46.3 / 5	50.9	50.3	53.7%

Tab. 6.7: Results of the power law fits to pion spectra for the top 5% central events. The errors are statistical. The last three columns list the yields calculated from the data within the fit range, the yield estimated from the fit within the fit range and the fraction of the counted yield to the total yield, i.e. the coverage of the setting.

	y interval	fit range	dN/dy	T_{eff} (MeV)	$\langle p_T \rangle_{\text{fit}}$ (MeV/c)	χ^2/N_{dof}	$(dN/dy)^{\text{counting}}_{\text{fitrange}}$	$(dN/dy)^{\text{fit}}_{\text{fitrange}}$	Fraction
K^+	$-0.10 \leq y \leq 0.00$	$0.2 \leq p_T \leq 2.0$	47.6 ± 0.9	295.2 ± 4.0	709.8 ± 10.8	17.7 / 16	41.2	43.0	86.5%
K^-			43.1 ± 1.1	295.3 ± 4.6	710 ± 13.2	19.0 / 16	37.8	38.9	87.8%
K^+	$0.00 \leq y \leq 0.10$	$0.2 \leq p_T \leq 2.0$	46.8 ± 1.3	296.5 ± 5.5	712.4 ± 15.5	22.7 / 16	42.0	42.3	89.7%
K^-			44.0 ± 0.9	293.1 ± 4.3	705.9 ± 11.6	18.7 / 16	39.3	39.8	87.8%
K^+	$0.40 \leq y \leq 0.60$	$0.1 \leq p_T \leq 1.8$	46.7 ± 0.9	288.7 ± 4.9	697.5 ± 14.2	11.4 / 15	44.3	44.6	94.7%
K^-			44.3 ± 0.8	280.7 ± 4.8	682.0 ± 14.2	21.6 / 15	42.8	42.4	96.5%
K^+	$0.60 \leq y \leq 0.80$	$0.3 \leq p_T \leq 1.6$	45.6 ± 0.5	301.3 ± 4.4	727.2 ± 12.6	24.4 / 11	35.9	35.9	78.6%
K^-		$0.1 \leq p_T \leq 1.7$	44.1 ± 0.6	284.8 ± 4.3	686.8 ± 11.6	9.0 / 14	41.3	41.7	94.0%
K^+	$0.80 \leq y \leq 1.00$	$0.2 \leq p_T \leq 1.5$	44.4 ± 0.6	305.3 ± 5.3	728.2 ± 10.8	17.4 / 11	38.1	38.0	85.7%
K^-		$0.2 \leq p_T \leq 1.4$	42.1 ± 0.5	288.1 ± 4.6	696.4 ± 9.6	4.9 / 10	35.1	35.5	83.3%
K^+	$1.00 \leq y \leq 1.20$	$0.3 \leq p_T \leq 1.3$	42.8 ± 0.8	281.8 ± 8.2	683.8 ± 14.4	6.1 / 8	30.7	31.4	71.7%
K^-		$0.3 \leq p_T \leq 1.2$	40.6 ± 0.8	305.0 ± 11.1	728.7 ± 22.6	2.8 / 7	27.7	28.2	68.1%
K^+	$2.00 \leq y \leq 2.20$	$0.5 \leq p_T \leq 1.7$	33.3 ± 2.9	270.8 ± 15.8	666.5 ± 38.2	10.9 / 10	19.1	18.8	57.4%
K^-		$0.2 \leq p_T \leq 1.6$	29.2 ± 1.1	261.6 ± 9.5	645.4 ± 24.3	10.7 / 12	25.0	25.6	85.6%
K^+	$2.30 \leq y \leq 2.50$	$0.6 \leq p_T \leq 1.3$	27.6 ± 1.2	263.2 ± 20.7	645.8 ± 37.4	2.4 / 5	11.4	10.9	41.3%
K^-	$2.20 \leq y \leq 2.40$	$0.4 \leq p_T \leq 1.2$	24.6 ± 1.1	259.2 ± 18.7	640.9 ± 46.2	9.6 / 6	14.4	14.6	58.6%
K^+	$2.90 \leq y \leq 3.00$	$0.8 \leq p_T \leq 2.1$	23.7 ± 2.2	241.5 ± 10.1	606.8 ± 39.2	7.3 / 11	6.0	5.9	25.3%
K^-		$0.7 \leq p_T \leq 2.1$	18.0 ± 0.5	227.1 ± 6.3	577.0 ± 32.8	1.6 / 12	5.3	5.4	29.7%
K^+	$3.00 \leq y \leq 3.10$	$0.7 \leq p_T \leq 2.1$	22.2 ± 1.8	241.0 ± 11.4	608.9 ± 32.6	33.8 / 12	7.7	7.3	34.7%
K^-		$0.6 \leq p_T \leq 1.8$	16.4 ± 1.0	231.0 ± 9.5	578.5 ± 22.8	23.3 / 10	6.5	6.6	39.6%
K^+	$3.10 \leq y \leq 3.20$	$0.6 \leq p_T \leq 1.9$	20.1 ± 1.0	233.2 ± 7.6	590.9 ± 20.7	14.8 / 11	7.9	8.1	39.6%
K^-		$0.6 \leq p_T \leq 1.8$	15.3 ± 0.8	219.2 ± 7.0	563.8 ± 19.3	12.7 / 10	5.8	5.8	37.6%
K^+	$3.20 \leq y \leq 3.40$	$0.5 \leq p_T \leq 1.7$	18.1 ± 0.6	245 ± 9.1	613.5 ± 16.7	20.3 / 10	10.0	9.6	55.0%
K^-		$0.4 \leq p_T \leq 1.7$	11.4 ± 0.4	228.5 ± 7.6	581.8 ± 16.3	9.2 / 11	7.3	7.2	64.2%

Tab. 6.8: Results of the m_T–exponential fits to kaon spectra for the top 5% central events. The errors are statistical.

Chapter 7

Discussion

Energy systematics of kaon and pion production are presented and reveal a remarkable continuity from SPS to RHIC. The rapidity dependence of kaon and pion observables are compared to HIJING and AMPT predictions. Finally, the statistical models are investigated and reveal a very good agreement with the data.

7.1 Energy systematics

The results presented in the previous chapter are compared with lower energy data from SIS ($\sqrt{s_{NN}} \sim 1\,\mathrm{GeV}$) to RHIC. This follows the discussion introduced in Sec. 2.3.

7.1.1 Pions

Figure 7.1 shows the rapidity distribution of π^- ((π^+ rapidity distributions from SPS are not available). The overall multiplicity increases with increasing incident energy while the shape of the distribution does not show a drastic change and scales with the beam rapidity. In Tab. 7.1 are listed the fit parameters from the Gaussian sum (as discussed in the previous chapter) applied to all π^- distributions. As can be seen, the mean y_0 is shifted toward higher

$\sqrt{s_{NN}}$ (GeV)	$y_{beam}\,(CM)$	y_0	σ_y
1.9	0.46	0.44 ± 0.16	0.62 ± 0.19
2.3	0.75	0.06 ± 2.18	0.64 ± 0.21
3.0	1.08	0.37 ± 0.10	0.65 ± 0.09
3.6	1.28	0.06 ± 1.44	0.81 ± 0.12
4.1	1.42	0.04 ± 0.75	0.85 ± 0.04
8.8	2.22	0.67 ± 0.01	0.87 ± 0.01
12.2	2.57	0.76 ± 0.01	0.97 ± 0.01
17.3	2.91	0.72 ± 0.02	1.18 ± 0.02
200	5.36	1.27 ± 0.08	1.81 ± 0.11

Tab. 7.1: Gaussian sum fit parameters on π^- rapidity distributions from SIS to RHIC energies (the fit is not always adequate on low energy data).

rapidities and the width σ_y is significantly broader at RHIC than at all lower energies.

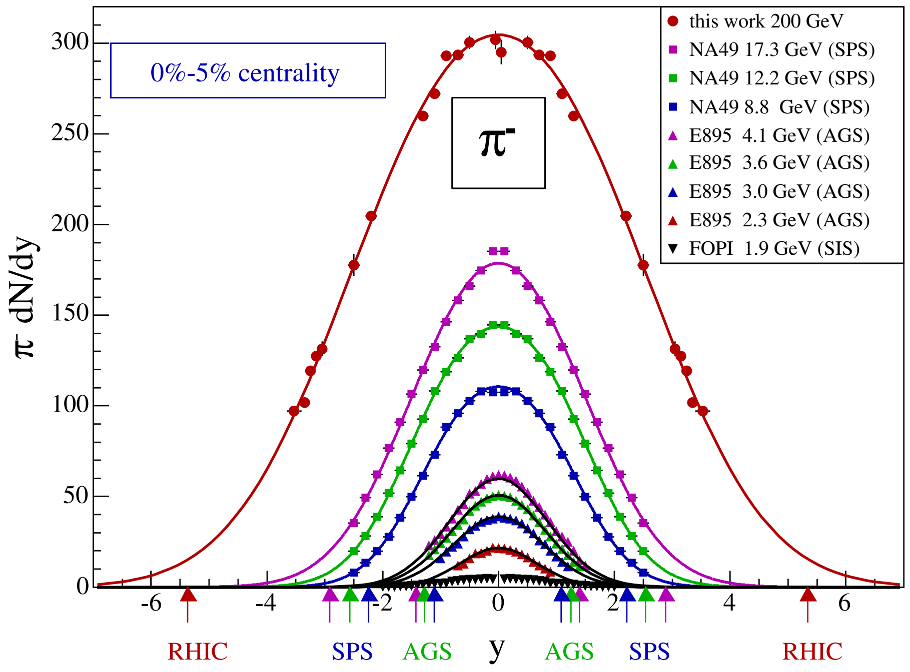

Fig. 7.1: Pion rapidity density as a function of rapidity and $\sqrt{s_{NN}}$ from SIS to the top RHIC energies. The NA49 data are taken from [42], the AGS data from [43, 44] and the SIS data from [45, 46].

Figure 7.2 shows the positive and negative pion mid–rapidity and 4π multiplicities (top panel) and ratios (bottom panel) as a function of $\sqrt{s_{NN}}$. Both π^- and π^+ multiplicities, whether total or only at mid–rapidity, show a systematic increase with $\sqrt{s_{NN}}$ but the increase from SPS to RHIC is less pronounced than from SIS to the top SPS energy. The ratio $N(\pi^-)_{RHIC}/N(\pi^-)_{SPS}$ is ~ 2.8 (also for π^+) while the ratio $N(\pi^-)_{SPS}/N(\pi^-)_{SIS}$ is ~ 46 (95 for π^+). At mid–rapidity, these ratios are 1.7 (1.8) and 37.3 (70.8). Another noticeable feature is the increasing ratio $N^{\pm}/(dN^{\pm}/dy)_{y=0}$. It shows that the total multiplicity of positive and negative pions is less and less dominated by the mid–rapidity multiplicity. It points to the fact, together with parameters of Tab. 7.1, that the shape of the mid–rapidity region flattens more and more and tends to the Bjorken picture [11] where yields are boost invariant over a few units of rapidity. At the same time, the π^-/π^+ ratio decreases from ~ 1.9 at $\sqrt{s_{NN}} = 1.9\,\text{GeV}$ to ~ 1.0 at $\sqrt{s_{NN}} = 200\,\text{GeV}$, with the same magnitude at mid–rapidity and over the full rapidity range. This leads to the conclusion that $u\bar{u}$ and $d\bar{d}$ quark pairs are produced in equal amount at RHIC (string break–up) in contrast with low energy data, where it has been shown that pion production is dominated by the $\Delta(1232)$ resonance decay [46] and charge exchange reaction $NN \rightarrow NN\pi$. Indeed, at $\sqrt{s_{NN}} \lesssim 2\,\text{GeV}$, the ratio π^-/π^+ ratio can be deduced by studying the isospin branching ratios of these production modes [43, 115]:

	π^-	π^0	π^+
nn	5	1	0
pp	0	1	5
$np = pn$	1	4	1

The branching ratios go like the absolute square of the scattering amplitudes, which are determined by the Clebsch–Gordan coefficients for the corresponding isospin combinations

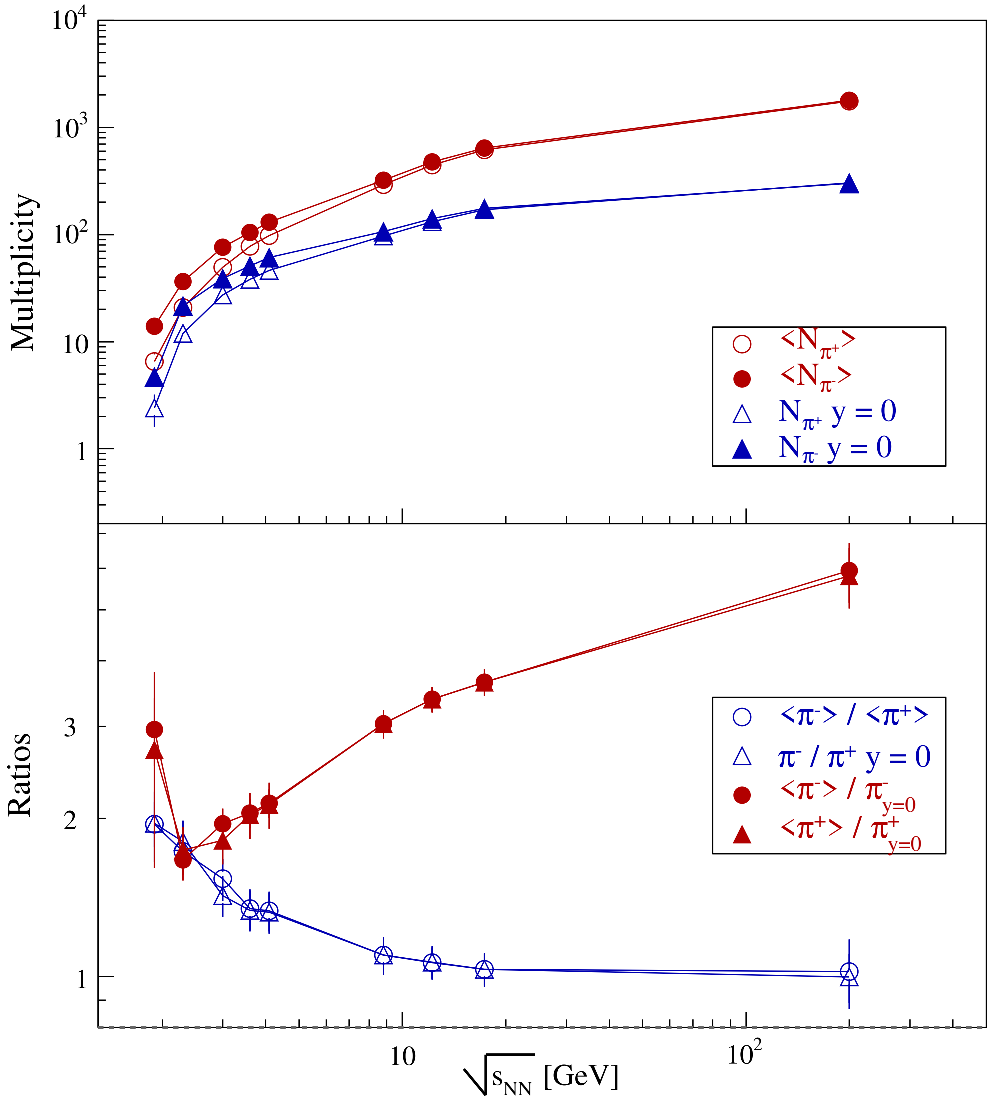

Fig. 7.2: Energy systematic of positive and negative pion multiplicities and ratios. Solid lines are drawn to guide the eye. The errors are systematic.

($I_\pi = |1>$ and $I_N = |1/2>$). Since the measured ratios are inclusive, they include all processes, be they $NN \to NN\pi$ or from nucleonic resonance decays such as $\Delta(I_\Delta = |3/2>)$ or $N^*(I_{N^*} = |1/2>)$. In Au+Au, there are 2×118 neutrons and 2×79 protons. In the most central collisions, assuming that all nucleons participate, there are a maximum of 118^2, 79^2 and $2 \times 118 \times 79$ nn, pp and pn collisions respectively that could to the production of pions. By summing these production ratios weighted according to the pion branching ratios, the charged pions are expected to be produced in the ratio

$$\frac{\langle N_{\pi^-} \rangle}{\langle N_{\pi^+} \rangle} \approx \frac{5N^2 + NZ}{5Z^2 + NZ} = 1.95 \tag{7.1}$$

which is the measured value at SIS. The decreasing of this ratio quantifies the increasing role of pair production.

7.1.2 Kaons

Do kaons exhibit the same features as pions ? It has already been noticed in the previous chapter how K^+ and K^- rapidity distributions and ratio are strongly rapidity dependent. This is explained by the net–proton evolution with rapidity. Figure 7.3 is a compilation of rapidity density distributions of K^+ and K^- at different $\sqrt{s_{NN}}$.

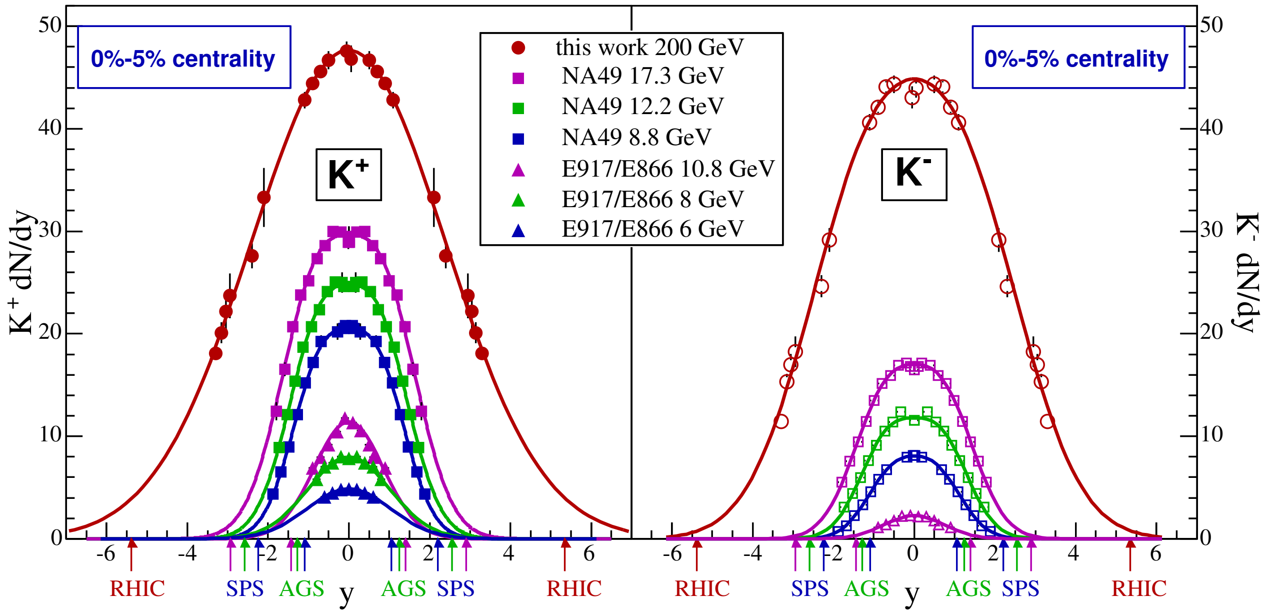

Fig. 7.3: Kaon rapidity density as a function of rapidity and $\sqrt{s_{NN}}$. The NA49 data are taken from [42], the AGS data from [47, 48, 49]. The very low multiplicities are not drawn for clarity.

De visu, the relative difference between K^+ and K^- multiplicities at $\sqrt{s_{NN}} = 200\,\text{GeV}$ is not as pronounced as with lower energy data. For the latter, the negative kaon distributions are much lower than the positive distributions even at SPS energies. The single Gaussian fit parameters of the distributions are listed in Tab. 7.2. Note that in reference [42] (NA49), the fit function is the Gaussian sum as defined in Chap. 6. The choice of the single Gaussian fit used here is for qualitative comparison since the AGS data are not well described by the NA49 fit function.

$\sqrt{s_{NN}}$ (GeV)	$y_{beam}(CM)$	$\sigma_y(K^+)$	$\sigma_y(K^-)$
2.3	0.75	0.82 ± 0.04	below production threshold
3.0	1.08	0.95 ± 0.03	0.74 ± 0.02
3.6	1.28	0.96 ± 0.03	0.74 ± 0.03
4.1	1.42	0.97 ± 0.05	0.75 ± 0.04
4.7	1.57	0.96 ± 0.06	0.71 ± 0.04
8.8	2.22	1.15 ± 0.03	0.91 ± 0.02
12.2	2.57	1.28 ± 0.03	1.13 ± 0.03
17.3	2.91	1.51 ± 0.04	1.26 ± 0.03
200	5.36	2.40 ± 0.04	2.12 ± 0.02

Tab. 7.2: Distribution width from single Gaussian fit on kaon rapidity distributions from AGS to RHIC energies.

Like for pions, the width increases with increasing $\sqrt{s_{NN}}$ but only at energies above the AGS energy range. Figure 7.4 shows the dependence of the width of the kaon multiplicity distributions with the beam rapidity in the center of mass frame. There is no significant width

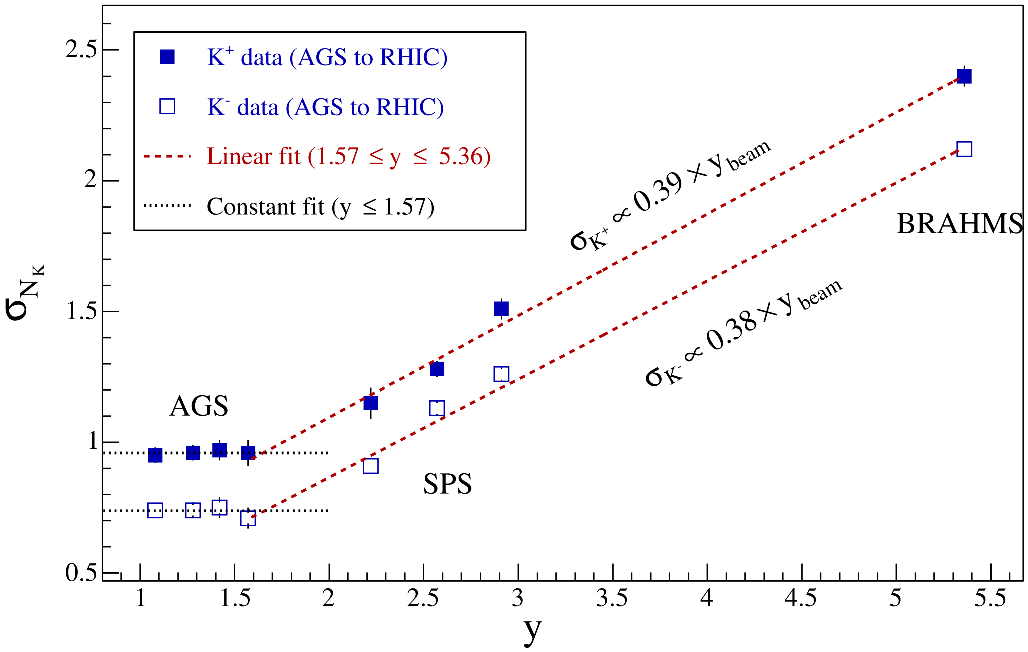

Fig. 7.4: Width of kaon rapidity distribution as a function of beam rapidity (in the center of mass frame) for the top 5% central collisions. Widths are obtained from a Gaussian fit, errors are statistical.

increase in the AGS energy domain but then, a sharp and linear increase occurs from the top AGS energy to RHIC energy. A linear fit have been performed within this particular range (red dashed lines). The slope of the linear fit is similar for K^+ and K^-, and amounts to ~ 0.4. The picture emerging is that of a system with increasing longitudinal flow, a more and more elongated fireball along the beam axis with increasing transparency. It is indeed observed that the maximum stopping measured in central Au+Au collisions is achieved at the top AGS energy (see [30] and references therein). By studying the net–charge $N(K^+) - N(K-)$, the correlation between net–kaons and net–baryons is even more remarkable, as can be seen in Fig. 7.5, directly comparable to Fig. 1.17 of Sec. 1.4.2. Note that the BRAHMS kaon data presented here do not cover the full fragmentation region, the spectrometer acceptance ceases just before this region. The other main noticeable thing is the relatively low net–charge at the top RHIC energy in comparison with the lower energy data, although kaon multiplicities are much higher at $\sqrt{s_{NN}} = 200\,\mathrm{GeV}$.

The elongation along the longitudinal direction, occurring from the top AGS energy, is seen in the transverse activity of kaons, already mentioned in Sec. 2.3 and illustrated Fig. 2.7. In Fig. 7.6 is summarized the slope information with the addition of the measured inverse slope at $\sqrt{s_{NN}} = 200\,\mathrm{GeV}$. On the left panel, data points are plotted on a logarithmic energy scale. Indeed, a plateau structure is visible in the SPS energy range, as reported in [52]. But the right panel of this figure shows the data points plotted on a linear energy scale. It is clear that the discussion on the plateau structure ([52]) requires more data at energies intermediate between SPS and RHIC. The other important thing to notice is the sharp change in the

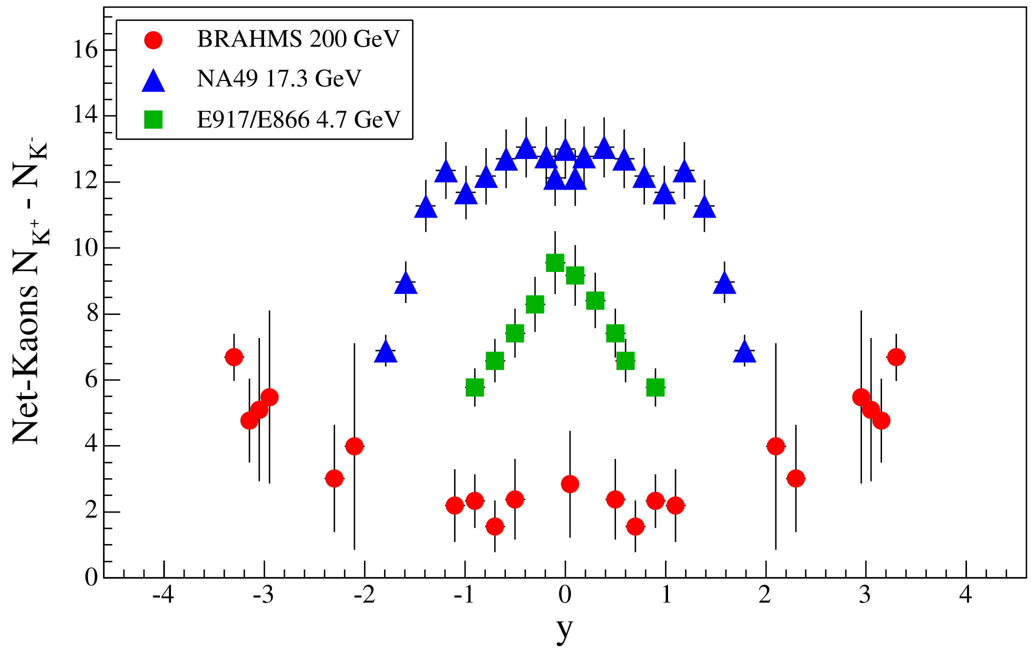

Fig. 7.5: Net–kaon multiplicity versus rapidity and $\sqrt{s_{NN}}$. Errors are statistical.

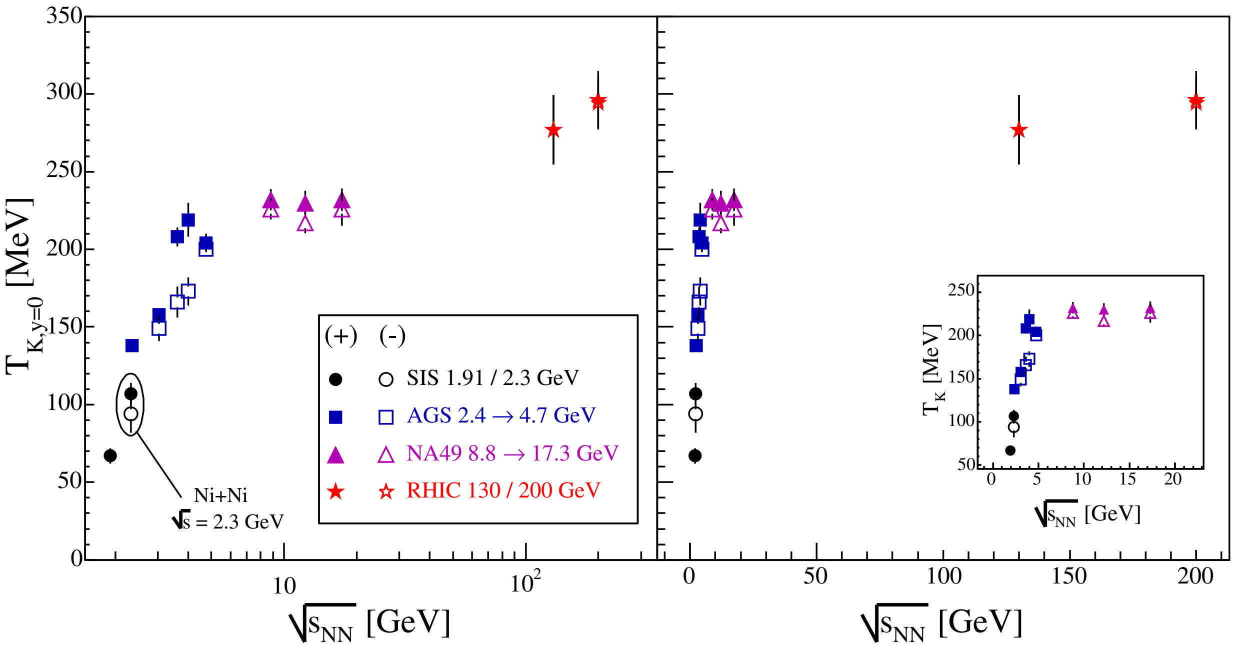

Fig. 7.6: Inverse slope parameter extracted from an exponential in m_T fit on kaon spectra as a function of $\sqrt{s_{NN}}$. SIS data are taken from [50, 51], AGS data from [48, 47], SPS data from [42] and RHIC at $\sqrt{s_{NN}} = 130\,\text{GeV}$ from [116]. Error bars are full errors (syst. + stat). The data in the right panel (same as left) are plotted on a linear energy scale.

slope increase around the energy between AGS and SPS. It supports the statement about the strength of the longitudinal flow taking over the transverse expansion. The question is: why does it happen so sharply? Since pions cannot be fitted to a single exponential in m_T, such an analysis is not straightforward. However, one could investigate mean transverse momenta $\langle p_T \rangle_\pi$ as a function of $\sqrt{s_{NN}}$. An alternative slope measurement of the singly strange baryon Λ at mid–rapidity [117] is shown in Fig. 7.7 as a function of $\log\sqrt{s_{NN}}$. The systematic

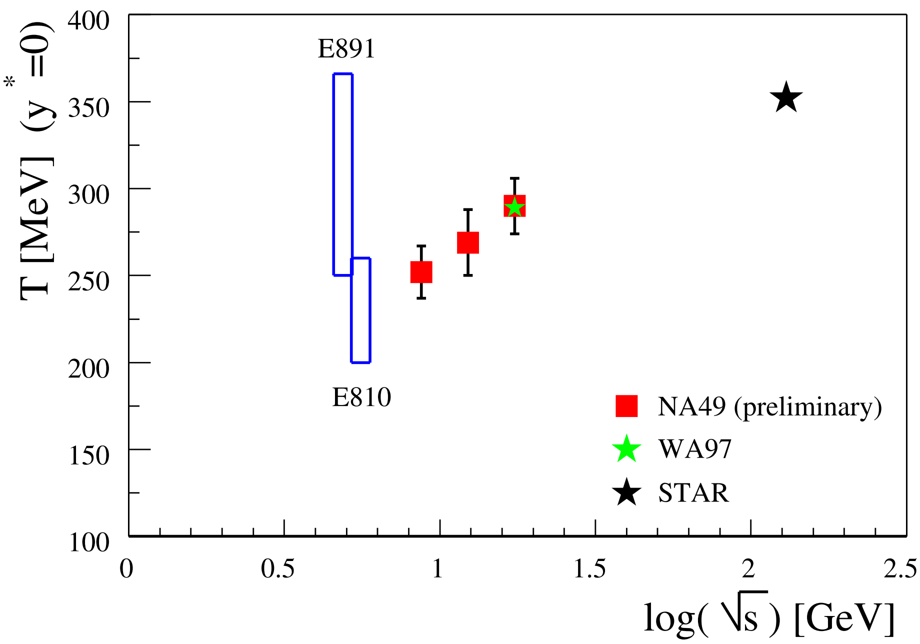

Fig. 7.7: Inverse slope parameter extracted from an exponential in m_T fit on Λ spectra as a function of $\sqrt{s_{NN}}$ (figure from [117]).

consists of a steady increase from AGS energies (but with large errors) to RHIC, no plateau is visible.

Multiplicities and Ratios

Multiplicities and ratios are correlated to $\sqrt{s_{NN}}$ in Figure 7.8. Like for pions, the big discrepancies seen at low energy between K^+ and K^- tend to disappear as $\sqrt{s_{NN}}$ approaches the RHIC top energy. The energy systematic between the AGS and SPS energy domains is somewhat a turning point in the reaction dynamics, as has been already noticed from Fig. 7.4. It is also visible in the multiplicities (4π and at mid–rapidity). The ratios $\langle K \rangle \,/\, (dN/dy)_{y=0}$ also show (together with pion ratios) that the source is more and more elongated as $\sqrt{s_{NN}}$ increases.

7.1.3 Kaons versus Pions

In this section, the study of kaons w.r.t. pions, started in Chap. 2 is carried along. Here is reviewed the energy dependence of the correlation between kaon and pion multiplicities. As was mentioned in Chap. 2, kaons carry a large fraction of the produced strangeness and differ from pions in that respect.

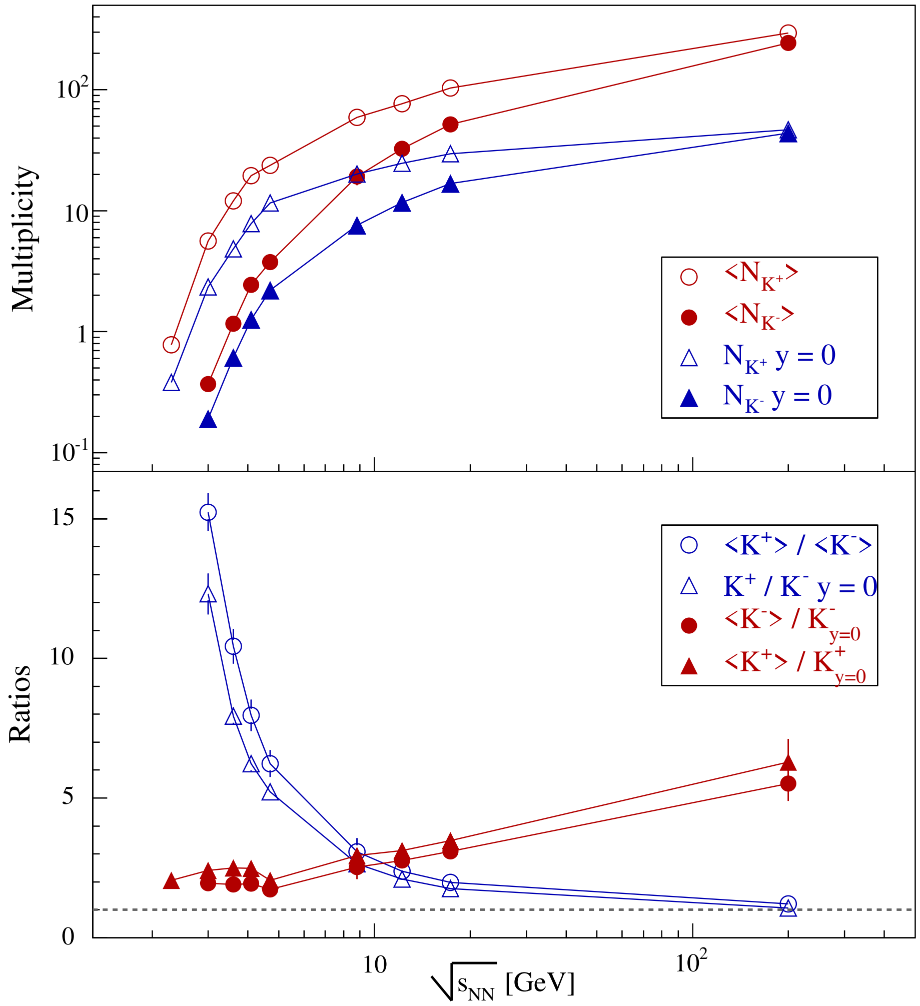

Fig. 7.8: Energy systematic of positive and negative kaon multiplicities and ratios. Solid lines are drawn to guide the eye. Errors are systematic. Note the similitude between the $\langle N_K \rangle / K_{y=0}$ ratio and the energy systematic of the rapidity distribution width (Fig. 7.4).

Multiplicity Correlation

Figure 7.9 shows the kaon multiplicities $N_{K^+}+N_{K^-}$ as a function of $N_{\pi^+}+N_{\pi^-}$. The BRAHMS data points correspond to the different rapidity intervals covered in this analysis. The data point at the topmost pion multiplicities represents the extrapolated 4π multiplicities and ratio. There is a remarkable linearity between the BRAHMS data points. A linear fit gives $N_{K^++K^-} \propto 0.16\, N_{\pi^++\pi^-}$, with a confidence level $\chi^2/N_{dof} = 10.2/10$. The SPS data can also be described by a linear function. A fit gives $N_K = 0.12 N_\pi + 3.90$. The AGS data points cannot be described this way since connecting mid–rapidity data to 4π data does not lead to a linear correlation. It is also interesting to note that high rapidity regions in Au+Au collisions at $\sqrt{s_{NN}} = 200\,\mathrm{GeV}$ recover the mid–rapidity physics of Pb+Pb collisions at low SPS energies. This is supported by the kaon inverse slope parameters, in the order of $\sim 230\,\mathrm{MeV}$ in both cases. The conclusion is that there is a total charged kaon multiplicity enhancement from SPS to RHIC, relative to charged pion multiplicity. However, saying that it is a strangeness

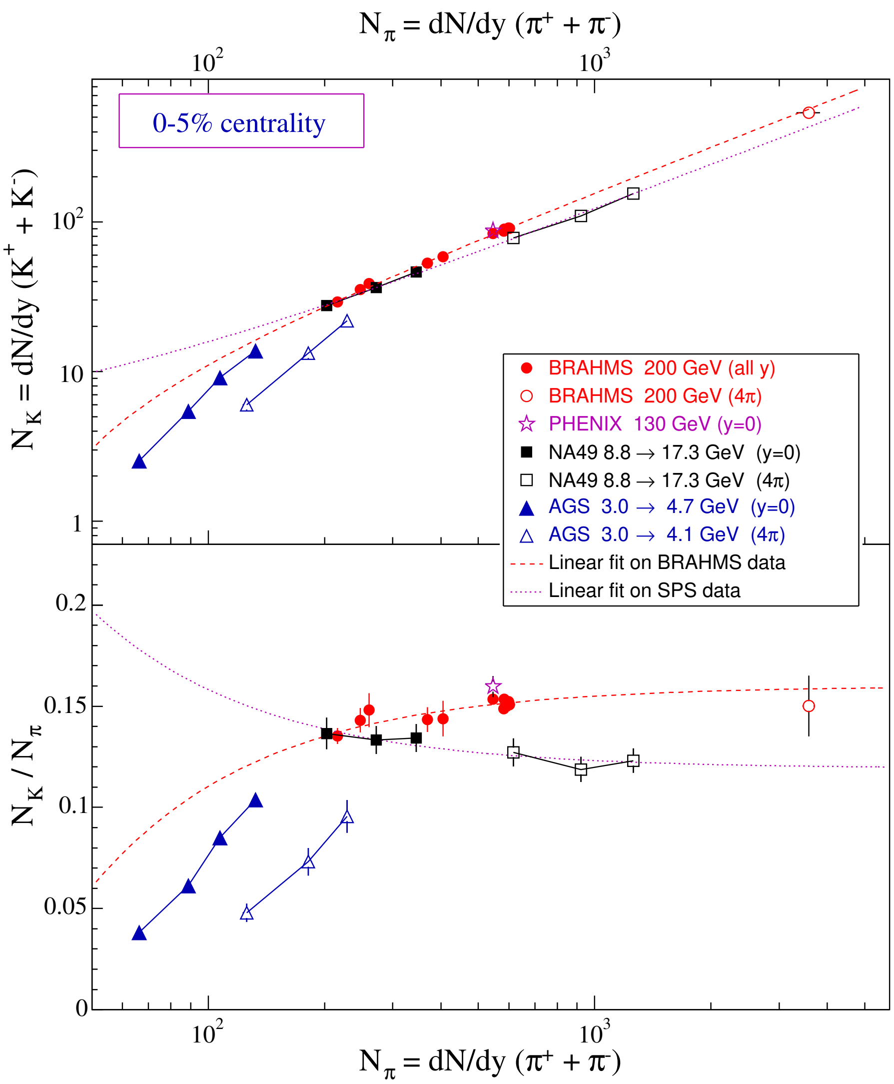

Fig. 7.9: Top: Sum of K^+ and K^- dN/dy versus sum of π^+ and π^- dN/dy. Bottom: ratio between kaon and pion multiplicities versus pion multiplicities. The dashed line in the top panel is a linear fit on the BRAHMS data. In the bottom panel, the fit is divided by the pion multiplicity. Solid lines are drawn to guide the eye. Errors are statistical

enhancement needs a study of neutral kaon, pion[1] and strange baryon production.

Charged Kaon to Pion Ratios

The other relevant correlation is the signed kaon to pion multiplicity ratios. Both are mesons, pions are the lightest non–strange hadrons while kaons are the lightest strange hadrons and carry a good fraction of the strangeness produced during collisions. The ratio between the multiplicities of these particles therefore characterizes strangeness production w.r.t. non strange light quarks. Figure 7.10 shows the kaon to pion ratios obtained from mid–rapidity multiplicities. The ratios obtained at $\sqrt{s_{NN}} = 200\,\mathrm{GeV}$ from the present analysis show how they converge toward the same value ($\sim 15\%$). The measured values are $15.5\% \pm 0.3\%$ (stat) and $14\%.6 \pm 0.3\%$ (stat) respectively. Do full multiplicity ratios follow this trend? In Fig. 7.11 are

[1] From isospin consideration, K^0_S (π^0) total multiplicities can be taken as the average between charged kaons (pions).

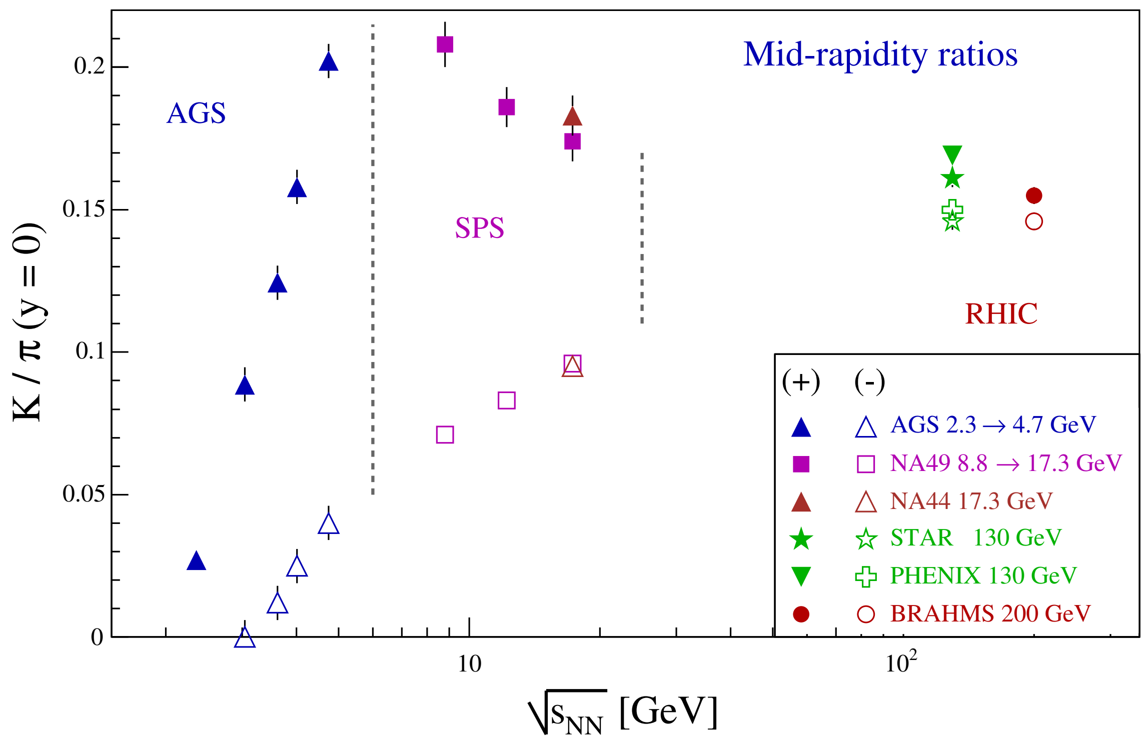

Fig. 7.10: Mid–rapidity kaon to pion ratio as a function of $\sqrt{s_{NN}}$ from AGS to RHIC energies. Errors are statistical.

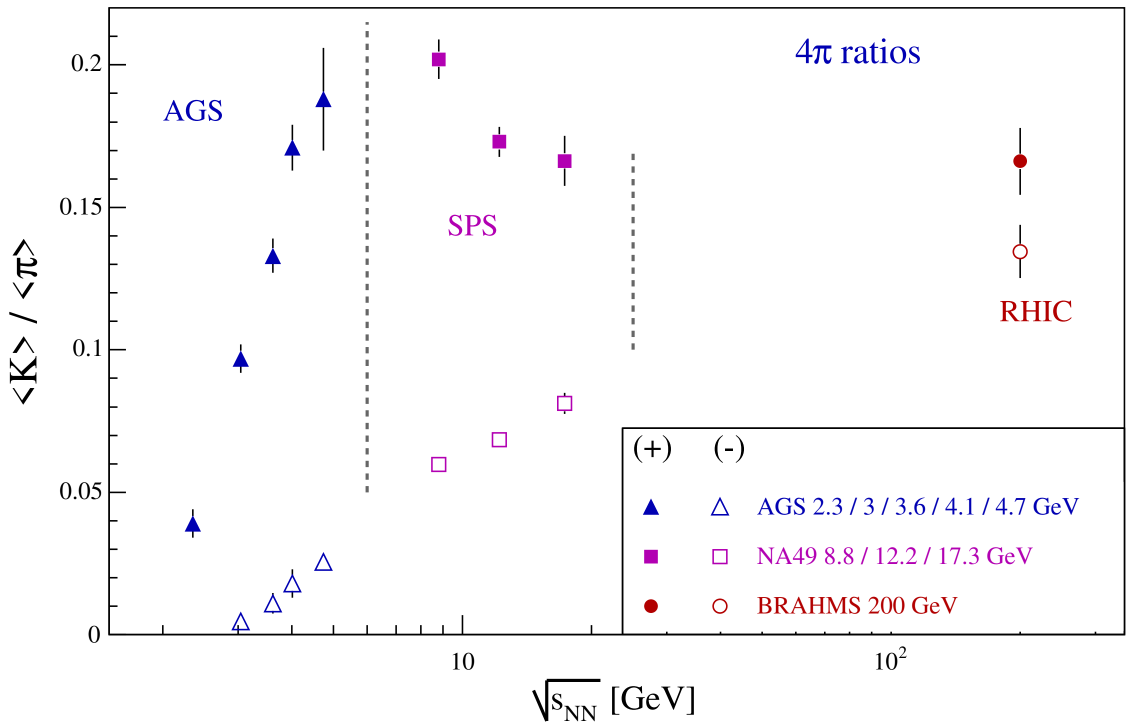

Fig. 7.11: 4π kaon to pion ratio as a function of $\sqrt{s_{NN}}$ from AGS to RHIC energies.

plotted the 4π ratios, after the estimates of the total multiplicities. The positive ratio sharply rises within the AGS energy domain up to $\sim 20\%$ here too but remains remarkably constant at 16.6% from the top SPS energy to RHIC. This is partly due to the contributions of non mid–rapidity kaon multiplicities which cannot only be accounted for direct pair production (cf. Fig. 6.12). The negative ratio is comparable with the ratio restricted to mid–rapidity but is still somewhat lower than the latter, even at $\sqrt{s_{NN}} = 200\,\mathrm{GeV}$ where it amounts to 13.4% $\pm$ 0.1% (stat), again because of high rapidity effects like K^- absorption (higher net–baryon than at $y = 0$).

7.2 Model Comparison

The models chosen for comparison are HIJING, AMPT and two versions of the statistical model (the hadron gas model and the statistical model of the early stage), introduced in Chap. 2.

7.2.1 Microscopic Models

The event generators HIJING and AMPT have been used to simulate the most central Au+Au collisions at $\sqrt{s_{NN}} = 200\,\mathrm{GeV}$. The centrality determination is achieved by requiring an impact parameter lower than 3.1 fm. This value comes from a cut on the total distribution of the impact parameter (5% of the distribution)[2]. Since hyperons can contribute to pion and kaon multiplicities, two simulations, with and without hyperon decay, have been performed with HIJING, but AMPT calculations are without weak decay[3]. Quantum number conservation has been checked. It is found that the total energy, total electrical charge and baryonic numbers are conserved. However, from the calculations without weak decay, it has been found that total strangeness is conserved in AMPT but not in HIJING. The deviation from zero strangeness is shown in Fig. 7.12. The comparison between HIJING and experimental data

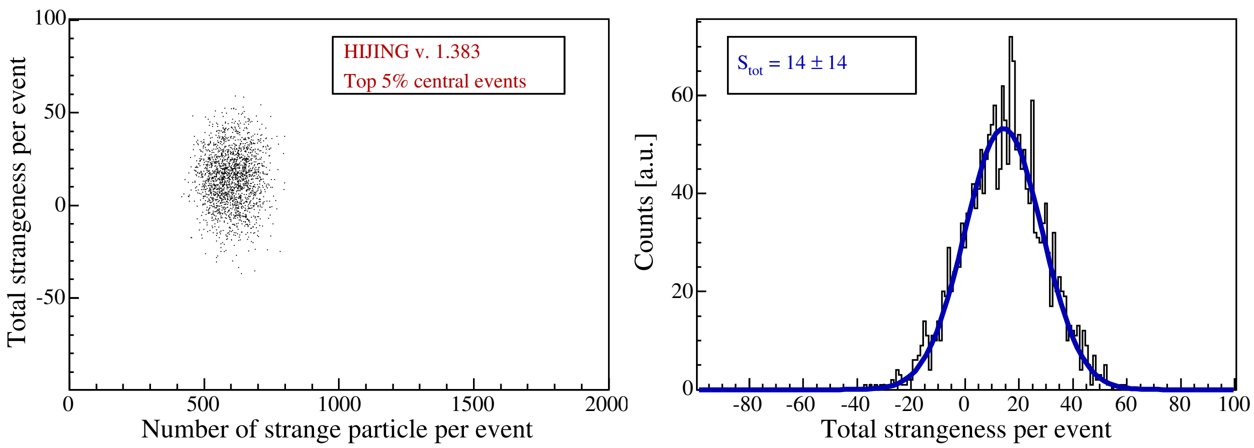

Fig. 7.12: Strangeness is not conserved in HIJING. In the left panel is shown the total strangeness versus the number of strange particle per event. In the right panel is shown the projection onto the total strangeness axis. The mean total strangeness found is 14 ± 14.

[2]Cutting on the charged particle multiplicity distribution does not affect the results.
[3]The calculated data were kindly provided by the authors since the code is not yet available.

suffers from this error. The authors of this model suspect a weak decay leak even when weak decay is switched off.

Rapidity distributions

Figure 7.13 shows the rapidity density distributions of charged kaons and pions predicted by HIJING and AMPT, together with the experimental data of this analysis. Overall, the

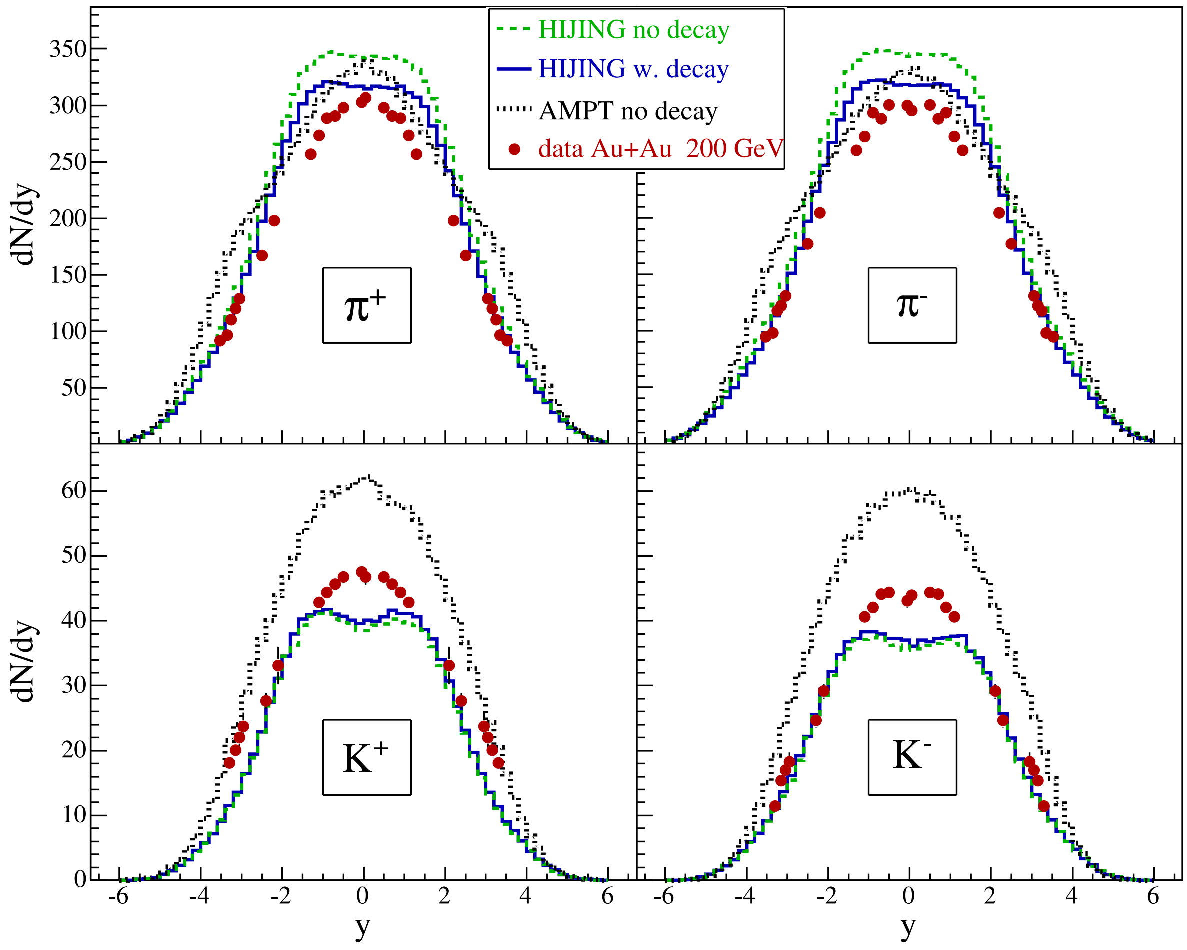

Fig. 7.13: Charged pion and kaon distribution calculated by HIJING and AMPT for the top 5% central collisions. The dashed histograms represent the simulation with weak decay. The markers represent the data. Errors are statistical.

event generators do not reproduce the rapidity distributions. Pions are overestimated by both AMPT and HIJING while kaons are underestimated by HIJING and overestimated by AMPT. The high rapidity data ($2 \lesssim y \lesssim 4$) are reasonably reproduced by HIJING except for K^+. AMPT predicts distributions systematically too broad. At mid–rapidity, HIJING and AMPT do not reproduce the data for all charged mesons, with or without weak decay. The disagreement seen for high rapidity K^+ can be explained by the absence of rescattering between hadrons in the model (no associated production resulting from multiple NN interactions). However, AMPT which does contain hadronic rescattering, slightly over-predicts the K^+ multiplicities at $|y| > 3$. At mid–rapidity, the plateau (pions) and even depletion (kaons) seen in

Particle ID		$\langle N \rangle$	σ_y
π^+	HIJING no decay	1901 ± 20	1.54 ± 0.02
	HIJING weak decay	2053 ± 20	1.53 ± 0.02
	AMPT no decay	2046 ± 20	1.56 ± 0.02
	data	1733 ± 13	1.81 ± 0.12
π^-	HIJING no decay	1925 ± 20	1.60 ± 0.03
	HIJING weak decay	2094 ± 20	1.60 ± 0.03
	AMPT no decay	2050 ± 20	1.57 ± 0.02
	data	1769 ± 13	1.81 ± 0.11
K^+	HIJING no decay	229 ± 7	1.29 ± 0.05
	HIJING weak decay	224 ± 7	1.29 ± 0.05
	AMPT no decay	337 ± 8	1.31 ± 0.03
	data	286 ± 4	2.40 ± 0.04
K^-	HIJING no decay	214 ± 6	1.28 ± 0.04
	HIJING weak decay	209 ± 6	1.29 ± 0.04
	AMPT no decay	325 ± 8	1.25 ± 0.03
	data	239 ± 2	2.12 ± 0.02

Tab. 7.3: Comparison between HIJING and experimental data rapidity distributions. The parameters are from a fit to the Gaussian sum.

the HIJING distributions are not experimentally measured. On the other hand, AMPT fails also at describing the width of the distributions. In Tab. 7.3 are listed the widths of the rapidity distributions after fits to a Gaussian sum (cf. Chap. 6). The widths estimated from fits to HIJING and AMPT data are systematically narrower then the experimental widths. The discrepancy with the data is more visible when looking at the ratio as a function of rapidity (cf. Fig. 7.14). The π^-/π^+ ratio is very well reproduced along the rapidity range covered by the data despite the discrepancy in the absolute yields. The K^-/K^+ is well described over the rapidity range $|y| \lesssim 2$ but fails at higher rapidities: HIJING predicts an increase toward unity while the data show a significant decrease, AMPT does predict a decrease but starting at a higher rapidity (between 3 and 3.5). The kaon to pion ratios are not reproduced at all except for the highest rapidity intervals of the negative ratio (AMPT). The conclusion is that HIJING needs to include some rescattering between hadrons following partonic cascade while AMPT has to decrease it.

Transverse Properties

HIJING and AMPT are compared to the mean p_T data as a function of rapidity. The simulated spectra have been constructed at the rapidity intervals used for the experimental measurements. Figure 7.15 shows the comparison with the experimental data. As can be seen, the mean transverse momentum from HIJING is systematically lower than the measured $\langle p_T \rangle$ at all rapidities. The same goes for AMPT but the latter shows a higher mean transverse momentum than HIJING for kaons. The HIJING kaon (pion) values are $\sim 35\%$ (15%) lower on average while AMPT values are 15% (10%) lower. This shows that these event generators do not include collective transverse flow. However, the trend of the rapidity dependence is reasonably reproduced, a mid–rapidity plateau followed by a small decrease at high rapidities ($\sim 20\%$). In conclusion, although HIJING and AMPT reasonably describe the proton data of reference [30] and the overall charged particle multiplicity [100, 101], the charged meson abundances are not well reproduced.

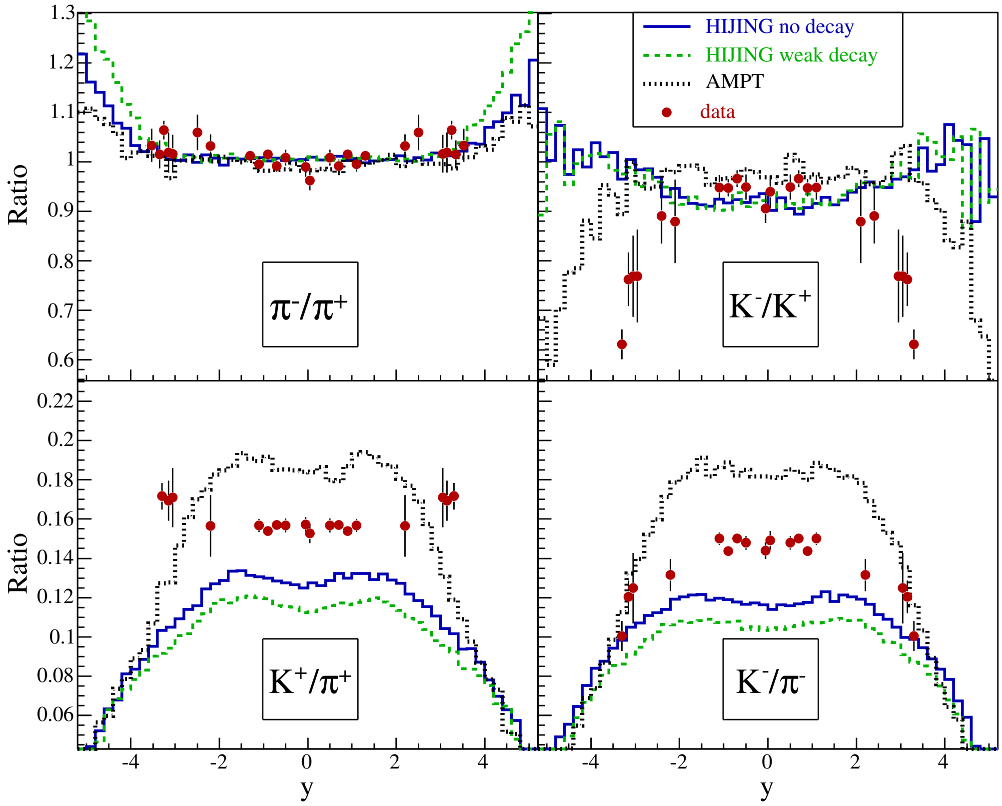

Fig. 7.14: Charged pion and kaon ratios as a function rapidity calculated by HIJING and AMPT for the top 5% central collisions. Data errors are statistical.

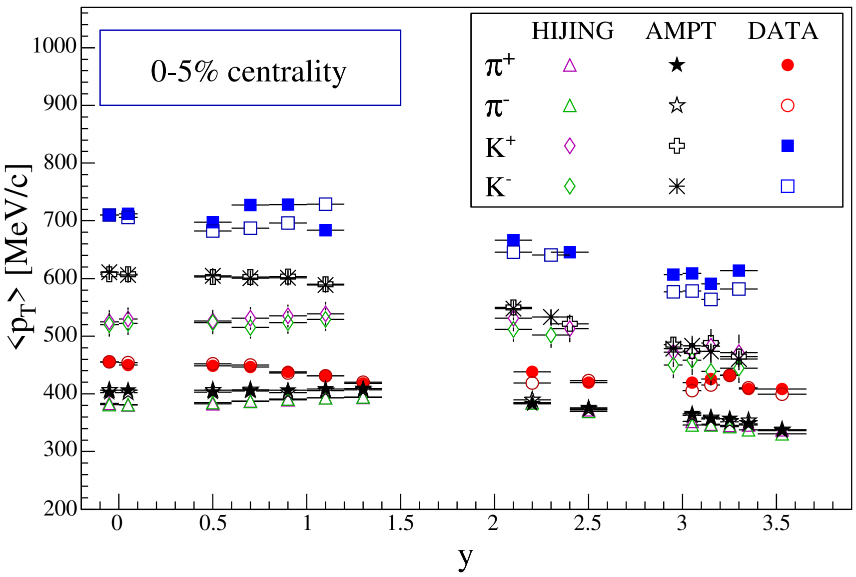

Fig. 7.15: Mean transverse momentum predictions.

7.2.2 Statistical Models

In this section are discussed the main "predictions" of the statistical model, although prediction is not really the right word for the hadron gas model since it aims at fitting the existing data in order to extract a common temperature identified as the chemical freeze–out temperature, and the baryo–chemical potential μ_B (cf. Sec. 2.4.1).

Hadron Gas Model

In the Boltzmann approximation, the rapidity distribution of particles emitted from a thermalized source of temperature T, at rest in the center of mass frame of the system is given by the equation:

$$\frac{dN}{dy} = 2\pi A \left[m^2 T^* + 2mT^{*2} + 2T^{*3}\right] \tag{7.2}$$

where T^* is the apparent temperature or inverse slope parameter of particle spectra and A a normalization constant. In this case, $T^* = T/\cosh y$. A quick inspection of Fig. 6.7 shows that the rapidity dependence of T^* is very small, i.e. T (static source) changes with rapidity, in contradiction with a thermalized static source. Figure 7.16 shows the measured rapidity distributions compared to the Boltzmann description, using the measured mid–rapidity T^* as the source temperature T (since $\cosh(0) = 1$). The distributions are clearly not described by

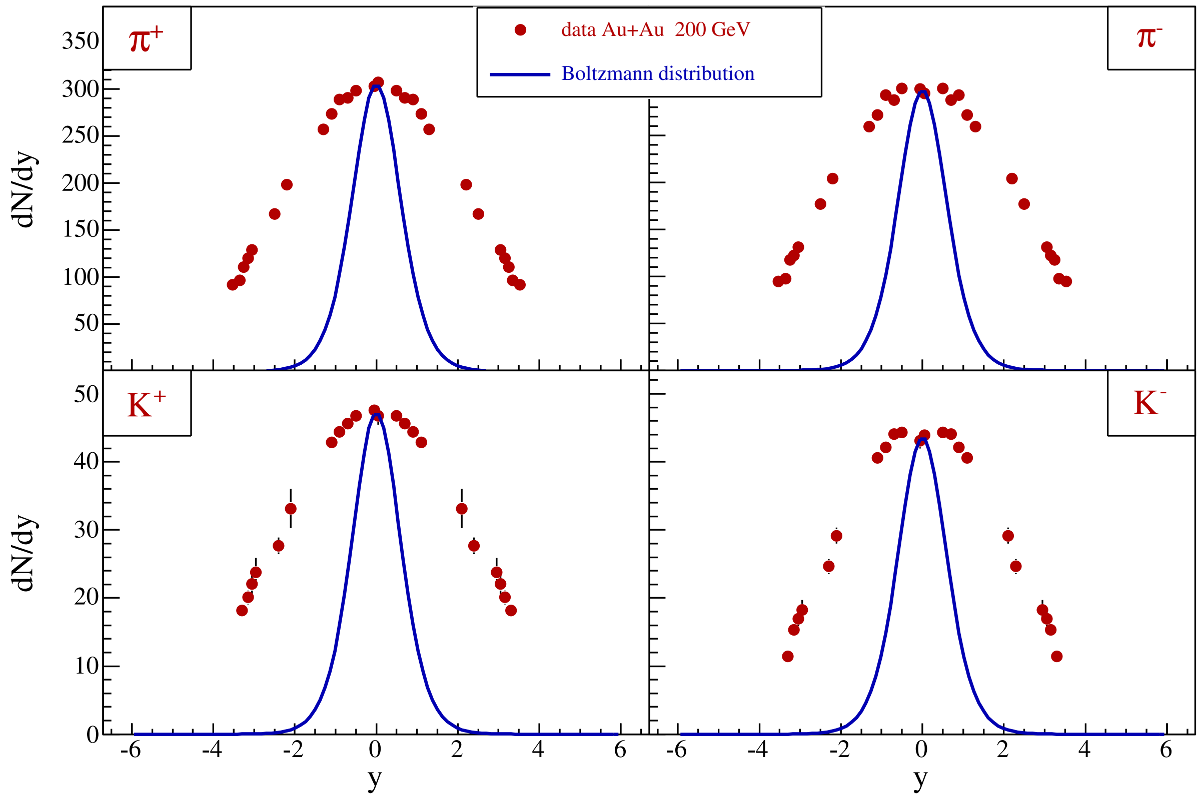

Fig. 7.16: Expected thermal rapidity distributions (Boltzmann) from a source at rest at mid–rapidity with a temperature equal to that measured at $y = 0$.

the Boltzmann approximation as expected. Nevertheless, a study on particle ratios conducted by BRAHMS [38] has shown that when correlated with the $\bar{p}/p$ ratio, the kaon ratio K^-/K^+ at $\sqrt{s_{NN}} = 200\,\mathrm{GeV}$ within the rapidity range covered, strikingly follows the calculated correlation from the thermal model developed by Becattini *et al* [27], illustrated in Fig. 7.17. The difference between the dashed line and the prediction from Becattini is the introduction

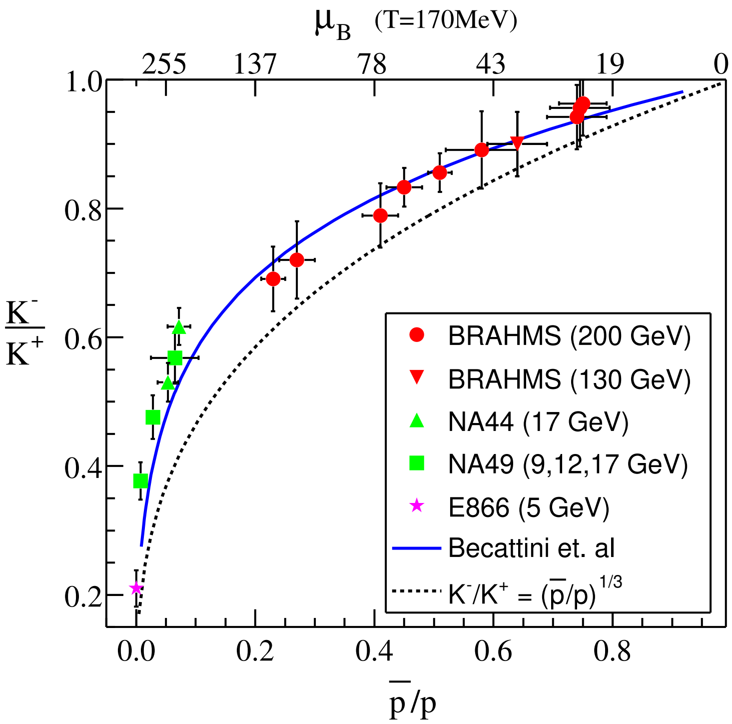

Fig. 7.17: Kaon ratio versus proton ratio. The BRAHMS data points from Au+Au at $\sqrt{s_{NN}} = 200\,\mathrm{GeV}$ correspond to different rapidity interval. The dashed line is obtained by quark counting. The solid line is a prediction from Becattini *et al* [27].

of a strangeness suppression factor in the latter, as mentioned in 2.4.1. The model curve is at a constant temperature, here $T = 170\,\mathrm{MeV}$. The good agreement between the data and the model suggests that the system looks chemically equilibrated with a common temperature, although not as a thermalized source at rest at $y = 0$. Pion and kaon data presented here can qualitatively support this statement. Indeed, from the effective temperatures plotted in Fig. 6.7, one can check if there is a common temperature at each rapidity interval after having removed the transverse flow contribution ($T_{eff} \approx T_{fo} + m\,\langle\beta\rangle^2$ for $m \lesssim 1\,\mathrm{GeV/c^2}$). The resulting temperature is by no means the chemical freeze–out temperature nor even the kinetic freeze–out temperature, the latter would require a real blast–wave analysis (like e.g. in [16]) including all particle species, but it would hint to a constancy of these temperatures with rapidity. Figure 7.18 shows the effective temperatures of Fig. 6.7 as a function of mass for each rapidity interval. By fitting the data points with a linear function and extrapolating the latter to the zero mass axis, it can be seen that the resulting temperature is consistent with a constant along the rapidity axis. This suggests that despite the strong dynamics (transverse and longitudinal flows) and different particle production mechanisms, the system has probably frozen out at the same time over almost 7 units of rapidity! Moreover, it suggests that the pion and kaon rapidity distributions can be described by a sum of folded thermal distributions, as proposed by Cleymans and Redlich in [118]. These authors propose to explain the observed

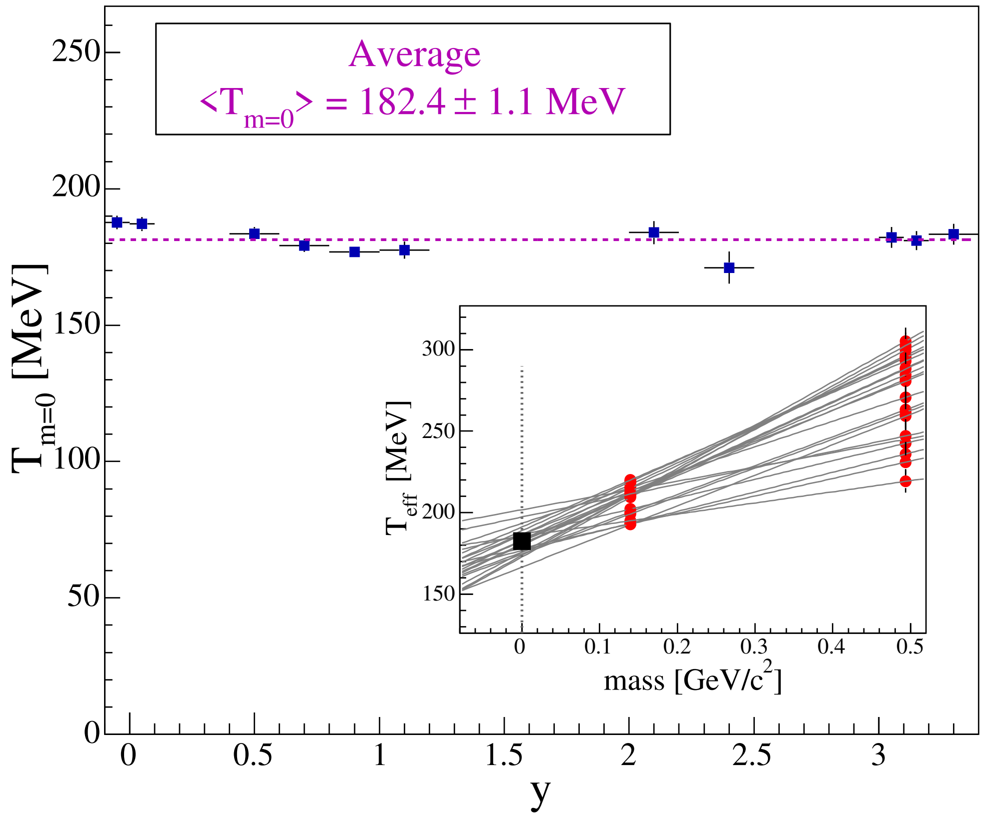

Fig. 7.18: Effective temperatures versus mass and rapidity. From linear fits at each rapidity interval, the extrapolated temperature at zero mass (no flow) is consistent with a constant as a function of rapidity.

rapidity distribution as a superposition of "fireballs" along the rapidity axis:

$$n_i = \int_{-\infty}^{\infty} dy \int_{-Y}^{Y} dY_{FB}\, \rho(Y_{FB}) \frac{dn_i^0}{dy}(y - Y_{FB}) \tag{7.3}$$

where n_i is the total multiplicity of particle specie i, n_i^0 the same restricted to the fireball FB at rapidity y. The integration over the fireballs depends on the distribution of fireballs $\rho(Y_{FB})$ along the rapidity axis. Since it is possible to interchange the integration limits, it follows that

$$n_i = n_i^0 \int_{-Y}^{Y} dY_{FB}\, \rho(Y_{FB}) \tag{7.4}$$

When fireballs have the same temperature, particle ratios n_i/n_j do not anymore depend on the dynamics, which cancels out, but resemble that of a purely thermal Boltzmann distribution. This might explain the success of the statistical model in reproducing the particle ratios and 4π multiplicities (in which case, the dynamics can be ignored). In reference [26] are given predictions of particle ratios at $\sqrt{s_{NN}} = 200\,\text{GeV}$, assuming a temperature of 177 MeV and a baryo–chemical potential $\mu_B = 29\,\text{MeV}$. The charged meson ratios amount to $\pi^-/\pi^+ = 1.004$, $K^-/K^+ = 0.932$ and $K^-/\pi^- = 0.147$. From these values, the K^+/π^+ ratio is derived:

$$\frac{K^+}{\pi^+} = \frac{K^+}{K^-} \times \frac{K^-}{\pi^-} \times \frac{\pi^-}{\pi^+} \tag{7.5}$$

which leads to $K^+/\pi^+ = (1/0.932) \times 0.147 \times 1.004 = 0.158$. Note that the authors tuned the model parameters in order to describe the central region $|y| < 0.5$. The experimental ratios presented here, averaged over the mid–rapidity region[4] $|y| < 1.3$, are listed in Tab. 7.4. A remarkable agreement is noticed between the experimental measurements and the model

	π^-/π^+	K^-/K^+	K^+/π^+	K^-/π^-
Model [26]	1.004	0.932	0.147	0.158
Measurements (this work)	1.012 ± 0.004	0.937 ± 0.007	0.147 ± 0.001	0.156 ± 0.001

Tab. 7.4: Comparison between charged meson ratios from this analysis and statistical model predictions from [26]. Errors are statistical.

predictions. Therefore, it is tempting to conclude that the system is indeed in chemical equilibrium. However, one needs to investigate multiplicities from other particle species. The $\bar{p}/p$ reported in [38] amounts to 0.75 ± 0.04, very close to the prediction from [26] equal to 0.752. But using yields reported in [30], the $\bar{p}/\pi^-$ ratio is equal to 0.068 ± 0.001 (stat) while the prediction is 0.089. Nevertheless, the systematic error on this ratio makes the prediction and the measurement consistent.

The Statistical Model at the Early Stage

The SMES predicts an enhancement of the effective degrees of freedom from NN to AA collisions occurring around the SPS energy range, visible when the ratio of entropy S to number of participants N_{part} is correlated with the Fermi variable F. It has been mentioned in Sec. 2.4.1 that the observed increase from experimental data is deduced from a linear fit from SPS to RHIC energy domains on AA and NN data. The problem discussed then concerns the AA data from RHIC. The entropy is deduced from the total number of charged particles (unidentified) corrected after the measured particle ratios at RHIC and isospin to account for non measured π^0 and K^0's. Here is the opportunity to confront the model with yields of identified pions and kaons (multiplied by respectively 1.5 and 2 for non detected neutral pion and kaon yields). The model identifies the entropy per unit of pion entropy as being

$$S_\pi \sim \langle \pi \rangle + \kappa \left\langle K + \bar{K} \right\rangle + \delta \langle N_{part} \rangle \sim \langle N_{part} \rangle \times F \tag{7.6}$$

with $\kappa = 1.45$ and $\delta = 0.35$ [73, 78]. The number of participants N_{part} has been estimated from a Glauber calculation (HIJING and AMPT) for the top 5% central events and amounts to 366 ± 11 for AMPT and 360 ± 15 for HIJING (in both cases, the number of participants is calculated numerically). For the present exercise, the average is chosen: $N_{part} = 363 \pm 9.3$. Figure 7.19 shows the SMES entropy as a function of the Fermi variable F. The entropy derived from the total pion and kaon yields shows a very good agreement with the estimation deduced from PHOBOS data at $\sqrt{s_{NN}} = 200\,\mathrm{GeV}$ and confirms the divergence between AA and NN collisions. However, the parameter δ fixed at a value of 0.35 has been deduced from the net–baryon data from SPS and is assumed to be the same at RHIC energies. From data reported in [30], it is clear that the stopping measured at SPS is significantly from what is reported at $\sqrt{s_{NN}} = 200\,\mathrm{GeV}$. One needs to calculate δ from this recent measurement on stopping.

[4] This fit range is chosen in order to minimize the error since the ratios are rapidity boost invariant within this range.

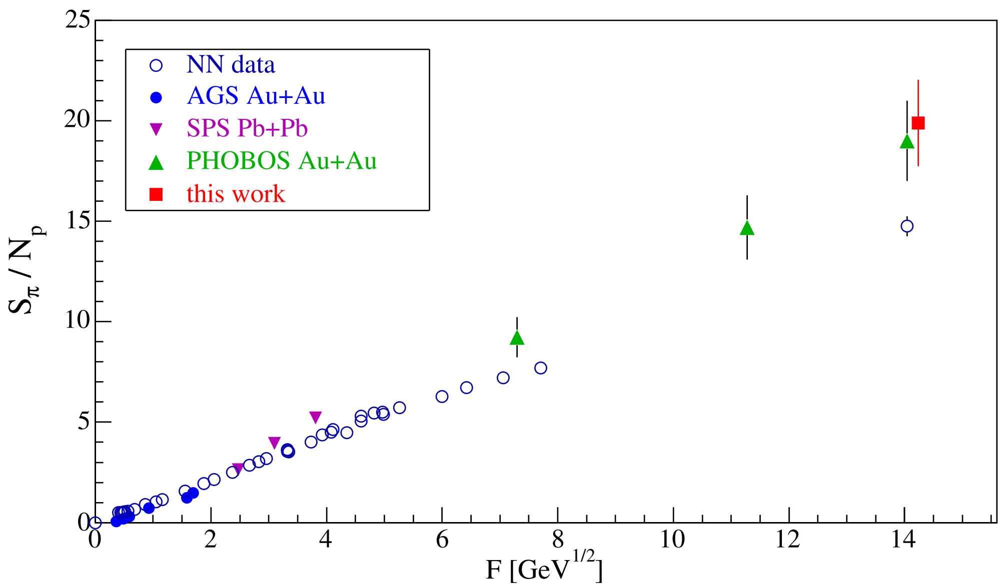

Fig. 7.19: Entropy as defined by the SMES model [73] as a function of the Fermi variable F. Errors are stat. + syst. The result of the present analysis has been shifted along the F axis for clarity.

The SMES model also predicts the ratio "strangeness to non–strange entropy". This ratio is defined as

$$R_\pi = 4\,\frac{N_{\bar{s}} + N_s}{S} \equiv \frac{\langle \Lambda + \bar{\Lambda} \rangle + \langle K + \bar{K} \rangle}{\langle \pi \rangle} \tag{7.7}$$

where $\langle \Lambda \rangle$ is the total yield of hyperon Λ (other hyperon yields are neglected). This ratio is predicted to saturate at g_s/g in the massless limit with $g_s/g \simeq 0.22$ in case of a thermalized QGP, and $\simeq 0.5$ if no QGP was formed at an early stage (cf. Sec. 2.4.1). Unfortunately, the total yields of Λ and $\bar{\Lambda}$ are not known. The STAR and PHENIX experiments measure only mid–rapidity yields. Therefore, only model dependent estimations can be given here. The models predict the following yields (Tab. 7.5):

		HIJING	AMPT
Total	Λ	56	45
	$\bar{\Lambda}$	32	42

Tab. 7.5: Λ and $\bar{\Lambda}$ yields from Au+Au at $\sqrt{s_{NN}} = 200\,\mathrm{GeV}$ calculated by HIJING and AMPT over the full rapidity rang..

There are discrepancies between HIJING and AMPT in individual Λ yields but the sum of totals are consistent with each other. Therefore, the strangeness to entropy ratio leads to

$$R_\pi \sim \frac{(42 + 45) + 2 \times (294 + 243)}{1.5 \times (1774 + 1809)} = 0.22 \pm 0.05 \tag{7.8}$$

Consequently, g_s/g is consistent with the expectation for the ideal gas of massless particles if a thermalized QGP existed at the early stage of the collisions. But it should be recalled that this estimation relies on HIJING or AMPT prediction on total hyperon yields and that the SMES parameters have to be tuned for the RHIC energy domain.

♣♣♣♣♣♣

Chapter 8

Summary and Conclusion

Inclusive invariant yields dN/dy of charged pions and kaons have been measured by the BRAHMS experiment over the rapidity range $-0.1 < y < 3.6$ from the top 5% central Au+Au collisions at $\sqrt{s_{NN}} = 200\,\text{GeV}$. Both kaons and pions show a significant multiplicity decrease from mid–rapidity to the highest rapidity interval covered. Pion rapidity densities amount to $300 \pm 3 \pm 8\%$ for π^+ and π^- over the rapidity range $|y| < 0.6$, and $94.5 \pm 5.4 \pm 10\%$ and $97.2 \pm 1.7 \pm 15\%$ at $y = 3.5$ respectively. The pion ratio is found consistent with unity over the full rapidity range and amounts to $1.015 \pm 0.004 \pm 0.05$. The estimated difference between negative and positive pion yields is not more than 2% in favor of an excess of π^- when summed over the rapidity range and extrapolated to rapidities outside the spectrometer acceptance. The estimated total yields are $1774 \pm 9 \pm 15\%$ for π^+ and $1809 \pm 9 \pm 15\%$ for π^-. The mean transverse momentum is found nearly constant as a function of rapidity and amounts to $\sim 460\,\text{MeV/c}$ at mid–rapidity and $\sim 420\,\text{MeV/c}$ at $y > 3$. The difference between K^+ and K^- is significant. K^- yields shows no significant difference over the rapidity range $|y| < 0.8$ and amount to $44.0 \pm 0.4 \pm 7\%$ while K^+ yields amount to $47.1 \pm 0.6 \pm 10\%$ over the range $|y| < 0.6$. As the rapidity increases, the difference between K^+ and K^- increases. At $y = 3.3$, yields are $18.1 \pm 0.6 \pm 10\%$ and $11.4 \pm 0.4 \pm 8\%$ respectively. The estimations of the total yields are found to be $294 \pm 6 \pm 15\%$ and $243 \pm 2 \pm 15\%$. The mean transverse momentum varies with rapidity more than for pions. At mid–rapidity, $\langle p_T \rangle$ amounts to $\sim 710\,\text{MeV/c}$ over the range $|y| < 1.1$ and decreases down to $\sim 580\,\text{MeV/c}$ at $y > 3$. The kaon to pion ratios also show a significant difference between positive and negatively charged mesons , related to the K^+ and K^- differences. At mid–rapidity, K^+/π^+ is $0.155 \pm 0.003 \pm 12\%$ while K^-/π^- is $0.146 \pm 0.003 \pm 11\%$. The ratios between total yields are found to be $0.166 \pm 0.003 \pm 15\%$ and $0.134 \pm 0.002 \pm 15\%$.

The energy systematics between SIS and topmost RHIC energies has been studied. It has been found that between the top AGS and low SPS energy (around $\sqrt{s_{NN}} = 8\,\text{GeV}$), a significant change in the dynamics occurs. Below this energy, the system does not seem to be driven by longitudinal expansion, which is proved by a study of net–proton rapidity density [30]. The net–baryon density is maximum close to the top AGS energy, the rapidity distributions of pions and kaons show no significant increase in width along the rapidity axis. But for higher $\sqrt{s_{NN}}$, the change in stopping is fast, the system undergoes a strong longitudinal flow which broadens the meson rapidity distributions. The kaon distribution widths are proportional to the beam rapidity. It shows how the net–baryon density decreases regularly, which reduces the importance of the strangeness associated production while string break–up and pair production are favored. This dynamics is reflected in the energy systematics of kaon to pion ratios, where a maximum of the positive ratio is found between top AGS and SPS energy, while the negative ratio increases steadily from AGS to RHIC energies. However, an intriguing behavior of the kaon inverse slope parameter with $\sqrt{s_{NN}}$ is noticed. A plateau structure is visible between the top AGS and top SPS energies, while an increase is measured from medium and top RHIC energies. An energy scan between SPS and RHIC is needed to investigate this behavior interpreted as a signature of deconfinement occurring at SPS [52].

The data of the present analysis have been compared to model predictions. It is found that the parton cascade models HIJING and AMPT fail at describing the data except for the π^-/π^+ ratio. HIJING underestimates mid–rapidity yields but describe high rapidity yields reasonably well within the full error of the data. AMPT systematically over-predicts multiplicities, especially for kaons (20% higher). The longitudinal and transverse dynamics are not reproduced either. HIJING and AMPT do not contain collective transverse flow and fail at describing the width of the rapidity distribution. Since the difference between the two models is mainly hadron rescattering in AMPT, the latter, based on resonance studies from AGS data (ART transport model), is probably not tuned properly for RHIC. Statistical models on the other hand turn out to describe the data in very good agreement with the measured ratios (hadron gas model) and entropy (model of the early stage). Since the hadron gas model does not make any assumption of the early stage, the apparent chemical equilibrium is not explained. The SMES, which introduces an early deconfined phase in chemical and thermal equilibrium (QGP), predicts an increase of entropy driven by the multiplicity of pions and kaons from NN to AA collisions. Indeed, the entropy deduced from the present data does fit with the prediction. The model also gives the strange to non strange entropy ratio at the high energy and density limit (vanishing mass of strange degrees of freedom). By including the total yields of Λ and $\bar{\Lambda}$ predicted by HIJING or AMPT (found equal in both cases), this ratio measured with the present data is found to be consistent with the prediction in case of a QGP phase at the early stage.

Bibliography

[1] J. Pochodzalla *et al.* , Phys. Rev. Lett. **75** (1995) 1040.

[2] L. G. Moretto, G. J. Wozniak, and reference therein , Ann. Rev. Nucl. Part. Sci. **43** (1993) 379.

[3] S. Bethke `hep-ex/0211012`.

[4] T. R. Klassen , Phys. Rev. **D 51** (1995) 5130.

[5] F. Karsch , Nucl. Phys. **A 698** (2002) 199.

[6] E. Laermann, 'Recent results from Lattice QCD calculations,' , Nucl. Phys. **A 610** (1996) 1c.

[7] J. Rafelski, J. Letessier, and A. Tounsi , Acta Phys. Pol. **B 27** (1996) 1037.

[8] R. J. Glauber, 'High-Energy Collision Theory,'. In *Lo, S.Y. (ed.): Geometrical pictures in hadronic collisions*, 83-182. (see Book Index).

[9] C. Y. Wong and Z. D. Lu , Phys. Rev. **D 39** (1989) 2606.

[10] X. N. Wang and M. Guylassy , Phys. Rev. **D 44** (1991) 3501.

[11] J. D. Bjorken , Phys. Rev. **D 27** (1983) 140.

[12] J. Schnaffer-Bielich, J. Bondorf, and I. Mishustin , Nucl. Phys. **A 625** (1997) 325.

[13] M. Mang. PhD thesis, IKF, Univ. Frankfurt, 1997.

[14] P. Senger , Acta Phys. Pol. **B 31** (2000) 2313.

[15] NA44 Collaboration, I. G. Bearden *et al.* , Phys. Rev. Lett B **79** (1997) 2080.

[16] D. Sandberg Master's thesis, Copenhagen University, 2002.

[17] N. Herrmann, J. P. Wessels, and T. Wienold , Ann. Rev. Nucl. Part. Sci. **49** (1999) 581–632.

[18] H. van Hecke, H. Sorge, and N. Xu , Phys. Rev. Lett. **81** (1998) 5764–5767.

[19] H. Sorge , Phys. Rev. **C 52** (1995) 3291.

[20] E. Schnedermann and U. Heinz , Phys. Rev. **C 47** (1993) 1738.

[21] T. Matsui and H. Satz , Phys. Lett. **B 178** (1986) 416.

[22] NA50 Collaboration, F. Prino *et al.* `hep-ex/0101052`.

[23] T. Hatsuda , Nucl. Phys. **A 544** (1992) 27c.

[24] W. Weise , Nucl. Phys. **A 610** (1996) 35c.

[25] F. Antinori *et al.* , Nucl. Phys. **A 698** (2002) 118.

[26] P. Braun-Munzinger, D. Magestro, K. Redlich, and J. Stachel , Phys. Lett **B 518** (2001) 41.

[27] F. Becattini , Z. Phys. **C 69** (1996) 485.

[28] R. Stock , Phys. Lett **B 456** (1999) 277.

[29] U. Heinz , Nucl. Phys. **A 661** (1999) 140.

[30] P. L. H. Christiansen. PhD thesis, Niels Bohr Institute, 2003.

[31] PHENIX Collaboration, S. Mioduszewski 2003.

[32] BRAHMS Collaboration, I. Arsene *et al.* , Phys. Rev. Lett. **91** (2003) 072305.

[33] C. M. G. Lattes, G. P. S. Occhialini, and C. F. Powell , Nature **160** (1947) 453.

[34] C. M. G. Lattes, G. P. S. Occhialini, and C. F. Powell , Nature **160** (1947) 486.

[35] H. Yukawa , Prog. Phys. Math. Soc. Jap. **17** (1935) 48.

[36] G. D. Rochester and C. C. Butler , Nature **160** (1947) 855.

[37] S. A. Bass *et al.* , Prog. Part. Nucl. Phys. **41** (1998) 225, `nucl-th/9803035`.

[38] BRAHMS Collaboration, I. G. Bearden *et al.* , Phys. Rev. Lett. **90** (2003) 102301.

[39] B. Andersson, G. Gustafson, G. Ingelman, and T. Sjöstrand , Phys. Rept **97** (1983) 31.

[40] J. Ranft , Phys. Rev. **D 37** (1988) 1842.

[41] PHENIX Collaboration, K. Adcox *et al.* , Phys. Rev. Lett. **88** (2002) 242301.

[42] NA49 Collaboration, S. V. Afanasiev *et al.* , Phys. Rev. **C 66** (2002) 054902.

[43] J. L. Klay, 'Transverse Mass and Rapidity Spectra o Pions and Protons from Au+Au Collisions at the AGS,'. PhD thesis, University of California, Davis, 2001.

[44] E895 Collaboration, J. L. Klay `nucl-ex/0306033`.

[45] FOPI Collaboration, N. Herrmann , Nucl. Phys. **A 610** (1996) 49c.

[46] FOPI Collaboration, D. Pelte *et al.* , Z. Phys. **A 357** (1997) 215.

[47] E866 Collaboration, L. Ahle *et al.* , Nucl. Phys. **A 661** (1999) 472.

[48] E866/E917 Collaboration, L. Ahle, B. B. others, Back, *et al.* , Phys. Lett. **B 490** (2000) 53.

[49] E866/E917 Collaboration, L. Ahle, B. B. others, Back, *et al.* , Phys. Rev. **C 60** (1999) 044904.

[50] KaoS Collaboration, D. Miśkowiec *et al.* , Phys. Rev. Lett. **72** (1994) 3650.

[51] KaoS Collaboration, M. Menzel *et al.* , Phys. Lett. **B 495** (2000) 26.

[52] M. I. Gorenstein, M. Gaździcki, and K. Bugaev `hep-ph/0303041`.

[53] J. Letessier and J. Rafelski , Int. J. Mod. Phys. **E 9** (2000) 107.

[54] H. Sorge , Phys. Rev. **C 52** (1995) 3291.

[55] M. Bleicher *et al.* , J. Phys. **G 25** (1999) 1859.

[56] K. Werner , Phys. Rep. **232** (1993) 87.

[57] W. Cassing and E. L. Bratkovskaya , Phys. Rep. **308** (1999) 65.

[58] B. Andersson and G. Gustafson , Z. Phys. **C 57** (1993) 485.

[59] S. Jeon and J. Kapusta , Phys. Rev. **C 56** (1997) 468.

[60] B. Andersson, G. Gustafson, G. Ingelman, and T. Sjöstrand , Phys. Rep. **97** (1983) 31.

[61] B. Zhang, C. M. Ko, B. Li, and Z. Lin , Phys. Rev. **C 61** (2000) 067901.

[62] Z. Lin, S. Pal, C. M. Ko, B. Li, and B. Zhang , Phys. Rev. **C 64** (2001) 011902.

[63] J. Ellis and K. Geiger , Phys. Rev. **D 54** (1996) 1967.

[64] R. Stock `hep-ph/0212287`.

[65] A. Bialas , Nuc. Phys. **A 715** (2003) 95c.

[66] R. Hagedorn , Nuovo Cimento **35** (1965) 395.

[67] F. Becattini and G. Pettini , Phys. Rev. **C 67** (2003) 015205.

[68] A. K. Wroblewski , Acta. Phys. Pol. **B 16** (1985) 379.

[69] F. Becattini , J. of Phys. **G 28** (2002) 1553.

[70] Z. Fodor and S. D. Katz , JHEP **03** (2002) 014.

[71] Z. Fodor and S. D. Katz, 'Lattice QCD results at finite T and μ,' `hep-lat/0204029`.

[72] P. Braun-Munzinger and J. Stachel , Nucl. Phys. **A 606** (1996) 320.

[73] M. Gaździcki and M. I. Gorenstein , Acta Phys. Pol. **B 30** (1995) 2705.

[74] E. Fermi , Prog. Theor. Phys. **5** (1950) 570.

[75] L. D. Landau , Izv. Akad. Nauk SSSR Ser. Fiz. **17** (1953) 51.

[76] L. Van Hove , Phys. Lett. **B 118** (1982) 138.

[77] M. Gaździcki and D. Röhrich , Z. Phys. **C 65** (1995) 215.

[78] M. Gaździcki , Z. Phys. **C 66** (1995) 659.

[79] M. Gaździcki and D. Röhrich , Z. Phys. **C 71** (1996) 55.

[80] P. Brady and J. Dunn , Eur. Phys. J. **C 5** (1998) 357.

[81] J. C. Dunlop and C. A. Ogilvie. PhD thesis, 2000.

[82] A. Tounsi and K. Redlich `hep-ph/0111159`.

[83] A. Tounsi and K. Redlich , Nucl. Phys. **A 715** (2003) 565c.

[84] S. Yacoob and J. Cleymans `hep-ph/0208246`.

[85] NA49 Collaboration, V. Friese *et al.* `nucl-ex/0305017`.

[86] W. M. Geist , Phys. Rep. **197** (1990) 263.

[87] P. V. Kajantie and J. Lindfors , Phys. Rev. Lett. **59** (1987) 2517.

[88] K. J. Eskola, P. V. Kajantie, and J. Lindfors , Nucl. Phys. **B 323** (1989) 37.

[89] G. Calucci and D. Treleani , Phys. Rev. **D 41** (1990) 3367.

[90] X. N. Wang and M. Guylassy technical report, 1991.

[91] PHOBOS Collaboration , Phys. Rev. Lett. **85** (2000) 3100.

[92] S. A. Bass *et al.* , Nucl. Phys. **A 661** (1999) 205.

[93] B. Zhang , Comp. Phys. Comm. **109** (1998) 193.

[94] C. M. Ko and B. Li , Phys. Rev. **C 52** (199) 2037.

[95] BRAHMS Collaboration, I. G. Bearden *et al.* , Phys. Rev. Lett. **87** (2001) 112305.

[96] M. Harrison, S. Peggs, and T. Roser , Annu. Rev. Nucl. Part. Sci. **52** (1998) 425.

[97] Y. Blyakhman. PhD thesis, New York University, 2001.

[98] M. Chiu *et al.* , Phys. Rev. Lett. **89** (2002) 012302.

[99] H. Ito. PhD thesis, Kansas Univeristy, 2002.

[100] BRAHMS Collaboration, I. G. Bearden *et al.* , Phys. Lett. **B523** (2001) 227.

[101] BRAHMS Collaboration, I. G. Bearden *et al.* , Phys. Rev. Lett. **88** (2002) 202301.

[102] E. Jakobsen Master's thesis, Niels Bohr Institute, 2001.

[103] C. H. Christensen Master's thesis, Niels Bohr Institute, 2003.

[104] BRAHMS Collaboration, M. Adamczyk *et al.* , Nucl. Inst. Meth. **A 499** (2003) 437.

[105] B. H. Samset Master's thesis, University of Oslo, 2001.

[106] J. I. Jøordre Master's thesis, University of Bergen, 2000.

[107] P. Staszel, 'Brahms analysis notes 27, 29, 34 and 38,' technical report.

[108] R. Karabowicz Master's thesis, University of Krakow, 2002.

[109] P. A. Cherenkov , Nucl. Instrum. Meth. **A 248** (1986) 1–4.

[110] PHENIX Collaboration, H. Ohnishi , Nucl. Phys. **A698** (2002) 659–662.

[111] C. E. Jørgensen. PhD thesis, Niels Bohr Institute, 2004.

[112] T. M. Larsen Master's thesis, University of Oslo, 2002.

[113] BRAHMS Collaboration, D. Ouerdane, 'Tof analysis,' technical report, 2003.

[114] R. Brun and F. Rademakers, 'Root - an object oriented data analysis framework,' in *Proceedings AIHENP'96 Workshop, Lausanne*, vol. A 389, p. 81. 1997. See also `http://root.cern.ch/`.

[115] H. Stock , Phys. Rep. **135** (1986) 259.

[116] STAR Collaboration, J. Castillo , Nucl. Phys. **A 715** (2003) 518.

[117] A. Mischke *et al.* , J. Phys. **G 28** (2002) 1761.

[118] J. Cleymans and K. Redlich , Phys. Rev. **C 60** (1999) 054908.

[119] D. E. Groom *et al.* , Eur. Phys. Jour. **C15** (2000) 1.

Appendix A

The BRAHMS Collaboration

I. G. Bearden[7], D. Beavis[1], C. Besliu[10], Y. Blyakhman[6], B. Budick[6], H. Bøggild[7], C. Chasman[1], C. H. Christensen[7], P. Christiansen[7], J. Cibor[3], R. Debbe[1], E. Enger[12], J. J. Gaardhøje[7], M. Germinario[7], K. Hagel[8], O. Hansen[7], A. Holm[7], A. K. Holme[12], H. Ito[11], E. Jakobsen[7], A. Jipa[10], F. Jundt[2], J. I. Jørdre[9], C. E. Jørgensen[7], R. Karabowicz[4], T. Keutgen[8], E. J. Kim[1], T. Kozik[4], T. M. Larsen[12], J. H. Lee[1], Y. K. Lee[5], G. Løvhøiden[12], Z. Majka[4], A. Makeev[8], B. McBreen[1], M. Mikelsen[12], M. Murray[8], J. Natowitz[8], B. S. Nielsen[7], J. Norris[11], K. Olchanski[1], J. Olness[1], D. Ouerdane[7], R. Płaneta[4], F. Rami[2], C. Ristea[10], D. Röhrich[9], B. H. Samset[12], D. Sandberg[7], S. J. Sanders[11], R. A. Scheetz[1], P. Staszel[7], T. S. Tveter[12], F. Videbæk[1], R. Wada[8], A. Wieloch[4], Z. Yin[9], I. S. Zgura[10]

[1] Brookhaven National Laboratory, Upton, New York 11973, USA
[2] Institut de Recherches Subatomiques and Université Louis Pasteur, Strasbourg, France
[3] Institute of Nuclear Physics, Krakow, Poland
[4] Smoluchkowski Inst. of Physics, Jagiellonian University, Krakow, Poland
[5] Johns Hopkins University, Baltimore 21218, USA
[6] New York University, New York 10003, USA
[7] Niels Bohr Institute, Blegdamsvej 17, Copenhagen University, Denmark
[8] Texas A&M University, College Station, Texas, 17843, USA
[9] University of Bergen, Department of Physics, Bergen, Norway
[10] University of Bucharest, Romania
[11] University of Kansas, Lawerence, Kansas 66049, USA
[12] University of Oslo, Department of Physics, Oslo, Norway

Appendix B

Variables and Coordinate Systems

Kinematic Variables

The notation given in Tab. B.1 is used in the entire thesis.

Definition	Notation
ion beam axis (direction of motion)	z
transverse axes to z	x (horizontal) and y (vertical)
angle between particle momentum direction and z	θ
particle momentum length	p
particle transverse momentum length	$p_T = p\,|\sin\theta|$
particle rest mass	m
particle transverse mass	$m_T = \sqrt{p_T^2 + m^2}$
angle between direction of p_T and x	ϕ
particle rapidity	y (not to be confused with axis y)
particle pseudo-rapidity	η

Tab. B.1: List of definitions and notations of the most common kinematic variables encountered in heavy-ion collision analyzes.

Since particles evolve at velocities $\beta = v/c$ close to 1, it is more convenient to deal with the rapidity y, which is an additive quantity (Galilean transformation) under a Lorentz boost: $y' = y + y_{boost}$. The rapidity is expressed as follows:

$$y = \frac{1}{2}\ln\left(\frac{E+p_z}{E-p_z}\right) = \frac{1}{2}\ln\left(\frac{1+\beta\cos\theta}{1-\beta\cos\theta}\right) \tag{B.1}$$

with E the total energy of the particle ($E^2 = p^2 + m^2$).

Another useful quantity is the pseudo-rapidity η, which is the infinite momentum limit or zero mass limit of y :

$$\eta = \lim_{p\to\infty}^{m\to 0} y = \frac{1}{2}\ln\left(\frac{p+p_z}{p-p_z}\right) = \frac{1}{2}\ln\left(\frac{1+\cos\theta}{1-\cos\theta}\right) = -\ln\left(\tan\frac{\theta}{2}\right) \tag{B.2}$$

With these definitions, the energy can be rewritten $E = m_T \cosh y$.

Center of Mass Energy

For fixed target experiments, the reaction energy is denoted E_{lab}, which is the beam energy per projectile nucleon (the target is at rest) in the laboratory frame. The other natural frame is the *center of mass* (CM), where the energy is $\sqrt{s}$, such that $s = (E_{proj} + E_{targ})^2|_{CM}$, which represents the true energy available for the reaction. In order to calculate the beam energy E_{CM} as a function of E_{lab}, the invariance of the scalar product under a Lorentz boost is used. For symmetric systems ($m_{proj} = m_{targ}$), the nucleus–nucleus CM corresponds to the NN CM. Therefore, if $p_p^\mu = (E_{lab}, \vec{p}_p)$ and $p_t^\mu = (m_N, \vec{0})$ are respectively the projectile and target momentum four–vectors in the laboratory frame (where m_N is the nucleon mass), $p_p^\nu = (E_{CM}, \vec{p}_p)$ and $p_t^\nu = (E_{CM}, \vec{p}_t) = (E_{CM}, -\vec{p}_p)$ in the CM frame, it follows that

$$p_p^\mu \cdot p_{\mu,t}\,|_{lab} = p_p^\nu \cdot p_{\nu,t}\,|_{CM} \tag{B.3}$$

$$m_N\, E_{lab} = E_{CM}^2 + \vec{p}_p^{\,2} = 2E_{CM}^2 - m_N^2 \tag{B.4}$$

$$E_{CM} = \sqrt{m_N\,(E_{lab} + m_N)/2} \tag{B.5}$$

Consequently, $\sqrt{s_{NN}} = 2\,E_{CM} = \sqrt{2m_N\,(E_{lab} + m_N)}$. For collider experiments, like BRAHMS at RHIC, collisions occur between two Au beams accelerated to the same energy but in opposite direction so that the laboratory frame coincides with the center of mass frame. In that case, $\sqrt{s}$ is simply the sum of both beam energies in the laboratory frame.

Coordinate Systems

There are two coordinate systems used in the analysis. One is defined with respect to the beam line and is called the global coordinate system. The other coordinate system is local to a given detector. The origin is defined as the center of the reactive volume (most of the time a squared box), axes are defined according to the natural axes of the box. Coordinate systems are illustrated in Fig. B.1.

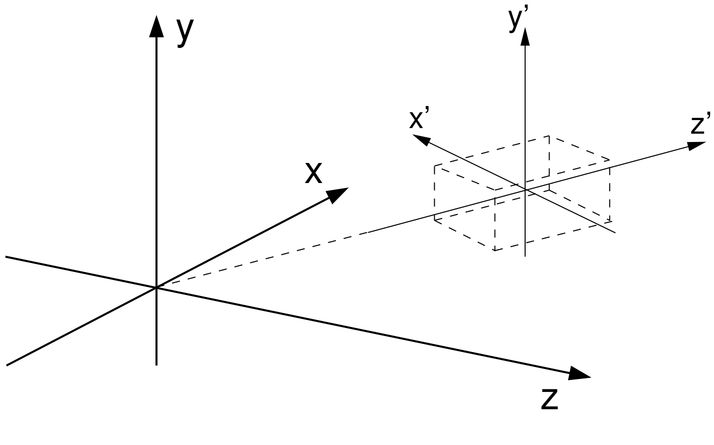

Fig. B.1: Global and local coordinate systems used in the analysis.

Appendix C

Hyperon and Resonance Decays

	Mass (MeV/c^2)	Full width Γ (MeV)	Decay products	Branching ratio
		Mesonic resonances		
η	547.3	0.00118	$\pi^+\,\pi^-\,\pi^0$	23.1%
			$\pi^+\,\pi^-\,\gamma$	4.77%
ρ	770.0	150.7	$\pi\,\pi$	$\sim$ 100%
ω	781.9	8.41	$\pi^+\,\pi^-\,\pi^0$	88.8%
			$\pi^+\,\pi^-$	2.2%
η'	957.8	0.203	$\pi^+\,\pi^-\,\eta$	43.8%
ϕ	1019.4	4.43	$K^+\,K^-$	49.1%
			$\rho\pi\,\pi^+\,\pi^-\,\pi^0$	15.5%
K^*	892	50.8	$K\,\pi$	$\sim$ 100%
		Baryonic resonances		
Δ	$\approx$ 1232	$\approx$ 120	$N\,\pi$	>99%
N	$\approx$ 1440	$\approx$ 350	$N\,\pi$	60–70%
			$N\,\pi\,\pi$	30–40%
			$N\,\Delta\,\pi$	20–30%
N	$\approx$ 1520	$\approx$ 120	$N\,\pi$	50–60%
			$N\,\pi\,\pi$	40–50%
			$N\,\Delta\,\pi$	15–25%
		Hyperons		
Λ	1115.7	$c\tau = 7.89\,\mathrm{cm}$	$p\,\pi^-$	63.9%
Λ	1407	50	$\Sigma\,\pi$	100%
Λ	1519.5	15.6	$N\,K$	45%
			$\Sigma\,\pi$	42%
			$\Lambda\,\pi\,\pi$	10%
Σ^+	1189.4	$c\tau = 2.396\,\mathrm{cm}$	$n\,\pi^+$	48.31%
Σ^-	1197.4	$c\tau = 4.43\,\mathrm{cm}$	$n\,\pi^-$	99.8%
Σ	$\approx$ 1385	$\approx$ 37	$\Lambda\,\pi$	88%
			$\Sigma\,\pi$	12%
Ξ^-	1321.32	$c\tau = 4.91\,\mathrm{cm}$	$\Lambda\,\pi^-$	99.89%
Ω^-	1672.45	$c\tau = 2.46\,\mathrm{cm}$	$\Lambda\,K^-$	67.8%
			$\Xi^0\,\pi^-$	23.6%

Tab. C.1: Hadronic resonances and hyperons with at least one charged meson in the decaying products. Data are taken from [119].

Appendix D

Beam–Beam Counter Vertex

A collision occurs at z_{vtx} between the BBC arrays. Particles are emitted and a few are detected by some BBC tubes. A sketch is shown on Fig. D.1.

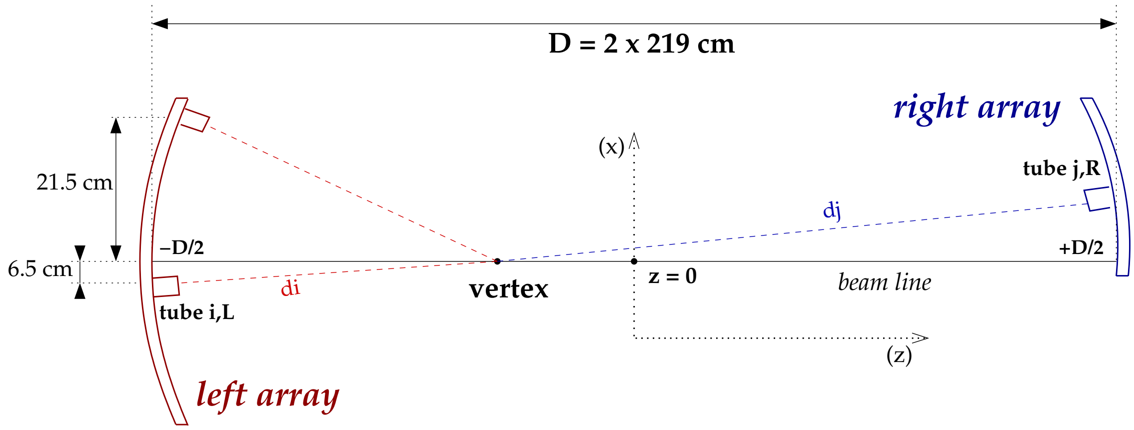

Fig. D.1: BBC vertex reconstruction scheme (top view). Dashed lines are particle paths.

If tube i from the left array and j from the right array deliver signals, according to Eq. 4.6, it follows that

$$tdc_{Li} = tof_{Li} + off_{Li} + slew_{Li} - t_{start} \tag{D.1}$$
$$tdc_{Rj} = tof_{Rj} + off_{Rj} + slew_{Rj} - t_{start} \tag{D.2}$$

Subscripts $_L$ and $_R$ are now removed for readability. The particle flight time tof is equal to $d/(\beta c)$ but can be approximated by d_z/c where d_z is the longitudinal distance from z_{vtx} to the tube due to the high momentum of forward scattered particles. With $z_{IP} = 0$ and the left (right) array located at $z = -(+)D/2$ with D the distance between the BBC arrays, it follows that

$$tdc_i = (z_{vtx} + D/2)/c + off_i + slew_i - t_{start} \tag{D.3}$$
$$tdc_j = (D/2 - z_{vtx})/c + off_j + slew_j - t_{start} \tag{D.4}$$

If Eq. D.4 is summed with and subtracted to Eq. D.3,

$$tdc_{i+j} = \frac{D}{c} + off_{i+j} + slew_{i+j} - 2t_{start} \tag{D.5}$$
$$\Delta tdc_{ij} = \frac{2}{c}\, z_{vtx} + \Delta off_{ij} + \Delta slew_{ij} \tag{D.6}$$

Consequently,

$$t_{start} = \frac{1}{2}\left[\left(\mathit{off}_{i+j} + \mathit{slew}_{i+j}\right) + \frac{D}{c} - \mathit{tdc}_{i+j}\right] \quad \text{(D.7)}$$

$$z_{vtx} = \frac{c}{2}\left[\Delta \mathit{tdc}_{ij} - \Delta \mathit{off}_{ij} - \Delta \mathit{slew}_{ij}\right] \quad \text{(D.8)}$$

But for any tube i, $\mathit{tdc}_i - \mathit{off}_i - \mathit{slew}_i = t_i$, the calibrated time. The equations finally become

$$t_{start} = \frac{1}{2}\left[\frac{D}{c} - t_{i+j}\right] \quad \text{(D.9)}$$

$$z_{vtx} = \frac{c}{2}\,\Delta t_{ij} \quad \text{(D.10)}$$

The last equations reveal that given any pair of hits (i_L, j_R), vertex and start–time can be derived by respectively subtracting and summing the calibrated times of these two hits. But using only one pair of hits would not lead to the best resolution. That is why a time average is built for each array. Eq. D.9 and D.10 can be written

$$t_{start} = \frac{1}{2}\left[\frac{D}{c} - \langle t_L\rangle - \langle t_R\rangle\right] \quad \text{(D.11)}$$

$$z_{vtx} = \frac{c}{2}\left(\langle t_L\rangle - \langle t_R\rangle\right) \quad \text{(D.12)}$$

Appendix E

Momentum Spectra

Definition

Particle transverse momentum spectra are by definition the number of particles of transverse momentum (mass) p_T (m_T) as a function p_T (m_T) per unit of rapidity. This number is related to the differential cross section by the following equation (identical in p_T or m_T) :

$$\frac{dN}{2\pi\, m_T dm_T dy} = E\,\frac{d^3\sigma}{\sigma\, dp^3} \tag{E.1}$$

where σ is the total cross–section. The right member of this equation, and consequently the left one, is boost invariant. The equality comes from the transformation of the momentum space $dp_x dp_y dp_z$ to the space $dm_T dy d\phi$. The factor $1/2\pi$ is a normalization coming from the integration over ϕ because particle distributions from central heavy ion collisions exhibit an azimuthal symmetry (isotropy in ϕ). The transverse mass differential $d\,/m_T dm_T$ can be replaced by $d\,/p_T dp_T$. Indeed, according to the definition of m_T:

$$\begin{aligned} m_T^2 &= p_T^2 + m^2 && \text{(E.2)} \\ d\left(m_T^2\right) &= d\left(p_T^2\right) + 0 && \text{(E.3)} \\ 2m_T dm_T &= 2p_T dp_T && \text{(E.4)} \\ m_T dm_T &= p_T dp_T && \text{(E.5)} \end{aligned}$$

Fit Functions

The fit functions used in the analysis are meant to describe the momentum spectra over the p_T range covered. They are then used to estimate the total yield by extrapolating to p_T regions outside the acceptance. The functions used in this thesis are

$$\begin{aligned} \text{Exponential in } m_T &: \quad A\exp\left[-\frac{(m_T - m)}{T}\right] \\ \text{Sum of exponentials in } m_T &: \quad B_1\exp\left[-\frac{(m_T - m)}{T_1}\right] + B_2\exp\left[-\frac{(m_T - m)}{T_2}\right] \\ \text{Power law in } p_T &: \quad C\left(1 + \frac{p_T}{p_0}\right)^{-n} \end{aligned}$$

The T parameters are called the inverse slope parameters and are identified as the apparent temperature of the particle source. This jargon originates from statistical physics, where distribution functions are given by the Fermi or Bose statistics (quantum case) or Boltzmann statistics (classical case, high temperature limit of the quantum distributions). The coefficients A, $B_{1,2}$ and C are normalization factors that can be related to the integrated yield at rapidity y. For example, the coefficient A is obtained as follows:

$$
\begin{aligned}
\frac{dN}{dy} &= \int_m^\infty 2\pi m_T\, A \exp\left[-\frac{(m_T - m)}{T}\right] dm_T \\
&= 2\pi A \int_m^\infty m_T \, \exp\left[-\frac{(m_T - m)}{T}\right] dm_T \\
&= 2\pi A \left\{ -T\, m_T \exp\left[-\frac{(m_T - m)}{T}\right]\right\}_m^\infty + 2\pi AT \int_m^\infty \exp\left[-\frac{(m_T - m)}{T}\right] \\
&= 2\pi ATm + 2\pi AT \left\{ -T \exp\left[-\frac{(m_T - m)}{T}\right]\right\}_m^\infty \\
&= 2\pi AT(m+T), \text{ so that} \\
A &= \frac{dN/dy}{2\pi\, T(m+T)}
\end{aligned}
$$

B_1 and B_2 are also obtained in the same way. For the power law, it reads

$$
\begin{aligned}
\frac{dN}{dy} &= \int_0^\infty 2\pi p_T C \left(1 + \frac{p_T}{p_0}\right)^{-n} dp_T \\
&= 2\pi C \int_0^\infty p_T \, \left(1 + \frac{p_T}{p_0}\right)^{-n} dp_T \\
&= 2\pi C \left[\frac{p_0\, p_T}{1-n} \left(1 + \frac{p_T}{p_0}\right)^{1-n}\right]_0^\infty - \; 2\pi C \int_0^\infty \frac{p_0}{1-n} \left(1 + \frac{p_T}{p_0}\right)^{1-n} dp_T \\
&= 0 \text{ (if } n > 1) \; - \; 2\pi C p_0 \left[\frac{p_0}{(1-n)(2-n)} \left(1 + \frac{p_T}{p_0}\right)^{2-n}\right]_0^\infty \\
&= \frac{2\pi\, C p_0^2}{(1-n)(2-n)}, \text{ if } n > 2, \text{ so that} \\
C &= \frac{(n-1)(n-2)}{2\pi\, p_0^2} \frac{dN}{dy}
\end{aligned}
$$

The power n has to fulfill the condition $n > 2$. Experimentally, fits on pion spectra give $n \gtrsim 20$.

Appendix F

Fermi Variable

The Statistical Model of the Early Stage (SMES) predicts the production of entropy in central AA collisions, introduced by Fermi [74] and Landau [75], revisited by Gaździcki [73]. In this model, the entropy is produced at the early stage of the collision when all incident matter is highly excited. The thermalized matter is assumed to expand adiabatically to the freeze–out point, preserving the early stage entropy. The energy density ϵ available for particle production is estimated from the Lorentz contracted volume of the overlapping nuclei and $\sqrt{s_{NN}}$:

$$\begin{aligned} V &\sim \frac{V_0}{\gamma} = \frac{2m_N V_0}{\sqrt{s_{NN}}} \\ \epsilon &= \frac{E}{V} \sim \frac{\left(\sqrt{s_{NN}} - 2m_N\right)\sqrt{s_{NN}}}{2m_N V_0} \end{aligned}$$

In order to relate the entropy density σ to the energy density ϵ, an equation of state is needed. Since most of the produced particles are pions, the entropy is nearly proportional to the pion multiplicity. This led Landau to choose the equation of state of a relativistic gas of massless pions as a first order approximation, $p = \epsilon/3$, where p is the pressure. For a relativistic black body with $\epsilon \sim T^4$, with T the temperature, the relation between σ and ϵ reads:

$$T\sigma = \epsilon + p - \mu n = \frac{4}{3}\epsilon$$

The chemical potential μ is zero for massless pions, which implies $\sigma \sim \epsilon^{4/3}$. Therefore, the early stage entropy S_E is:

$$\begin{aligned} S_E &= \sigma V \\ &\sim V\left[\left(\sqrt{s_{NN}} - 2m_N\right)\sqrt{s_{NN}}\right]^{3/4} \end{aligned}$$

In practice, even in central collisions, not all nucleons participate. The volume has to be scaled according to the average number of participant nucleons. By using a geometric Glauber calculation and the inelastic cross–section for nucleon interaction $\sigma_N N$, the average number of participants at a given impact parameter is [9]:

$$\langle N_{part} \rangle = \frac{\sigma_{pA}}{\sigma_{AA}} (A + A)$$

where σ_{pA} and σ_{AA} are production cross–section in nucleon–nucleus and nucleus–nucleus collisions respectively. The participant volume V can now be expressed in terms of $\langle N_{part} \rangle$. The early stage entropy becomes

$$S_E \sim \langle N_{part} \rangle \, \frac{\left(\sqrt{s_{NN}} - 2m_N\right)^{3/4}}{\sqrt{s_{NN}}^{1/4}}$$

The dependence of S_E on $\sqrt{s_{NN}}$ was obtained by Fermi [74] for high energy collisions, which led him to define the variable F:

$$F \equiv \frac{\left(\sqrt{s_{NN}} - 2m_N\right)^{3/4}}{\sqrt{s_{NN}}^{1/4}}$$